POLYTECHNIQUE MONTRÉAL

affiliée à l'Université de Montréal

Modeling and experimental validation of a water-to-water heat pump

GEOFFREY VIVIESCAS IBARRA

Département de génie mécanique

Thèse présentée en vue de l'obtention du diplôme de *Philosophiæ Doctor*

Génie mécanique

Septembre 2024

POLYTECHNIQUE MONTRÉAL

affiliée à l'Université de Montréal

Cette thèse intitulée :

Modeling and experimental validation of a water-to-water heat pump

présentée par **Geoffrey VIVIESCAS IBARRA**

en vue de l'obtention du diplôme de *Philosophiæ Doctor*

a été dûment acceptée par le jury d'examen constitué de :

Huu Duc VO, président
Michaël KUMMERT , membre et directeur de recherche
Michel BERNIER, membre et co-directeur de recherche
Robert LEGROS, membre
Vincent LEMORT, membre externe

DEDICATION

To my family: My father, Elmer Viviescas, who taught me to work hard, to be strong, and showed me what a man should and should not do. To my mother, who instilled in me the value of family, the home, taking care of each other as a team, and being one for all and all for one.

To my younger sister, Deissy, so beautiful, tender, hardworking, and with an honest heart, I express my sincere admiration. To my older sister, Yenny, whom I consider the heart of the family, full of love, sensitivity, kindness, and unconditional support. Thank you for making this family not only a beautiful one but also a larger one.

I love you all; you mean everything to me

.

ACKNOWLEDGEMENTS

I would like to extend my sincere gratitude to Professor Michel Bernier. Primarily, I am grateful for his belief in me during our initial virtual interview from my home country in Colombia, and for giving me the opportunity to undertake this research. At that moment, I recognized it as a significant professional opportunity, and now, five years later, I am certain it was the right path. I am thankful not only for his supervision but also for his motivation and challenges throughout my academic program. I owe a great debt of gratitude for his patience, inspiration, and unwavering support, as he guided me through this project, always demanding my best efforts. I have nothing but admiration for his professional life and the knowledge he generously shared.

To my colleagues and friends in the group, Aziz Mbaye, for our time in classes and office chats; to Carlos Prieto, who, though never an office mate was always close by, I express my sincere admiration for his great discipline and clarity of thought. To my friend Seperh Gholamrezaie, for making the doctoral experience complete with his humor, charisma, and for helping me improve my English through our trivial, professional, philosophical, and heartfelt conversations.

I also want to thank the cherished gem who has been my companion since the start of this journey, whom I love with all my heart and hope for eternal happiness. I am grateful for the wonderful moments we have shared and for the countless lessons, you have taught me, making me a better person.

To my two sisters, Yenny and Deissy, my mother Fatima, and my father Elmer, each trip back to Colombia was a renewal of energy and motivation to continue this path. Thank you for your support from afar.

Additionally, I extend my gratitude to Professors Massimo Cimmino and Michaël Kummert for their invaluable teachings and enjoyable evenings from 5 to 7. The workgroup couldn't have had better professors humane, sensitive, and passionate about their work.

At the end of this journey, I had the opportunity to join Canmet Energy as a part-time researcher. Thank you, Dr. Messaoud, for your trust, motivation, and understanding during this crucial stage.

This research was initially supported by the Fonds de Recherche du Québec - Nature et Technologies (FRQNT) in the form of a research team grant. The support of the National Sciences and Engineering Research Council of Canada is also gratefully acknowledged.

RÉSUMÉ

Cette étude porte sur le développement d'un modèle élaboré pour analyser l'efficacité énergétique et le comportement opérationnel des pompes à chaleur eau-eau, en se concentrant sur celles utilisant des compresseurs à vitesse fixe et variable.

Dans la première partie de ce travail, l'effort de modélisation porte sur les échangeurs de chaleur intermédiaires, les détendeurs, et les configurations impliquant l'utilisation de compresseurs multiples et de compresseurs à vitesse variable. Il est démontré que l'intégration d'échangeurs intermédiaires entre le condenseur et l'évaporateur peut améliorer le coefficient de performance (COP) des pompes à chaleur. Cependant, l'augmentation du COP dépend significativement du fluide frigorigène sélectionné et des paramètres opérationnels du système. Les détendeurs ont le potentiel d'augmenter le COP des pompes à chaleur en produisant du travail en utilisant la différence de pression entre le condenseur et l'évaporateur. Des augmentations de COP de l'ordre de 6 à 13 % sont possibles. L'utilisation de plusieurs compresseurs à vitesse fixe de différentes capacités et connectés en parallèle peut augmenter le facteur de performance saisonnier (SPF) d'environ 12 %. Les compresseurs à vitesse variable offrent une amélioration supplémentaire de 8 % du SPF par rapport aux compresseurs à vitesse fixe.

Ensuite, l'approche de modélisation est raffinée en se concentrant sur la modélisation de composants réels. Des contributions sont apportées dans le domaine de la modélisation des échangeurs de chaleur à plaques (condenseur et évaporateur) ainsi que dans la prédiction des performances des compresseurs en utilisant une version améliorée de la norme AHRI pour les compresseurs à vitesse variable. Résoudre le modèle complet d'une pompe à chaleur nécessite de gérer un ensemble complexe d'équations non linéaires impliquant des calculs de propriétés thermo-physiques, des coefficients de transfert de chaleur et des surfaces d'échange thermique. Cet ensemble d'équations est sensible aux valeurs de départ, ce qui rend difficile l'exécution de simulations à long terme pour des paramètres d'entrée changeant rapidement. Pour contourner ce problème, un modèle TRNSYS basé sur des cartes de performance est amélioré en incluant une vitesse minimale de fonctionnement ainsi qu'une représentation précise de la consommation d'énergie à charge partielle. Le modèle est ensuite utilisé pour examiner l'impact de l'opération à vitesse variable sur la longueur du forage de puits géothermiques utilisés pour pompes à chaleur

géothermiques. Il est montré que la courbe de couverture énergétique de la pompe à chaleur en fonction du pourcentage de couverture des besoins maximums est similaire à celle observée avec les compresseurs à vitesse fixe.

La validation expérimentale du modèle est réalisée à l'aide d'un banc d'essai spécifiquement construit pour cette étude. L'installation comprend deux boucles secondaires à température contrôlée permettant la validation en régime permanent du modèle. Il est démontré que les prédictions de COP du modèle correspondent aux données expérimentales dans les limites de l'incertitude expérimentale. Le modèle est capable de prédire des scénarios où la surface de sous-refroidissement se réduit à zéro, une condition non souhaitable, suggérant une condensation incomplète du fluide frigorigène, ce qui pourrait interférer avec le fonctionnement de la valve d’expansion thermostatique. Ces prédictions coïncident avec les directives fournies par le fabricant pour ces conditions non désirées.

ABSTRACT

Central to this study is the creation of an elaborate model to analyze the efficiency and operational behavior of water-to-water heat pumps, with a focus on those employing fixed-speed and variable-speed compressors.

In the first part of this study, the modeling effort encompasses a detailed look at developments like intermediate heat exchangers, expanders, and configurations involving the use of multiple compressors and variable-speed compressors. It is shown that the integration of intermediate heat exchangers between the condenser and evaporator can enhance the efficiency of heat pumps. However, the degree of enhancement is significantly dependent on the selected refrigerant and the operational parameters of the system. Expanders have the potential to increase the efficiency of heat pumps by providing work using the pressure difference between the condenser and evaporator: COP increases in the order of 6 to 13% are possible. Employing multiple fixed-speed compressors (MC) of different capacities piped in parallel can increase the seasonal performance factor (SPF) by about 12%. Variable-speed compressors offer an extra 8% of SPF improvement over MC.

Then, the modeling approach is improved by focusing on modeling real components. Contributions are made in the area of modeling plate heat exchangers (condenser and evaporator) as well as in the prediction of compressor performance using an improved version of the AHRI standard for variable speed compressors. Solving the complete model of a heat pump requires handling a complex set of nonlinear equations involving thermo-physical property calculations, heat transfer coefficients and heat transfer areas. This set of equations is sensitive to initial guess values which makes it difficult to perform long-term simulations for fast changing inlet parameters. To circumvent this problem an improved TRNSYS performance-based model is proposed which include a minimum operational speed along with an accurate representation of power consumption at part load. The model is then used to examine the impact of variable speed operation on the borehole length of ground-source heat pumps. It is shown that the curve of energy coverage versus effect coverage is similar to the one experienced by fixed-speed compressors.

Experimental validation of the model is performed with a test bench specifically built for this study. The facility includes two temperature controlled secondary loops which enable steady-state validation of the model. It is shown that the COP predictions fall within the limits of experimental

uncertainty in every case. The model can predict scenarios where the subcooling surface area reduces to zero, a non-desirable condition, suggesting incomplete condensation of the refrigerant, which could interfere with the operation of the expansion valve. These predictions coincide with the guidelines provided by the manufacturer for non-operational conditions.

TABLE OF CONTENTS

LIST OF TABLES

LIST OF FIGURES

LISTE OF SYMBOLS AND ABBREVIATIONS

A_x	Channel flow area (m^2)
A_{cond}	Surface of the PHX used for condensation (m^2)
A_{dsh}	Surface of the PHX used for desuperheating (m^2)
A_{sc}	Surface of the PHX used for subcooling (m^2)
$C_{p,w}$	Average water heat capacity (kJ/kg-K)
$C_{p,r}$	Average refrigerant heat capacity (kJ/kg-K)
D_h	Hydraulic diameter (m)
h	Enthalpy (kJ/kg)
h_w	Heat transfer coefficient for water (kW/m^2-K)
h_{ref}	Heat transfer coefficient for refrigerant (kW/m^2-K)
Hz	Compressor speed (Hertz)
$\dot{m}_{corrected}$	Corrected refrigerant mass flow rate (kg/s)
$\dot{m}_{rated}$	Refrigerant mass flow rate at rated superheat (kg/s)
$\dot{m}_r$	Refrigerant mass flow rate (kg/s)
$\dot{m}_{w_L}$	Secondary fluid flow rate on the load side (kg/s)
$\dot{m}_{w_S}$	Secondary fluid flow rate on the source side (kg/s)
P	Power at reference conditions (kW)
P_b	Saturation pressure at bulb temperature (kPa)
P_e, P_{evap}	Evaporator pressure (kPa)
$P_{c,}P_{cond}$	Condenser pressure (kPa)
P_{dis}	Discharge compressor pressure (kPa)
Q_{cond}	Heat transferred in the condensation zone (kW)
Q_{dsh}	Heat transferred in the desuperheating zone (kW)
Q_{evap}	Heat transferred in the evaporating zone (kW)
Q_g	Heat exchanged with the ground (kW)
Q_L	Heat extracted from the load (kW)
Q_S	Heat rejected at the source (kW)
Q_{sc}	Heat transferred in the subcooling zone (kW)
$Q_{T_{cond}}$	Total heat transferred in the condenser (kW)

$Q_{T_{evap}}$	Total heat transferred in the evaporator (kW)
R_{b}	borehole thermal resistance (m-K/W)
T_1	Temperature of the refrigerant leaving the evaporator (°C)
T_2	Discharge compressor temperature (°C)
T_3	Temperature of the refrigerant leaving the condenser (°C)
T_4	Temperature of the refrigerant leaving the TEV (°C)
T_b	Borehole wall temperature (°C)
T_H	Temperature of the hot reservoir (°C)
T_L	Temperature of the cold reservoir (°C)
$T_{x,1}$	Vapor saturation temperature in the evaporator (°C)
$T_{x,2}$	Vapor saturation temperature in the condenser (°C)
T_{amb}	Ambient temperature (°C)
T_D	Discharge dew-point temperature (°C)
T_S	Suction dew-point temperature (°C)
T_{set}	Load set point temperature (°C)
T_w	Water temperature (°C)
$T_{w_{S_{in}}}$	Inlet source temperature to the heat pump (°C)
$T_{w_{S_{out}}}$	Outlet source temperature from the heat pump (°C)
$T_{w_{L_{in}}}$	Inlet load temperature to the heat pump (°C)
$T_{w_{L_{out}}}$	Outlet load temperature from the heat pump (°C)
U_{global}	Global heat exchange coefficient (kW/m^2-K)
$\dot{v}$	Compressor volumetric displacement rate (m^3/h)
W	Electrical power supplied by the compressor (kW)
$x_{A_{cond}}$	Fraction of the total heat exchanger surface area used in condensation (-)
$x_{A_{dsh}}$	Fraction of the total heat exchanger surface area used in desuperheating (-)
$x_{A_{sc}}$	Fraction of the total heat exchanger surface area used in subcooling (-)

Indices and exponents

aux	Auxiliary, often referred to as heating provided by electrical resistances
Carnot	Reversible Carnot heat pump cycle
C	Cold reservoir side
cond	Condenser
evap	Evaporator
ex	Exergy
ext	Exterior
int	Interior
in	Property valued at the input of a specific component
out	Property valued at the output of a specific component
is	Isentropic process
H	Hot reservoir side
load	Refers to a variable or property of the system that represents the heat sink
source	Refers to a variable or property of the system that represents the heat source
nom	Nominal
L	Load
S	Source
sat_c	Property evaluated in the condenser as saturated vapor
sat_e	Property evaluated in the evaporator as saturated vapor
w	Water
s	Suction
D	Discharge

Nomenclature (related to the PHX model)

ϕ	Surface enlargement factor
β	Chevron angle
Re	Reynolds number $\left(Re = \frac{\rho V D}{\mu}\right)$
Nu	Nusselt number $\left(Nu = \frac{hD}{k}\right)$
k_p	Plate thermal conductivity (W/m-K)

X_m	Mean vapor quality
G	Mass flux $\left(\frac{\text{kg}}{\text{m}^2}\text{s}\right)$
G_{eq}	Equivalent mass flux $\left(\frac{\text{kg}}{\text{m}^2}\text{s}\right)$
μ_l	Viscosity of the liquid phase (Pa.s)
h	Heat transfer coefficient $\left(\frac{\text{W}}{\text{m}^2}℃\right)$
q	Heat transfer rate (kW)
P_r	Actual pressure P over critical pressure P_c (-)
M	Molar mass $\left(\frac{\text{kg}}{\text{kmol}}\right)$

Greek symbols

α	Pressure equivalent of a static superheat setting (kPa)
β	Constant flow area of the TEV (m^2)
ε	Heat exchanger effectiveness (-)
η	Efficiency (-)
ρ_s	Refrigerant density at the compressor suction (kg/m^3)
ρ_{rco}	Saturated liquid refrigerant density in the condenser (kg/m^3)

Abbreviations

BPHE	Brazed plate heat exchangers
CCHP	Cold-climate heat pump
COP	Coefficient of performance
COP_C	Coefficient of performance in cooling
COP_H	Coefficient of performance in heating
DHW	Domestic hot water
FSC	Fixed-speed compressor
FSHP	Fixed-speed heat pump
GHE	Ground heat exchanger
GSHP	Ground source heat pump
HP	Heat Pump
HVAC	Heating, Ventilation, and Air Conditioning

NTU	Number of transfer units
PHX	Plate heat exchangers
PHX	Plate heat exchanger
PLF	Part Load Factor
PLR	Part Load Ratio
PR	Pressure ratio
RPI	Relative performance index
RWI	Relative work index
SC	Subcooling (°C)
SH	Superheat (°C)
SLHX	Suction line heat exchangers
SPF	Seasonal performance factor
TEV	Thermal expansion valve
VCC	Vapor compression cycle
VSC	Variable-speed compressor

LIST OF APPENDICES

CHAPTER 1 INTRODUCTION

Heat pumps are pivotal in the energy transition, providing efficient heating and cooling solutions for residential, commercial, and industrial applications. In heating, they can reduce energy consumption by a factor of 2 to 5 compared to electric resistance heating.

This project is part of a research team project funded by the FRQNT with the goal of designing improved heat pumps with small low-cost centrifugal compressors. As an initial first step towards that goal, this study focusses on detailed modeling of heat pump components and the design and construction of an experimental test bench.

To evaluate heat pump performance and model behavior, various approaches can be employed, each requiring different levels of input detail. One approach involves using standards like EN 14511 [1] and EN 14825[2], and their American equivalents, AHRI 210/240 [3] and AHRI 340/360 [4]. These standards ensure consistent performance evaluation of air conditioners and heat pumps. EN 14511 and AHRI 210/240 focus on fixed-condition performance testing, while EN 14825 and AHRI 340/360 assess seasonal performance, considering variable temperatures and part-load conditions. ISO 13256 [5, 6] targets water-source heat pumps, specifying testing conditions and methods to determine capacities and efficiency.

Another approach to evaluate their annual performance is to use dynamic simulations to evaluate their performance under specific or variable operational conditions, using software tools such as TRNSYS [7], EnergyPlus [8], EES [9] and Modelica [10]. In these tools, the mathematical representation of heat pumps can be classified into several types: performance maps, characteristic curves, equation-fit models, parameter estimation-based models, and physical models. As the complexity of these models increases from characteristic performance and equation-fit models to parameter estimation-based and physical models, so do the computational effort, level of detail, and required expertise. For designing intricate systems and conducting extended observation periods, simpler models with manageable computational demands are preferred [11].

Conventional heat pump models frequently rely on simplifying assumptions that fail to capture real-world operating conditions, leading to potential inaccuracies. Common assumptions include constant temperature differences between the refrigerant and secondary fluid in heat exchangers,

constant isentropic efficiency in compressors, fixed degrees of superheat or subcooling, and neglecting variations in phase changes within heat exchangers. These simplifications can cause significant deviations from actual system performance, impacting both energy consumption estimates and system sizing accuracy.

Therefore, developing more accurate heat pump models is crucial to study various operational conditions, enabling the optimization of design and operation of heat pumps.

The physical-based model approach enables the optimization of the heat pump or its individual components at both the refrigerant cycle and the component geometry levels. It also allows adaptation to evaluate new compressor technologies, such as variable speed compressors, multi-stage compressors, and even small-scale centrifugal compressors. Moreover, physical models enable the integration of heat pumps into HVAC systems that incorporate new emerging technologies by using new refrigerants or adapting existing systems to new trends through drop-in refrigerants [12-15], heat pumps coupled systems like direct expansion geothermal systems [16-18], thermosyphon heat exchangers [19-21], high-temperature industrial heat pumps [22-26] or cold climate heat pumps [27-29]. Some of these topics are detailed in Chapter 2 in the literature review, and some are specifically addressed as research topics in Chapters 4, 5, and 6.

This project focuses on two main objectives: optimizing the thermodynamic cycle by developing a comprehensive model to simulate various configurations to improve the coefficient of performance (COP), detailed in Chapters 4 and 5, and developing a test bench for water-to-water heat pumps to conduct experimental testing under realistic conditions, as discussed in Chapter 6.

The rest of this introduction presents general concepts and definitions that will set the stage for the remaining of this work.

1.1 Overview of heat pumps

As shown in Figure 1.1, sub-critical vapor compression heat pumps (HP) consist of five main components: evaporator, condenser, compressor, reversing valve, and expansion valve. The corresponding thermodynamic cycle is presented in Figure 1.2 in a classic *P*-*h* diagram.

For a HP operating in heating mode (Figure 1.1), stages 7→1 and 1→2 occur in the evaporator. In stage 7→1, the refrigerant evaporates and absorbs heat from the surroundings (Q_L). Typically, the pressure loss in the evaporator is small and a constant pressure process is generally assumed for

azeotropic refrigerants. At point 1, the fluid has evaporated completely. Before its entry into the compressor, the vapor may undergo a slight superheating (stage 1→2), thus preventing liquid from being drawn into the compressor. Superheat values of about 5 °C are routinely encountered.

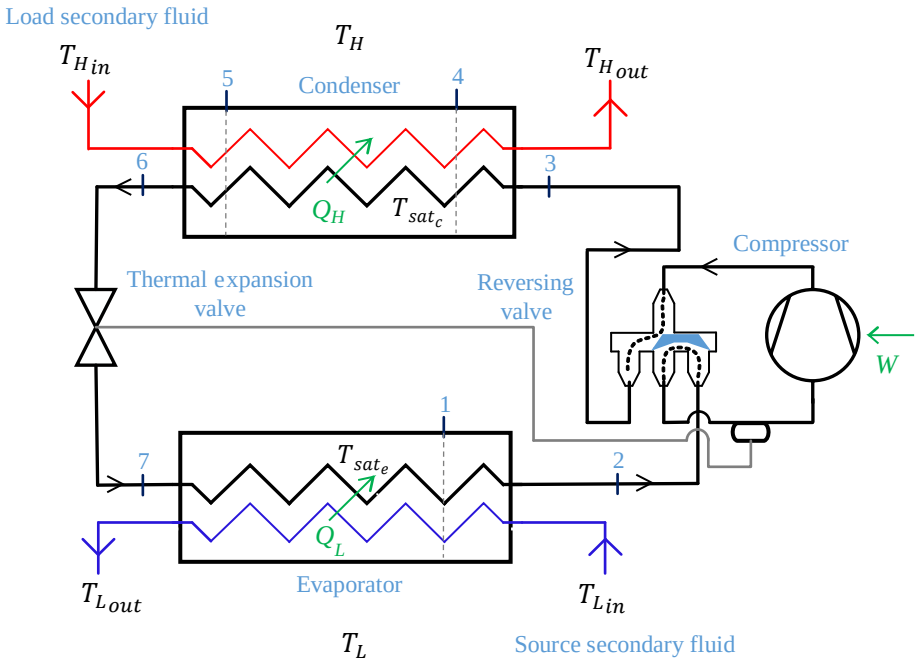

Figure 1.1 Main components of a vapor compression heat pump

In stage 2→3, the refrigerant remains a superheated vapor, i.e. to the right of the *P-h* dome. It is compressed, and its temperature increases. The amount of work done per unit mass by the compressor (W) depends on the size and type of compressor, as well as mechanical and electrical efficiencies of the motor.

Next, stages 3→4, 4→5, and 5→6 occur in the condenser. Much like for the evaporator, this process is generally assumed to occur at constant pressure. From 3→4, the superheated vapor cools (desuperheating) upon contact with the colder secondary fluid in the condenser. From 4→5, the refrigerant condenses and at point 5 the refrigerant is completely liquid. Cooling of the liquid from 5→6 is also possible with a temperature decrease. This process to the left of the dome is referred to as subcooling. The total heat transferred in the condenser between points 3 and 6 is Q_H. Finally, there is an isenthalpic pressure drop in the expansion valve from 6 to 7, and the refrigerant enters the evaporator at point 7 as a two-phase mixture.

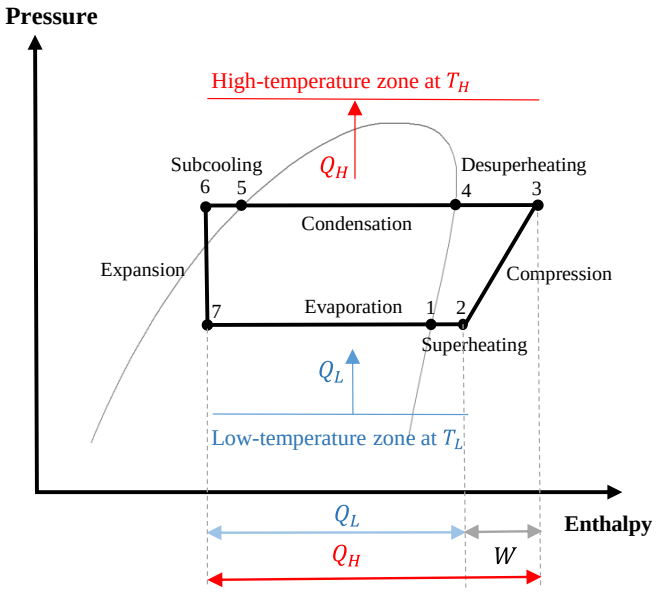

Figure 1.2 P-h diagram of a vapor compression heat pump

In the case of a thermostatic expansion valve, a temperature-sensing device located at the evaporator outlet controls the valve opening until the required degree of superheat is achieved.

The HP can be switched to cooling mode by using a reversing valve. In the case of Figure 1.1 a guide vane slides from left to right. With this action, the flow of refrigerant is reversed (except in the compressor) and the roles of the evaporator and condenser are now interchanged. The cycle shown in Figure 1.2 still applies although the evaporating and condensing pressure will not be at the same levels in the *P-h* diagram.

Under the dome, evaporation and condensation occur at constant temperature (horizontal line in the pressure-enthalpy diagram) for azeotropic refrigerants, whereas for zeotropic mixtures, there is a temperature glide, and these changes do not occur at constant temperature.

1.2 The ideal vapor compression cycle

For a heat pump operating in heating mode, the heat Q_H is transferred to a zone at a temperature T_H by extracting heat Q_L from a low-temperature zone at T_L. Basic thermodynamics indicates that the coefficient of performance (COP) in heating of a reversible Carnot heat pump operating between T_L and T_H is given by Equation 1.1.

$$COP_{H_{Carnot}} = \frac{T_H}{T_H - T_L} \tag{1.1}$$

For refrigeration, the COP is defined by the Equation 1.2:

$$COP_{R_{Carnot}} = \frac{T_L}{T_H - T_L} \tag{1.2}$$

Equations 1.1 and 1.2 show that a small difference between T_H and T_L leads to high COP values. Therefore, there is a strong incentive to operate heat pumps with the warmest possible cold sources and the coldest possible hot sinks. This is why a water-to-water ground-source heat pump supplying low-temperature radiant floor heating systems and using relatively warm ground-source temperature is generally more efficient than a conventional air-to-air heat pump which supplies warm air at a relatively high temperature and uses cold outside temperature as its source.

Due to the finite heat transfer surface of heat exchangers, there is a temperature difference between the refrigerant and the temperatures T_H and T_L. This temperature difference is typically about 5 °C. For example, for temperatures T_H and T_L of 0 and 20 °C, the evaporating and condensing temperature of the refrigerant would approximately be equal to -5 and 25 °C. The source/sink temperature difference then increases from 20 to 30 K due to the finite heat transfer surface. This results in a reduction of $COP_{H_{Carnot}}$ and $COP_{R_{Carnot}}$ by 32% and 35%, respectively.

Figure 1.3 schematically shows another form of the ideal vapor compression cycle on a *P-h* diagram where expansion is considered isentropic. The expansion is accompanied by the production of some work. This evolution between the condenser and the evaporator differs from the conventional approach that advocates an isenthalpic evolution between points 3 and 4. It is the one suggested by Radermacher and Hwang [30] in their reference book to represent the ideal cycle.

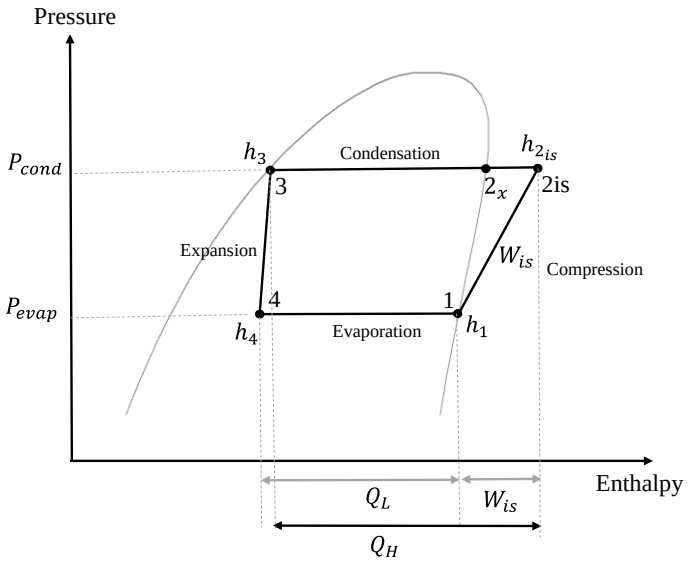

Figure 1.3 Ideal vapor compression cycle of a heat pump with isentropic expansion

For this ideal cycle, it is sufficient to specify two pieces of information to plot the complete cycle on the *P–h* diagram, either the pressure or the saturation temperature at the evaporator $(T_{sat_e}$ or $P_{sat_e})$ and the temperature or pressure at saturation in the condenser (T_{sat_c} or P_{sat_c}).

1.3 Real vapor compression cycles

Under realistic operating conditions, several effects that have a significant impact on the cycle performance must be considered. A real vapor compression cycle is illustrated in a *P-h* diagram in Figure 1.4.

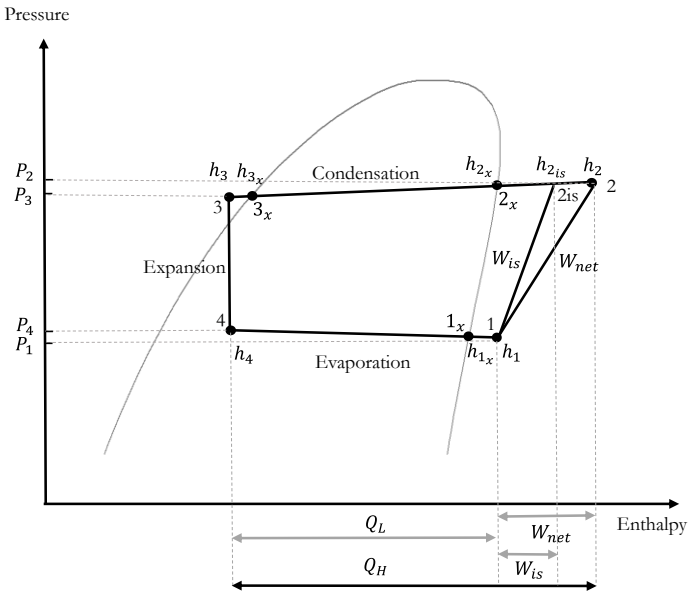

Figure 1.4 Real vapor compression cycle of a heat pump

The first difference compared to the ideal cycle diagram is the slope of the lines indicating the processes in the evaporator (line 4→1) and condenser (line 2→3), which occurred isobarically in the ideal cycle. For azeotropic refrigerants, this slope in the process (pressure drop) is due to the refrigerant friction as it passes through the heat exchanger, accessories, and piping.

The second significant difference from the ideal cycle is the presence of superheating: line 1_x→1. This superheating is intentionally done, firstly, to ensure that the entire refrigerant evaporates to take advantage of the heat of vaporization, and secondly, to ensure that the compressor only receives vapor without any liquid that could damage the compressor. Due to the pressure drop in the evaporator and superheating at the evaporator outlet, the compression process starts at a lower

pressure and further to the right of the *P-h* dome. Thus, the compressor must do more work because the pressure difference is larger. Additionally, the compressor's work increases due to the higher temperature of the suction vapor combined with isentropic lines, which tend to be more inclined as point 1 moves further to the right of the dome.

The third difference occurs during compression. The compression process is generally irreversible due to internal friction and heat transfer with the surroundings resulting in higher compression work. Point 2 is therefore to the right of point 2_{is} that would be reached with isentropic compression.

The metric used to quantify irreversibilities in a compressor is the isentropic efficiency (η_{is}). This efficiency compares the actual work done on the compressor to the work that would be required in an ideal, isentropic process.

The definition of the isentropic efficiency (η_{is}) of a compressor is given in Equation 1.3.

$$\eta_{is} = (h_{2_{is}} - h_1)/(h_2 - h_1) \tag{1.3}$$

Where,

h_1 = enthalpy of the refrigerant vapor at the compressor inlet

h_2 = enthalpy of the refrigerant vapor at the compressor outlet

$h_{2_{is}}$ = enthalpy of the refrigerant vapor at the compressor outlet if the compression were isentropic

The isentropic efficiency is influenced by several factors, both intrinsic to the compressor's design and to external operational conditions.

Figure 1.5 displays the isentropic efficiency curves (η_{is}) for three different commercially available compressors as reported by Viviescas, et al. [31]. These curves illustrate that η_{is} varies according to the compressor model, evaporating pressure, and the pressure ratio (PR), i.e. the ratio of refrigerant pressures in the condenser and evaporator. Notably, the peak of each compressor's efficiency curve occurs at distinct pressure ratios, suggesting that selecting the appropriate compressor during the heating season could optimize the annual heat pump COP (which is usually refered to as the seasonal performance factor, SPF). Additionally, Figure 1.5 also indicates that the variation in η_{is} is influenced by the evaporating pressure; for instance, for compressor #4, η_{is} is lower at an evaporating pressure of 320 kPa compared to 460 kPa.

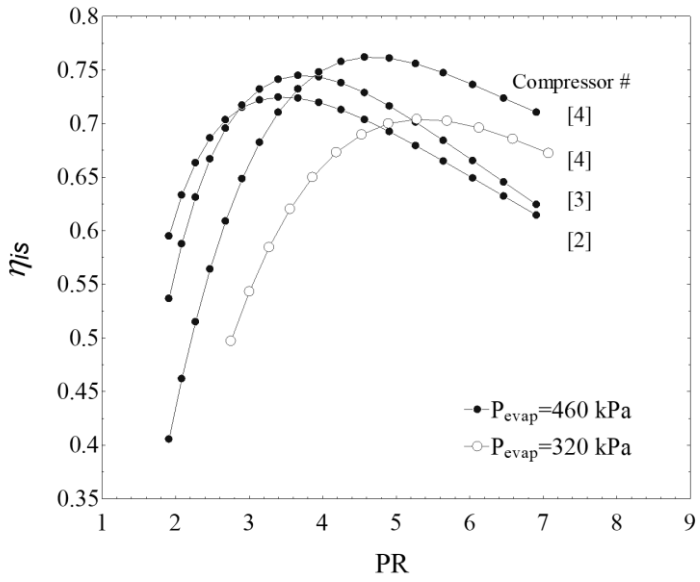

Figure 1.5 Isentropic efficiencies for three compressors as a function of the pressure ratio (PR) for two evaporating pressures

In addition to efficiency, variations in heat pump capacity are crucial for selecting compressors. Lower source temperatures lead to decreased evaporating temperatures and reduced saturation pressures, which in turn lower the density of the refrigerant exiting the evaporator and entering the compressor. This reduction in refrigerant density causes a decrease in the mass flow rate (for a constant speed compressor) of the refrigerant and consequently reduces the heating capacity at the condenser. For instance, the vapor density of saturated R-407C falls from 20.48 kg/m³ to 13.82 kg/m³, (31% reduction) as the saturation pressure drops from 460 kPa to 320 kPa. Without any other variation, this change in density directly results in a 31% decrease in refrigerant flow rate and capacity.

The fourth difference is related to the inherent difficulties in constructing an expander that produces some work in a two-phase regime. Real cycles use instead an isenthalpic process using an expansion valve (line 3→4).

A final variation from the ideal cycle is subcooling that occurs in the condenser (line 3_x→3). This ensures that only liquid enters the expansion valve, allowing better flow control. However, excessive subcooling indicates that a significant portion of the condenser volume is filled with liquid, reducing the area available for heat transfer by condensation, which is detrimental to heat exchange. The degree of subcooling at the condenser outlet is mainly determined by the amount of refrigerant charged in the system and the surface area of the condenser.

1.4 Classification of heat pumps based on the type of source and sink

Various environmental heat sources and sinks are used with heat pumps in building heating and cooling applications. A common approach involves extracting heat from the ambient air using an air-refrigerant heat exchanger and delivering the heat inside the building through a refrigerant-air heat exchanger. This type of device is known as an air-to-air heat pump.

Other sources are possible and include free-flowing water-courses, rivers, open static surface water sources, lakes and ponds, the sea, water wells, solar panels, runoff from rainwater, industrial or process residual heat [32]. The use of the ground as a source is gaining popularity. Both open and closed loops are used with standing column wells or borehole heat exchanger. In both cases, a water-refrigerant heat exchanger is used on the source side of the heat pump and depending on the type of heat exchanger on the sink side (refrigerant-air or refrigerant-water), there is either a water-to-air or water-to-water heat pump. The latter type of heat pump is the subject of this study.

Ground-source water-to-water heat pumps generally exhibit higher efficiency compared to conventional air-to-air heat pumps, primarily due to the more favorable and stable ground temperature, which remains around +10 °C in Montréal, in contrast to ambient air temperatures that can drop to nearly -30 °C in winter. Unlike the significant fluctuations of ambient air temperatures throughout the heating season, ground temperatures remain relatively constant, with corresponding higher COPs [33]. Furthermore, the capacity of ground-source heat pumps remains relatively high because of favorable source temperatures.

1.5 Coefficients of performance of a heat pump

The coefficient of performance (COP) of a heat pump is a parameter that indicates the efficiency of energy transferred between the cold and hot sources. The COP is the useful effect (heat or cold production) divided by the supplied work. Referring to Figure 1.2, and assuming no heat losses to the ambient, the COP in heating mode, COP_H, is therefore given by:

$$COP_H = \frac{Q_H}{W} = \frac{h_2 - h_3}{h_2 - h_1} \tag{1.4}$$

The COP in cooling, COP_C, is defined by Equation 1.5.

$$COP_C = \frac{Q_L}{W} = \frac{h_1 - h_4}{h_2 - h_1} \tag{1.5}$$

A heat pump with a COP_H of 4 means that for every unit of energy supplied to the compressor, four units of energy are delivered as heat, and three units are drawn from the environment.

Exergy efficiency

The exergy efficiency (η_{ex}) of a heat pump indicates how effectively it converts the available exergy (useful energy) into the desired mechanical work relative to a given reference temperature. It evaluates how well the system minimizes losses when compared to an ideal, reversible process. The exergy efficiency (η_{ex}) is determined by the ratio of the actual COP to the reversible (Carnot) COP.

$$\eta_{ex} = \frac{COP}{COP_{carnot}} \tag{1.6}$$

This relationship emphasizes how closely the heat pump's actual performance aligns with the thermodynamic limit established by the Carnot cycle. Typically, heat pumps have η_{ex} around 0.5.

1.6 Part-load operation

In a fixed-speed heat pump system, a thermostat controls the heat pump operation, switching it off when the set point temperature is reached and switching it on again when the temperature falls below a certain threshold. Consequently, the heat pump operates in successive on/off cycles. This results in the average performance differing from steady-state performance, typically showing some degradation.

When a heat pump cycles, two types of energy losses occur:

1. Standby energy consumption: Certain components, such as control circuits, consume energy even when the system is off.

2. Refrigerant migration: During the off cycle, refrigerant can migrate from the condenser to the evaporator, causing energy loss.

The dynamic COP of a heat pump represents the efficiency measured under transient or varying operating conditions, unlike the steady-state COP determined under constant conditions. It accounts for factors such as start-up losses, which occur when the heat pump transitions from off to operating mode, requiring extra energy to reach steady-state performance. Additionally, it

includes the impact of stand-by electrical consumption during off periods, where the system draws power for control systems, and other components, even when not actively running. This measure provides a realistic understanding of the heat pump's performance in real-world applications.

In water-to-water heat pumps, the dynamic COP is nearly quasi-steady with negligible start-up losses as reported by Corberán, et al. [34]. However, the significant factor in COP degradation is the stand-by electrical consumption during the off period, particularly at low load ratios.

According to Henderson, et al. [35] these losses can result in annual energy penalties ranging from 5 to 10 %, leading to a corresponding increase in energy consumption.

To account for these additional losses, a correction factor is typically applied to the energy consumption during full-load operation. This correction is made using curves or equations that provide the Part Load Factor (PLF) as a function of the Part Load Ratio (PLR).

The PLR of heat pumps is a measure of the operational building load demand (Q) relative to the heat pump maximum capacity (full capacity) for given conditions. It is calculated as:

$$PLR = \frac{\text{building load}}{\text{Heat pump full capacity}} = \frac{Q}{Q_{FC}} \tag{1.7}$$

The PLF expresses part load effects in terms of a degradation of COP as follow:

$$PLF = \frac{COP_{Part-load}}{COP_{fullcapacity}} = \frac{\left[\frac{Q}{W}\right]}{\left[\frac{Q_{FC}}{W_{FC}}\right]} \tag{1.8}$$

W_{FC} represents the power required at full capacity. The required power at partial load can be calculated from:

$$W = \left(\frac{W_{FC}}{PLF}\right) PLR \tag{1.9}$$

It is also common to refer to this last term as the fraction of full load power (FFLP) also named EIR_{FFLP} defined as:

$$EIR_{FFLP} = \left(\frac{W_{FC}}{PLF}\right) PLR \tag{1.10}$$

Various models have been developed to account for energy losses during cycling, starting with Parken, et al. [36] who were the first to recognize that the two factors mentioned above could be combined to form a part load correlation. They utilized this concept to develop the part load degradation coefficient (C_d), as shown in Equation 1.11.

$$PLF = 1 - C_d(1 - PLR) \tag{1.11}$$

Numerous studies have been conducted to try to improve Equation 1.11 [37-39]. Most of these studies have focused on air-to-air and air-to-water systems. The dynamic performance and degradation at partial load of water-to-water and water-to-air systems have been investigated by a few researchers and are detailed below.

Corberán, et al. [34] studied the cyclic losses of water-to-water units operating under on/off control. The degradation of performance can be assessed by the following expression, identical to that used in the standard EN-14825:2016 [2].

$$PLF = \frac{1}{1 + \frac{W_{sb}}{W_{HP}} \frac{(1 - PLR)}{PLR}} \tag{1.12}$$

where W_{sb} is the standby electrical consumption of the unit, and W_{HP} is the electrical consumption of the heat pump when the compressor is running.

Furthermore, the PLF correlation defined in the UNI standard [40, 41] is based on the assumption of a linear relationship between a parameter Z and the PLR, which provides an expression for the PLF in the following form:

$$PLF = \frac{PLR}{Z} = \frac{PLR}{a + bPLR} \tag{1.13}$$

where the coefficients a and b, defining the linear relationship between Z and PLR, are obtained experimentally. Regarding the European standard EN-14825:2016 [2], the correlation for the PLF for water-to-water heat pumps is given by:

$$PLF = \frac{PLR}{C_c PLR + (1 - C_c)} \tag{1.14}$$

Here C_c is the degradation coefficient that quantifies efficiency loss when the heat pump operates below full capacity.

Later, Fuentes, et al. [42] presented a comprehensive experimental study on the performance of water-to-water heat pumps under part load conditions. Through meticulous semi-virtual laboratory experiments, the authors assessed various parameterizations against actual performance, leading to the development of a novel method for characterizing heat pump efficiency that accounts for both stand-by and start-up losses represented in Equation 1.15.

$$PLF = \frac{1}{1 + \frac{C_d(1 - PLR)}{1 - C_d(1 - PLR)} + (1 - C_c)\frac{1 - PLR}{PPLR}} \tag{1.15}$$

where C_d (= 0.22) and C_c (= 0.998) are so-called start-up and stand-by degradation coefficients.

1.7 Seasonal performance factor

It is also useful to calculate the seasonal performance factor (commonly referred to as SPF in the literature) to assess the performance of a heat pump over a heating season. The SPF is defined here as the ratio of the annual heating energy supplied to the load to the annual energy consumption of the heat pump, including that of the compressor and auxiliary heating. It is expressed as follows:

$$SPF = \frac{\sum_{j=1}^{n} Q_{load_j}\ \Delta t}{\sum_{j=1}^{n}(W_{net,j} + Q_{aux,j})\Delta t} \tag{1.16}$$

Where Δt is the time step (typically 1 hour), Q_{load_j} , $W_{net,j}$, and $Q_{aux,j}$ are the required heating power, the heat pump and auxiliary power at time step j, and n is the number of time steps in the heating season.

CHAPTER 2 LITERATURE REVIEW

This chapter presents a literature review on vapor compression refrigeration cycles, divided into four main sections. Section 2.1 explores advances in vapor compression technologies, focusing on subcooling cycles, expansion loss recovery cycles, and multi-stage and multi-compressor cycles. Section 2.2 covers the modeling of heat pumps, with an overview of heat pump technologies based on secondary fluids, and a classification of modeling including analytical models, experimentally driven models and gray box type models. Section 2.3 delves into the modeling of heat exchangers, compressors, and expansion valves. Finally, Section 2.4 addresses the experimental determination of heat transfer coefficients in heat exchangers. This chapter constitutes a complement to the literature reviews included in the two journal papers presented in Chapters 5 and 6 of this thesis.

2.1 Advances in vapor compression technologies

Vapor compression technology has seen significant advancements aimed at improving efficiency and reducing environmental impact. This section reviews key developments in the field, focusing on subcooling cycles, expansion loss recovery cycles, and multi-stage and multi-compressor cycles. These innovations enhance system performance through better temperature control, energy recovery, and optimized configurations, reflecting the continuous evolution of vapor compression technology as noted by Park, et al. [43].

2.1.1 Subcooling cycles

Typical heat pumps are engineered to ensure subcooled liquid at the condenser outlet for several reasons. First, this practice prevents flash gas formation and the entry of vapor into the expansion valve, which can reduce operational efficiency. Secondly, subcooling enhances system efficiency by maximizing the energy absorbed in the evaporator.

Hervas-Blasco, et al. [44] found that the performance of vapor-compression systems using subcritical cycles varies significantly with the degree of subcooling. Optimal subcooling maximizes efficiency but depends on operating conditions, requiring adaptable control systems. They concluded that the implementation of a temperature approach control strategy is efficient, as evidenced by its experimental reliability, stability, and robustness. This strategy involves regulating the temperature differential between the refrigerant outlet from the condenser and the building zone temperature. The method, distinguished by its simplicity of implementation and

precision, resulted in a COP enhancement of up to 30% under specific conditions. This approach finds validation in a variable optimization study by Jensen and Skogestad [45].

Pitarch, et al. [46] show that optimal subcooling significantly impacts subcritical refrigeration cycle performance. Their analysis of refrigerants R290, R134a, R1234yf, and R32 revealed that the optimal subcooling varies with the temperature lift of the secondary fluid. This optimal condition is achieved when two pinch points occur in the condenser, one at the condenser outlet and another at the refrigerant dew point. Exergy analysis showed that the maximum COP is reached under these conditions. The study highlights the critical need for subcooling control to enhance refrigeration efficiency, providing a methodology to determine optimal subcooling based on external conditions.

Dalkilic and Wongwises [47] used an ideal vapor-compression refrigeration system to study the performance of new refrigerant mixtures as substitutes for R12, R134a, and R22. Emphasizing subcooling's effect, they found that mixtures R290/R600a (40/60) and R290/R1270 (20/80) were optimal for R12 and R22 replacements. Higher evaporating temperatures increased the COP, and superheating/subcooling optimization improved performance further.

Min-Hsiung and Rong-Hua [48] investigated the performance of vapor-compression refrigeration systems at various degrees of subcooling for different refrigerants. They identified optimal subcooling degrees between 2 °C and 7 °C for R134a, R22, R410A, and R717, minimizing cost and exergy destruction. Performance improves with lower condenser water temperatures and optimal adjustments in condensation and evaporation temperatures, while superheating in the evaporator has minimal impact.

Following are three methods to provide subcooling: Suction line heat exchangers (SLHX), thermoelectric subcooling, and mechanical subcooling. Each approach offers unique methods and benefits for achieving subcooling.

Suction line heat exchanger

An intermediate heat exchanger also referred to as a suction line heat exchanger (SLHX), is often used between the condenser and the evaporator of refrigeration systems as shown in Figure 4.1 in Chapter 4. The corresponding operating points in a P-h diagram are shown in Figure 4.2. The refrigerant exits the intermediate heat exchanger as subcooled refrigerant on one side and as a superheated vapor on the other side.

This technique enhances the heat pump's capacity and can improve the COP by increasing the subcooling of the liquid refrigerant. This subject is covered in section 4.1 of this thesis following previous studies conducted by Domanski, et al. [49] and Klein, et al. [50].

The colder refrigerant exiting the evaporator is connected to the SLHX before entering the compressor, cooling the hotter stream from the condenser. This process results in two main effects: an increase in evaporator capacity and an increase in the compressor suction temperature. The latter reduces compressor efficiency due to a decrease in refrigerant density and less efficient compression. These two effects will be evaluated in detail in Chapter 4.1.

Pottker and Hrnjak [51] conducted an experimental study on the effect of condenser subcooling on the performance of an air conditioning system using R134a and R1234yf. It was found that the COP increases up to 18% for R1234yf and 9% for R134a due to subcooling. The study confirmed that R1234yf benefits more from subcooling than R134a. Additionally, the presence of an SLHX reduces the COP improvement due to subcooling, yet the combined use of SLHX and subcooling still results in a more efficient system, particularly for R1234yf.

The use of SLHX is widely used in refrigeration systems using CO2. Wang, et al. [52] investigated its impact on the performance of transcritical CO2 air source heat pumps used for space heating. The study employed energy, exergy, and exergoeconomic analyses to compare systems with and without the SLHX. Results indicated that the SLHX increased the COP from 1.25 to 2.96 and from 1.05 to 2.17 and reduced throttling valve irreversibility by 40.36 to 50.73%. Other studies which show significant improvements in CO2 cycle performance using SLHX include the ones by Otón-Martínez, et al. [53] and Sánchez, et al. [54].

Mechanical subcooling and thermoelectric subcooling

Mechanical subcooling involves the use of an additional refrigeration system or mechanical device to further cool the refrigerant after it leaves the condenser. Subcooling the refrigerant at the condenser exit allows it to enter the evaporator with lower quality, enhancing heat absorption and improving the system's coefficient of performance (COP). Numerous studies have been conducted on mechanical and dedicated subcooling of vapor compression refrigeration systems, as discussed in the following sections.

Thornton, et al. [55] investigated the impact of dedicated mechanical subcooling cycles, which use a small mechanical vapor-compression cycle coupled to the main cycle at the condenser exit to

provide subcooling. The study identified that the evaporator temperature significantly influences the overall cycle's performance. An ideal dedicated subcooling cycle predicted an optimal evaporator temperature dependent on sink and refrigerated space temperatures. A property-dependent model, accounting for irreversibilities, confirmed these trends and showed a 10% improvement in overall COP for supermarket applications.

Solanki, et al. [56] compared the performance of dedicated mechanical subcooled vapor compression refrigeration (DMS-VCR) systems with actual vapor compression refrigeration (VCR) systems of the same capacity (100 kW). Results showed that the DMS-VCR system outperformed the VCR system at a constant condenser temperature (40 °C) with varying evaporator temperatures (0 °C, 5 °C, and 10 °C). At 0 °C, the DMS-VCR system achieved a 4.60% higher COP and a 4.38% higher exergetic efficiency, making it more favorable for water chilling applications.

Khan and Zubair [57] explored the impact of mechanical subcooling on vapor-compression refrigeration systems. The integrated mechanical subcooling system utilizes a small vapor-compression cycle, coupled to the main cycle at the condenser exit, to perform subcooling. Thermodynamic models were developed to simulate the system's performance, particularly focusing on subcooler saturation temperature and heat exchanger areas. Results showed that the optimal subcooler saturation temperature, which maximizes COP, is approximately halfway between condensation and evaporation temperatures. Additionally, the optimal heat exchanger area distribution favors the condenser over the evaporator, minimizing irreversibilities and maximizing system efficiency.

Thermoelectric subcooling employs thermoelectric modules to create a temperature difference via the Peltier effect. These modules can be integrated into the vapor compression cycle to achieve subcooling without the need for additional mechanical components, offering a compact and efficient alternative to traditional methods. The primary advantages of this technology are its robustness, compact design, absence of working fluid, and simplicity of operation. Numerous studies have primarily focused on transcritical vapor compression cycles using CO2 [58-61].

2.1.2 Expansion loss recovery cycles

Expansion loss recovery cycles tackle the inherent inefficiencies in traditional vapor compression systems by addressing expansion losses. The typical vapor compression cycle (VCC) utilizes devices like capillary tubes, thermostatic expansion valves (TEV), and electric expansion valves (EEV) to reduce the high pressure of the refrigerant after it exits the condenser. This expansion process is not isentropic and leads to thermodynamic losses [62]. Techniques such as using expansion turbines or ejectors have been explored to recover and utilize this lost energy. This subsection focuses on the use of expanders and ejectors, two innovative approaches to improving the thermodynamic efficiency of vapor compression cycles. The expander will be discussed in detail later in section 4.2.

Expanders

An expander is a mechanical device that recovers energy from the refrigerant as it expands and reduces pressure from the condenser to the evaporator. An expander can be seen as a compressor operating in reverse. The expander can improve the COP of the system in two ways by increasing the cooling capacity through an isentropic process and by utilizing the recovered expansion losses for assisting the compressor or some other device in the refrigeration cycle (fan, controller), which results in a reduced overall heat pump input power. Typically, the expander consists of a nozzle that converts the energy of the high-pressure refrigerant into a high-velocity jet. This jet then impacts a radial-in axial-out turbine, which is connected to a generator, allowing to produce power as the refrigerant expands and its pressure drops (As shown in Figures 4.10 and 4.11 in Chapter 4). This process not only aids in energy recovery but also enhances the overall efficiency of the heat pump system.

Barta, et al. [63] conducted experimental and theoretical analyses to investigate the design and control of a turbomachine expander for energy recovery and control in an R-410A split-system heat pump. The study compared the performance and control capabilities of a variable nozzle and a fixed nozzle with phase separation and evaporator bypass flow metering. The variable nozzle showed a significant decrease in expander isentropic efficiency, while evaporator bypass control improved the system's COP by 2.3% with an overall expander isentropic efficiency of 18.8%. The research highlights the potential benefits of expanders in enhancing VCC efficiency.

Murthy, et al. [64] investigated the performance of a four-intersecting-vane expander in an R134a vapor compression refrigeration system, focusing on different expander placement arrangements. A custom test rig determined the system's COP with either a throttling valve or an expander under identical conditions. Results indicated a 6.4% improvement in COP with the expander, achieving a maximum expansion efficiency of 34.9% at 500 rpm. The highest performance was observed when the expander was placed immediately after the condenser.

Huff, et al. [65] developed a method to estimate the performance of positive displacement compressors and expanders by analyzing valve losses, internal leakage, and heat transfer. Using work-extracting expansion instead of isenthalpic throttling in CO2 cycles can improve COP by 40%-70% and capacity by 5%-15%.

Nickl, et al. [66] demonstrated that integrating an expander with work recovery in transcritical CO2 refrigeration cycles offers two key advantages: improved COP and reduced exhaust pressure of the main compressor. Several expander designs have been proposed and some prototypes tested. Their laboratory developed a three-stage expander that replaces the throttle valve and expands into the two-phase region. For optimal system integration, a vapor-liquid separator is installed between the second and third expansion stages. The vapor returns to the third expander stage, while the liquid is directed to the cooling stations via thermostatic or electronic expansion valves.

Dumont, et al. [67] conducted an experimental investigation aimed at facilitating the selection of expanders for small-scale Organic Rankine Cycles (ORCs). Their study compared the performance of four different expander technologies - piston, screw, scroll, and roots - through experimental testing on two similar small-scale ORC units utilizing R245fa as the working fluid. The results revealed varying maximum effective isentropic efficiencies, with the piston and screw expanders achieving 53%, the variable-speed scroll reaching 76%, and the roots expander attaining 48%. However, the authors noted that these measured efficiencies did not necessarily represent the highest achievable efficiencies for each expander due to experimental limitations in the test rigs. To address this, semi-empirical models were calibrated based on the measurements to predict isentropic efficiency under optimal conditions. The study concluded with guidelines to aid in the proper selection of a volumetric expander, emphasizing the importance of considering factors such as expander technology, ORC architecture, power range, operating conditions, and working fluid for the specific application.

Ejectors

An ejector utilizes the high-velocity flow of a primary fluid to entrain and compress a secondary fluid, effectively recovering energy from the expansion process. Ejectors are known for their simplicity, reliability, and ability to enhance the performance of vapor compression cycles by reducing throttling losses and improving refrigerant distribution.

Ameur and Aidoun [68] presented a thermodynamic model to simulate a CO2 transcritical heat pump cycle integrating a two-phase ejector. The study demonstrated that controlling the ejector geometry with varying operating conditions maximizes overall efficiency. Simulations indicated that at an evaporator temperature of -20 °C, the cycle COP, gas cooler capacity, and evaporator capacity are improved by 9%, 14%, and 23%, respectively, compared to a conventional cycle. These improvements were associated with a 4% increase in compressor work. The research highlighted the importance of optimal ejector geometry and operational conditions to enhance performance.

Pottker and Hrnjak [69] presented experimental data comparing the performance of an R410A ejector vapor compression system with a conventional expansion valve system. The study aimed to separately quantify the improvements from work recovery and liquid-fed evaporators. Compared to the liquid-fed evaporator system, the ejector system showed COP improvements from 1.9% to 8.4% due to work recovery. When compared to the conventional expansion valve system, the ejector setup enhanced COP from 8.2% to 14.8%, benefiting from both liquid-fed evaporator and work recovery.

2.1.3 Multi-stage and multi-compressor cycles

Multi-stage cycles involve the use of multiple stages of compression and intercooling to improve the thermodynamic efficiency of vapor compression systems. These cycles are particularly beneficial for high-temperature lift applications and systems requiring large capacity. By dividing the compression process into stages and optimizing each stage, these systems can achieve higher efficiencies and improved reliability.

Multi-compressors are used in refrigeration systems to enhance efficiency, capacity, and reliability. In parallel configurations, capacity is increased and energy efficiency is improved by staging compressors to match the cooling load, which reduces cycling and extends compressor life. Series

compressors are employed for applications requiring higher pressure ratios, improving efficiency for high-lift applications and providing better temperature and pressure control.

Commercial single-speed heat pumps are designed to operate optimally at one operating point (where the compressor efficiency is maximum). However, due to the variability of environmental conditions, the heat pump operates most of the time under non-optimal conditions. This challenge can be addressed by using multiple compressors. Selecting the best compressor at any given time optimizes the COP, reducing electrical consumption and minimizing partial load operation. Another method is to use a variable-speed compressor (VSC) equipped with an inverter. This mechanism varies the compressor's rotational speed (typically between 20 and 200% of the nominal speed), allowing more or less refrigerant to be admitted per unit of time, thus varying the unit's capacity and avoiding stop/start cycles.

The use of multiple compressors and variable speed compressors is analysed in Section 4.3.

Multi-Stage cycles

The use of multi-stage compression systems is one of the main methods to increase the energy efficiency of heat pumps. It involves multiple compression stages arranged in series with intermediate cooling.

Barbouchi [70] presents an in-depth study on the sizing, simulation, and performance of a two-stage heat pump equipped with a subcooling exchanger. The study outlines the development of a detailed model for simulating the heat pump's behavior, utilizing sub-models for each component. Key aspects of the study include defining the optimal design point for the heat exchangers, crucial for maintaining seasonal performance, and performing a sensitivity analysis to understand the influence of various parameters on system efficiency. Following the design phase, a prototype was constructed and tested in a controlled laboratory environment. The comparison of experimental results with simulation outputs showed a high degree of accuracy, with a discrepancy of only 10% for the COP. The prototype achieved a COP of 1.7 at an air temperature of -15 °C with a heating capacity of 11.5 kW, and a COP of 3.2 at an air temperature of 7 °C with a heating capacity of 8.9 kW. This study validates the high performance and reliability of two-stage heat pump systems across a wide range of operating conditions

Lee, et al. [71] using a heat pump simulation model, compared the seasonal performance factor (SPF) of a single-stage heat pump, a two-stage injection heat pump, and a two-stage injection heat

pump modulated with rotary compressors. The SPF of the two-stage injection heat pump was 1.3% higher than that of the single-stage heat pump. The modulated two-stage injection heat pump showed a 1.4% higher SPF than the single-stage heat pump under typical heating conditions.

There are also cascade-type multi-stage cycles, consisting of two or more simple refrigeration cycles connected in which an intermediate heat exchanger operates in one of them as an evaporator and in the other as a condenser (Chua, et al. [72]). Jung, et al. [73] conducted experiments on a multifunctional cascade heat pumps for domestic hot water heating. It demonstrated higher water heating capacity than a single-stage heat pump. Additionally, the multifunctional cascade heat pump provided more stable heating capacity.

Detailed descriptions and analyses of results for multi-stage heat pumps can be found in several studies, including those by Agrawal and Bhattacharyya [74]; Arpagaus, et al. [75]; Bertsch and Groll [76]; Chen, et al. [77]; Jiang, et al. [78]; Wang, et al. [79].

Multi-Compressors

The use of multiple compressors in parallel or in series allows the heat pump to adjust the refrigerant mass flow rate so that the capacity more closely matches the demand.

Inampudi and Elbel [80] conducted a comprehensive experimental study comparing various scroll compressor modulation strategies in residential and commercial air conditioning systems. The study evaluated single-speed, two-stage, tandem combinations, and variable-speed compressors using R410A. Testing revealed that variable speed compressors achieved the highest seasonal performance, followed by tandem combinations. The study also noted that heat exchanger performance significantly influences overall efficiency. While the variable speed compressor excelled in cooling applications, it faced limitations in heating applications due to a restrictive operating envelope at lower compressor speeds, causing unexpected cycling losses. The study recommended using continuous capacity modulation methods, like variable speed compressors, for variable condenser outlet temperature conditions. The findings underscore the importance of selecting appropriate compressor modulation strategies based on specific application needs and operating conditions.

Shen, et al. [81] developed a cold-climate heat pump (CCHP) that uses tandem compressors. Compared to a single-speed heat pump, the CCHP achieved over 40% energy savings when demand was at its peak. Similarly, Shen, et al. [82] developed another CCHP prototype using two

identical compressors in parallel with vapor injection and an inter-stage flash tank. At moderately low ambient temperatures, a single compressor is engaged, and at lower ambient temperatures, both compressors are used. They concluded that the seasonal performance was 5% higher than that of single-speed compressors in tandem without vapor injection.

Hu, et al. [83] simulated a heat pump with a 2 kW centrifugal compressor. They compared the performance of three types of systems: two compressors in one cycle, two compressors in parallel, and two cycles in parallel. According to the simulation results, the parallel two-cycle system has significant advantages in terms of heating capacity, power, and system COP. The COP of the parallel two-compressor system is 5.2% and 10.2% higher than that of the two-compressor one-cycle system for evaporator inlet water temperatures of 30 °C and 60 °C, respectively.

2.1.4 Centrifugal compressors

Residential small-capacity heat pumps typically use scroll compressors. The isentropic efficiency of these compressors generally ranges from 50% to 60%. In contrast, compressors employed in modern gas turbines for aviation propulsion exhibit isentropic efficiencies around 80% to 90%. Increasing the isentropic efficiency of the compressor from 60% to 75% by replacing the scroll compressor with a centrifugal compressor could potentially raise the COP of the cycle by approximately 25%. Apart from the research conducted by Arpagaus, et al. [84] and Schiffmann [85], there is limited information in the literature regarding the incorporation of centrifugal compressors into residential-type heat pumps.

2.2 Modeling of vapor compression heat pumps

Accurate modeling of vapor compression heat pumps is essential for predicting performance and optimizing design. The following section includes additional references that complement those provided in Chapters 5 and 6 on heat pump modeling.

2.2.1 Classification of models

Modeling heat pumps involves developing mathematical or computational representations to simulate and forecast their performance under various conditions. Several approaches exist for modeling heat pumps. On one end, analytical models utilize basic conservation laws of mass, energy, and momentum, along with equations of state and fundamental heat transfer correlations, to predict the refrigerant's state throughout the cycle. On the other end, models rely solely on

experimental data, either through curve-fitting or performance maps. Semi-empirical models, which blend aspects of both analytical and empirical approaches, fall in between these extremes [86].

At times, certain models incorporate components that are described using analytical models or physical principles, while other components within the same model are treated as gray or black boxes. This blending of approaches complicates model categorization. In such cases, these models will be classified according to the group that most accurately represents the predominant modeling approach used for the majority of the heat pump's components. This literature review follows these categories, first discussing analytical methods, then empirical, and finally semi-empirical models.

Analytical Models

Analytical models are mathematical representations based on the fundamental principles of thermodynamics and heat transfer. These models are used to predict the performance of vapor compression systems under various operating conditions. Analytical models are essential for understanding the theoretical limits of system performance and for designing efficient components.

Heinz, et al. [87] developed a numerical model for a novel storage tank system integrating a heat pump (HP) condenser and desuperheater. The model was designed for detailed design calculations and annual system simulations. It calculates heat transfer coefficients and pressure drops for the heat exchangers using empirical correlations based on geometry, flow conditions, and thermal properties. The water mass flow rate through the condenser is calculated based on natural convection principles. The model includes a semi-physical compressor model that calculates the thermodynamic refrigerant cycle and thermal properties of the refrigerant. It uses a performance map of the compressor to determine efficiency and electric consumption, extending to detailed simulation of the condenser and desuperheater.

Empirical models

Experimental models are valuable for their accuracy in predicting real-world performance, as they account for the complexities and non-idealities of actual systems. Such models are crucial for validating analytical models and for designing systems where precise performance predictions are required.

Bordignon, et al. [88] developed a flexible reversible heat pump model, implemented as a freely released TRNSYS Type using REFPROP for refrigerant properties. This model simulates single-stage and cascade heat pumps and incorporates performance data from manufacturers. They investigated a ground source heat pump in three climates, showing that the cascade cycle configuration has a minor long-term performance penalty due to thermal drift, while the single-stage cycle configuration displayed varied seasonal efficiency ratios. The study emphasizes the flexibility of the model, allowing users to adjust parameters like compressor polynomials and heat exchanger efficiency. This adaptability makes it particularly valuable for evaluating and optimizing heat pump performance in complex systems, such as historic buildings with architectural constraints.

Gray box type models

Gray box models combine the strengths of both analytical and empirical approaches. These models use fundamental principles to establish the framework and empirical data to refine and calibrate the model for improved accuracy. Gray box models are particularly useful in situations where some system parameters are known theoretically, but others need to be determined experimentally.

Mbaye and Cimmino [89] introduced a physics-based and modular variable refrigerant flow (VRF) heat pump model designed for multi-year simulations. This model accommodates multiple indoor units (IUs), outdoor units (OUs), and compressors, and includes a parameter estimation procedure and a control strategy using manufacturer data. Validation against data from a VRF system in the former ASHRAE Headquarters Building in Atlanta, comprising 22 IUs, 2 OUs, and 8 compressors, showed accurate predictions of total energy consumption over a two-month cooling period, with a relative error of 1%, a normalized mean bias error (NMBE) of 1.6%, and a coefficient of variation of the root mean square error (CVRMSE) of 16.7%.

2.2.2 Modeling of heat pump components

The modeling of vapor compression cycles is heavily dependent on the accurate modeling of their individual components. This section focuses on modeling of key components such as heat exchangers, compressors, and expansion valves.

Modeling of heat exchangers

In a vapor compression system, there are two distinct heat exchangers: one serves as a condenser, while the other functions as an evaporator. The modeling of these heat exchangers can be broadly classified into four types, each differing in accuracy and computational time: lumped parameter models, moving boundary models, tube-by-tube models, and segment-by-segment (distributed parameter) models. The following sections will discuss these modeling approaches in detail, including their applications and the rationale for their use. Additionally, this section will address the various limitations of these modeling techniques [90].

Modeling heat exchangers involves the application of heat transfer principles to predict their performance. Factors such as heat transfer coefficients, pressure drops, and temperature profiles are considered to optimize their design and integration into the system.

The use of brazed plate heat exchangers (BPHE) in vapor compression systems, as opposed to traditional tubular heat exchangers, can further reduce the environmental impact As these exchangers lower the refrigerant mass charge without compromising performance [91].

Lumped Modeling Approaches

The lumped modeling approach stands out as the most straightforward modeling techniques. This approach treats the entire heat exchanger as a single control volume, utilizing an overall heat conductance (UA) value to evaluate the heat exchanger's performance. The heat exchanger is calculated using either the log-mean temperature difference (LMTD) method or the ε-NTU method. However, this model does not consider any phase change transitions occurring within the heat exchanger.

Herbas, et al. [92] describe a model for condensers where the overall heat transfer coefficient (U_c), is constant and based on the maximum temperature difference. They assume that the cooling medium (air or water) has known properties such as temperature, flow rate, and specific heat. The U_c value must consider the desuperheating section of the condenser. Additionally, the overall heat loss coefficient U_l is determined, with heat losses assumed to occur only between the refrigerant and the cooling medium.

Moving boundary approaches

The moving boundary modeling method provides a more comprehensive analysis compared to lumped modeling techniques because it incorporates the phase change transition of the refrigerant. On the airside, it accounts for the shift from dry to wet conditions if air dehumidification takes place. This approach divides the heat exchanger into single-phase and two-phase regions, with each region being addressed using a lumped method.

Martins Costa and Parise [93] developed a mathematical model for the performance prediction of air-cooled condensers. The model considers the heat exchanger as formed by three distinct zones: desuperheater, condenser, and subcooler. Each piece of straight tube, between two return bends, is treated as a separate heat exchanger, enabling the overall effectiveness of each zone to be determined with the use of correlations available in the literature. Despite its simplicity, the method produces results comparable to those produced by more sophisticated local analyses.

Chen and Yang [94] introduced a new moving-boundary model for predicting the steady-state heat transfer rate of water-cooled CO2 gas coolers. Unlike traditional models used in subcritical regions, which rely on fluid phase, this model separates the gas cooler into up to three zones based on local thermal capacitance rates. Experimental data validated the model, demonstrating prediction accuracy comparable to the finite volume method, with deviations in heating capacities within ±5% and CO2 outlet temperatures within ±4 °C. The model's computation time averaged 22% of that required by the finite volume method.

Ge and Cropper [95] developed a simulation model for air-cooled finned-tube condensers using a modified lumped method. The model divides the condenser into four sections: a superheated section, two two-phase regions, and a subcooled section, based on experimental data on refrigerant condensation heat transfer. The model was validated with test data and used to compare the performance of different condenser configurations with refrigerants R22 and R404A. It offers guidelines for designing and developing various condenser arrangements. The simulation assumes a cross-flow configuration for refrigerant and air, employs NTU calculations, and carefully selects local correlations for condensing refrigerant heat transfer coefficients and pressure drops, assuming a proportional relationship between pipe length and refrigerant quality.

Segment-by-segment approaches

The segment-by-segment modeling approach is a detailed analytical method employed in the study of heat exchangers, which involves dividing the exchanger into smaller segments or control volumes. This approach enables the accurate representation of temperature and heat transfer variations along the length of the heat exchanger. By iteratively calculating local heat transfer rates and temperature changes for each segment, this method provides a precise evaluation of performance, making it invaluable for design, optimization, and troubleshooting of heat exchangers. Its advantages include detailed analysis and high accuracy, while its disadvantages encompass increased computational intensity and complexity.

Judge and Radermacher [96] developed a heat exchanger simulation for both transient and steady state cycle simulations of mixtures and pure components. The simulation specifically targets air-to-refrigerant condensers and evaporators used in residential heat pumps. It solves the differential momentum, continuity, species, and energy equations for these components, with steady state results validated through experiments. The simulation's predicted capacities for four cross-flow heat exchangers, used as condensers and evaporators with four different refrigerants, matched the experimental data within a +8.0% margin. The heat exchangers are modeled with 100 nodes, determined by analyzing capacity changes with varying node counts, and the differential equations are discretized using a second-order accurate implicit scheme.

Gholamrezaie, et al. [97] developed a model for a heat exchanger where the energy equation is solved iteratively using a backward scheme to ensure energy balance. In this model, the fluid is a 30% glycol/water mixture, the model, implemented in FORTRAN, is incorporated into a new TRNSYS type and uses a 1D discretization with 12 nodes.

Sánchez, et al. [98] developed a steady-state coaxial heat exchanger model utilizing water as the cooling fluid. The model, based on finite-volume methodology, was validated with experimental data, achieving an uncertainty of less than ±10% in heat transfer rates and less than ±3 °C in the outlet temperatures of both fluids. Various correlations for estimating the CO2 heat convection coefficient were evaluated to select the best fit for the model. The model accounts for the sudden variations in CO2 thermophysical properties in the pseudocritical region by using constant properties within each finite-volume segment.

Compressor modeling

Dechesne and Lemort [99] conducted an experimental study on a residential heat pump with a variable speed scroll compressor using refrigerant injection and R410A. The study examined the compressor's performance under different evaporating and condensing temperatures and rotational speeds. A detailed empirical compressor model was developed based on five dimensionless relations: volumetric efficiency, isentropic efficiency, drive efficiency, injection ratio, and ambient losses ratio. The model accurately predicted mass flow rates, electrical consumption, and discharge temperature, with low average errors. Results indicated that reducing suction superheat increased COP and heating capacity, while decreasing discharge temperature. The study emphasizes the importance of compressor modeling for enhancing heat pump performance.

In this model, the volumetric efficiency (ε_v) and isentropic efficiency (η_s) are expressed as functions of the pressure ratio $\left(r_p\right)$ and the rotational speed ratio of the compressor $\left(\frac{N}{N_{max}}\right)$ (Equations 2-1 and 2-3). The model also includes energy losses to the environment.

$$\varepsilon_v = a_0 + a_1 r_{p,tot} + a_2 \frac{N}{N_{max}} \tag{2.1}$$

$$X_{inj} = b_0 \ln\left(b_1 r_{p,inj}\right) \tag{2.2}$$

$$\eta_s = \frac{c_0 \exp\left(-c_1\left(r_{p,tot} - c_2\right)\right)}{1 + \exp(-c_3\left(r_{p,tot} - c_2\right)} \tag{2.3}$$

$$\eta_{drive} = \sum_{n=0}^{3} d_n \left(\frac{N}{N_{max}}\right)^2 \tag{2.4}$$

$$X_{loss} = e_0 \tag{2.5}$$

With, b_i or $c_i = c_{i,0}\left[1 + c_{i,1}\frac{N}{N_{max}} + c_{i,2}\left(\frac{N}{N_{max}}\right)^2\right], \forall i \in [0,3] \cup \mathbb{Z}$

η_{drive} is the ratio between the electrical power provided to the compressor motor and the total electrical power delivered to the drive $\dot{W}_{el}$, X_{inj} is the injection mass flow rate, $X_{loss} = \frac{\dot{Q}_{loss}}{\dot{W}_{el}}$ are the ambient losses ratio. The pressure ratios are the injection pressure ratio $r_{p,inj}$, i.e. the ratio

between the injection and the suction pressure, and the total pressure ratio $r_{p,tot}$, i.e. the ratio between the pressures at the discharge and suction ports.

Gholamrezaie, et al. [97] introduced a transcritical CO2 compressor model, which has been developed using a third-order polynomial based on data provided by the manufacturer for a semi-hermetic reciprocating compressor. The model effectively represents the compressor's performance across various operating conditions. Key inputs to the model include suction pressure (P_{suc}), discharge pressure (P_{dis}), and compressor speed in Hertz (Hz), which are essential for determining the compressor's performance. The model provides two crucial outputs: the power input (W) in kW and the CO2 mass flow rate ($\dot{m}_r$) in kg/hr. The equations governing this compressor model are as follows:

$$\begin{aligned} X = {} & a_1 + a_2 * Hz + a_3 * Hz^2 + a_4 * Hz^3 + a_5 * P_{dis} + a_6 * P_{dis}^2 + a_7 * P_{dis}^3 + a_8 * P_{suc} + a_9 * P_{suc}^2 \\ & + a_{10} * P_{suc}^3 + a_{11} * Hz * P_{dis} + a_{12} * Hz * P_{dis}^2 + a_{13} * Hz * P_{suc} + a_{14} * Hz * P_{suc}^2 \\ & + a_{15} * Hz^2 * P_{dis} + a_{16} * Hz^2 * P_{dis}^2 + a_{17} * Hz^2 * P_{suc} + a_{18} * Hz^2 * P_{suc}^2 + a_{19} \\ & * P_{dis} * P_{suc} + a_{20} * P_{dis} * P_{suc}^2 + a_{21} * P_{dis}^2 * P_{suc} + a_{22} * P_{dis}^2 * P_{suc}^2 \end{aligned} \quad (2.6)$$

where X can be the power input or the mass flow rate based on the constants detailed in their work.

Byrne, et al. [100] conducted a comprehensive review of scroll compressor modeling studies and introduced a thermodynamically realistic scroll compressor model for refrigeration and heat pump systems. Initially developed for R407C, the model was adapted to hydrocarbons. The study emphasized the importance of accurate compressor modeling, detailing adaptation procedures for different refrigerants and compressor sizes. The model, based on the semi-empirical Winandy, et al. [101] approach, required only one operating point for setting parameters and demonstrated accuracy within ±10% for mass flow rate and power, and ±5 K for discharge temperature. However, the model is based on simplified assumptions. It assumes zero degrees of superheat and subcooling, no pressure losses and a constant isentropic efficiency of 0.7.

Expansion valve modeling

Accurate modeling of expansion valve configurations necessitates a comprehensive understanding of flow characteristics, pressure drops, and responses to varying operating conditions.

A crucial role of expansion valves is to regulate refrigerant flow as operating conditions change. Consequently, various models have been developed to predict refrigerant mass flow rates under

different conditions, each employing different mathematical formulations and reporting varying levels of accuracy. A forward modeling approach requires detailed data on the geometry of the throttling section, which is often inaccessible to modelers. Hence, gray-box models (inverse models) are beneficial as they are not specific to any valve or refrigerant but are grounded in fundamental mathematical principles [102].

Given their crucial role in refrigeration cycles, thermostatic expansion valves (TEV) have been the focus of numerous studies by researchers. Ndiaye and Bernier [103] predicted the mass flow rate through the bleed port of a TEV in their research using a separated flow model. The model was validated against experimental data, showing that for inlet fluid in a sub-cooled or two-phase state, 95% of the data were predicted within ±20%, and for vapour state inlet fluid, 96% of the data were predicted within ±16%.

Conde and Suter [104] developed a mathematical model to simulate the steady-state operation of TEV up to 30 kW in refrigeration capacity. This model, essential for component matching in heat pumps and refrigeration machines, considers the interdependence between the valve's throttling and control functions and requires a few experimentally determined parameters alongside detailed geometry of the throttling section. The study emphasized that while manufacturers' participation could ease data collection and reduce uncertainties, the necessary data can still be obtained independently. This model aids manufacturers in optimizing TEV settings for improved performance.

The steady-state operation of a TEV is achieved when the forces acting on the diaphragm reach equilibrium (see Figure 6.2). This equilibrium is mathematically expressed by Conde and Suter [104] as:

$$F_b = F_r + F_s + F_{dy} \tag{2.7}$$

where F_b is the force generated by the bulb pressure on the upper face of the diaphragm, F_r is the force generated by the operating fluid (refrigerant) on the lower face of the diaphragm, F_s is the sum of the forces exerted by both springs, and F_{dy} is a force resulting from the imbalance of pressures around the poppet due to the acceleration of the flow.

The force F_b depends exclusively on the current temperature at the thermostatic bulb and the type of charge it contains. The spring force F_s can be broken down into three components:

$$F_s = F_{s,o} + F_a + K_s X \tag{2.8}$$

where $F_{s,o}$ is the sum of the forces exerted by both springs when the valve is completely closed, at the factory settings; F_a results from an adjustment of the static opening superheating of the valve, using the screw; and $K_s X$ is the component due to the poppet displacement, with K_s assumed to be constant (linear springs).

Eames, et al. [105] developed and evaluated generalized steady-state and transient mathematical models for TEV used in commercial refrigeration systems. These models do not require specific performance or geometrical data to operate. The models were validated against current standards and manufacturer data, showing close agreement. The study concluded that the models provide high fidelity in simulating TEV behavior within complex refrigeration systems under realistic loading conditions.

Behfar and Yuill [106] reviewed and analyzed four gray-box mass flow rate models for TEV used in air-conditioning and commercial refrigeration systems. The study tested these models using data from a commercial walk-in cooler and a freezer, including both normal and faulted conditions. While the models performed well for the freezer, predicting mass flow rates within 10% of the measured values, they showed significant deviations for the cooler. These deviations were attributed to factors such as the difficulty in calculating the TEV diaphragm force, uncertainties in determining two-phase refrigerant properties at the valve inlet, the presence of a liquid line receiver, and simplifications in the high side pressure calculations. The study concluded that more complex models with additional regression parameters provided slightly better predictions but increased the risk of overfitting. The findings guide users in deciding the appropriate model fidelity for specific applications.

2.2.3 Determination of heat transfer coefficients in plate heat exchangers

Plate heat exchangers (PHE) such as the ones used in the present study are heat exchangers that utilize a series of thin, corrugated plates to create multiple parallel flow channels for the hot and cold fluids. This design significantly enhances heat transfer due to the extensive surface area provided by the plates and the induced turbulence from the corrugation patterns [107]. The performance and efficiency of a PHE are heavily influenced by several key geometric parameters (see Figure 2.1), including the chevron angle, enlargement factor, mean flow channel gap, channel

flow area, and channel equivalent diameter [108]. The chevron angle (β) is the angle of the corrugation pattern on the plates, ranging from 22° to 65°. This angle is crucial as it determines the thermal hydraulic performance of the PHE, distinguishing between "soft" angles (resulting in low thermal efficiency and pressure drop) and "hard" angles (leading to high thermal efficiency and pressure drop). The enlargement factor (φ) represents the ratio of the developed length of the flow path to its projected length. It indicates the increase in surface area due to the corrugation pattern, which enhances heat transfer efficiency. The mean flow channel gap (b) is the actual gap available for fluid flow between two plates. It is calculated as b = p - t, where p is the pitch (the distance between the peaks of the corrugations) and t is the thickness of the plate. This gap affects the flow resistance and the velocity of the fluid, influencing both the heat transfer rate and the pressure drop.

The channel flow area (A_x) is the cross-sectional area through which the fluid flows in the channel. It is defined as $A_x = bw$, where w is the width of the channel. The flow area directly impacts the volumetric flow rate and fluid velocity, affecting the overall heat transfer and pressure drop in the PHE. The channel equivalent diameter (d_e) is a parameter used to characterize the flow within the channel. It is defined as $d_e = \frac{4A_x}{P}$ where $P = 2(b + \Phi w)$. Since $b \ll w$ this simplifies to $P = 2\Phi w$ and then $d_e = \frac{2b}{\Phi}$.

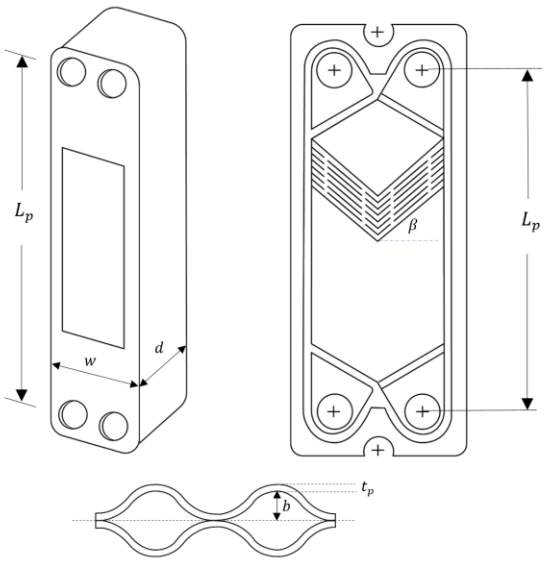

Figure 2.1 Illustration of a plate heat exchanger and a cross-sectional view of two adjoining plates

The equivalent diameter is essential for determining the Reynolds number and other dimensionless numbers necessary for analyzing the flow characteristics and heat transfer performance of the PHE.

Single-phase heat transfer coefficients

Many researchers have significantly advanced the knowledge of single-phase flow heat transfer and pressure drop in plate heat exchangers. Due to space constraints, it is impossible to name all of them in this document. Numerous researchers have proposed correlations for single-phase heat transfer coefficients, with most taking the form:

$$Nu = C \times Re^{n} \times Pr^{m} \tag{2.9}$$

where Nu is the Nusselt number, Re is the Reynolds number, and Pr is the Prandtl number. Here C, n, and m are empirical constants specific to the correlation. Among the many suggested correlations for single-phase flow, only a select few, which are particularly relevant or widely used, will be discussed in this thesis. These correlations are shown in Table 2.1.

Two phase heat transfer coefficients

Table 2.2 presents significant correlations used to calculate heat transfer coefficients for two-phase flow during both evaporation and condensation.

Heat transfer in flow boiling is often described as a combination of nucleate boiling and convective evaporation contributions. In nucleate boiling, the heat transfer coefficient depends strongly on the heat flux, whereas in convective evaporation, it primarily relies on mass flux and vapor quality. Plate heat exchangers, used exclusively for direct evaporation, present a direct correlation between heat flux and mass flux, complicating the differentiation between these contributions.

Unlike single-phase flow, the heat transfer coefficient in flow boiling is not uniform across the heat exchanger. As the temperature of the heat source fluid decreases from inlet to outlet, the heat flux on the refrigerant side varies, affecting the heat transfer coefficient. Changes in vapor fraction also influence heat transfer, with the coefficient potentially decreasing at high vapor qualities. Additionally, a few degrees of superheat in the evaporator are often required at the outlet during direct expansion, and the heat transfer in the superheating section is lower than in the boiling section, making the average heat transfer coefficient dependent on the outlet superheat

Table 2.1 Single-phase heat transfer correlations

Investigator	Correlation	Comments
Troupe, et al. [109]	$Nu = \left(0.383 - \frac{0.505L^p}{b}\right) Re^{0.65} Pr^{0.4}$	$Re > Re_{cr}$ $10 < Re_{cr} < 400$, water
Muley and Manglik [110]	$Nu = \left[0.2668 - 0.006967(90 - \beta) + 7.244 \times 10^{-5(90-\beta)^2}\right] \times [20.78 - 50.94\varphi + 41.16\varphi^2 - 10.51\varphi^3] \times Re^{\left[0.728+0.0543\sin\left(\frac{\pi(90-\beta)}{45}\right)+3.7\right]} \mathrm{Pr}^{\left(\frac{1}{3}\right)\left(\frac{\mu}{\mu w}\right)^{0.14}}$	$Re \geq 10^3$, $30 \leq \beta \leq 60$, $1 \leq \varphi \leq 1.5$
Kumar [111]	$Nu = C_1 Re^m \mathrm{Pr}^{0.33} \left(\frac{\mu}{\mu_w}\right)^{0.17}$	C_1 and m are constants, defined as functions of Re and β.
Thonon [112]	$Nu = C_1 Re^m \mathrm{Pr}^{0.33}$	C_1 and m are constants, defined as functions of Re and β.
Wanniarachchi, et al. [113]	$Nu = \left({Nu_t}^3 + {Nu_l}^3\right)^{\frac{1}{3}} Pr^{\frac{1}{3}} \left({\mu_b}/{\mu_w}\right)^{0.17}$ $Nu_l = \frac{3.65\phi^{0.661} Re^{0.339}}{(90-\beta)^{0.455}}$ $Nu_t = \frac{12.6\phi^{1-m} Re^m}{(90-\beta)^{1.142}}$ $m = 0.646 + 0.0011(90 - \beta)$	$1 < Re < 10^4$ $20° \leq \beta \leq 62°$
Marriot [114]	$Nu = 0.374 Re^{0.668} \mathrm{Pr}^{0.333} \left(\frac{\mu}{\mu w}\right)^{0.14}$	Turbulent flows (water), $4 < de < 10$ mm $10 < \mu < 100$ kg/m-s
Okada, et al. [115]	$Nu = 0.157 Re^{0.64} Pr^{0.4} \beta = 60°$ $Nu = 0.249 Re^{0.64} Pr^{0.4} \beta = 45°$ $Nu = 0.327 Re^{0.65} Pr^{0.4} \beta = 30°$ $Nu = 0.478 Re^{0.62} Pr^{0.4} \beta = 15°$	$700 < Re < 25000$, water
Roetzel, et al. [116]	$Nu = 0.371 Re^{0.703} Pr^{0.33}$	$400 < Re < 2000$, water, chevron plate ($\beta = 20°$) $L\,p$ =176.5 mm, w =71 mm, t =0.5 mm, b=2 mm
Talik, et al. [117]	$Nu = 0.2 Re^{0.75} Pr^{0.4}$ $Nu = 0.248 Re^{0.75} Pr^{0.4}$	$10 < Re < 720$, water/glycol ($70 < Pr < 450$) $1450 < Re < 11460$, water ($2.5 < Pr < 5.0$)
Kim and Park [118]	$Nu = 0.1452\phi^{2.079} Re^{0.764} Pr^{0.33}$	$400 < Re < 1400$

Studying flow boiling in plate heat exchangers is challenging due to experimental difficulties in measuring local heat transfer coefficients. This challenge arises from the difficulty of measuring surface temperatures in the compact flow channel geometry and the variation of the heat transfer coefficient on the heat source side within each cell, influencing local heat flux and nucleate boiling contribution along the heat exchanger and within each cell [107].

Experimental measurement of heat transfer coefficients

Experimental methods provide essential data for validating and refining theoretical models used in vapor compression cycles. This section outlines the experimental techniques employed to determine heat transfer coefficients in heat exchangers. Accurate measurement of these coefficients is crucial for enhancing the reliability of models and improving the overall performance and efficiency of heat exchangers within vapor compression systems.

Heat transfer coefficients are fundamental parameters for the design and analysis of heat exchangers in vapor compression systems. Experimental determination of these coefficients involves conducting controlled experiments to measure the heat transfer performance under various conditions. Accurate determination of heat transfer coefficients is crucial for validating theoretical models and for designing efficient and reliable heat exchangers. This section discusses the methodologies for experimental measurements and the significance of these coefficients in enhancing system performance.

Cattelan, et al. [119] developed a numerical model for the condensation heat transfer of R1234ze(E) and R134a inside a brazed plate heat exchanger (BPHE), with the model validated against experimental data. The BPHE consisted of four plates, creating one refrigerant channel and two water channels. The refrigerant entered the BPHE as superheated vapor and was condensed using counter-current water flow.

Two types of tests were conducted: partial and complete condensation tests. Partial condensation tests varied the vapor quality between 0.05 and 0.67, with the refrigerant entering as superheated vapor. Complete condensation tests varied superheating and subcooling degrees, with the refrigerant entering as superheated vapor and exiting as subcooled liquid. The tests revealed that R1234ze(E) had slightly lower heat transfer coefficients compared to R134a, and subcooling significantly impacted performance, especially at low mass flux. The validated model accurately

predicted heat transfer coefficients and system behavior, proving useful for designing and simulating heat pump and refrigeration systems.

Table 2.2 Two phase heat transfer correlations

Investigator	Correlation	Comments
Ayub [108]	$h_{tp} = C\left(\frac{k_l}{d_e}\right)Re^2\left(\frac{h_{fg}}{L_p}\right)^{0.4124}\left(\frac{p}{p_{cr}}\right)^{0.12}\left(\frac{65}{\beta}\right)^{0.35}Pr^{0.33}$	C = 0.1121 for flooded and thermo-syphon and C = 0.0675 for direct expansion (DX).
Yan, et al. [120]	$Nu = \frac{hD_h}{k_l} = 4.118{Re_{eq}}^{0.4}\,\mathrm{Pr}_l^{\frac{1}{3}}$ $G_{eq} = G\left[1 - X_m + X_m\left(\frac{\rho_l}{\rho_v}\right)\right]$ $Re_{eq} = \frac{G_{eq}D_h}{\mu_l}$	60 kg/m^{2}s $\leq G \leq$ 120 kg/m^{2}s $0.1 \leq X_m \leq 0.9$
Cooper [121]	$\frac{h}{(q/A)^{0.67}} = 55P_r^{[0.12-0.2log_{10}R_p]}(-logP_r)^{-55}M^{-0.5}$	$0.0001 \leq P_r \leq 0.5322$ $40 \leq M \leq 90$
Jokar, et al. [122]	$Nu_{tp} = 0.603Re_{lo}^{0.5}Pr^{0.1}x^{-2}\left(\frac{G^2}{{\rho_l}^2C_{p,l}\Delta T_s}\right)^{-0.1}\left(\frac{{\rho_l}^2 i_{lv}}{G^2}\right)^{-0.5}\left(\frac{\rho_l\sigma}{\mu_l G}\right)^{1.1}\left(\frac{\rho_l}{\rho_l-\rho_v}\right)^2$	Flow boiling data, dh = 4.0 mm, β = 60 °, R134a, ammonia, three different plate configurations (34, 40, 54 plates), suitable for mean analysis.
Park and Kim [123]	$Nu_{tp} = 12.47Re_{eq}^{0.33}Pr^{0.333}$ $G_{eq} = G\left[(1-x) + x\left(\frac{\rho_l}{\rho_v}\right)^{0.5}\right]; Re_{eq} = \frac{G_{eq}D_h}{\mu_l}$	$1700 \leq Re_{eq} \leq 12500$
Ayub, et al. [124]	$Nu_{tp} = \left(1.8 + 0.7\frac{\beta}{\beta_{max}}\right)Re_{eq}^{\left(0.49-0.3\frac{\sigma_{ref}}{\sigma_{ammonia}}\right)}Bo^{-0.2}$	$\beta_{max} = 65\,°C$ $313 \leq Re_{eq} \leq 12700$ $0.000136 \leq Bo \leq 0.0019$
Kwon, et al. [125]	$Nu_{tp} = 10.887Re_{eq}^{1.146}Re_{lo}^{-0.354}Bo^{0.292}Ge^{0.903}\mathrm{Pr}^{0.333}$	R-1233zd(E) $500 \leq Re_{eq} \leq 2400$ $5 \leq Bo_{eq} \leq 240$

Mancin, et al. [126] conducted experimental studies on the partial condensation of superheated vapors of R410A and R407C inside two BPHE prototypes with different geometries. The condensation heat transfer coefficients were measured at constant inlet saturation temperatures of 36.5 °C for R410A and 41.8 °C for R407C, with refrigerant mass velocities ranging from 15 to 40 kg m^{-2} s^{-1} and outlet vapor qualities between 0.01 and 0.58. The tests aimed to validate a new model proposed by Mancin, et al. [127] for simulating the condensation process in BPHEs. The refrigerant entered the BPHE as superheated vapor and was condensed using counter-current water flow.

The study found that the condensation heat transfer coefficient increased with vapor quality and decreased with temperature difference. At low mass velocities, the heat transfer coefficient was relatively independent of refrigerant mass flow rate, but it increased significantly at higher mass velocities. The model by Mancin, et al. [127] showed good agreement with the experimental data, with a relative deviation of 1.5%, an absolute deviation of 5.9%, and a standard deviation of 7.7%.

CHAPTER 3 OBJECTIVES AND THESIS STRUCTURE

3.1 Objectives

The general objective is to develop an experimentally validated model of a water-to-water heat pump. This includes operation with a fixed-speed and variable-speed compressors. This general objective is accomplished by fulfilling four specific objectives listed below:

1. Develop relatively simple models that allow the evaluation of new trends in heat pump design, including the use of intermediate heat exchangers, expanders, multi-compressors and variable-speed compressors.

2. Develop a comprehensive physical model of a heat pump. Unlike other modeling studies that fix one or several points in the refrigeration cycle, this study lets the model find the equilibrium state of the cycle based on the given inlet conditions (flow rate and temperature) of the water at the inlets of the evaporator and condenser.

3. Expand the base model to include variable-speed compressors and adapt this model to improve an existing TRNSYS Type and to analyze the impact of variable-speed operation on heat pump performance as well as on the sizing of ground heat exchangers.

4. Build an experimental test bench to validate the heat pump model.

3.2 Thesis outline

The thesis encompasses eight chapters, starting with an introductory that presents some of the basic concepts used throughout this study. Following this, Chapter 2 provides a review of the pertinent literature on water-to-water heat pumps with an emphasis on the various modeling approaches. Chapter 3 presents the objectives of the thesis and outlines the subsequent structure of the work. Moving forward, Chapter 4 examines with a relatively simple approach some possible improvements to heat pumps such as the use of an intermediate heat exchanger and expanders. It also explores the benefits of using fixed-speed multi-compressors and variable speed compressors.

Chapters 5 and 6 extend the analysis by introducing a more comprehensive modeling approach of water-to-water heat pumps. Each of these two chapters corresponds to a journal publication. Chapter 5 presents a detailed examination of a variable-speed heat pump model tailored for ground-

source applications. Chapter 6 introduces a steady-state model of a water-to-water heat pump with experimental validation.

Chapter 7 proposes a discussion on the findings from preceding chapters. Finally, Chapter 8 concludes the thesis by summarizing key contributions and offering recommendations for future research.

At the end, Appendix A presents the calibration procedures and results. This appendix provides an overview of the procedures and experimental setups used to calibrate the thermocouples, thermopiles, and flowmeters utilized in this study. Appendix B details experimentally derived overall heat transfer coefficients for the condenser and evaporator.

3.3 Acknowledgement of assistance from artificial intelligence

It should be noted that ChatGPT, a language model developed by OpenAI, was used exclusively to improve the translation, wording, and grammar of this thesis. As a non-native English speaker, the author sought assistance to ensure clarity and coherence in the presentation of ideas and findings. This tool did not influence the original content and analytical insights of the work.

CHAPTER 4 HEAT PUMP PERFORMANCE IMPROVEMENTS

In the early stages of this work, three possible performance improvements to heat pumps were examined and are reported in this chapter. The first study examines the implementation of an intermediate heat exchanger between the condenser and the evaporator. The second investigation explores the adoption of an expander or expansion turbine to replace the expansion valve. Finally, the third analysis compares the efficiency and performance of variable speed compressors against those of fixed speed parallel multi-compressors. The first two studies complement other findings found in the literature while the third one offers a new perspective on the use of multi-compressor to maximize compressor efficiency during a heating season.

4.1 Intermediate heat exchanger

An intermediate heat exchanger also referred to as a suction line heat exchanger (SLHX), is often used between the condenser and the evaporator of refrigeration systems as shown in Figure 4.1. The corresponding operating points in a *P-h* diagram are shown in Figure 4.2. In this system, the liquid refrigerant at the exit of the condenser is subcooled in the intermediate heat exchanger before entering the expansion valve, where it is throttled to the evaporator pressure. The refrigerant exits the intermediate heat exchanger as subcooled refrigerant at a temperature T_3' on one side and as a superheated vapor at a temperature T_1' on the other side. The amount of heat exchanged is denoted by Q in Figures 4.1 and 4.2.

SLHXs affect the heat pump performance in five different ways. First, the heat exchanger contributes to an increase in the enthalpy differences in the evaporator (from $h_4 - h_1$ to $h_4' - h_1$) and condenser (from $h_2 - h_3$ to $h_2' - h_3$). In principle, according to Equations 1.3 and 1.4, this increase should increase the COP in heating and cooling.

Secondly, superheating is enhanced as refrigerant vapor enters the compressor at T_1' instead of T_1. This enables a safer operation of the compressor as it minimizes the risk of damage linked to liquid refrigerant ingestion.

Thirdly, enhanced subcooling brings the refrigerant's expansion process in the valve closer to an isentropic process [49].

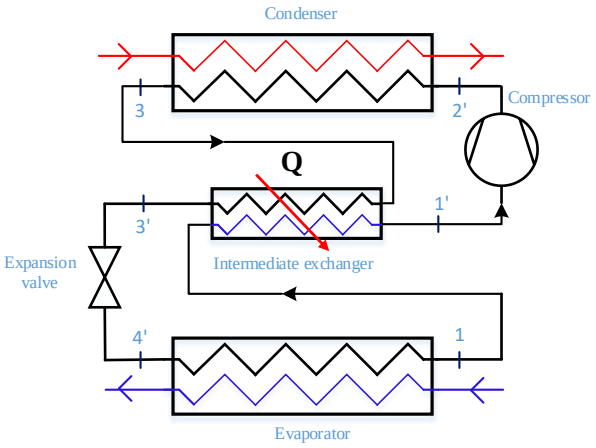

Figure 4.1 Location of the intermediate heat exchanger in a refrigeration system

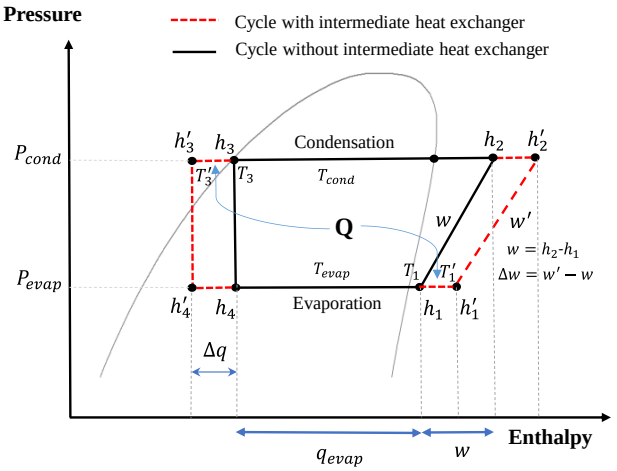

Figure 4.2 Changes in the operating conditions with the introduction of an intermediate heat exchanger

Indeed, as shown in Figure 4.3, the expansion process from h_3 to h_4, which is isenthalpic in nature, progressively approximates an isentropic expansion (indicated by the dotted line) as it moves towards the subcooled region. Consequently, the expansion process from h_3'' to h_4'' becomes more efficient by nearing the isentropic curve at s_3''.

Fourthly, as shown in Figure 4.3, as superheat levels rise, the work per unit mass, w, increases over the same pressure ratio.

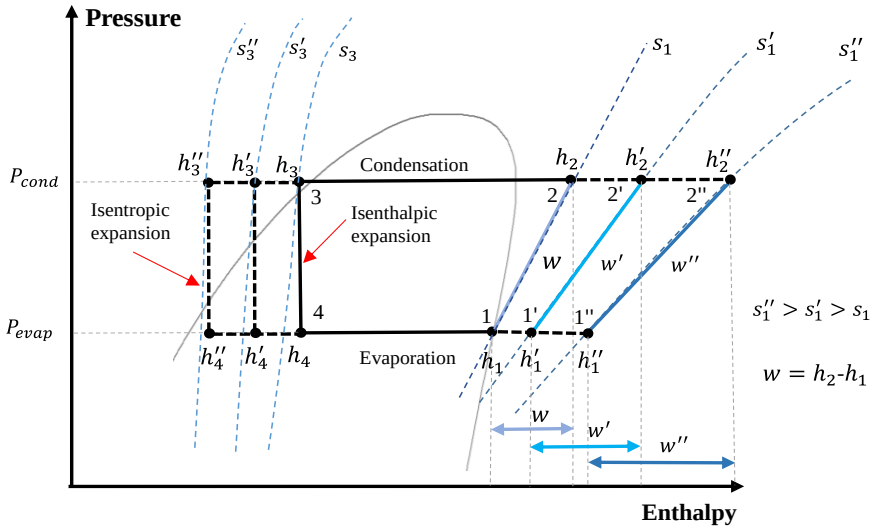

Figure 4.3 *P-h* diagram showing the impact of a SLHX

This is because most refrigerants have isentropic curves which tend to bend towards higher enthalpy values in the superheated region. This suggests that an increase in superheating is typically associated with an increase in the work per unit mass required, i.e. $w'' > w' > w$.

Finally, an increase in the temperature at the compressor's suction point leads to a reduction in refrigerant density, which in turn lowers the mass flow rate through the compressor. This effect and the fourth effect might neutralize each other, implying that the overall energy consumption might not be significantly affected by changes in superheating levels, in accordance with the observations made in AHRI 540 standard [128].

The following paragraphs examine the interconnecting effects of these five changes associated with the use of a SLHX. The analysis is performed using four common refrigerants (R134a, R32, R410A, R454B). The next sub-section describes the heat pump model used to perform this analysis. This is followed by definitions of the metrics used to judge changes made. Finally, results are presented.

4.1.1 Heat pump model

The following paragraphs present the heat pump model utilized in the analysis of the SLHX. A relatively simple model (compared to the more elaborate model presented later) is used to focus on the SLHX.

For the compressor, the isentropic efficiency, η_{is}, is modelled as a second-order polynomial as a function of the pressure ratio (PR), i.e. the ratio of the condenser pressure over the evaporator pressure (P_{cond}/P_{evap}):

$$\eta_{is} = a_1 + b_1 PR + c_1 PR^2 \tag{4.1}$$

Coefficients a_1= 0.594, b_1= 0.0268 and c_1= -0.00213 are used in this study.

The volumetric efficiency, η_v, is defined as the actual volumetric flow rate over the maximum theoretical flow rate associated with the total volume swept by the compressor (Equation 4.3). Given its dependence on the PR, it is modeled here using this relationship:

$$\eta_v = a_2 + b_2(PR^n - 1) \tag{4.2}$$

where a_2= 1, b_2= 0.04, and n = 0.7

The effect of the PR on the isentropic efficiency and volumetric efficiency is illustrated in Figure 4.4.

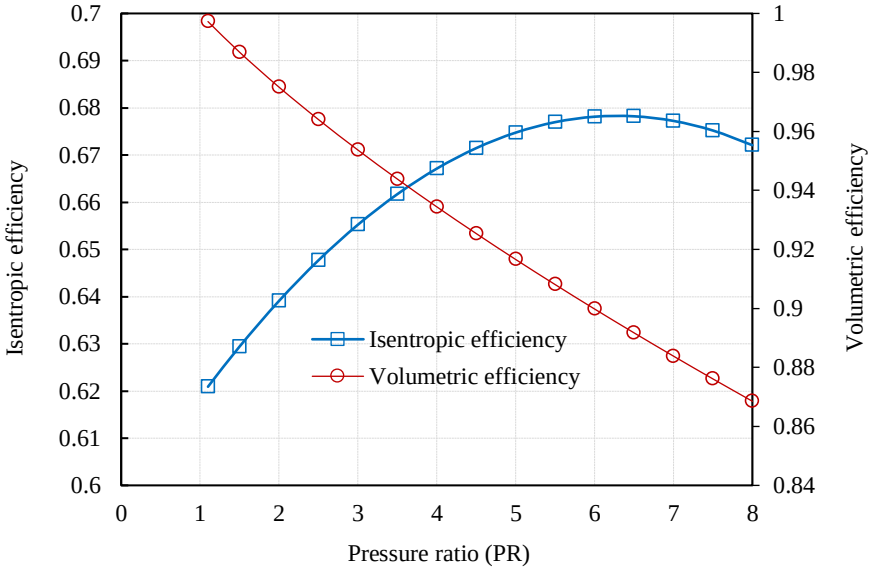

Figure 4.4 Effect of Pressure Ratio on isentropic and volumetric efficiency

The values of the parameters in Equations 4.1 and 4.2 were determined based on manufacturer data for a residential-size scroll compressor.

The mass flow rate, $\dot{m}_r$, is calculated based on the refrigerant density at the compressor inlet, ρ_s, the volumetric efficiency, η_v, and the volumetric displacement rate, $\dot{v}$:

$$\dot{m}_r = \dot{v}\eta_v\rho_s \tag{4.3}$$

where $\dot{v}$ is set to 5 m^3/h which represent a typical rate for a residential heat pump.

If the operation of the SLHX does not introduce significant pressure drops in the cycle as suggested by Klein et al. [36], the outlet temperatures of the refrigerant from the heat exchanger, T_3' and T_1', depend on the heat exchanger effectiveness, ε_{SLHX}. The outlet temperature of the heat exchanger on the liquid side, T_3' can be obtained using the following relationship:

$$\varepsilon_{SLHX} = \frac{Q}{Q_{max}} = \frac{\dot{m}_r C_{p,r_{liq}}(T_3 - T_3')}{\dot{m}_r C_{p,r_{vap}}(T_3 - T_1)} = \frac{C_{p,r_{liq}}(T_3 - T_3')}{C_{p,r_{vap}}(T_3 - T_1)} \tag{4.4}$$

where $C_{p,r_{liq}}$ refers to the mean liquid refrigerant specific heat capacity in the range between T_{cond} and T_{evap} at the condensing pressure (P_{cond}), while $C_{p,r_{vap}}$ denotes the mean specific heat capacity for superheated vapor at the mean temperature between T_1 and T_1'. Once T_3' is known, the outlet temperature of the heat exchanger on the vapor side, T_1', is obtained through a simple energy balance on the heat exchanger.

The refrigeration capacity, Q_{evap}, and the compressor power, W, without the SLHX can be expressed by:

$$Q_{evap} = \dot{m}_r(h_1 - h_4) = \dot{v}\eta_v\rho_s(h_1 - h_4) \tag{4.5}$$

$$W = \frac{\dot{m}_r\left(h_{2_{is}} - h_1\right)}{\eta_{is}} = \dot{m}_r(h_2 - h_1) \tag{4.6}$$

The condenser and evaporator are not modelled per say. Instead, the evaporating and condensing temperatures are fixed. This facilitates the solution of the governing equations in order to focus on the performance of the SLHX. The Engineering Equation Solver (EES) [9] is used to solve the governing equations.

4.1.2 Performance indices

To characterize the changes in the refrigeration cycle resulting from the use of a SLHX, three indices are defined below to represent the changes in capacity, performance, and compressor work.

With reference to Figure 4.2, the increase in cooling capacity, Δq, and the modified coefficient of performance in cooling mode, COP', are given by Domanski, et al. [49]:

$$COP' = \frac{q_{evap} + \Delta q}{w + \Delta w} \approx COP\left(1 + \frac{\Delta q}{q_{evap}} - \frac{\Delta w}{w}\right) \tag{4.7}$$

where, $q_{evap} = h_1 - h_4$ and $w = h_2 - h_1$.

As noted by Domanski, et al. [49], the ratio $\frac{\Delta q}{q_{evap}}$ is invariably positive. Similarly, $\frac{\Delta w}{w}$ is consistently positive because the slope of constant entropy lines, which represent the ideal compression process, diminishes with an increase in vapor superheat on the *P-h* diagram. Consequently, the performance impact of the SLHX is determined by the relative rates at which $\frac{\Delta q}{q_{evap}}$ and $\frac{\Delta w}{w}$ vary.

Relative Capacity Index (RCI):

The effect of an SLHX on refrigeration capacity can be quantified using a Relative Capacity Index (RCI) as defined in the following equation (Klein, et al. [50]):

$$\text{RCI}=\left(\frac{\Delta Q_{evap}}{Q_{evap}}\right)\times 100 \tag{4.8}$$

with $\Delta Q_{evap} = Q'_{evap} - Q_{evap}$, where Q_{evap} is given by Equation 4.5 and Q'_{evap} is the capacity at the evaporator with the SLHX:

$$Q'_{evap} = \dot{m}'_r(h_1 - h'_4) = \dot{m}'_r q'_{evap} \tag{4.9}$$

It is to be noted that the refrigerant flow rates are not the same in Equation 4.5 and 4.9.

Relative Performance Index (RPI)

The Relative Performance Index (RPI) can be expressed as follows:

$$\text{RPI} = \left(\frac{COP' - COP}{COP}\right)\times 100 \tag{4.10}$$

$$COP = \frac{q_{evap}}{w},\ COP' = \frac{q_{evap} + \Delta q}{w + \Delta w} \tag{4.11}$$

This index can also be expressed in the following way:

$$\text{RPI} = \left(\frac{\frac{q_{evap}+\Delta q}{w+\Delta w} - \frac{q_{evap}}{w}}{\frac{q_{evap}}{w}}\right)\times 100 = \left(\frac{\Delta q \times w - q_{evap}\times \Delta w}{q_{evap}(w+\Delta w)}\right)\times 100$$

Preliminary calculations have shown that the term $\Delta q \times w$ is approximately 100 times greater than the term $q_{evap} \times \Delta w$, and therefore, the latter term can be considered negligible. This simplification leads to the following relationship:

$$\text{RPI} = \frac{\Delta q}{q_{evap}}\frac{w}{w'} \tag{4.12}$$

with $w' = w + \Delta w$

Relative Work Index (RWI)

The use of an intermediate heat exchanger causes superheating of the refrigerant at the compressor's suction. This superheating results in a change in the physical properties of the fluid, which vary from one refrigerant to another. For this reason, the work done for the same pressure ratio differs for each refrigerant. To quantify this impact, the Relative Work Index (RWI) is defined as:

$$\mathrm{RWI} = \left(\frac{W' - W}{W}\right) \times 100 = \frac{\Delta W}{W} \times 100 \tag{4.13}$$

Where W' and W are the compressor power with and without the SLHX.

The effects of a SLHX are quantified in this section for various cases using the indices presented above. The results presented in the following paragraphs build on those presented by Domanski, et al. [49] with two major changes. First, a more accurate representation of compressor behavior is utilized. Secondly, current refrigerants are used.

4.1.3 Capacity enhancement

Figure 4.5 illustrates the change in refrigeration capacity as a function of the SLHX effectiveness using the RCI for four different refrigerants. The capacity is not only a function of the enthalpy change, which is undoubtedly greater than the enthalpy changes of the basic cycle, but it is also a function of the change in mass flow rate of the refrigerant caused by a decrease of refrigerant density at the suction of the compressor. In order to distinguish between these two effects, two sets of RCI curves for each refrigerant are presented: one assuming that the mass flow rate is constant and another where the mass flow rate changes with the change in refrigerant density.

The first observation regarding Figure 4.4 is that RCI values vary almost linearly as a function of the SLHX effectiveness. Under the assumption of a constant mass flow rate, refrigerants R410A and R134a have a RCI of 20%, while R454B and R32 have a RCI of about 12% for a SLHX effectiveness of 1. When adopting a more realistic scenario that accounts for the temperature's influence on suction density which influences the mass flow rate, the values of the RCI change drastically and only refrigerant R134a and R410A have positive values of the RCI. For a SLHX effectiveness of 1, R134a exhibits a modest capacity increase of around 3% while refrigerant R32 undergoes a decrease of 4%.

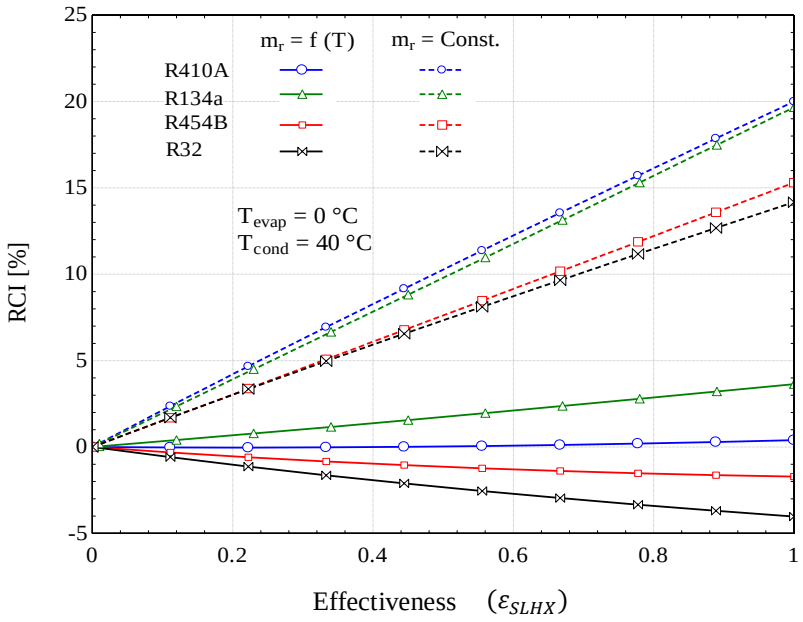

Figure 4.5 Relative capacity increase as a function of the SLHX effectiveness for four refrigerants

4.1.4 COP enhancement

The RPI is an indication of COP enhancement caused by the presence of the SLHX. Figure 4.6 illustrates the value of the RPI as a function of the SLHX effectiveness. Values of the RCI presented earlier are also shown. In both cases the variation of the mass flow rate resulting from the use of a SLHX is accounted for.

It can be shown that the RCI and RPI curves follow the same trend. For a given refrigerant, there are discrepancies between these two curves. It is notably apparent with R134a, which shows about a one percentage point difference between the RCI and RPI curves for a SLHX effectiveness of 1 while it is almost negligible for R32.

These discrepancies between RPI and RCI values are primarily attributed to the increase in compressor power due to refrigerant superheating at the outlet of the SLHX. This superheating alters the physical properties of the fluid exiting the evaporator and entering the compressor, varying based on the refrigerant used. To quantify this effect, the Relative Work Index (RWI), defined in Equation 4.14, is used and Figure 4.7 illustrates the RWI for the same four refrigerants.

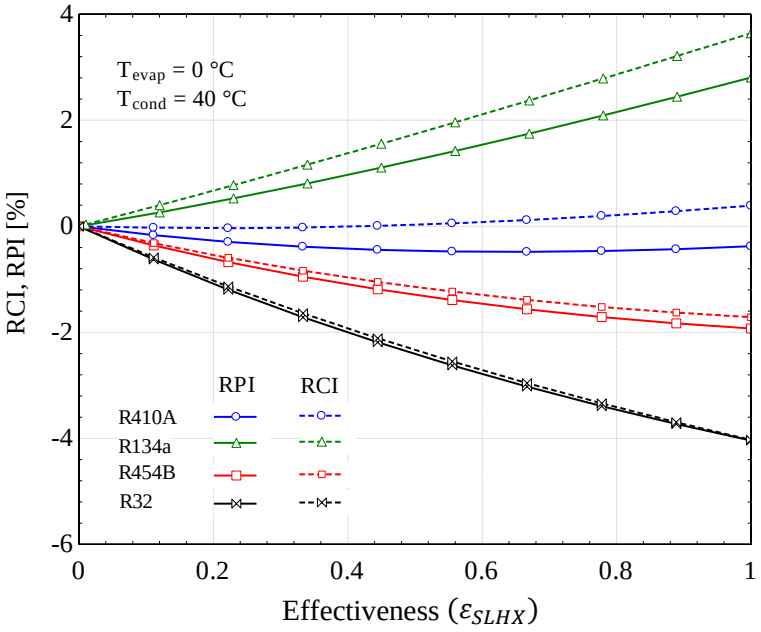

Figure 4.6 RPI and RCI as a function of the SLHX effectiveness for four refrigerants

As shown in Figure 4.7, the increase in compressor power does not exceed 1% in any of the cases presented. R454B and R32 show the smallest increase in compressor power which explains why curves for RPI and RCI are nearly identical for these refrigerants as shown in Figure 4.6.

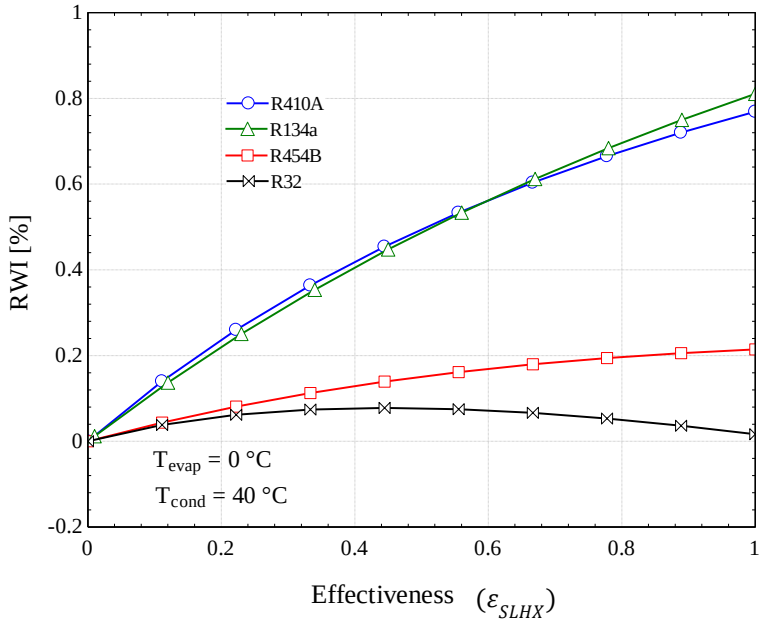

Figure 4.7 RWI as a function of the SLHX effectiveness for four refrigerants

As previously noted in Figure 4.6, the RPI depends on operational conditions. It was shown that for refrigerant R410A, the increase in performance is almost negligible under the evaluated

conditions with an evaporating temperature of 0 °C and a condensing temperature of 40 °C. However, this does not imply similar behavior under all conditions. To analyze this further, Figure 4.8 is presented.

The RPI for R410A is calculated using condensation temperatures ranging from 20 °C to 55 °C, and evaporation temperatures from -10 °C to 10 °C and for a SLHX effectiveness of 0.5. It is observed that achieving positive RPI values necessitates maintaining a condensation temperature above 47 °C.

This performance gain is further pronounced with a decrease in the evaporation temperature. It is possible to realize a performance enhancement of up to 3% at a condensation temperature of 55 °C and an evaporation temperature of -10 °C. Finally, it is observed that the minimum and maximum values of RPI for R410A are reached at the lowest evaporation temperature of -10°C, with an RPI of -1.1% at a condensation temperature of 20 °C and 3% at 55 °C.

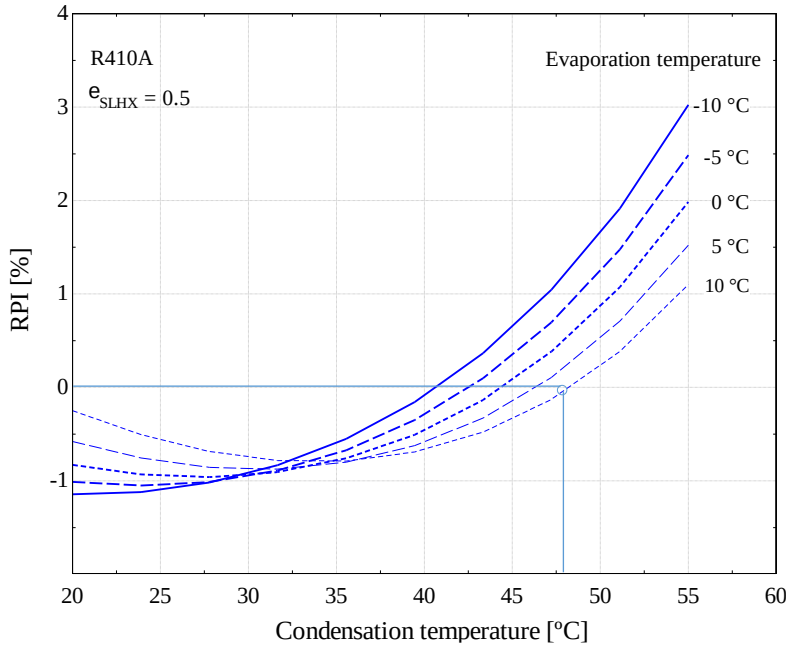

Figure 4.8 Effect of different condensation and evaporation temperatures on RPI for R410A and for a SLHX effectiveness of 0.5

4.1.5 Conclusion

The study reveals that the integration of an intermediate exchanger into refrigeration systems has varying effects on different refrigerants, with the impact largely dependent on the refrigerant's properties and operational conditions. Under idealized conditions of constant mass flow rate,

R410A and R134a show significant capacity increases of 20%, while R454B and R32 show increases around 12% for a SLHX effectiveness of one. However, more realistic conditions accounting for temperature effects on suction density significantly alter the outcomes, with only R134a showing a marginal capacity increase of 3% and R32 experiencing a 4% decrease.

Power consumption changes are generally marginal but can impact performance improvements depending on operational conditions and the refrigerant used. For refrigerants like R-410A, commonly used in residential systems, the use of a SLHX only yields performance benefits under specific operating conditions. Under the conditions of this study, condensation temperatures exceeding 47 °C result in an increase in RPI, regardless of the evaporation temperature.

In essence, while intermediate heat exchangers can improve efficiency, the extent of this improvement is heavily influenced by the chosen refrigerant and the system's operating parameters. This underscores the importance of selecting refrigerants and designing systems that align with their unique properties for optimized performance.

4.2 Evaluation of expansion turbines (expanders)

The expansion process between the condenser and evaporator is traditionally carried out by throttling in a capillary tube or an expansion valve. Previous studies have shown that this process is one of the sources of irreversibility in a vapor compression refrigeration system (Ahamed, et al. [129]; Pitarch, et al. [130]). Therefore, it is desirable to find solutions to reduce this loss.

Some researchers have proposed modifying the expansion process to extract some work from it. This can be achieved by using two alternative technologies, an ejector or an expansion turbine (expander). An ejector uses the expansion energy to increase the pressure of the refrigerant in the compressor suction line to reduce the compressor ratio and thus reduce the work of the compressor. Recent reviews on ejector technologies are available in the literature (Elbel and Lawrence [131]; Besagni, et al. [132]). In general, ejectors are simpler to construct than expanders. However, ejectors require a more extensive modification of the cycle. On the other hand, expanders are easier to install while generally being more efficient than ejectors (Elbel and Lawrence [131]). Figure 4.9 shows a schematic representation of the expander's position in the cycle. Here, the refrigerant at the exit of the condenser is shown in the diagram with two possible paths that are the focus of this study. The first path is where the refrigerant follows the route of the classic cycle, passing through

the thermostatic expansion valve (TEV), and the second is where the refrigerant takes the path through the expander, against which the classic cycle will be compared.

An expander functions essentially as a compressor in reverse. It takes in fluid at high pressure and expands it to a lower pressure, generating energy in the process. This energy can be utilized to produce electricity through a generator. One major difficulty is that the process occurs under the dome, thus involving two-phase flows.

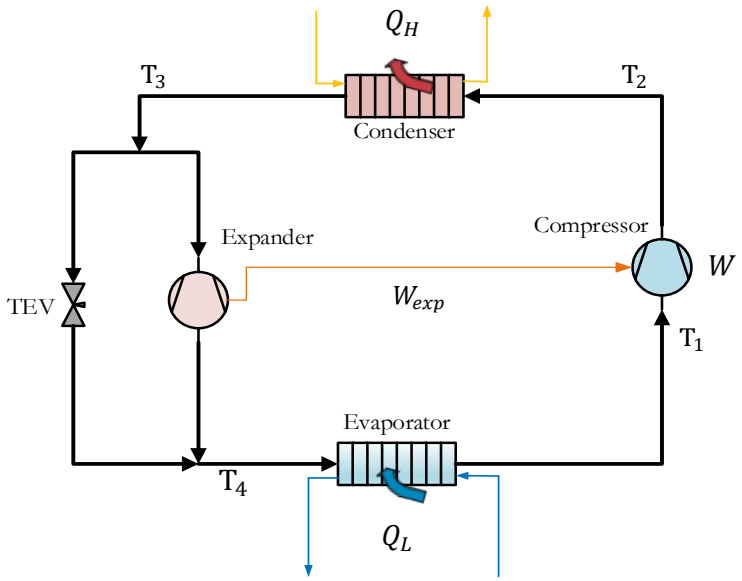

Figure 4.9 Position of the expander in a vapor compression refrigeration cycle

There have been some efforts to build expander for refrigeration systems. One notable study was performed by Barta, et al. [63]. The initial expander used is shown in Figure 4.10a. It consists of a nozzle to convert the potential energy of the high-pressure refrigerant into a high-velocity jet. The jet then impacts a radial-in axial-out turbine (Figure 4.11) which is connected to a generator for power production. Barta, et al. [133] have shown that the maximum recovered power is 45 W for a residential-type heat pump. A second design was investigated by Barta, et al. [63] and is shown in Figure 4.10b. An outlet is installed at the top for vapor discharge while the bottom outlet is used for liquid. Vapor flow is controlled via a metering valve connected to the evaporator outlet.

The following analysis concerns the first design with a two-phase outlet. The energy that can be harnessed from this process can be depicted on a *P-h* diagram, as illustrated in Figure 4-11. The

ideal expansion pathway is shown as an isentropic transition from points 3 to 4_{is} (illustrated by the blue curve), while in practice, the expansion typically follows an isenthalpic process from points 3 to 4_{ih} (indicated by the solid red line) in a TEV.

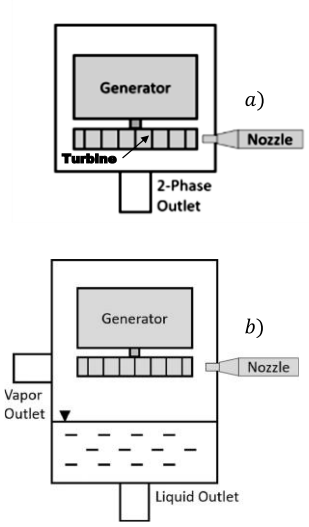

Figure 4.10 Modified expander housing. Reprinted with permission from Barta, et al. [63]

Figure 4.11 Rendering of radial-in axial-out turbine. Reprinted with permission from Barta, et al. [63]

In practice, the expansion process is somewhere between isentropic and isenthalpic processes (represented by the dotted red line). Equation 4.14 defines the isentropic efficiency of the expander. An efficiency of one indicates isentropic expansion, while an efficiency of zero corresponds to isenthalpic expansion.

$$\eta_{expander} = (h_4 - h_3)/(h_{4_{is}} - h_3) \tag{4.14}$$

The work per unit mass generated by the expander is quantified by the enthalpy differential, represented as $w_{exp} = (h_4 - h_3)$. The compressor is modeled following the same method defined by Equations 4.1 and 4.2. As was done for the study of the SLHX, the evaporator and condenser are not modeled and fixed condensation and evaporation temperature are used.

As illustrated in Figure 4.12 for R134a, with the evaporation and condensation temperatures set at -5 °C and 50 °C, respectively, an expansion from the saturated liquid curve indicates that the heat of evaporation ($h_1 - h_{4_{ih}}$) amounts to 116.5 kJ/kg. Following an isentropic expansion, the extra useful heat available for utilization ($h_{4_{ih}} - h_{4_{is}}$) is 9.9 kJ/kg, an increase of 8.5%.

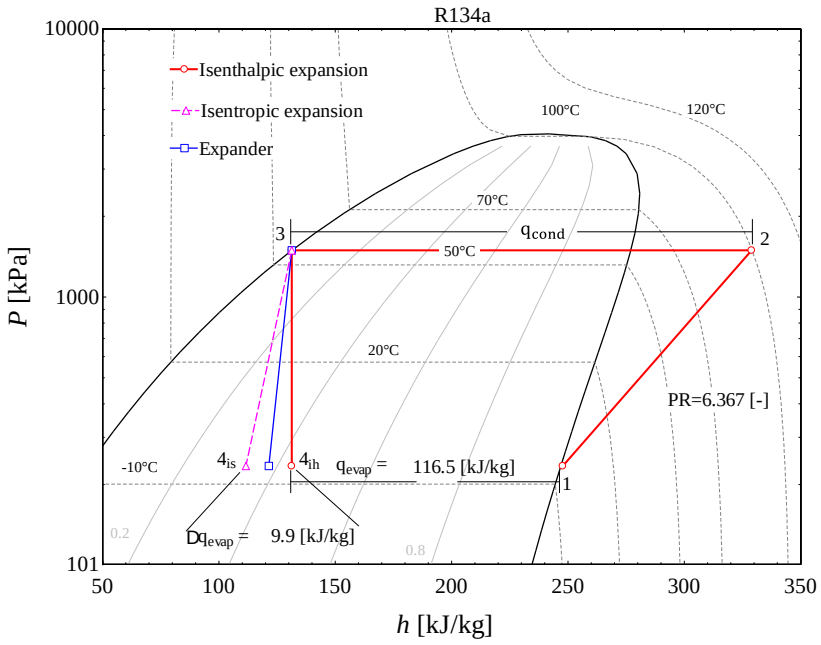

Figure 4.12 *P-h* diagram for R134a with a isenthalpic TEV (3 to 4_{ih}) and an isentropic expander (3 to 4_{is})

The coefficients of performance in cooling and heating ($COP_{exp,C}$ and $COP_{exp,H}$) of a system incorporating an expander are defined as follows:

$$COP_{exp,C} = \frac{q_{evap} + \Delta q_{evap}}{w - w_{exp}} \tag{4.15}$$

$$COP_{exp,H} = \frac{q_{cond}}{w - w_{exp}} \tag{4.16}$$

As shown in Equation 4.15, $COP_{exp,C}$ is influenced by the increase in capacity (Δq_{evap}), and the use of w_{exp} in form of work. The value of $COP_{exp,H}$ is increased due to the production of work at the expander.

In the following analysis of COP improvements, it is assumed that the refrigerant exits the evaporator in a fully saturated vapor state and exits the condenser in various degrees of subcooling as this affects the isentropic line as noted in conjunction with Figure 4.3. The evaporation and condensation temperatures are fixed at 5 and 40 °C, respectively, and the expander has an isentropic efficiency of 50%. Results are shown in Figure 4.13 and 4.14 for the four refrigerants examined previously.

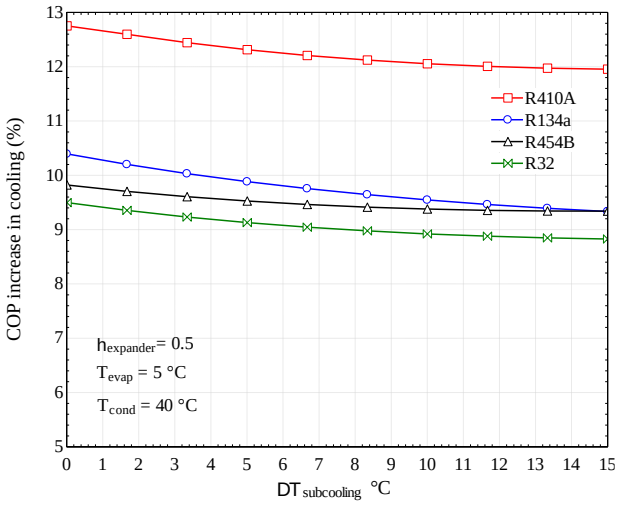

Figure 4.13 Effect of using an expander on the COP as a function of subcooling in cooling mode

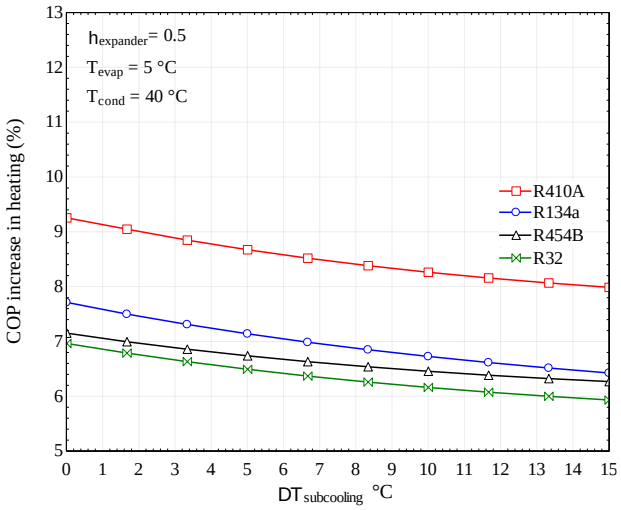

Figure 4.14 Effect of using an expander on the COP as a function of subcooling in heating mode

As expected, the COP increase is greater in cooling than in heating. For zero degrees of subcooling and for refrigerant R410A, the increase in COP reaches values of 12.8% and 9.2% in cooling and heating, respectively. There are also notable differences between refrigerants with R410A being the clear winner. The increase in COP is affected by the degrees of subcooling. For all the refrigerants studied, increasing the degrees of subcooling to 15 °C results in a reduction of the COP improvement by about 0.5 to 1 percentage points.

To summarize, the use of an expander can improve the COP of a heat pump. For the cases studied here, increases ranging from 6 to 13 % are observed. The level of improvement is dependent on the refrigerant use with R410A experiencing the highest increase. It is also shown that the COP increase diminishes as the degrees of subcooling are increased.

4.3 Energy performance advantages of using multiple compressors and variable speed compressors

As shown in section 1.3, the isentropic efficiency of compressors (and consequently the heat pump COP) varies with the pressure ratio, which is proportional to the difference between the source and sink temperatures. It is maximum for a certain pressure ratio. Furthermore, a decrease in source temperature (for a constant sink temperature) leads to a decrease in capacity. During a heating season, source and sink temperatures will vary and, consequently, the pressure ratio will vary which will influence both the COP and capacity. The objective of this section is to examine two ways to

improve the COP and maintain capacity (to avoid auxiliary heating) during a heating season. First, the use of multi-compressors operating in parallel one at a time, each with its own peak efficiency and capacity, is examined. Then, the use of variable speed compressors, which enables capacity variation, is studied. The results obtained are compared to the operation of a standard fixed-speed compressor.

This section presents modifications and improvements to an earlier study published as a conference paper by Viviescas, et al. [31]. The first change has to do with compressor modeling. Compressors were modeled using the 10 coefficient approach of the AHRI standard [128] in the conference paper. In this section, they are modeled using isentropic efficiencies which peak at the same value but at different pressure ratios. This enables the examination of scenarios where the operation of compressors is optimum for a certain pressure ratio. The second major change is the inclusion of variable speed compressors. While chapter 5 of this thesis is devoted to a more thorough analysis of variable speed compressors in heat pumps, especially for compressor modeling, the analysis provided in this section, using isentropic efficiency curves, enables a more direct comparison with multiple compressor operation.

The overall objective of this section is to examine whether the use of multiple compressors or variable speed compressors improves the seasonal performance of a water-to-water heat pump which uses the ground, via a heat exchanger, as the source temperature over a heating season for a residential system.

4.3.1 System under study

Figure 4.15 presents schematically the system under study with the three possible scenarios: one fixed-speed compressor (FSC), a multi-compressor (MC) system with five single-speed compressors linked in parallel but with only one operating at any given time, and a variable speed compressor (VSC). In each scenario, the heat pump provides space heating to a residence. The remaining components (condenser, evaporator and expansion valves) are the same for each scenario.

The heat pump uses a ground heat exchanger as the thermal source. During the heating season, a decrease of the ambient temperature has two consequences. First, the building load increases, and the heat pump needs to supply more heat. In certain cases, auxiliary heat (resistance heating) is

required as the heat pump cannot supply the full heating load. Secondly, the return temperature from the ground heat exchanger decreases which decreases the heat pump COP.

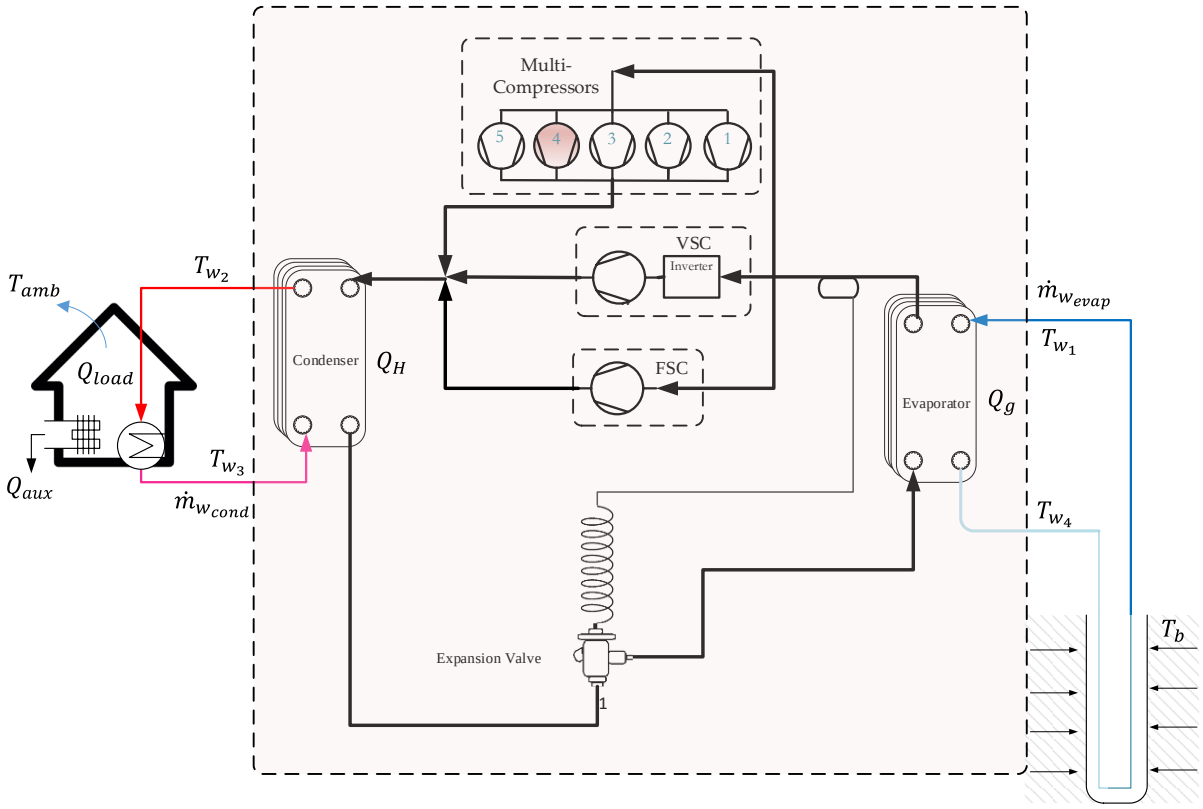

Figure 4.15 System under study showing the FSC, MC, and VSC scenarios

The heat pump model uses four inputs associated with the secondary fluids (see Figure 4.15): inlet temperatures and secondary fluid flow rates at the evaporator and condenser, T_{w_3}, T_{w_1}, $\dot{m}_{w_{evap}}$, and $\dot{m}_{w_{cond}}$, respectively.

The evaporator and condenser fluid flow rates are constant and equal to $\dot{m}_{w_{evap}} = 0.5\,\frac{\text{kg}}{\text{s}}$ and $\dot{m}_{w_{cond}} = 0.5\,\frac{\text{kg}}{\text{s}}$, respectively. Water is used as the heat transfer fluid. The inlet temperatures T_{w_3} and T_{w_1} will vary as the conditions evolved during the heating season.

4.3.2 Modeling approach

Simulations are performed in the EES environment [9] using the ambient temperature data contained in the typical meteorological year for Montréal. Energy from circulating pumps is not considered in this study. Finally, it is assumed that the system operates in steady-state conditions

at each time step. Cycling losses associated with on/off operation are handled using a part load factor approach which is described below.

Building model

A simple building model is used. It is assumed to be composed of a single zone maintained at a constant temperature, T_{int}. The building load at time j, $Q_{load,j}$, is calculated using Equation 4.17.

$$Q_{load,j} = UA \times \left(T_{int} - T_{ext,j}\right) - Q_{gains} \tag{4.17}$$

where UA is the building overall heat transfer coefficient, $T_{ext,j}$ is the ambient temperature at time j and Q_{gains} are internal heat gains. The UA was estimated to be 0.4 kW/K and constant. This value was derived based on the assumption of building heat losses from a relatively large residential building with standard insulation levels. The value of Q_{gains}assumed to be constant and equal to 1 kW. It represents the internal thermal gains from occupants, lighting, and electrical appliances. This assumption provides a simplified estimate of the combined heat contributions within a building of this size.

The resulting peak building load is 19.5 kW. The building load is met with heat from the heat pump, Q_H, and auxiliary heat, Q_{aux}:

$$Q_{load,j} = Q_{H,j} + Q_{aux,j} \tag{4.18}$$

Finally, the amount of required ground heat is the amount of heat exchanged at the evaporator and is given by:

$$Q_{g,j} = Q_{H,j} - W_j \tag{4.19}$$

where W_j is the compressor power.

The heat pump is regulated to achieve the desired outlet temperature, T_{w_2}, which is adjusted using a simple external air temperature (or ambient temperature, T_{amb}) reset control commonly used by manufacturers [134]:

$$T_{w_2} = -0.556 \times T_{amb} + 33.3 \quad \text{(where } T_{amb} \text{ is in ℃)} \tag{4.20}$$

Thus, T_{w_2} is lowered as the ambient temperature increases and the heating load decreases.

Ground heat exchanger model

The model used for the ground heat exchanger has been described by Saidi [135]. It uses the so-called cylindrical heat source analytical solution to obtain the borehole wall temperature, $T_{b,j}$, at a given time step *j* as a function of the ground load and undisturbed ground temperature. The thermal history of ground heat extraction is accounted for using a temporal superposition scheme. Assuming that borehole thermal capacity effects are negligible, the hourly mean fluid temperature, $T_{m,j}$, is then obtained assuming a constant borehole thermal resistance, R_b of 0.1 m-K/W, using Equation 4.21:

$$T_{m,j} = T_{b,j} - Q_{g,j} \times R_b \tag{4.21}$$

The inlet temperature to the heat pump is then determined by:

$$T_{w_1,j} = 2T_{m,j} - T_{w_4,j} \tag{4.22}$$

where $T_{w_4,j}$ represents the inlet temperature to the borehole at a given time step. The determination of the necessary borehole length is conducted using a trial-and-error approach where the length is adjusted so that the inlet temperature to the heat pump, represented as $T_{w_1,j}$, reaches a threshold value of 0 ºC at the peak of the heating season. The length depends on the type of system being simulated. It is 300 m for the multi-compressor and variable speed compressor scenarios. When fixed-speed compressors are used, the required lengths are 200, 250, 300, 330, 350 m for compressors #1 to #5, respectively.

Heat pump model

Condenser and evaporator model:

Plate heat exchangers (PHX) are utilized in both the evaporator and condenser. Comprehensive heat transfer models for these PHXs have been established and reported by Viviescas and Bernier [86] and are presented in detail in chapter 5 and 6.

Despite the vast number of correlations available for calculating heat transfer coefficients in both single-phase and two-phase systems, the accuracy of these models is strongly linked to the geometric parameters, fluids, and operational conditions of each study as shown in Chapter 2. For single-phase heat transfer, the Wanniarachchi, et al. [113] model was chosen because good results

for a wide variety of cases have been shown by several studies[118]. For evaporation, the Cooper model [121] was selected due to its relative simplicity, requiring only the system pressure and the fluid properties of the fluid. It has been demonstrated by Palm and Claesson [107] , García, et al. [136], and Longo, et al. [137] that Cooper's correlation provides reasonable heat transfer coefficients with other refrigerants and other plate heat exchangers, and at different pressure levels. Finally, the Yan, et al. [120] model was chosen for condensation due to the simplicity of its model and because good results for several refrigerants including R410A.

The analysis of the PHXs employs a moving boundary approach, as described by Sarfraz, et al. [90], which segments the PHXs into distinct zones. This moving boundary approach was selected for this thesis because it provides a more realistic and comprehensive analysis of heat exchanger performance than lumped models, while maintaining a manageable level of computational complexity compared to segment-by-segment models. This makes it an optimal choice for applications requiring a detailed yet efficient evaluation of heat exchanger performance. These include the desuperheating, condensation, and subcooling zones within the condenser, and the evaporating and superheating zones in the evaporator, effectively modeling both single-phase and two-phase regions. This model will be thoroughly explored and utilized in this section, Chapter 5, and Chapter 6, where its application and benefits will be discussed in detail.

Thermostatic expansion valve model:

The thermostatic expansion valve has been modeled in a simplified manner as an isenthalpic expansion process and the superheat is maintained constant at 5°C during the modeling.

Compressor model:

The compressor is modeled using an isentropic efficiency which varies as a function of the pressure ratio.

The isentropic efficiency for fixed-speed compressors is given by:

$$\eta_{is_i} = a(PR - b_i)^2 + k \tag{4.23}$$

with:

$$\eta_{is_i} = \frac{h_{2_{is_i}} - h_{1_i}}{h_{2_i} - h_{1_i}} \tag{4.24}$$

Where the index "i" represents the compressor number.

Based on data from a commercially available scroll compressor (Emerson ZP25KE series for R410A refrigerant), the coefficients a, b and k in equation 4.23 were determined. Here, b represents the pressure ratio (PR) at which the isentropic efficiency reaches its peak, and k denotes the maximum isentropic efficiency value. The b values were then systematically adjusted to ensure that the efficiency maxima correspond to different PR values according to the compressor size, as detailed in Table 4.1.

Table 4.1 Isentropic efficiency and nominal capacity for the fixed-speed compressors

Compressor	a	b	k	Nominal capacity (kW) at $T_{w_3} = 30°C$, $T_{w_1} = 10°C$
1	0.0336	2	0.75	9
2	0.0336	2.5	0.75	11
3	0.0336	3	0.75	13
4	0.0336	3.5	0.75	15
5	0.0336	4	0.75	18

Isentropic efficiencies as determined using Equation 4.24 are plotted in Figure 4.16. It is shown that each compressor has the same peak value, but this peak occurs at different pressure ratios.

The variable speed compressor isentropic efficiency is expressed as:

$$\eta_{is} = d(PR - h)^2 + e(Hz - f)^2 + k \tag{4.25}$$

With $= -0.03$ $e = -4.2 \times 10^{-6}$, $h = 2.5$, $f = 60$, and $k = 0.75$

The parameters of the equation were found based on data from a commercially available variable speed compressor (Danfoss VZH028CJ). The selection of the parameters for the VSC has been adapted to have a maximum at a frequency of 60 Hz and a pressure ratio of 2.5 closely corresponding to fixed-speed compressor #2 (at 60 Hz) as shown in Figure 4.16. Curves for operation at 30 Hz and 100 Hz are also shown in Figure 4.16.

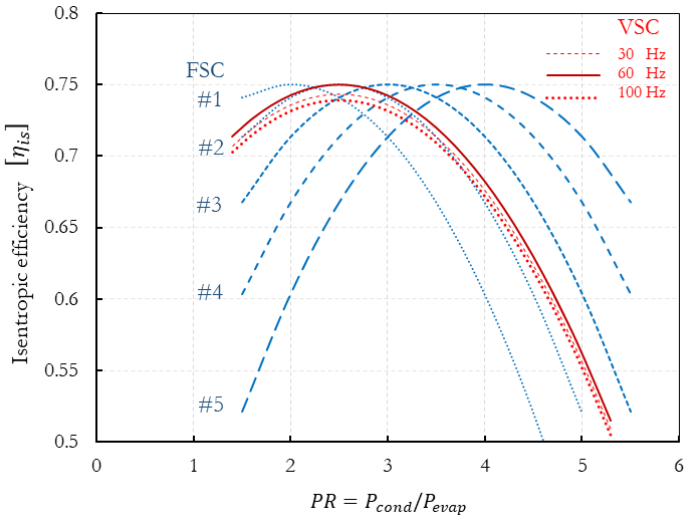

Figure 4.16 Isentropic efficiency for the FSC and VSC

As indicated earlier in Table 4.1, compressors #1 through #5 have nominal capacities of 9, 11, 13, 15, and 18 kW, respectively. These values correspond, respectively, to 50, 60, 70, 80 and 100% of the maximum peak building load.

The volumetric efficiency, η_v ,for the fixed-speed compressors is given by:

$$\eta_v = x + y(PR^n - 1) \tag{4.26}$$

With $x = 0.061, y = 0.00998$

This equation is a curve-fit on the data of compressor #3 (Copeland Scroll compressor ZP25KE series). As shown in Figure 4.17, Equation 4.26 represents volumetric efficiency adequately. It is assumed that the volumetric efficiency of the other compressors has the same behavior.

For the variable speed compressor, the volumetric efficiency is given by:

$$\eta_v = x + yHz(1 + z - zPR^n) \tag{4.27}$$

with $z = 1.077$ and $n = 0.057$

As shown in Figure 4.18, there is good agreement between Equation 4.27 and the volumetric efficiency of the variable speed compressor.

With a knowledge of the volumetric efficiency, the mass flow rate of refrigerant is then determined using Equation 4.3.

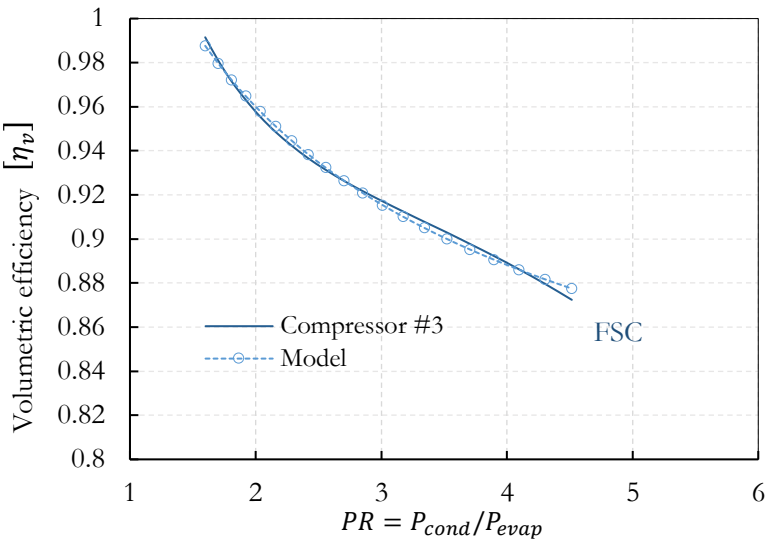

Figure 4.17 Comparison between the modeling equation for volumetric efficiency and real data for compressor #3

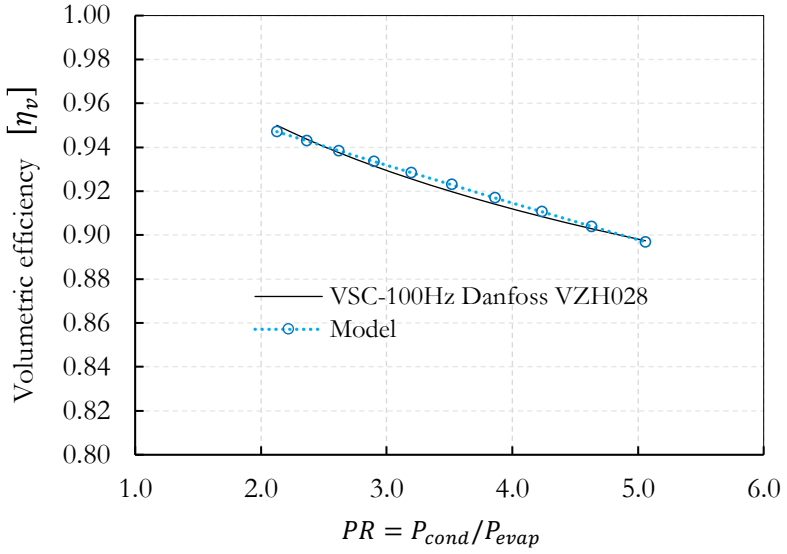

Figure 4.18 Comparison between the modeling equation for volumetric efficiency and the data for a variable speed compressor

When operating in steady state, assuming ambient losses are neglected, the heat pump power consumption at time step *j* is given by:

$$W_j = \dot{m}_{r,j}\left(h_{2_j} - h_{1_j}\right) \tag{4.28}$$

For fixed-speed compressors, the heat pump operates in on/off mode which implies that the heat pump must cycle to meet the building load. Heat pump cycling losses are handled using the part

load factor/part load ratio ($\frac{PLF}{PLR}$) approach proposed by Fuentes, et al. [42] and presented in Chapter 1. The PLF and PLR at time step j are thus obtained using the following equations:

$$PLF_j = \frac{1}{1 + \frac{C_d(1 - PLR_j)}{1 - C_d(1 - PLR_{ij})} + (1 - C_c)\frac{1 - PLR_j}{PLR_j}} \tag{4.29}$$

$$PLR_j = \min\left[1, \frac{Q_{load_j}}{Q_{H,j}}\right] \tag{4.30}$$

with C_d= 0.22 and C_c = 0.998 as indicated earlier. The resulting net heat pump power consumption, $W_{net,j}$, is given by:

$$W_{net,j} = W_j \frac{PLR_j}{PLF_j} \tag{4.31}$$

The effects of cycling and restart inertia of heat pump operation on capacity are not considered here.

At each time step, a modified COP value, which accounts for auxiliary heat, is evaluated using:

$$COP_{mod,j} = \frac{Q_{load_j}}{W_{net,j} + Q_{auxj}} \tag{4.32}$$

where the amount of auxiliary heat is defined as:

$$Q_{aux,j} = \max([Q_{load_j} - Q_{H,j}], 0) \tag{4.33}$$

Finally, the seasonal performance factor (SPF), is evaluated using:

$$SPF = \frac{\sum_{j=1}^{n} Q_{load_j}\ \Delta t}{\sum_{j=1}^{n}(W_{net,j} + Q_{aux,j})\Delta t} \tag{4.34}$$

Where Δt is the time step (1 hour) and n is the number of simulation hours.

During a given time step the solution proceeds as follows. The building load (Equation 4.17) is first calculated based on the ambient temperature and the outlet temperature on the load side of the heat pump (Equation 4.20). Then, the heat pump model is solved iteratively until convergence.

Convergence is facilitated by the fact that the number of degrees of superheat is assumed to be fixed at 5 ^{o}C.

In the simulation of a multi-compressor system, each compressor's performance is evaluated, and the one with the lowest energy consumption is selected at each time step. While, in practical applications, the selection of the optimal compressor in a real multi-compressor system could rely on a control strategy based on ambient temperature and the return temperature of the water from the geothermal well, the modeling approach offers a more refined method. Specifically, the model leverages the direct calculation of the COP at each instant, allowing for the selection of the most efficient compressor in real time, ensuring optimal performance throughout the simulation.

The amount of extracted heat from the ground (Equation 4.19) is also based on which compressor is selected at a given time step. If the capacity of each heat pump exceeds the building load at a given time step (i.e., $Q_H > Q_{load}$), the partial load ratio (PLR) is calculated using Equation 4.30. The actual power consumption will be determined by Equation 4.31, and the power extracted from the borehole will be given by $Q_g \times PLR$). For the VSC scenario, the compressor frequency is adjusted until the value of T_{w_2} is reached for a given value of T_{w_1} and the heat pump output capacity matches the building thermal load at each time step, such that $Q_H = Q_{load}$.

4.3.3 Results

The system under study is simulated over a complete heating season (5400 hours) from November 1st to May 1st with a 1-hour time step. Figure 4.19 shows the resulting building load, which reaches a maximum value of 19.5 kW as indicated earlier.

Figure 4.20 shows the evolution of the ambient temperature and inlet temperature to the heat pump for the multi-compressor scenario during the heating season. As shown, the ambient temperature varies from -29 ℃ to 16 ℃. The return fluid temperature from the ground heat exchanger fluctuates between +8 °C and 0 °C during the winter season. A similar evolution for the VSC scenario and individual FSC (with their respective ground heat exchanger length) has also been observed.

This return temperature is affected by the evaporator's exit temperature $T_{w_{4,j}}$, which in turn depends on Q_g, the COP, and the heat pump capacity. In the FSC and VSC cases, it is directly linked to the capacity of the installed compressor.

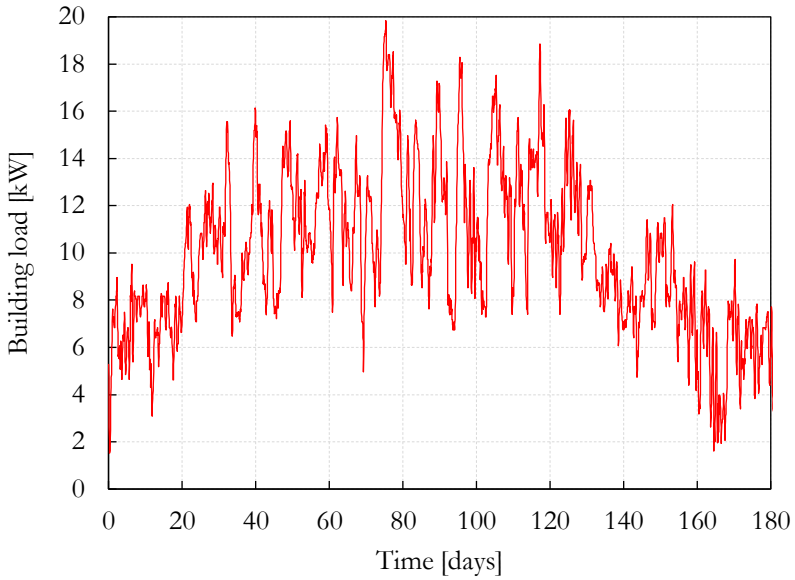

Figure 4.19 Building load for the simulation period

However, in the MC scenario, the model first identifies the compressor with the highest performance (largest COP_{mod}) and then calculates the heat pump exit temperature to the borehole based on the capacity of the selected compressor.

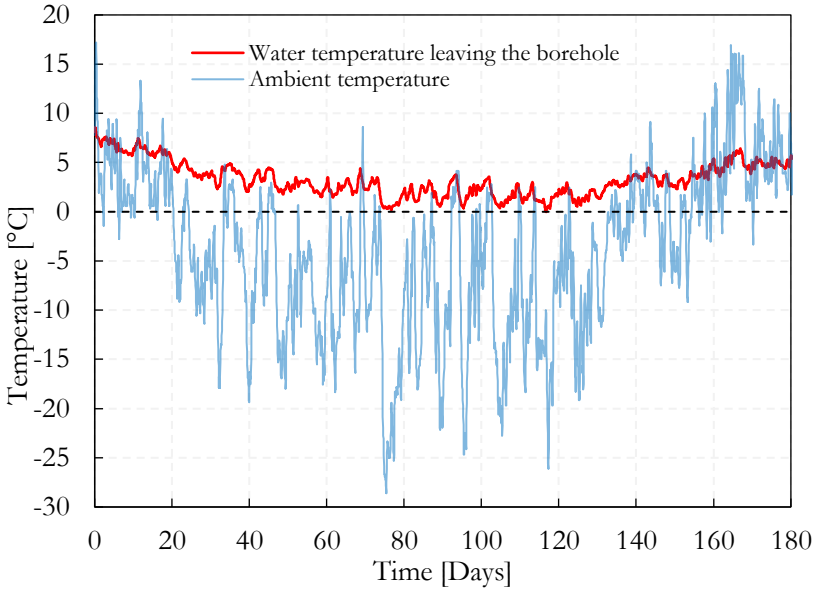

Figure 4.20 Ambient temperature and return water temperature from the ground heat exchanger during the heating season for the multi-compressor scenario

The results for the three cases are presented below starting with the FSC and MC followed by the VSC.

FSC and MC

Figure 4-21 displays the value of COP_{mod} for each of the five compressors of the MC system, as calculated using Equation 4-32 for the entire heating season as a function of the ambient temperature. It is to be noted that when individual FSC with their respective borehole length are used, values of COP_{mod} are almost identical to those shown in Figure 4-20.

The corresponding pressure ratios and individual heat pump COP are presented in Figure 4.22 and Figure 4.23 for the MC scenario. Figure 4-21 also shows which is the best compressor for a given ambient temperature.

Three distinct regions are identified in Figure 4.21. In region 1, the building load exceeds the heat pump capacity necessitating the use of large quantity of auxiliary heating for compressors #1 to #4 which lowers the COP significantly. For example, compressor #1 has a value of COP_{mod} of 1.4 at -28 ℃. However, as the ambient temperature rises, COP_{mod} increases rapidly as the need for auxiliary heating is reduced and the heat pump COP improves. The increase in the COP is attributed to the narrowing of the temperature difference between the source (return temperature from the borehole) and the load (return temperature from the building) as ambient temperatures rise.

The largest compressor (#5) does not require auxiliary heating even at the lowest temperature, resulting in an almost constant value of COP_{mod} (~ 4.1) in region #1. The small negative slope experienced by compressor #5 in this area is due to cycling losses which offsets the increase in COP caused by rising ambient temperature (i.e. rising return fluid temperature from the borehole).

In region 2, when the heat pump capacity matches or surpasses the building load, operation shifts to partial load, initiating compressor cycling. This occurs at $-20, -15, -9, -1$ ℃ for compressors #4, #3, #2 and #1, respectively. In this region, the COP_{mod} for compressor #5 still has a small negative slope associated with cycling losses.

This region not only involves competition in terms of auxiliary energy consumption but also hinges on identifying the compressor with superior isentropic efficiency that incurs the least penalty from cycling. As the temperature rises, reducing the building load, compressors #4, #3, #2, and #1 are sequentially chosen. Figure 4.22 shows the pressure ratio (PR) for each compressor as a function of ambient temperature. As expected, lower ambient temperatures result in higher PRs. The PR values determines the isentropic efficiency of each compressor, as depicted in Figure 4.16.

Figure 4.23 illustrates the COP for each compressor, excluding the impact of power consumption increases due to cycling, focusing solely on the influence of ambient temperature. It is observed that as the ambient temperature rises, leading to a decrease in the PR, compressors with higher isentropic efficiency at lower PR values (smaller size) exhibit a more pronounced linear increase in COP. However, this increase in COP due to the reduction in PR is less than the decrease in COP caused by the additional power consumption from cycling, resulting in a negative slope in COP_{mod} in region 2.

In region 3, where building loads are reduced due to higher ambient temperatures, the system selects the smallest compressor that delivers the highest isentropic efficiency at lower pressure ratios (PR) and minimizes cycling penalties. At these ambient temperature levels, the pressure ratio is lower, resulting in reduced power consumption. Additionally, the heating capacity increases due to the higher refrigerant density at the compressor suction, which is driven by the elevated return temperature of the secondary fluid from the borehole. This combination yields the highest COP values throughout the entire heating session.

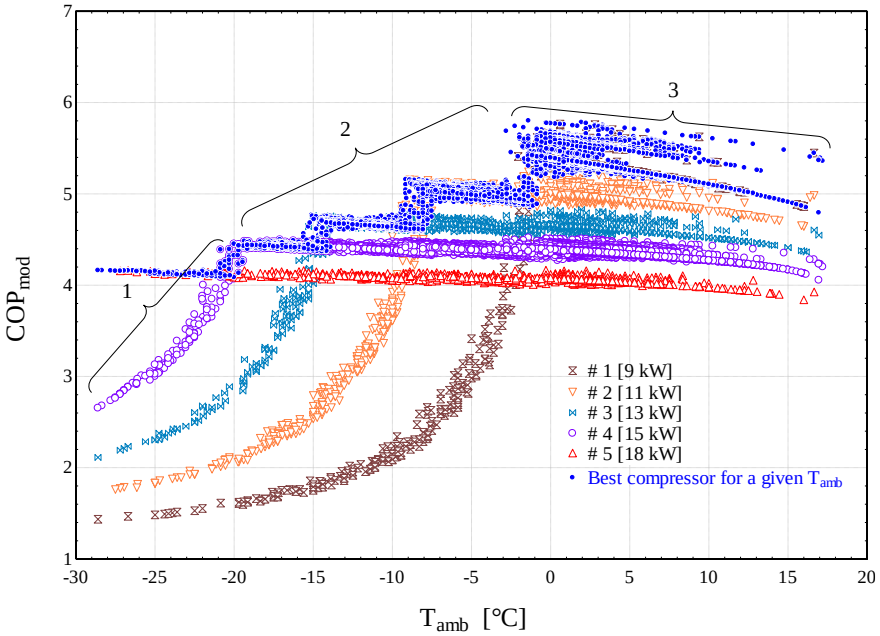

Figure 4.21 Modified COP of the five fixed-speed compressors as a function of the ambient temperature

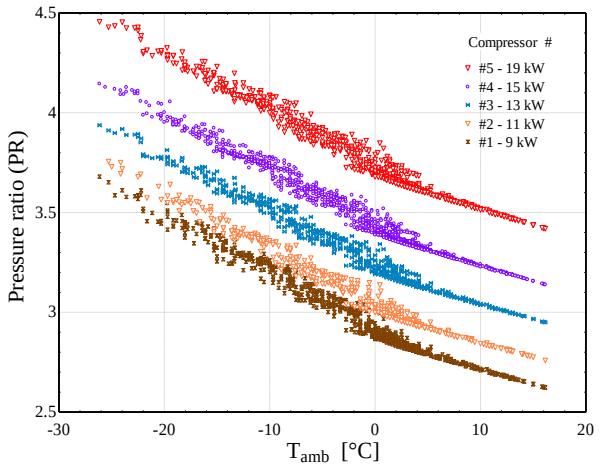

Figure 4.22 Pressure ratio as a function of ambient temperature for the five fixed-speed compressors

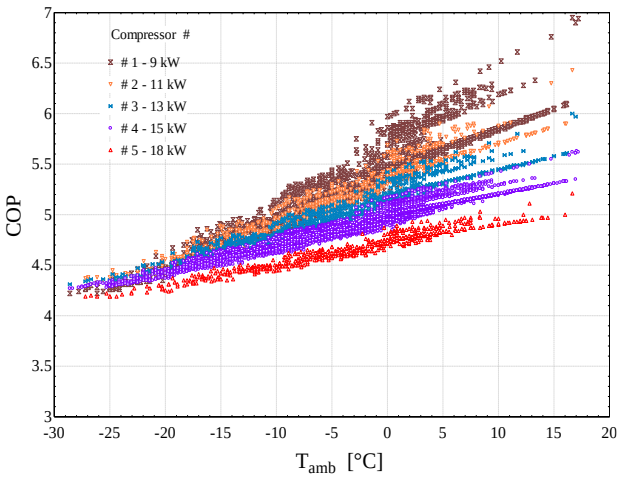

Figure 4.23 COP as a function of ambient temperature for the five fixed-speed compressors

The outlier COP_{mod} values in regions 3, are primarily attributed to a sudden increase in the average return temperature from the borehole caused by a ground temperature recovery due to a pause in ground heat extraction. For example, at an ambient temperature of 10°C, the coefficient of performance (COP_{mod}) for the best compressor (#1 in region 3) ranges from 5.2 to 5.6.

VSC

Figure 4.24 illustrates the performance of the variable speed compressor relative to the ambient temperature during the heating season. It is observed that a decrease in ambient temperature corresponds to an increase in building load and, consequently, an increase in compressor rotational speed (higher frequencies).

As mentioned earlier, the compressor size has been chosen to meet the maximum building load without resorting to auxiliary heating. The COP presents a variation ranging from 4.2 under conditions of maximum load (and consequently the highest-pressure ratio) to 8.0 when the building load is at its minimum (corresponding to the lowest pressure ratio, PR). Using a variable-speed compressor (VSC) prevents the increase in power consumption associated with using auxiliary heating and cycling operation, and therefore its efficiency is primarily influenced by the PR.

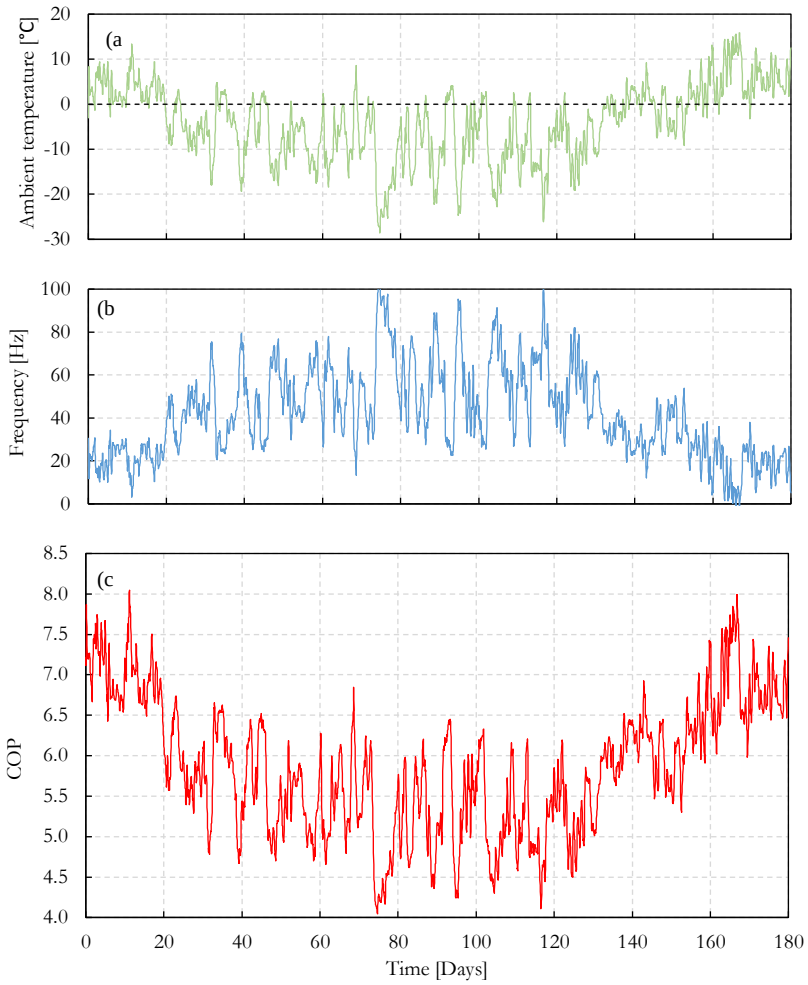

Figure 4.24 VSC performance during the heating season, a) ambient temperature, b) frequency, c) COP

As will be discussed later in chapter 5, under practical operating conditions, variable-speed compressors generally have a minimum rotational speed, usually corresponding to an input frequency between 15 and 30 Hz. In practical terms, this leads to VSC heat pump cycling, which was not accounted for in this section, when operating under low thermal loads. As shown in Figure 4.24, these conditions occur in the beginning and at the end of the heating season.

Comparative performance of Fixed-Speed compressor (FSC), Multi-Compressor (MC), and Variable Speed Compressor (VSC) Heat Pump Systems

Employing Equation 4.34, the SPF has been determined for each compressor operating independently, as well as for the collective multi-compressor system and the VSC configuration.

This comparison is presented in Figure 4-25. When the compressors are operating in FSC mode, compressor #4 as the highest performance with a SPF of 4.3. This performance can primarily be attributed to minimal use of auxiliary heating, a reduction in penalties from part-load operation, and favorable isentropic efficiency throughout the operating period. Conversely, the least efficient configuration was observed when utilizing the smallest compressor, owing to its substantial reliance on auxiliary energy consumption. The SPF for the multi-compressor system is 4.8, representing a 12% improvement over the most efficient single compressor. The VSC system as a SPF of 5.45, surpassing the MC scenario by 8%. This enhanced SPF for the VSC system is primarily attributed to the elimination of auxiliary heating requirements.

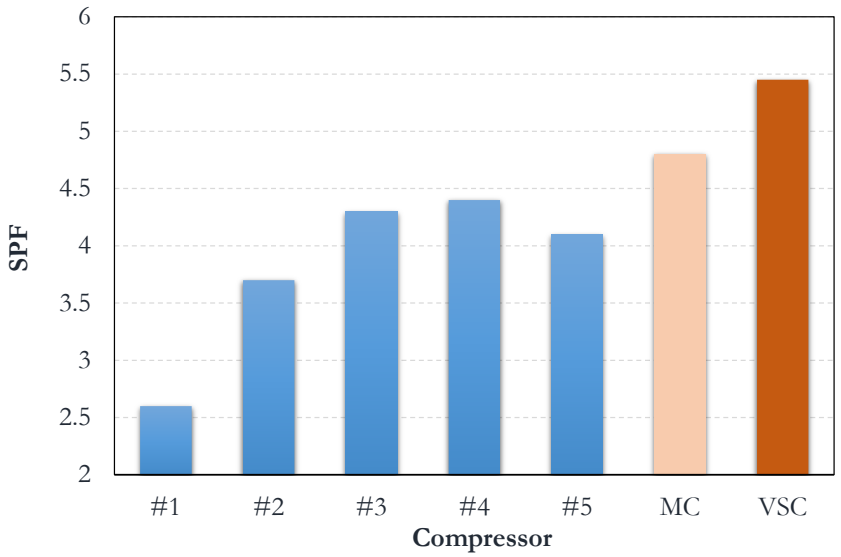

Figure 4.25 Seasonal performance factors (SPF) evaluated individually for each FSC and for the MC and VSC scenarios

In summary, section 4.3 has conducted a comparative evaluation of the operational efficiencies of heat pumps utilizing single fixed-speed compressors, fixed speed multi-compressors and variable speed compressors. Two significant observations can be drawn: Adaptability and efficiency at varying thermal loads is important and the superior performance of VSC.

The multi-compressor system shows considerable adaptability to changing thermal conditions, as evidenced by the distinctive COP performance across different compressors and operational regions. Notably, the system's ability to transition from reliance on auxiliary heating at lower ambient temperatures to efficient operation at partial loads highlights its potential for energy

savings in climates experiencing wide temperature fluctuations. This adaptability is further enhanced in the VSC system, where the compressor's variable speed allows for precise matching of the building's thermal demand, leading to a more consistent and higher COP across a broader range of temperatures.

The comparison between single fixed-speed compressors, the collective performance of multi-compressor systems, and VSC systems underscores the superior efficiency of variable speed technology. The VSC’s ability to eliminate the need for auxiliary heating by adjusting the compressor operational frequency in response to thermal load variations results in a notable improvement in the SPF, achieving a 8 % higher SPF compared to the MC.

CHAPTER 5 ARTICLE 1: A VARIABLE SPEED WATER-TO-WATER HEAT PUMP MODEL USED FOR GROUND-SOURCE APPLICATIONS

Article published in the journal: *Science and Technology for the Built Environment*, Volume 30, Issue 3, pages 266–279. Received 25 May 2023, Accepted 28 Nov 2023, Published 25 Jan 2024.

Authors: Geoffrey Viviescas and Michel Bernier (2023)

5.1 Abstract

The main objective of this study is to model variable speed water-to-water heat pumps ($VSHP$) and to examine the impact of the operation of such devices on ground heat exchanger sizing and energy consumption when they are used in ground-source applications. In the first part of the paper, a complete physics-based steady-state model of a variable-speed water-to-water heat pump is briefly presented. A performance map approach is also used by modifying an existing TRNSYS variable speed heat pump model to provide a minimum speed of operation and a better representation at part load. Simulation results over a heating season on a residential ground source $VSHP$ indicate that the energy coverage (i.e. percentage of annual heat supplied by the heat pump) increases at a faster rate than the effect coverage (i.e. percentage of peak building heat supplied by the heat pump) for a small value of the effect coverage. For example, for an effect coverage of 60%, the energy coverage is ~ 93%. It is also shown that the normalized length of the ground heat exchanger varies linearly up to an effect coverage of 60% where it is equal to 75% of the value encountered for an effect coverage of 100%.

5.2 Introduction

Heat pump system models are valuable for estimating carbon emissions and energy costs, determining appropriate heat pump and ground heat exchanger (GHE) sizing, and assessing the effectiveness of advanced cycles [138]. In this study, the emphasis is on variable speed operation which, in principle, should improve efficiency and performance [72].

Variable speed heat pumps ($VSHP$) offer the possibility of matching the building heating and cooling loads and improving thermal comfort by modulating the compressor speed. This is accomplished by tuning the inlet frequency (typically down to 15-30 Hz and up to 90-120 Hz) to the electric motor of the compressor. Contrary to fixed speed compressor heat pumps ($FSHP$) which operate in on/off mode, $VSHP$ operate continuously except for low load (speed) conditions. At low speeds, the oil may not circulate properly in the compressor, leading to lubrication issues [139]. In practical operating conditions, variable speed compressors usually have a minimum rotational speed, which corresponds typically to an inlet frequency between 15-30 Hz.

Relatively few studies have been conducted on the modeling of water-to-water heat pumps, and even fewer studies exist on those equipped with variable-speed compressors. Stefanuk, et al. [140] presented a steady-state simulation model of a water-to-water heat pump operating under superheat control. The model is derived from the basic conservation laws of mass, energy, momentum, and equations of state, as well as fundamental correlations of heat transfer. It is used to predict system performance over the full operating range of a heat pump. The results indicate that refrigerant superheats at the evaporator exit and that the refrigerant charge can be used as a control variable to maximize system performance.

Jin and Spitler [141] presented a steady-state simulation model for a water-to-water reciprocating vapor compression heat pump, intended for use in building simulation programs. The model was developed from basic thermodynamic principles and heat transfer relations. It comprises several unspecified parameters that are estimated from catalog data using a multi-variable optimization procedure.

A residential-size ground-source variable-speed integrated heat pump was developed by Rice, et al. [142]. The 2-ton (7 kW) unit has multiple functions such as space cooling, space heating, dedicated water heating, and simultaneous space cooling and water heating. A vapor compression simulation model in TRNSYS was calibrated for each of the four primary modes of operation using laboratory test data. The model was used to predict annual energy savings for five US locations. Their study indicates that $VSHP$ offers average savings of 55% when compared to a typical air source heat pump ($ASHP$).

Bouheret and Bernier [143] have proposed an approach to model a commercially available variable capacity water-to-air ground-source heat pump (ClimateMaster, 2022) that can provide heating,

cooling, and domestic hot water (DHW). They showed that the annual seasonal performance factor (i.e. ratio of the annual energy requirement for heating, cooling, and DHW over the annual electricity consumption) can reach 3.64.

Ndiaye [144] focused on the development of a dynamic model of a water-to-air heat pump to enable more accurate simulations. A literature review revealed that the existing models found in energy simulation programs are inadequate in reproducing the transient effects associated with cycling. The study uses an iterative algorithm that combines individual models of the various components to create a global model. The study also finds that the time constant used for modeling the start-up capacity is dependent on the operating conditions, which is a weakness of models found in simulation programs that use a fixed time constant.

The DOE/ORNL Heat Pump Design Model (HPDM) [145] is a widely used software tool for designing heat pump systems. The HPDM uses simplified assumptions, such as steady-state operation, uniform indoor and outdoor temperatures, and in some cases ideal components. It is not easily adaptable to perform annual simulations.

$VSHP$ used in ground-source applications will experience ground loads that are different than the ones of a $FSHP$. This will impact the required size of the ground heat exchanger (GHE) and heat pump energy consumption. The study by Rice, et al. [142] indicates that the required length of the GHE was 25% higher than a ground-source heat pump equipped with a desuperheater for heating domestic hot water.

Viviescas and Bernier [146] compared the required GHE length and seasonal performance factors (SPF) associated with $FSHP$ and $VSHP$ with various effect coverage (percentage of peak load covered by the heat pump). Results indicate that a $VSHP$ with a 100% effect coverage requires a GHE that is 40% longer than a typical $FSHP$ with a 90% effect coverage. However, the SPF is much better for the $VSHP$ (4.14 vs. 3.11 in favor of the $VSHP$).

Based on this review there is an apparent lack of detailed models of variable-speed water-to-water heat pumps. The objective of this paper is thus to develop such a model. The modeling of the evaporator and condenser (plate heat exchangers) has been presented elsewhere (Viviescas, et al. [31]). Emphasis is put in this paper on the prediction of the compressor behavior and the solution of the complete system of non-linear equations. Improvements to TRNSYS's Type 1323_v2a, which uses a performance-based approach, are also proposed. Finally, preliminary results

presented by Viviescas and Bernier [146] are expanded to present the impact of $VSHP$ operation on the energy coverage and GHE length for a range of effect coverage.

5.3 Detailed model

As stated earlier, this study aims to model a water-water heat pump featuring a variable speed compressor using two approaches: one based on detailed modeling of the various cycle components and the other based on performance maps generated from the complete detailed model.

The detailed $VSHP$ model presented here is part of a broader study aimed at developing a detailed physics-based and experimentally validated model of a water-to-water heat pump. Initial steps towards this goal were documented recently [31].

The $VSHP$ being modeled is shown schematically in Figure 5.1. The objective of the model is to predict the capacity (heating or cooling) and the required power for known inlet conditions (temperature and flow rate) on the load and source sides (i.e. $T_{w_{L_{in}}}, \dot{m}_{w_L}, T_{w_{S_{in}}}, \dot{m}_{w_S}$) as well as compressor speed.

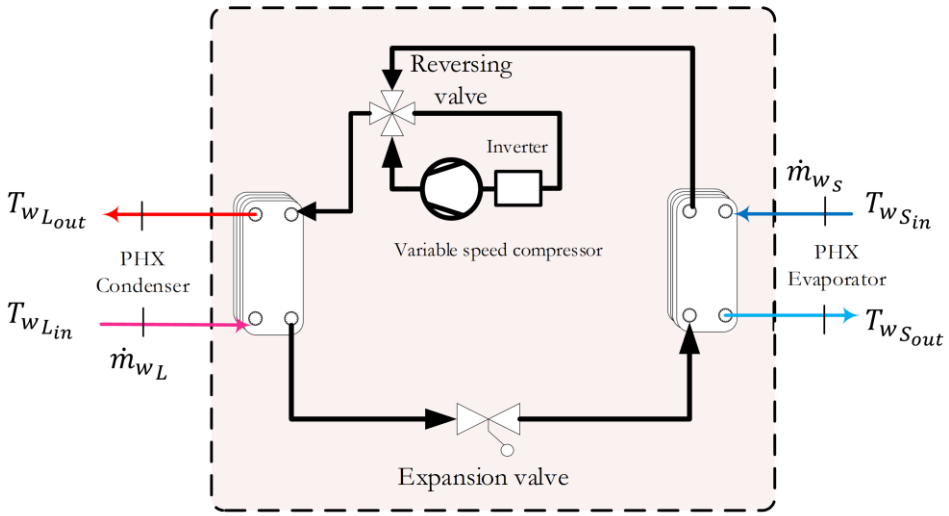

Figure 5.1 Schematic of the VSHP

Plate heat exchangers (PHX) are used in the evaporator and condenser. A variable speed motor (inverter in Figure 5.1) regulates the compressor speed and a thermostatic expansion valve controls the level of superheat at the evaporator exit. Individual models for these components are linked together via the refrigeration cycle.

The corresponding pressure-enthalpy ($P-h$) diagram is shown in Figure 5.2 where $PHXs$ are superimposed to show the heat exchanged with secondary fluids at the evaporator and condenser. The refrigerant (R-410A in the present case) leaves the evaporator as a superheated vapor at a temperature T_1 and exists the compression process at T_2. In the condenser, the refrigerant is first de-superheated from T_2 to $T_{x,2}$ and then condensed down to a saturated liquid at T_3. Then, there is an isenthalpic pressure drop in the expansion valve and the refrigerant enters the evaporator at T_4. In the evaporator, the refrigerant undergoes evaporation from T_4 to $T_{x,1}$ and is then superheated up to T_1.

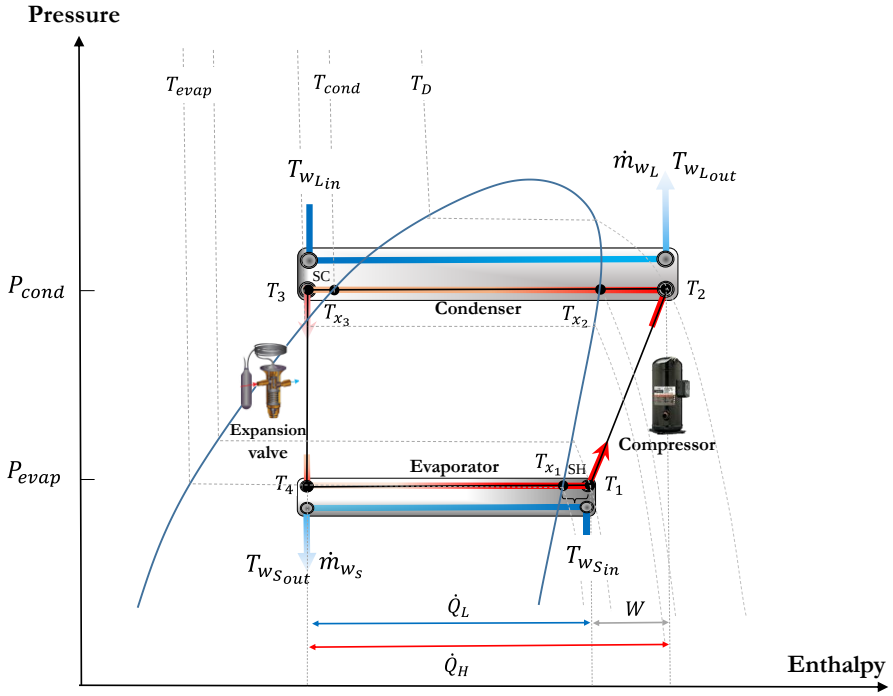

Figure 5.2 P-h diagram

Steady-state operation is assumed, and pressure drops in both heat exchangers and in the reversing valve are assumed to be negligible. There are no heat losses between the heat exchangers and the surrounding environment. Finally, the influence of circulating oil with the refrigerant is considered negligible.

Detailed heat transfer models are used for both PHXs and are documented by Viviescas, et al. [31]. A so-called moving boundary approach is used [90] where the PHXs are divided into separate zones (e.g., desuperheating, condensation, and subcooling zones in the condenser) that represent both single-phase and two-phase regions. Initially, the fractions of the total heat exchanger area

used for each zone are unknown and are assigned suitable guess values. Then an iterative process, encompassing a system of nonlinear equations (energy balances and epsilon-NTU equations in each zone) is employed to determine the heat exchanger area used for each zone for a given set of inlet conditions (temperature and flow rate) of the secondary fluids and refrigerant flow rate determined by the expansion valve model.

The overall heat transfer coefficient in each zone is required to obtain the NTU value. It is determined based on the sum of three thermal resistances associated with heat transfer coefficients on the water and refrigerant sides and the plate's thermal conductivity and thickness. For single-phase and two-phase flows heat transfer coefficients are obtained using correlations found in the literature [31].

Two improvements have been implemented in the overall heat pump model since the earlier work of Viviescas, et al. [31]. First, the refrigerant can exit the condenser as a subcooled liquid (determined by the PHX models) rather than in a fixed condition as a saturated liquid. Secondly, the heat exchangers can be modeled in both counterflow and parallel modes which implies that the cooling mode can now be modeled.

In summary, the heat exchanger models can predict the outlet refrigerant temperatures (T_1 and T_3) for given values of the secondary inlet fluid temperature fluids ($T_{w_{S_{in}}}$ and $T_{w_{L_{in}}}$) and flow rate ($\dot{m}_{w_S}$ and $\dot{m}_{w_L}$) and inlet refrigerant temperatures (T_4 and T_2) provided by the compressor and expansion valve models. The variable speed compressor requires special treatment and the next paragraphs describe the approach used here.

Researchers have proposed various approaches to model variable speed compressors. Winandy, et al. [101] proposed a semi-empirical gray-box model, known as the Winandy model, for forecasting scroll compressor performance. The model includes an isothermal wall that heats the suction gas, cools the discharge gas, absorbs electro-mechanical losses, and transfers heat to the ambient environment. The compression process is divided into two stages: first, isentropic compression up to an adjusted pressure, followed by adiabatic and isochoric compression up to the discharge pressure.

The Shao model (Shao, et al. [147]) is a black-box model that incorporates modulation by using performance data at various operational frequencies. To fit the variable speed data, the model employs a second-order function to the mass flow rate and power ratio. These ratios establish a

relationship between the mass flow and power at the base frequency and performance at different frequencies.

The Popovic and Shapiro model (Popovic and Shapiro [148]) is a semi-empirical compressor model derived to predict reciprocating compressor performance. The model utilizes an idealized polytropic compression and clearance volume re-expansion with constant pressure suction and discharge processes. This cycle is modified to include phenomena typical of a compressor. This includes utilizing volumetric efficiency, based on a clearance factor taken as an unknown. The authors then add suction and discharge pressure drop and, for simplicity, set the magnitudes equal. The model utilizes the thermodynamic work rate of a polytropic process as a basis for compressor power requirements.

A recent study by Gabel and Bradshaw [149] concludes that the AHRI model with ten coefficients performs exceptionally well when trained with data sets in both standard and variable superheat scenarios, with errors of only 0.43% and 0.57% for mass flow rate and power, respectively. Similar findings regarding training data performance were also reported by Aute, et al. [150] in their analysis of the AHRI model. However, the model is not recommended for data extrapolation and is superior to the Winandy, Shao, and Popovic models only within the range of data used for model training.

In the present work, the compressor is modeled using an extension of the approach suggested in standard CAN/ANSI/AHRI 540-2020 [128]. This standard proposes to fit fixed-speed experimental data into a third-order polynomial equation with 10 coefficients relating either the mass flow rate or power input to T_D , the discharge dew point temperature (i.e. condensing temperature corresponding to saturation at x=1), and to T_S, the suction dew point temperature (i.e. evaporating temperature corresponding to the vapor saturation line).

The AHRI model has been customized for variable speed compressors by Danfoss using a second-degree polynomial (Equation 5.1) with three variables and 30 coefficients: the two AHRI standard temperatures (T_D and T_s) and the operating frequency (S in Hz):

$$X = C_0 + C_1T_s + C_2T_D + C_3T_s^2 + C_4T_D^2 + C_5T_sT_DS^2 + C_6T_s^2T_DS^2 + C_7T_sT_D^2S^2 + C_8T_sT_DS + C_9T_s^2T_DS + C_{10}T_sT_D^2S + C_{11}T_sT_D + C_{12}T_s^2T_D + C_{13}T_sT_D^2 + C_{14}T_s^3 + C_{15}T_D^3 + C_{16}S + C_{17}T_sS + C_{18}T_DS + C_{19}T_s^2S + C_{20}T_D^2S + C_{21}T_s^3S + C_{22}T_D^3S + C_{23}S^2 + C_{24}T_sS^2 + C_{25}T_DS^2 + C_{26}T_s^2S^2 + C_{27}T_D^2S^2 + C_{28}T_s^3S^2 + C_{29}T_D^3S^2 \quad (5.1)$$

Where X is either the mass flow rate or the power consumption. For this study, the Danfoss VZH028-CJ compressor was selected (Danfoss 2022). When operating at 60 Hz it has a heating capacity of 10.5 kW under rated conditions ($T_{w_{sin}} = 4$ ℃ and $T_{w_{Lin}} = 35$ ℃), and 15.33 kW when the frequency is increased to 100 Hz. The coefficients for this compressor are presented in Table 5.1 and are valid for a superheat of 5 °C.

Table 5.1 Input coefficients to equation 5.1 for Danfoss VZH028-CJ

Coefficient	Power [W]	Mass-flow [kg/h]	Coefficient	Power [W]	Mass-flow [kg/h]
C_1	3.798E-01	-3.385E-01	C_{16}	-8.656E-07	-6.286E-08
C_2	1.219E-02	-8.774E-03	C_{17}	-1.659E-02	6.610E-02
C_3	-1.107E-02	7.639E-03	C_{18}	-1.024E-03	1.556E-03
C_4	3.360E-04	-6.869E-05	C_{19}	1.013E-03	-2.383E-04
C_5	1.791E-04	-5.442E-05	C_{20}	-2.246E-05	1.224E-05
C_6	-1.606E-07	2.317E-08	C_{21}	-1.214E-05	8.866E-07
C_7	-2.230E-09	6.884E-11	C_{22}	-1.725E-07	5.900E-08
C_8	1.376E-09	7.864E-11	C_{23}	6.137E-08	3.348E-09
C_9	3.163E-05	-3.597E-06	C_{24}	1.610E-04	-8.453E-05
C_{10}	3.516E-07	-8.793E-09	C_{25}	4.633E-06	-2.416E-06
C_{11}	-2.288E-07	-6.965E-09	C_{26}	-3.753E-06	1.615E-06
C_{12}	-4.840E-04	1.260E-04	C_{27}	1.186E-07	-2.200E-08
C_{13}	-6.353E-06	2.209E-07	C_{28}	6.308E-08	-5.057E-09
C_{14}	4.191E-06	-1.238E-07	C_{29}	1.115E-09	-5.063E-11
C_{15}	2.998E-06	-2.324E-07	C_{30}	-3.294E-10	-3.751E-11

It should be noted that the degrees of superheat are not always equal to 5 °C. The compressor power consumption is unaffected by variations in the degrees of superheat as stated in the AHRI 540 standard. However, the mass flow rate needs to be corrected and the equation contained in Appendix D of the AHRI standard is used. In these cases, the rated refrigerant mass flow rate at rated superheat, $\dot{m}_{rated}$, is corrected to obtain the corrected mass flow rate at the real suction conditions, $\dot{m}_{corrected}$, using equation 5.2.

$$\dot{m}_{corrected} = \left\{1 + F_V \left[\left(\frac{v_{rated}}{v_{corrected}}\right) - 1\right]\right\} \cdot \dot{m}_{rated} \quad (5.2)$$

In this equation, F_V is the volumetric efficiency correction factor. It varies based on the volumetric efficiency of the compression technology used. The standard suggests a value of one (1) as an approximation. The other terms in Equation 5.2 are $v_{corrected}$, the specific volume at the suction condition, and v_{rated} , the specific volume at the rated condition.

The compressor portion of the model obtained using Equations 5.1 and 5.2 with the coefficients in Table 5.11 was compared to the manufacturer's data measured under AHRI standard conditions with a superheat of 11.1°C. The results of this comparison are depicted in Figures 5.3 and 5.4. The maximum error in power is 0.15% with an RMSE of 0.077 kW, while the maximum error in mass flow rate is 0.65% with an RMSE of 0.011 kg/h. It should be noted that errors of up to 5% in mass flow rate prediction are obtained if the correction indicated in Equation 5.2 is not applied.

The compressor power and refrigerant mass flow rate given by Equation 5.1 are coupled to the rest of the components of the model resulting in a set of nonlinear equations. These equations are implemented in TRNSYS to form a stand-alone model (called a Type in TRNSYS). Thermophysical and thermodynamic properties are evaluated with CoolProp [151]. The modified Powell method [152] was implemented to solve the system of nonlinear equations within the TRNSYS Type.

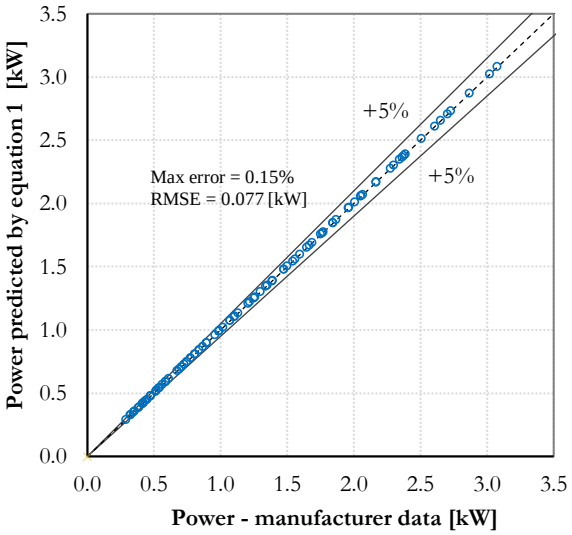

Figure 5.3 Power predicted by Equation 5.1

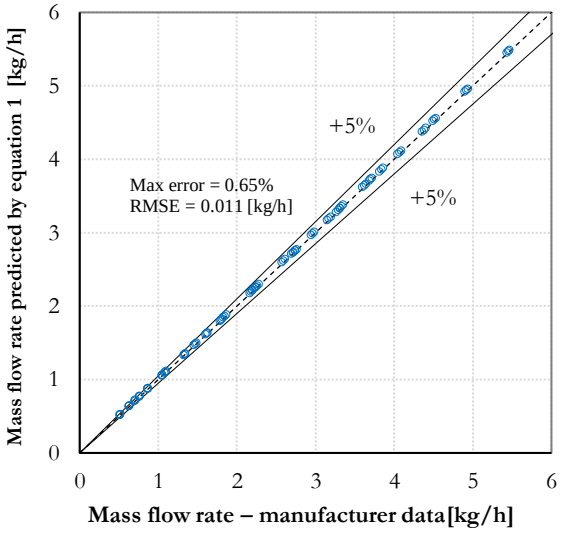

Figure 5.4 Mass flow rate predicted by Equation 5.1

In parallel to the development of the new TRNSYS Type, the individual component models were also implemented and linked together in the Engineering Equation Solver (EES) environment which provides easily adaptable guess values and a powerful internal equation solver. Some results of the complete EES model are shown in Figure 5.5 which illustrates how the coefficient of performance (COP) in heating mode varies with compressor speed at four different source temperatures (5, 10, 15, and 20 ºC) and three load-source temperature differences (20, 25, and 30 ºC). The figure highlights several notable observations. First, for identical temperature differences, higher source temperatures result in higher COP. This is because refrigerant density is increasing at the compressor suction leading to a corresponding increase in mass flow rate. Second, the COP curves exhibit a maximum value that is not necessarily coincident with full capacity (i.e. at maximum speed). For example, for a $\Delta T = 20$ ℃, the COP is maximum at 40 Hz and it decreases when the frequency is either increased or decreased. This is primarily because the compressor used in the present study reaches its maximum isentropic efficiency at speeds other than the maximum speed.

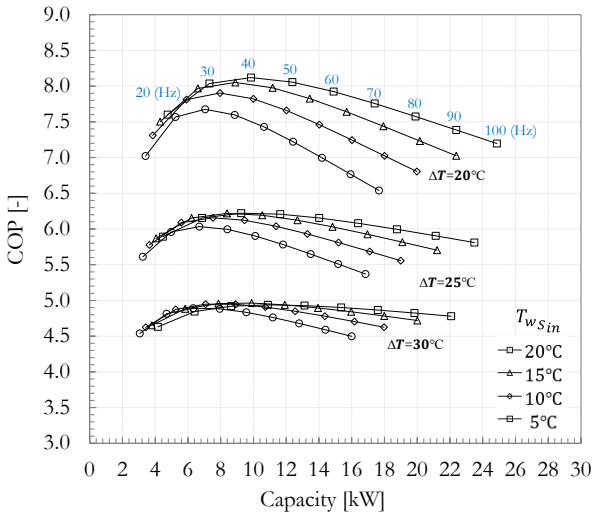

Figure 5.5 COP as a function of heating capacity for various operation conditions

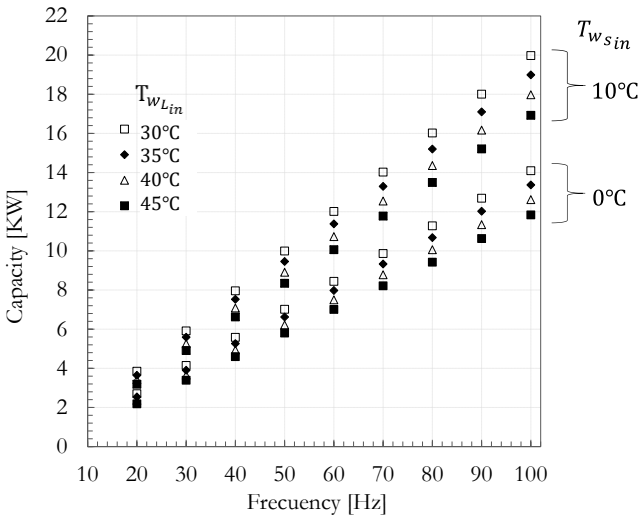

Figure 5.6 Heating capacity as a function of frequency for various operating

Figure 5.6 shows the heating capacity for eight (8) combinations of $T_{wL_{in}}$ and $T_{ws_{in}}$, and nine (9) frequencies. As expected, the heating capacity increases as the temperature difference between the source and load decreases for a given frequency. For given values of $T_{ws_{in}}$ and $T_{wL_{in}}$ the heating capacity increases linearly with frequency. This may seem surprising considering that Equation 5.1

has quadratic and cubic terms for frequency. However, statistical analysis revealed that these terms are significant for power prediction but have a negligible influence when mass flow rates are calculated.

Running annual system simulations is impractical in EES as it would require developing a specific model for the building, the GHE, etc. Faced with a possible non-converged solution for the TRNSYS type presented earlier and the impracticability of using EES in annual simulations, it was decided to use the complete EES model to develop performance maps that could be used in TRNSYS to perform annual simulations. In essence, performance maps present a solution to the complete model for a fixed set of inlet conditions.

5.4 Performance map model

In this section, a performance map model is developed for TRNSYS applications. TRNSYS is used to simulate the performance of energy systems including heat pump systems. TRNSYS has several heat pump models for fixed and variable speed heat pumps with either air or water as the source/sink fluids. Most of these models use performance maps extracted from catalog data to predict capacity and power usage. The maps can be non-dimensionalized to represent a family of heat pumps with similar characteristics but different sizes [153].

The existing TRNSYS Type1323_v2a served as the basis for developing the new model based on performance maps. Type1323_v2a models a variable-speed water-to-water heat pump that can operate from zero to maximum capacity to match the desired load-side outlet temperature. However, as indicated earlier, most variable-speed compressors have a minimum operational speed and thus a minimum capacity. In addition, Type 1323_v2a assumes that the normalized power consumption (also known as the Energy Input Ratio as a Function of Part Load Ratio – $EIRFPLR$) is only a function of the part load ratio (PLR), i.e. the ratio between the required capacity over the nominal capacity. However, as will be shown shortly, the $EIRFPLR$ is also a function of the temperature difference between the inlet temperatures of both secondary fluids.

These two shortcomings are corrected in this work and a new Type is created (Type 1328). Table 5.2 displays the main features provided by the new Type 1328 compared to Type 1323_v2a. As shown in this table, Type 1328 requires four performance maps to obtain the capacity (heating and cooling) at the minimum and maximum frequencies. In addition, a series of coefficients (different in heating and cooling) are required to obtain the $EIRFPLR$.

Table 5.2 Characteristics of Type 1323_v2a and Type 1328

Main differences		
	Type1323_v2a (current TRNSYS type)	Type1328 (New Type)
Operation	Continuous operation at all partial load ranges	Continuous operation between minimum and maximum recommended frequencies
Parameters	Three performance data files : *1.* Performance map at max. freq. in heating *2.* Performance map at max. freq. in cooling *3.* EIRFPLR ratio as a function of PLR	Four performance data files: *1.* Performance Map (at max. speed) in heating *2.* Performance Map (at max. speed) in cooling *3.* Performance Map (at min. speed) in heating *4.* Performance Map (at min. speed) in cooling
	The same EIRFPLR ratio in cooling and heating	$EIRFPLR = a_0 + a_1\Delta T + a_2\Delta T^2 + a_3 PLR + a_4 PLR^2 + a_5 PLR\Delta T$ a_i coefficients are different in heating and cooling
Similarities		
Inputs	Load and source inlet temperatures of secondary fluids $\left[T_{w_{S_{in}}}, T_{w_{L_{in}}}\right]$ Load and source mass flow rate of secondary fluids $\left[\dot{m}_{w_L}, \dot{m}_{w_S}\right]$ Desired outlet load temperature in cooling and heating $\left[T_{w_{L_{out}}}\right]$ A control signal (0 or 1) for heating or cooling	
Parameters	Rated capacity and power in cooling and heating $[Q_{ref}, P_{ref}]$ Load and source specific heat and density of secondary fluids $\left[C_{p_{w_L}}, C_{p_{w_S}}, \rho_{w_L}, \rho_{w_S}\right]$	
Outputs	Water outlet Load and Source Temperatures $\left[T_{w_{S_{out}}}, T_{w_{L_{out}}}\right]$ Heat transfer to load, to source, and power consumption in heating and cooling mode Coefficient of performance (COP)	

Tables 5.3 to 5.6 show these performance maps at maximum and minimum frequencies (100 and 15 Hz in the present study) in heating and cooling obtained from the full set of data (Appendix 5.A). These performance maps were obtained using the EES version of the complete model. For this study, the mass flow rates of the secondary fluids were kept constant (at 0.5 kg/s) to limit the number of independent variables. Data are normalized based on a set of reference conditions for the secondary fluid inlet temperatures: 4 °C on the source side and 35 °C on the load side for heating and 15 °C and 10 °C for cooling. During a given time step, the model evaluates the nominal capacity at the minimum and maximum frequencies ($Q_{nom_{min,f}}$ and $Q_{nom_{max,f}}$) and the corresponding power consumption ($P_{nom_{min,f}}$ and $P_{nom_{max,f}}$):

$$Q_{nom_{max,f}} = Cap_{ratio_{max,f}} \times Q_{ref} \text{ and } Q_{nom_{min,f}} = Cap_{ratio_{min,f}} \times Q_{ref} \quad (5.3)$$

$$P_{nom_{max,f}} = Power_{ratio_{max,f}} \times P_{ref} \text{ and } P_{nom_{min,f}} = Power_{ratio_{min,f}} \times P_{ref} \quad (5.4)$$

where Q_{ref} and P_{ref} are, respectively, the reference capacity and power at the maximum frequency for the reference conditions. If required, linear interpolations are performed in the performance map tables. One advantage of using normalized performance data is that they can be used for any heat pump size by scaling the values of Q_{ref} and P_{ref}. In doing so it is assumed that the heat pumps follow the behavior of the heat pump (Figures 5.5 and 5.6) on which the performance map is based. This was verified for the present study and results (not presented here) indicate that the performance of the selected compressor could be scaled to represent the power usage and capacity of compressors of the same family.

Table 5.3 Performance map of the VSHP in heating mode at full load (100 Hz)

Q_{ref}=15.33 kW; P_{ref}= 3.99 kW for $T_{w_{L_{in}}} = 35°C$, $T_{w_{S_{in}}} = 4°C$, 100Hz										
$T_{w_{L_{in}}}$ [°C]	30		35		40		45		50	
$T_{w_{S_{in}}}$ [°C]	Cap_{ratio}	$Power_{ratio}$	Cap_{ratio}	$Power_{ratio}$	Cap_{ratio}	$Power_{ratio}$	Cap_{ratio}	$Power_{ratio}$	Cap_{ratio}	$Power_{ratio}$
-2	0.874	0.893	0.870	0.968	0.865	1.049	0.859	1.137	0.852	1.233
0	0.917	0.903	0.912	0.979	0.906	1.061	0.900	1.150	0.890	1.247
2	0.960	0.912	0.956	0.990	0.949	1.073	0.941	1.163	0.931	1.260
4	1.005	0.920	1.000*	1.000*	0.993	1.085	0.984	1.176	0.972	1.273
6	1.052	0.927	1.046	1.010	1.038	1.096	1.027	1.188	1.014	1.287
8	1.099	0.934	1.093	1.018	1.083	1.107	1.071	1.200	1.055	1.299
10	1.147	0.940	1.139	1.026	1.128	1.117	1.114	1.211	1.096	1.311

* reference conditions

Table 5.4 Performance map of the VSHP in cooling mode at full load (100 Hz)

Q_{ref}=17.44 kW; P_{ref}= 2.398 kW for $T_{w_{L_{in}}} = 15°C$, $T_{w_{S_{in}}} = 10°C$, 100Hz								
$T_{w_{L_{in}}}$ [°C]	7		15		20		25	
$T_{w_{S_{in}}}$ [°C]	Cap_{ratio}	$Power_{ratio}$	Cap_{ratio}	$Power_{ratio}$	Cap_{ratio}	$Power_{ratio}$	Cap_{ratio}	$Power_{ratio}$
10	0.822	1.031	1.000*	1.000*	1.113	0.963	1.275	0.910
15	0.811	1.159	0.992	1.146	1.100	1.116	1.262	1.076
20	0.796	1.287	0.976	1.292	1.073	1.268	1.232	1.239
25	0.778	1.417	0.955	1.439	1.071	1.432	1.219	1.415
30	0.756	1.550	0.927	1.588	1.029	1.588	1.166	1.579
35	0.730	1.688	0.892	1.739	1.014	1.758	1.140	1.759
40	0.701	1.834	0.849	1.896	0.959	1.920	1.105	1.940
45	0.667	1.988	0.799	2.057	0.934	2.099	1.046	2.118

* reference conditions

Table 5.5 Performance map of the VSHP in heating mode at (15 Hz)

Q_{ref}=15.33 kW; P_{ref}= 3.99 kW for $T_{w_{L_{in}}} = 35°C$, $T_{w_{S_{in}}} = 4°C$, 100Hz										
$T_{w_{L_{in}}}$ [°C]	30		35		40		45		50	
$T_{w_{S_{in}}}$ [°C]	Cap_{ratio}	$Power_{ratio}$	Cap_{ratio}	$Power_{ratio}$	Cap_{ratio}	$Power_{ratio}$	Cap_{ratio}	$Power_{ratio}$	Cap_{ratio}	$Power_{ratio}$
-2	0.192	0.197	0.191	0.213	0.190	0.231	0.189	0.250	0.187	0.271
0	0.202	0.199	0.201	0.215	0.199	0.234	0.198	0.253	0.196	0.274
2	0.211	0.201	0.210	0.218	0.209	0.236	0.207	0.256	0.205	0.277
4	0.221	0.202	0.220*	0.220*	0.218	0.239	0.216	0.259	0.214	0.280
6	0.231	0.204	0.230	0.222	0.228	0.241	0.226	0.261	0.223	0.283
8	0.242	0.206	0.240	0.224	0.238	0.243	0.236	0.264	0.232	0.286
10	0.252	0.207	0.251	0.226	0.248	0.246	0.245	0.266	0.241	0.289

* reference conditions

Table 5.6 Performance map of the VSHP in cooling mode at (15 Hz)

Q_{ref}=17.44 kW; P_{ref}= 2.398 kW for $T_{w_{L_{in}}} = 15°C$, $T_{w_{S_{in}}} = 10°C$, 100Hz								
$T_{w_{L_{in}}}$ [°C]	7		15		20		25	
$T_{w_{S_{in}}}$ [°C]	Cap_{ratio}	$Power_{ratio}$	Cap_{ratio}	$Power_{ratio}$	Cap_{ratio}	$Power_{ratio}$	Cap_{ratio}	$Power_{ratio}$
10	0.181	0.227	0.220*	0.220*	0.245	0.212	0.280	0.200
15	0.178	0.255	0.218	0.252	0.242	0.246	0.278	0.237
20	0.175	0.283	0.215	0.284	0.236	0.279	0.271	0.273
25	0.171	0.312	0.210	0.317	0.236	0.315	0.268	0.311
30	0.166	0.341	0.204	0.349	0.226	0.349	0.256	0.347
35	0.161	0.371	0.196	0.383	0.223	0.387	0.251	0.387
40	0.154	0.403	0.187	0.417	0.211	0.422	0.243	0.427
45	0.147	0.437	0.176	0.453	0.205	0.462	0.230	0.466

* reference conditions

For example, using the data in Table 5.3, the nominal heating capacity and power for $T_{w_{S_{in}}}$ = 0 °C and $T_{w_{L_{in}}}$ = 30 °C at 100 Hz are 14.04 kW (0.917 × 15.33) and 3.60 kW (0.903×3.99), respectively.

At a given time step, the required capacity, Q_{load}, is given by:

$$Q_{load} = \dot{m}_{w_L} C_{p_{w_L}} \left(T_{w_{L_{out,d}}} - T_{w_{L_{in}}} \right) \tag{5.5}$$

Where $T_{w_{L_{out,d}}}$ is the user-specified desired outlet temperature on the load side. Then, depending on the value of Q_{load} in relation to $Q_{nom_{min,f}}$ and $Q_{nom_{max,f}}$, the model will perform the calculations shown in Table 5.7:

Table 5.7 Heat pump operational conditions

Condition	**Heat Pump operation**	**Required Power (excluding auxiliary heat)**	$T_{w_{L_{out}}}$
$Q_{load} < Q_{nom_{min,f}}$ $PLR < \sim 0.2$	OFF	$P = 0$	-
$Q_{nom_{min,f}} \leq Q_{load} < Q_{nom_{max,f}}$ $\sim 0.2 < PLR < 1$	ON	$P = EIRFPLR \times P_{nom_{max,f}}$	$= T_{w_{L_{out,d}}}$
$Q_{load} \geq Q_{nom_{max,f}}$ $PLR \geq 1$	ON + auxiliary heating	$P = P_{nom_{max,f}}$	$= \frac{Q_{nom_{max,f}}}{\dot{m}_{w_L} C_{p_{w_L}}} + T_{w_{L_{in}}}$
With $PLR = \frac{Q_{load}}{Q_{nom_{max,f}}}$			

Thus, when the required capacity is between the nominal capacities at the minimum and maximum frequencies, the required power (P) is obtained by multiplying the nominal required power at the maximum frequency by the *EIRFPLR*. If the required capacity is less than $Q_{nom_{min,f}}$ (which typically corresponds to a $PLR \sim 0.2$), then the heat pump stops. If it is greater than $Q_{nom_{max,f}}$, then the set temperature cannot be reached and $T_{w_{L_{out,d}}}$ is evaluated as shown in Table 5.7.

Values of the *EIRFPLR* were evaluated from the complete model. These values are shown in Figure 5.7 for the cooling mode (heating results are similar). It is apparent from these results that the $EIRFPLR$ is a function of the part load ratio (PLR) and the temperature difference (ΔT) between the inlet temperature of both secondary fluids ($T_{w_{L_{in}}} - T_{w_{S_{in}}}$). To account for this dependency, the methodology used by Knapp, et al. [154] is adopted to relate the $EIRFPLR$ to the PLR and ΔT using the DOE2-2 model [155]:

$$EIRFPLR = a_0 + a_1 PLR + a_2 PLR^2 + a_3 \Delta T + a_4 \Delta T^2 + a_5 PLR \Delta T \quad (5.6)$$

The coefficients a_i in each operating mode were obtained from linear regressions to the full set of data and are presented in Tables 5.A-1 and 5.A-2 in the Appendix. Curves based on Equation 5.6

are shown in Figure 5.7 where they represent a good fit for the data. In cooling, the RMSE is 0.0173, with a maximum error of 9.8%. In heating (not shown here) the RMSE is 0.0033 and the maximum error is 5.1%. Finally, it should be noted that the ΔT can take a negative value in cooling as shown in Figure 5.7.

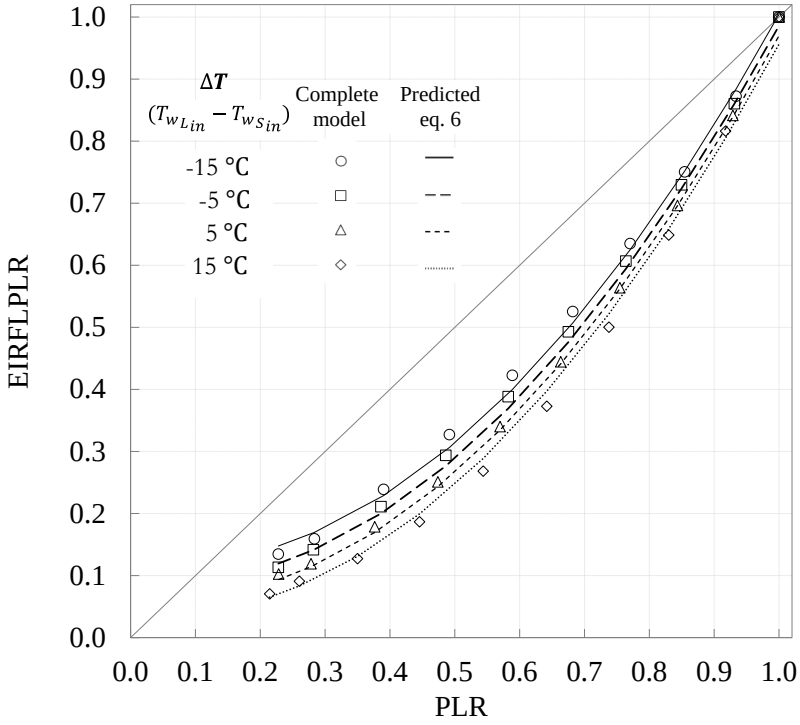

Figure 5.7 $EIRFPLR$ as a function of the PLR and ΔT

Table 5.8 Coefficients for the $EIRFPLR$ equation

Equation 5.6	Heating	Cooling
a_0	-0.0753787	0.076601
a_1	0.6873673	-0.098424
a_2	0.3638538	0.999283
a_3	0.0025503	-0.002881
a_4	-0.0000029	0.000012
a_5	-0.0017232	0.001280
RMSE	0.0033	0.0173
R^2 (%)	99.99	99.68
max error (%)	5.1	9.8

Results in Figure 5.7 indicate that $EIRFPLR$ values are all below the line where $EIRFPLR = PLR$. This indicates that the power consumption decreases at a faster rate than the required capacity. For

example, when the capacity is reduced to 20% ($PLR = 0.2$) and ΔT = 35 ºC, the value of the $EIRFPLR$ is ~ 0.15. Thus, this $VSHP$ is proportionally more efficient at part load. This is primarily attributed to the fact that the plate heat exchangers are oversized at part load which enhances the efficiency of the heat exchange and reduces the temperature difference between the condenser and the evaporator, leading to a decrease in power consumption. Finally, it should be noted that for a given PLR, the $EIRFPLR$ value decreases as the ΔT increases owing to the improvement in cycle efficiency.

5.5 Application

One of the reasons for developing a water-to-water heat pump model is to study the impact of such devices on the required length of GHE and heat pump energy consumption. The system chosen to undertake this study is shown in Figure 5.8 and the main characteristics of the system are presented in Table 5.9. It is a residential system located in a heating-dominated climate (Montréal, Canada). In such a system, the GHE length is determined based on the heating conditions and, therefore, only heating conditions are considered here. The $VSHP$ is linked to a vertical GHE on the source side and to a fan coil on the load side. An auxiliary electric heating system (10 kW) provides backup heat. The compressor speed is regulated to achieve the desired outlet temperature, $T_{w_{L_{out,d}}}$, which is adjusted using a simple external air temperature (or ambient temperature, T_{amb}) reset control commonly used by manufacturers [134].

$$T_{w_{L_{out,d}}} = -0.556 \times T_{amb} + 33.3 \quad \text{(where } T_{amb} \text{ is in °C)} \tag{5.7}$$

Thus, $T_{w_{L_{out,d}}}$ is lowered as the ambient temperature increases and the heating load decreases. This reduces the temperature difference $T_{w_{L_{in}}} - T_{w_{S_{in}}}$ and increases the heat pump COP as was shown earlier. The building is represented using Type 88, a single-zone lumped capacitance model.

The required borehole length is determined through a trial and error method, adjusting the length until the return water temperature from the geothermal well does not fall below 0°C over a 10-year period.. The system is controlled with a two-stage thermostat. First, the heat pump is activated to maintain the building set point temperature (21 °C) by providing the fan coil with a fluid at $T_{w_{L_{out}}}$. If the heat pump is unable to meet the building set point temperature, then the auxiliary heater is

activated. Two constant flow circulating pumps (source and load side) are activated whenever the heat pump is operating.

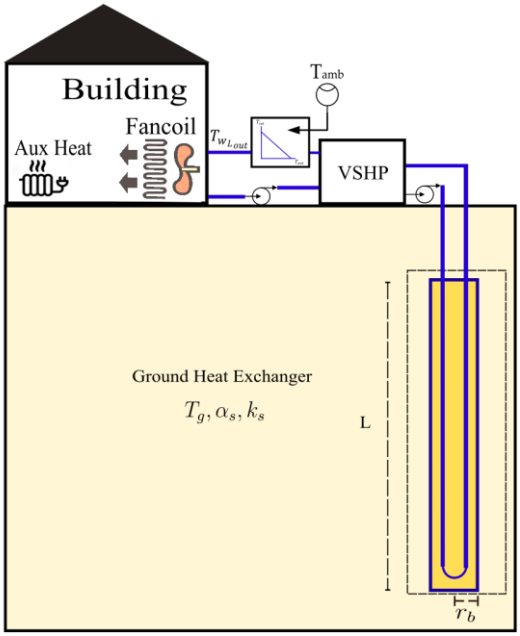

Figure 5.8 System under investigation

Component	TRNSYS TYPE	Principal characteristic	Value
Building	88	Overall building loss coefficient, UA [kW/K]	0.225
		Building mass, MCp [kJ/K]	20000
		Peak building load [kW]	11.1
		Internal gains [kW]	0.5
Fancoil	996	Rated Total Heating Capacity [kW]	10
		Rated Volumetric Air Flowrate [m3/h]	1700
		Rated Liquid Flowrate [kg/h]	2000
Auxiliary heat	930	Heating Capacity [kW]	10
VSGSHP	Type 1328	-Continuous operation between minimum and maximum recommended frequencies -Four (4) performance maps data files.	
Borehole	557b-2 Vertical U-Tube Ground Heat Exchanger	Borehole radius [m]	0.075
		Borehole thermal resistance [m-K/W]	0.13
		Ground thermal conductivity [W/m-K]	1.3
		Ground thermal diffusivity α_s [m^2/s]	6.5×10^{-7}
		Undisturbed ground temperature [°C]	10

Table 5.9 Main characteristics of the building and GHE

Before examining the impact of the $VSHP$ on the required length of the GHE and the heat pump energy consumption, the performance map approach (using Type 1328) is compared to the complete model for the system under investigation. The results of this comparison are presented in Figure 5.9 for the first 400 hours of a typical year based on simulations of the system presented in Figure 5.8 with a 6-minute time step. Results in Figure 5.9 have been integrated to be presented on an hourly basis. In this case, the $VSHP$ is sized to cover 80% of the peak building load when it operates at maximum speed. The top portion of the graph shows the evolution of the various temperatures and of the VSHP frequency obtained from the complete heat pump model. Over this period, the compressor is essentially always ON. It can be seen that during periods of low ambient temperatures (t > 330 h), the compressor operates at maximum frequency (100 Hz) and thus at maximum capacity. During that period, the return temperature from the borehole (i.e. heat pump inlet temperature) tends towards 0 °C. In contrast, when the ambient temperature is higher ($t \approx 200$ h) the heat pump reaches the minimum frequency of 30 Hz.

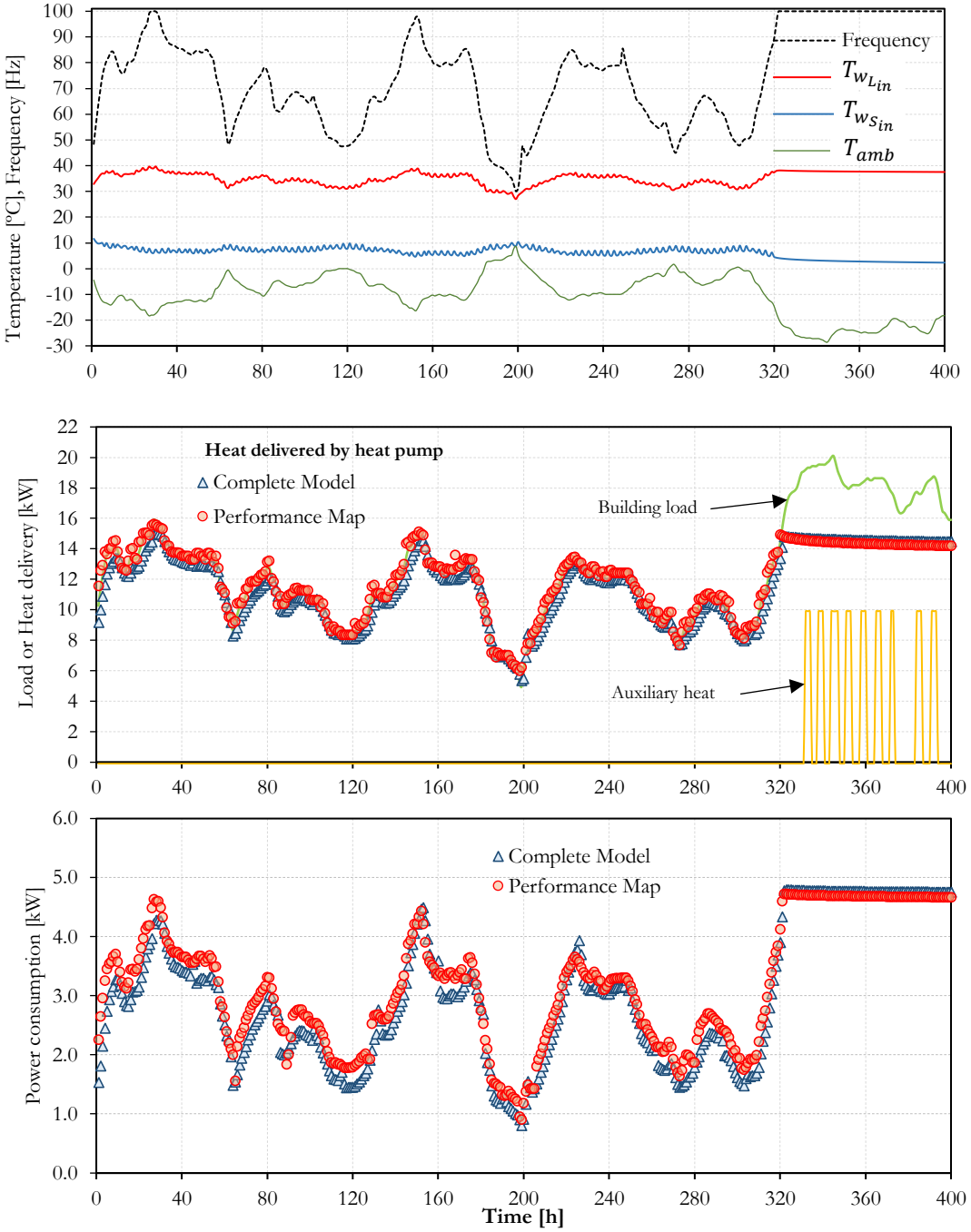

Figure 5.9 Comparison of the performance map approach with the complete model

As can be seen in the middle of the Figure 5.9, the heat delivered predicted by both approaches is quite similar except near peaks and valleys and also when the heat pump operates at full capacity (t > 330 h). Over the period 0 $<$ t < 400 h, the RMSE is 0.35 kW with a maximum error of 2.5%. At t ~ 330 h, the $VSHP$ capacity is less than the building load, and auxiliary heating is activated

periodically to meet the set point temperature. The performance map approach and the complete model predict essentially the same auxiliary heating values and both curves are superimposed in Figure 5.9. The bottom curves in Figure 5.9 shows the heat pump power predicted by both approaches. Here again, the agreement between the two approaches is good with an RMSE of 0.24 kW and a maximum error of 5.1%.

The relationship between the size of the $VSHP$ and the GHE length and energy consumption will now be examined. A full heating season, which extends from October 1st and May 1st (5088 hours) in Montréal, was simulated with a 6-minute time step using the most recent Typical Meteorological Year for Montréal for a building with a peak building load of 11.1 kW (Table 5.9). Results are also compared with simulations where the $VSHP$ (Figure 5.9) is replaced by a fixed-speed compressor heat pump ($FSHP$) equipped with the same type of compressor but running at one speed corresponding to a frequency of 60 Hz.

First, the heating capacities of the $VSHP$ and $FSHP$ are plotted as a function of ambient temperature (Figure 5.10). The heating capacity of a typical air-source heat pump ($ASHP$) is also shown for comparison. The rated capacity (Q_{ref}) is 8.88 kW at 100 Hz for the $VSHP$ and 60 Hz for the $FSHP$. The corresponding capacity of the $VSHP$ operating at 60 Hz at the same rated condition is 5.62 kW, a reduction of 36%. The curve for the $FSHP$ shows a slow decline of the heating capacity with a decrease in the ambient temperature. This is because as the building load increases, more heat is extracted from the ground and the return fluid temperature (not shown in Figure 5.10) from the borehole ($T_{ws_{in}}$) decreases (from ~10 down to ~ 0 °C). In turn, this decreases the heating capacity from ~9 to ~8 kW when T_{amb} decreases from ~10 °C down to ~ -30 °C. Below the balance point (i.e. at T_{amb} ~ -16 °C), the capacity of the $FSHP$ is insufficient, and auxiliary heat is required. The behavior of the $VSHP$ is different in the region where $-16\ ℃ < T_{amb} < 10\ ℃$ where, as expected, the heating capacity follows the building load curve. The balance point where auxiliary heating is required corresponds also to T_{amb} ~ -16 °C, which is to be expected as the $VSHP$ and $FSHP$ are both sized to cover 80% of the peak building load. For $ASHP$, the capacity is directly dependent on the ambient temperature and the slope of the heating capacity is steeper with a warmer balance point temperature. Thus, $FSHP$ and $VSHP$ require less auxiliary heat than a typical $ASHP$.

One way to quantify the amount of auxiliary heat required is to determine the so-called "energy coverage" defined as:

$$\text{Energy Coverage (\%)} = \frac{\text{Total heat supplied by the heat pump (excluding auxiliary heat)}}{\text{Total heat required by building over the heating season}} \quad (5.8)$$

The energy coverage will depend on the size of the heat pump in comparison to the peak building load. This is defined as the "effect coverage":

$$\text{Effect Coverage} = \frac{\text{Rated heating capacity of the heat pump (kW)}}{\text{Peak building load (kW)}} \quad (5.9)$$

For example, in Figure 5.10, the effect coverage of the $FSHP$ and $VSHP$ is 80% (8.88/11.1).

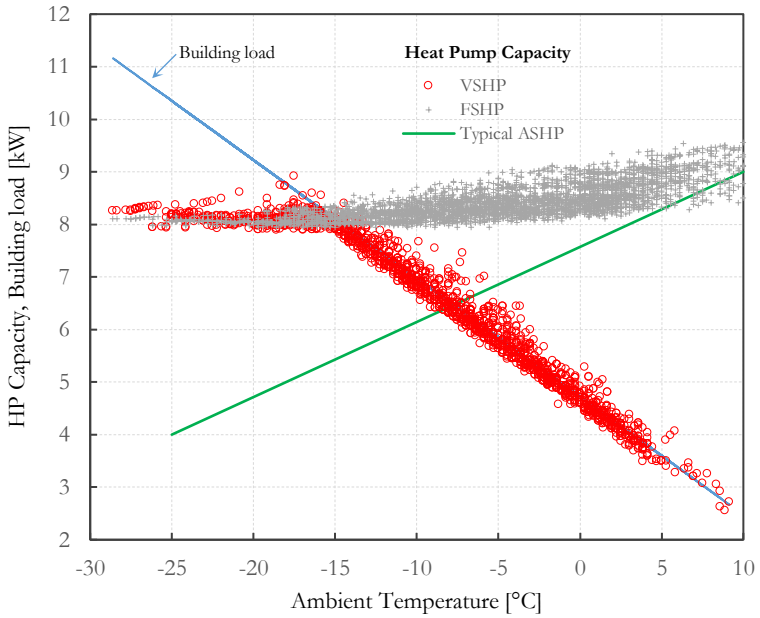

Figure 5.10 Variation of heating capacity as a function of ambient temperature for three types of heat pumps

Figure 5.11 shows a plot of the energy coverage as a function of the effect coverage. Three curves are shown: the curve reported by Rosén, et al. [156] for a typical Swedish home equipped with a $FSHP$ and curves obtained for the $FSHP$ and $VSHP$ described in this study and simulated using the performance map approach. The effect coverage is varied by keeping the building characteristics constant (Table 5.9) and varying Q_{ref} and P_{ref} for the heat pumps. The GHE length is different in each case and is determined, as indicated earlier, based on a minimum return borehole temperature of 0 ℃.

The curves in Figure 5.11 indicate that the energy coverage increases at a faster rate than the effect coverage up to an effect coverage of 60%. At that point, the energy coverage is ~ 93%. Thus, $VSHP$ designed to meet 60% of the peak building demand will provide 93% of the heat required while the remaining 7% will be supplied by auxiliary heat. Beyond an effect coverage of 60%, there is little gain in energy coverage. The curves for the $FSHP$ and $VSHP$ are almost identical. Thus, there appears to be no significant difference between the energy coverage curves for the $FSHP$ and $VSHP$. The curve presented by Rosén, et al. [156] is slightly different than the one in the present study. Rosén, et al. [156] do not give details related to his curve. Thus, it is difficult to identify the sources of the discrepancies. It might be due to different heat pump performance, climate, or ground properties.

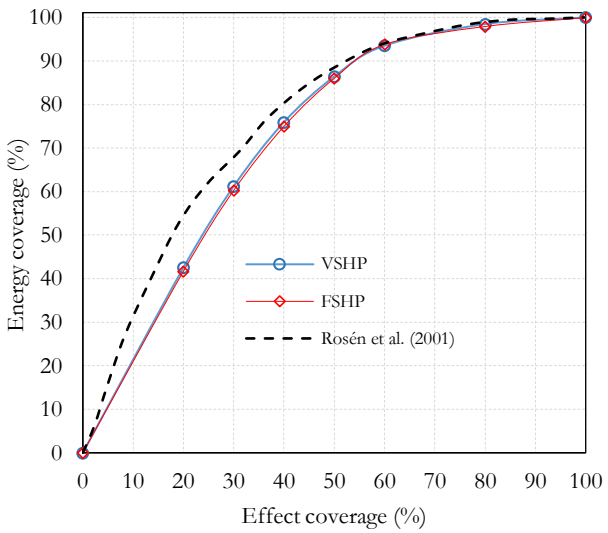

Figure 5.11 Energy coverage as a function of the effect coverage

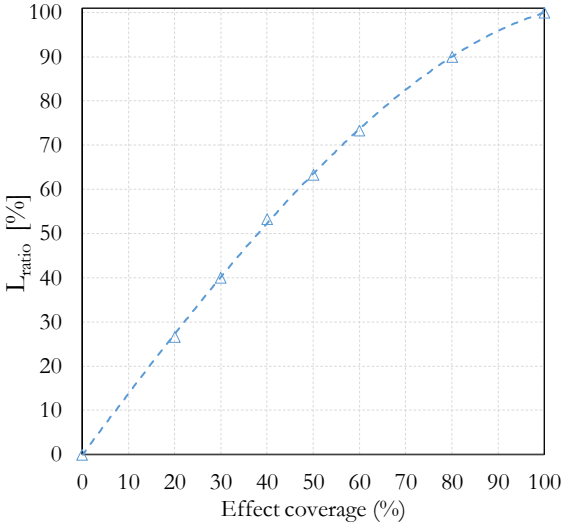

Figure 5.12 Normalised GHE length as a function of the effect coverage

The impact of effect coverage on the GHE length is shown in Figure 5.12. The length has been normalized with the length at a 100% effect coverage, which is 215 m in the present case. The L_{ratio} is proportional to the effect coverage up to an effect coverage of 60%. At that point, the normalized length is equal to 75%. After 60%, the L_{ratio} increases at a slower rate. The results presented in Figures 5.11 and 5.12 should be used with caution as the curves were obtained with a particular heat pump and specific ground properties. More work is needed to see how these curves vary for other conditions.

5.6 Conclusion

A complete water-to-water variable speed heat pump ($VSHP$) model is developed in this study. The physics-based approach incorporates individual models for the plate heat exchangers (evaporator and condenser), the expansion valve, and the variable speed compressor. The model requires five inputs: The inlet temperature and mass flow rate of both secondary fluids as well as compressor speed. The outputs are the capacity and power consumption. Using this model, it is shown (Figure 5.5) that the COP curves exhibit a maximum value that is not necessarily coincident with full capacity (at maximum speed). For example, for a temperature difference of 20 °C between the source and load temperatures, the COP is maximum at 40 Hz and it decreases when the frequency is either increased or decreased. It is also shown that the capacity varies linearly with frequency. The implementation of the complete model in a new TRNSYS type was not possible for long simulations due to convergence problems. Indeed, the convergence of the solution to the set of non-linear equations is highly dependent on the choice of guess values which becomes problematic for rapidly changing conditions in actual system simulation.

To solve this problem, a performance map approach, based on the complete model, is also developed based on an existing TRNSYS Type (Type1323_v2a). Two important modifications are made to this Type. First, a minimum speed of operation is implemented to reflect the fact that variable-speed compressors stop below a certain speed. Secondly, a more accurate representation of power consumption at part load is implemented. In a 400-hour simulation, the performance map approach produced good results when compared to the complete model, with maximum errors of 2.5% for the heating capacity and 5.1% for power.

The performance map-based model was used in an annual simulation of a $VSHP$ operating with a ground heat exchanger for a residential building in a heating-dominated climate. Results indicate that the energy coverage (i.e. percentage of annual heat supplied by the heat pump) increases at a faster rate than the effect coverage (i.e. percentage of peak building heat supplied by the heat pump) for values of the effect coverage below 60%. The energy coverage is $\sim$ 93% for an effect coverage of 60%. The non-dimensional GHE length is proportional to the effect coverage up to an effect coverage of 60%. At that point, the normalized length is equal to 75%. After 60%, the non-dimensional GHE length increases at a slower rate.

The energy-coverage versus effect-coverage curve was formulated following a set of particular parameters. Further investigations should be made for various heat pumps, ground thermal properties, and climates.

CHAPTER 6 ARTICLE 2: A WATER-TO-WATER HEAT PUMP MODEL WITH EXPERIMENTAL VALIDATION

Article published in the journal: *Energies*, Volume 17, Issue 8, 1858. Submission received: 20 February 2024 / Revised: 29 March 2024 / Accepted: 8 April 2024 / Published: 12 April 2024.

Authors: Geoffrey Viviescas and Michel Bernier (2024)

6.1 Abstract

An experimental validation of a steady-state model for water-to-water heat pumps is conducted on a 10 kW test bench. The objective of the model is to predict the capacity and the required compressor power, based on the inlet conditions of the secondary fluids in the evaporator and condenser. Detailed manufacturer performance maps based on the AHRI 540-2020 standard are utilized to model the fixed-speed scroll compressor. A new semi-empirical model for the thermostatic expansion valve incorporates condensing temperature effects on superheating prediction. Sub-models for individual components, including detailed representations of the evaporator and condenser, are integrated into a global model, resulting in a set nonlinear equation solved using an equation solver with appropriate guess values. The validation of the model is conducted in an experimental test facility equipped with two precisely controlled secondary fluid loops. The heat pump is instrumented to measure condensation and evaporation pressures, the compressor discharge temperature, compressor power, superheating, and subcooling. The results are divided into three sub-sections: the first validates the complete heat pump model by comparing its power consumption and COPs in heating and cooling; the second compares the predicted and measured operational conditions; finally, it is shown how the model can be used to predict the non-operational conditions of the heat pump for specific scenarios.

Keywords: water-to-water heat pump; modeling; expansion valve model; AHRI 540

6.2 Introduction

The development of accurate and reliable heat pump models can assist in enhancing the performance optimization of these systems and the overall efficiency of heating and cooling systems.

Most mechanical vapor compression heat pumps operate on a subcritical cycle below the critical point of the refrigerant. In their most basic configuration, heat is transferred from a source to a sink through a closed-loop refrigerant cycle, in four steps: evaporation, compression, condensation, and expansion [30]. In this article, water is used as the secondary fluid for both the source and sink. Water-to-water heat pumps are utilized in various applications, including ground-source heat pump (GSHP) systems [157].

This study aims to develop a validated experimental model for a water-to-water heat pump used to predict their overall performance as well as various critical parameters, including the thermodynamic states of the refrigerant at various cycle stages, their overall heat transfer coefficients, refrigerant flow rate, the discharge temperature from the compressor, and the degrees of superheat and subcooling. With the advent of various new refrigerants, such a detailed model can provide valuable and quick information on cycle performance. Unlike other modeling studies that fix one or several points in the refrigeration cycle, this study lets the model find the equilibrium state of the cycle based on the given inlet conditions (flow rate and temperature) of the water at the inlets of the evaporator and condenser. Additionally, the model identifies the non-operational states of the heat pump.

This paper is organized into five sections: The first section includes this short introduction. In the second section, the literature on water-to-water heat pumps is reviewed. This is followed, in the third section, by a presentation of the various sub-models used in the present study—a compressor, thermostatic expansion valve (TEV), and plate heat exchangers for the condenser and evaporator. The assembly of these sub-models into a comprehensive global model is also discussed. The experimental facility is presented in the fourth section, followed, in the last section, by a validation of the model and a presentation of its non-operational states.

6.3 Literature review

Modeling heat pumps involves creating mathematical or computational representations to simulate and predict their performance under various conditions. Various methods exist for modeling heat pumps, which range in complexity. Analytical models, which utilize fundamental conservation laws of mass, energy, and momentum, are found on one end of the spectrum. These models also incorporate equations of state and basic heat transfer correlations to forecast the refrigerant's state throughout the cycle. At the other end, there are models based solely on experimental data, which are either curve-fitted or arranged in performance maps. There are also semi-empirical models which lie in between these two extremes. The following literature review follows these categories by first presenting analytical approaches, and then empirical and semi-empirical models.

6.3.1 Analytical models

Parise [158] developed a simulation model for vapor compression heat pumps to predict their overall system performance. This is accomplished by using a straightforward model for the components within the heat pump cycle. Input data, such as compressor speed, source and sink temperatures, and flow rates for the cooling and heating fluids, are entered to determine the system's behavior. The condenser is regarded as having a constant overall heat transfer coefficient, which is determined based on its arithmetic overall temperature difference. A polytropic process is assumed to characterize the compression. Additionally, the superheat is assumed to be provided as an input.

Stefanuk, et al. [140] introduced a steady-state model for a water-to-water heat pump operating with superheat control. This model is entirely based on fundamental conservation laws and key correlations of heat transfer, aimed at forecasting the heat pump's performance across its entire operational range. The study's results revealed that adjusting the refrigerant charge is an effective control mechanism to enhance system performance.

Herbas, et al. [92] created a vapor compression model using straightforward mathematical representations for every component within the cycle. This approach resulted in a collection of nonlinear equations that were subsequently resolved using numerical techniques. Their model can predict the system's operational conditions, including its condensation and evaporation pressures. A comparison between the model's predictions and the performance of an existing unit showed a

significant correlation. In the compressor model, a constant index polytropic process is presumed. It is assumed that the condenser maintains a constant overall heat transfer coefficient and the expansion valve is omitted from the model, given that the superheat levels are predetermined.

As part of a serious effort to evaluate the performance of potential alternative refrigerants, several cycle simulation models were developed by researchers from the National Institute of Standards and Technology (NIST). Initially, a cycle model named Cycle 7 was developed by McLinden [159], comprising seven cycle state points. Cycle 7 evolved by incorporating a suction-line heat exchanger and enhancements to the compressor model, leading to the emergence of Cycle 11 [160], which now encompasses eleven state points. The potential performance comparison of possible replacement refrigerants has been carried out using Cycle 11 [161, 162]. Cycle 11 incorporates simplifications, including the absence of a pressure drop across heat exchangers, the utilization of polytropic compressor efficiency, constant degrees of superheat and subcooling, and fixed heat transfer coefficients in the heat exchangers.

Included within the models developed by the NIST is the Bicycle model [163], which serves the purpose of designing and evaluating the off-design performance of alternative refrigerant mixtures in vapor compression cycles. Among the primary assumptions employed are fixed degrees of superheating and subcooling. Fixed pressure drops across heat exchangers are also assumed, while the volumetric and isentropic efficiency of the compressor remain variable.

Since 1978, several versions of the DOE/ORNL Heat Pump Design Model (HPDM), which is a hardware-based steady-state performance simulation model, have been developed and disseminated by Oak Ridge National Laboratory (ORNL), as outlined by Rice [164]. The Mark V model has been released by ORNL [164].

Scarpa, et al. [165] developed a thermodynamic-based heat pump model that relies on inputs such as compressor isentropic efficiency, heat exchanger effectiveness, and refrigerant flow rate. Its performance outcomes show up to 10% variances when compared to manufacturer data.

Ndiaye [144] created a dynamic model for a water-to-air heat pump to enhance the accuracy of its simulations. The investigation revealed that current models within energy simulation software fall short of accurately capturing the transient effects associated with cycling. It was observed that the time constant utilized for modeling the heat pump’s start-up capacity depends on its operating conditions, highlighting a weakness in the models used by simulation programs that rely on a fixed

time constant. In a related study, Ndiaye and Bernier [166] developed a model predicting the state of the refrigerant throughout the circuit during typical operation and cycling conditions. The model can predict with relatively good accuracy the measured transient behavior of a GSHP. Similarly, to analyze the changes in energy consumption and capacity resulting from partial load operations and their associated shutdown and start-up processes, Ndiaye and Bernier [167] presented generalized one- and two-time-constant models.

IMST-ART (v4.10) is a software created for simulating refrigeration systems [168], with its applicability extending to heat pumps. The program offers multiple sub-models for compressors, heat exchangers, expansion valves, pipes, and accessories, allowing users to construct various refrigeration system configurations.

Dechesne, et al. [169] investigated a residential air-to-water heat pump, specifically a split system that operates with a variable speed scroll compressor and utilizes R410A refrigerant. The system features an internal heat exchanger that evaporates the refrigerant injected into the scroll during compression. Their model employs five dimensionless polynomials to forecast compressor performance, although it lacks specifics on the heat exchanger's design. The model inputs include the compressor's rotational speed and the ratios of the total and injection pressures. Their findings underscore the positive effects of superheat control on heat pump efficiency, demonstrating that reducing suction superheat enhances both the coefficient of performance (COP) and heating capacity, while also lowering its discharge temperature.

Correa and Cuevas [170] introduced a model for an air-to-water heat pump aimed at residential space heating and domestic hot water. Their modular approach, similar to the one used in the present study, to modeling divides the heat pump into three components: a compressor, condenser, and evaporator. The model assumes constant evaporator superheat controlled by the expansion valve and condenser subcooling dictated by the refrigerant's charge.

6.3.2 Experimentally based models

Experimentally based models prioritize simplicity and have the potential for high accuracy. With the growing availability of high-quality data from building energy metering and data-logging facilities, these models are expected to garner increasing attention [138]. They use statistical methods to establish the relationships between input parameters (e.g., ambient temperature, operating conditions) and the output performance of the heat pump (e.g., heating or cooling capacity, coefficient of performance). They are helpful when detailed theoretical equations are complex or when various system inefficiencies must be accounted for.

Gupta and Irving [171] established a correlation between heat pump performance and source/sink temperature difference using heat pump performance test results. When contrasted with the Building Research Establishment Domestic Energy Model (BREDEM) predictions, their resulting model exhibited an accurate reaction to variations in ambient temperature.

The validation of a black box heat pump model by Ruschenburg, et al. [172] employed field monitoring results from five ground-source installations. Discrepancies ranging from 1% to 32% are observed for its coefficient of performance (COP). It was also determined that the influence of standby losses significantly affects its prediction of power consumption. Within the assessed installations, the standby period contributes to an electrical consumption ranging from 2% to 5%.

Nyika, et al. [173] developed a ‘black box’ model based on experimental data. Generic equipment models were created to capture the performance of families of similar heat pumps, which can be utilized in building simulation programs. Tabatabaei, et al. [174] developed an empirical model specifically designed to ascertain the seasonal performance factor (SPF) of heat pumps directly. Their methodology encompasses six distinct approaches: four utilize polynomial functions, one employs an exponential function, and another uses the Carnot coefficient of performance (COP).

The TRNSYS software and its TESS library include some performance-map-based models, where heating (cooling) capacity and power consumption are given as a function of the source and load conditions. Actual performance is determined based on interpolation within the performance map. These models exhibit limitations, including diminished accuracy in their predictions of heat pump performance under part load conditions or when operating outside of the defined performance map. These shortcomings can be mitigated by integrating TRNSYS with additional software like the

Engineering Equation Solver [9] and constructing a more comprehensive heat pump model, as Ghoubali, et al. [175] suggested.

Bouheret and Bernier [143] presented the development of a model for a variable-capacity water-to-air ground-source heat pump. The model, designed for integration into TRNSYS, is constructed based on the manufacturer's steady-state performance maps. It supports four operating modes: space heating, dedicated space cooling, simultaneous space cooling and domestic hot water (DHW) production, and dedicated (DHW) production. Controlled by a PI-type thermostat, the heat pump allows for the assessment of the required compressor frequency. In the study, the proposed model is employed in annual simulations of two residential buildings equipped with both variable-capacity and fixed-capacity heat pumps.

St-Onge [176] presented a model of a variable-capacity air-source heat pump (VCASHP) in TRNSYS. By varying the heating loads and user-defined ambient temperatures, the impact of compressor frequency on the VCASHP's performance was explicitly measured. The VCASHP model was constructed using multiple polynomial regressions. In contrast, the performance data released by manufacturers indicate that VCASHP can provide a significantly enhanced performance and capacity compared to single-speed machines; laboratory and field tests have revealed that its actual performance does not consistently align with these expectations.

Bordignon, et al. [177] develop a streamlined model for simulating a ground heat exchanger and heat pump system. This model facilitates the estimation of energy usage and system efficiency in response to the operational conditions of its secondary fluids. Model parameters are calibrated using data from its operational performance or provided by manufacturers.

Woods and Bonnema [178] created a regression-based approach for modeling emerging heating, ventilation, and air-conditioning (HVAC) technologies, utilizing the user-defined coil object in the EnergyPlus building simulation software. The outputs from HVAC system models or experimental data can be employed to generate regression-based performance curves, which are subsequently utilized within building simulations. The regression approach is presented as an alternative to the direct modeling of new HVAC technologies in EnergyPlus.

6.3.3 Grey box models

A semi-empirical or grey box model is a mathematical model that combines both empirical data and theoretical principles to describe a system's behavior and is used when a purely theoretical or entirely empirical model is inadequate to capture the system's complexity or behavior accurately.

Underwood, et al. [179] developed a model with parameters that can be determined using manufacturer or experimental data. The compressor is at the heart of the model, characterized by exponential functions that incorporate four parameters. This model can forecast average test data values, exhibiting variations of up to 10% compared to experimental data. However, the model shows more significant discrepancies at elevated ambient temperatures.

Jin and Spitler [141] developed a steady-state simulation model for a reciprocating vapor-compression heat pump with a water-to-water configuration explicitly intended for incorporation into building simulation programs. This model is founded on basic thermodynamic principles and heat transfer relationships. It incorporates several undefined parameters, which are determined through a multi-variable optimization process using data provided by manufacturers.

Kinab, et al. [180] proposed a semi-empirical approach that relies on catalog data to establish their model parameters. This model features an isentropic compressor and employs polynomial laws to describe volumetric efficiency. Additionally, it accounts for the expansion valve and heat exchangers. This model can estimate the coefficient of performance (COP) of the heat pump within an accuracy of 8%.

Cimmino and Wetter [181] presented a Modelica model for simulating heat pumps. The model adopts a simplified vapor-compression cycle, encompassing only five refrigerant states. To determine the model's parameters, an optimization procedure was employed, aiming to minimize the disparities between the model's predicted heating capacities and power input and the corresponding values available in the manufacturer's technical data. As a result of the calibration process, the heating capacities and power input calculated by the adjusted model were within a range of 2.7% and 4.7% of the manufacturer's data, respectively.

Viviescas and Bernier [182] developed an exhaustive model for a variable-speed heat pump (VSHP) with a water-to-water configuration. The model is based on a physics-based methodology, integrating separate models for the plate heat exchangers (evaporator and condenser), the

expansion valve, and the variable-speed compressor. The model requires five inputs: the mass flow rate and temperature of both secondary fluids and compressor speed. Furthermore, a performance map was constructed based on this comprehensive model. This performance map strategy yielded favorable outcomes for annual simulations compared to the entire model, showing maximum discrepancies of 2.5% in heating capacity and 5.1% in power consumption.

Advantages and disadvantages exist for physical models based on the refrigeration cycle and empirical models employing curve fitting [183]. In physical models, adaptation to operating conditions beyond the standard range is allowed, encompassing variations in refrigerant flow, superheating, subcooling, and other factors. However, in many cases, this adaptation comes at the expense of some precision in the model. On the other hand, models relying on curve fitting maintain good accuracy when their operating conditions fall within the data ranges used for curve fitting. In this case, extrapolation is somewhat undesirable.

From this review, it can be concluded that a comprehensive, detailed model of a water-to-water heat pump, which integrates each component individually and allows for the determination of the refrigerant's energy performance and thermodynamic states, has not been found in the literature. More specifically, there does not appear to be many models that use the conditions of the secondary fluids (flow rate and inlet temperature) as input conditions. Furthermore, there is a notable absence of the experimental validation of such models.

6.4 Heat pump model

This model aims to predict the capacity (for either cooling or heating) and the necessary power of a heat pump based on predetermined inlet conditions for both secondary fluids (i.e., $T_{w_{L_{in}}}, \dot{m}_{w_L}, T_{w_{S_{in}}}, \dot{m}_{w_S}$ in Figure 6.1) without fixing cycle conditions such as its degrees of subcooling or superheating. This steady-state model also predicts the thermodynamic states of the refrigerant and the refrigerant flow rate ($\dot{m}_r$), the global heat exchange coefficients (UA) of both heat exchangers, and the degrees of superheat (SH) and subcooling (SC) at the exits of the evaporator and condenser, respectively. Plate heat exchangers (PHX) are used in the evaporator and condenser.

The heat pump features a fixed-speed scroll compressor, while a thermostatic expansion valve regulates the superheat level at the evaporator exit. Models for each component are interconnected

through the refrigeration cycle depicted in Figure 6.1, in a classic pressure–enthalpy diagram. The reversing valve has been omitted for clarity. While the model developed here applies to residential-size heat pumps, it can be used for larger commercial heat pumps of similar designs. The assumptions for each of the model components are listed in Table 6.1. Steady-state conditions are assumed for all components.

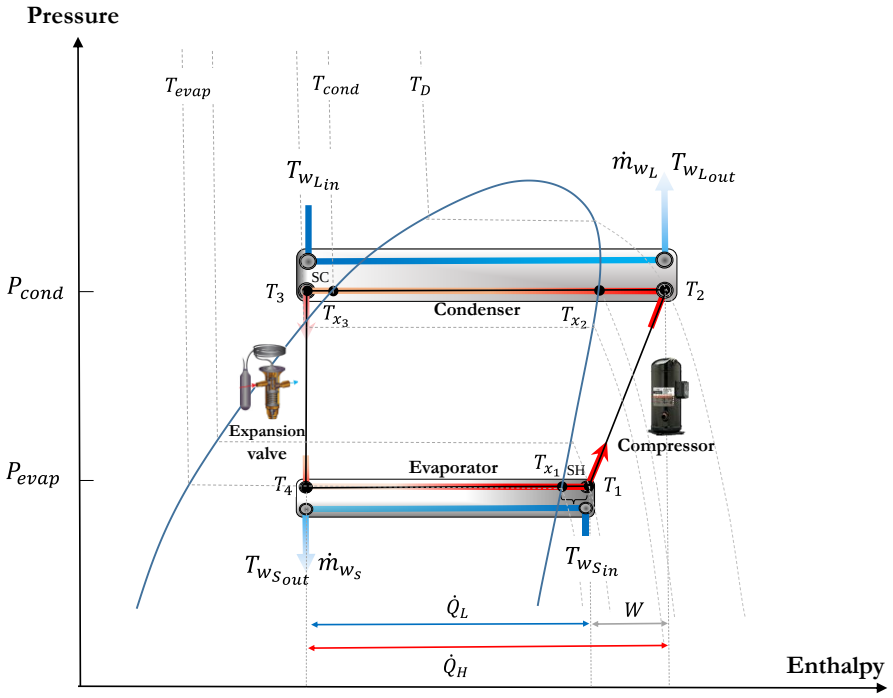

Figure 6.1 *P–h* diagram

Table 6.1 Assumptions used for the heat pump model and for all its components.

Component	**Assumption**
Evaporator and condenser	There are no pressure losses on the refrigerant side
	Heat losses between the exchangers and the surrounding environment are negligible
	Circulating oil has a negligible impact on heat transfer
Compressor	No heat losses between the compressor and the environment
Thermal expansion valve	Isenthalpic expansion process

In Figure 6.1, schematic overlays of the PHXs depict the heat transfer, involving secondary fluids at both the evaporator and condenser, when operating in heating mode. In cooling mode, $T_{w_{L_{in}}}$ and $T_{w_{S_{in}}}$ are reversed and represent the inlet secondary fluid temperatures to the evaporator and condenser, respectively.

The refrigerant, R-410A in this instance, leaves the evaporator as a superheated vapor at the temperature T_1 and completes the compression process at T_2. Within the condenser, the refrigerant undergoes an initial desuperheating from T_2 to $T_{x,2}$, condenses to a saturated liquid, and is further subcooled to T_3. Following this, an isenthalpic pressure reduction occurs in the expansion valve, leading to the refrigerant's entry into the evaporator at T_4. Here, the refrigerant experiences evaporation from T_4 to $T_{x,1}$ and is subsequently superheated to T_1.

6.4.1 Thermal expansion valve

The modeled thermal expansion valve is depicted in Figure 6.2. The semi-empirical model used here is based on the work of Eames et al. [36] and is shown in Equation (6.1). It has the advantage of not requiring geometrical data to obtain the mass flow through the valve.

$$\dot{m}_r = \beta[(P_b - P_e) - \alpha]\sqrt{2\rho_{rco}(P_c - P_e)}\ for\ \alpha \leq (P_b - P_e) \leq \delta \tag{6.1}$$

In Equation (6.1), $\dot{m}_r$ is the mass flow rate of the refrigerant in kg/s, α is the pressure equivalent of the static superheat setting (SSS) (in kPa), δ is the value of $(P_b - P_e)$ when the valve is fully opened, β is the constant flow area (in m^2/kPa), P_c and P_e are the evaporator and condenser pressures (in kPa), P_b represents the bulb pressure (in kPa), and ρ_{rco} corresponds to the density of the refrigerant in its saturated liquid state in the condenser (in kg/m^3).

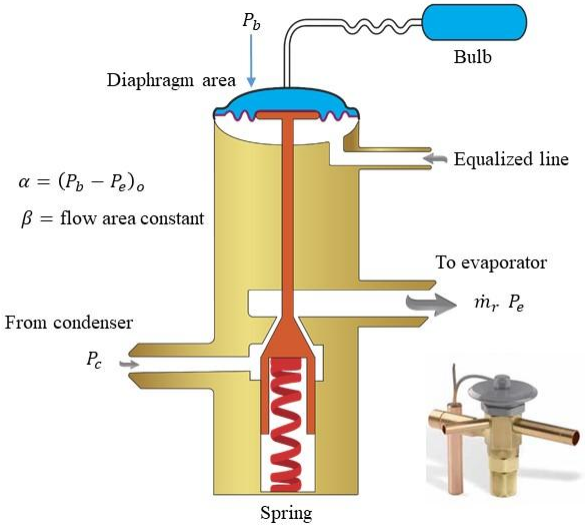

Figure 6.2 Schematic view of the externally equalized thermostatic expansion valve (TEV) used in this study

The values of α and β are evaluated, using the linear regression curve of $\frac{\dot{m}_r}{\sqrt{2\rho_{rco}(P_c-P_e)}}$ against $(P_b - P_e)$, from the experimental data obtained with the test bench developed for the present study. These regressions are presented in Figure 6.3.

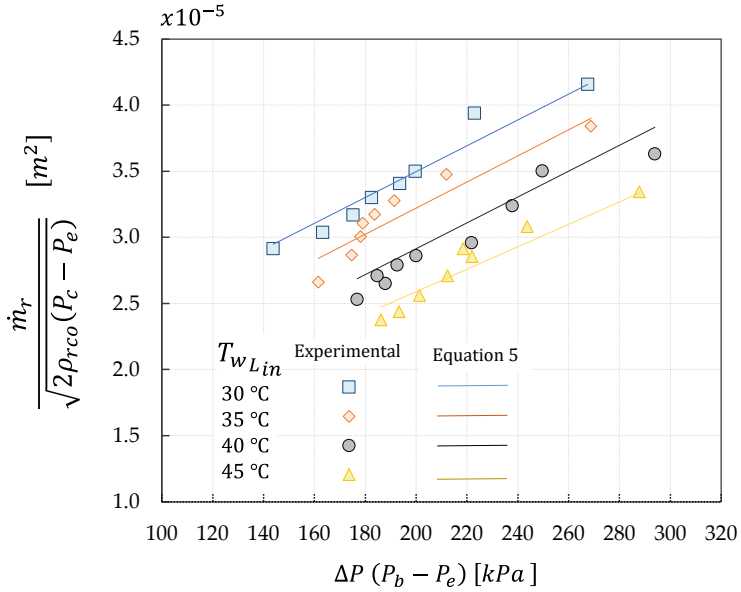

Figure 6.3 Linear regression to obtain $a, b,$ and β for Equation (6.4)

The pressures of the evaporator and condenser are measured using two pressure sensors, which have an accuracy of ±0.50% of the measured value. The bulb is usually installed on the suction line, which carries superheated vapor refrigerant from the evaporator to the compressor, and is positioned near the compressor. It is attached to the pipe using a mounting strap or clamp to ensure good thermal contact with the refrigerant flow for accurate readings. The bulb pressure is determined based on the temperature measured at the compressor suction.The refrigerant flow rate, $\dot{m}_r$, is calculated using the ten coefficients equation based on AHRI 540 [128], as a function of evaporating and condensing temperatures, as described later.

As observed in Figure 6.3, the lines depicting the refrigerant flow with a pressure drop between the compressor suction pressure (P_b) and the evaporating pressure (P_e) are influenced by the returning load fluid temperature ($T_{w_{L_{in}}}$).

To establish a unified equation encompassing this influence, a modified version of Equation (6.1) is proposed:

$$\frac{\dot{m}_r}{\sqrt{2\rho_{rco}(P_c - P_e)}} = \beta\left[(P_b - P_e) - f\left(T_{w_L}\right)\right] \tag{6.2}$$

where $f\left(T_{w_L}\right)$ is represented as a function of P_c, as shown in Equation (6.3).

$$f\left(T_{w_L}\right) = f(P_c) = aP_c + b \tag{6.3}$$

By combining Equations (6.2) and (6.3), the final model used here is represented by Equation (6.4).

$$\frac{\dot{m}_r}{\sqrt{2\rho_{rco}(P_c - P_e)}} = \beta(P_b - P_e) - aP_c - b \tag{6.4}$$

The calibration of the coefficients a, b, and β is pivotal for the precise estimation of both the superheat temperature and the refrigerant's mass flow rate. Using the experimental data and following a multivariable linear regression conducted using a popular statistical package, the model shows a multiple correlation coefficient R^2 of 0.94. Employing this model reveals a Root Mean Square Error (RMSE) of 1.9×10^{-3} kg/s and a maximum deviation of 7% in the prediction of the refrigerant's mass flow rate.

6.4.2 Condenser and evaporator models

Various techniques can be employed to describe the heat exchange occurring in the condenser and evaporator. The lumped approach is frequently employed due to its simplicity. In this method, the whole heat exchanger is considered a single control volume, with an overall heat conductance value (UA) used to assess its efficiency. The performance of the heat exchanger is determined by employing either the logarithmic mean temperature difference (LMTD) method or the ε-NTU method to calculate its capacity.

The lumped approach is predominantly utilized when it is assumed that only one phase is present within the heat exchanger. However, when accounting for phase change transitions within the heat exchanger, a more elaborate model becomes necessary, such as the moving boundary modeling approach. In this model, which is used here, the heat exchanger is split into distinct zones, representing single-phase and two-phase regions, to accurately account for the complexities associated with phase change phenomena [90]. Following this, the governing equations in each zone are solved using a lumped approach. Initially, the total heat exchanger area distributions

between each zone are undetermined and assigned initial guessed values. Then, an iterative procedure is employed, involving a set of nonlinear equations (comprising energy balances and epsilon-NTU equations within each zone) to ascertain the allocation of a heat exchanger area to each zone given the inlet conditions of the secondary fluids (flow rate and temperature).

The overall heat transfer coefficient (U_i) within each zone (A_i) is essential for calculating the NTUs (Number of Transfer Units) value, as expressed in Equation (6.5).

$$NTU_i = \frac{U_i A_i}{c_{min}} \tag{6.5}$$

This coefficient is computed based on the sum of three thermal resistances, as shown in Equation (6.6). In this equation, h_{hot} and h_{cold} are the convective heat transfer coefficients of the hot and cold sides, respectively, while t_p and k_p are the thickness and conductivity of the plate, respectively.

$$U = \frac{1}{\frac{1}{h_{hot}} + \frac{t_P}{k_P} + \frac{1}{h_{cold}}} \tag{6.6}$$

The term t_p/k_p accounts for only about 1% of the overall heat transfer coefficient.

Due to the wide range of plate heat exchanger designs and flow regimes, different correlations are available for h_{hot} and h_{cold}. Most of them are expressed based on the Nusselt number (Nu):

$$Nu = \frac{hD_h}{k} \tag{6.7}$$

where D_h is the hydraulic diameter and k is the fluid's thermal conductivity. The hydraulic diameter is defined as

$$D_h = \frac{4A_x}{p} \tag{6.8}$$

where A_x is the channel flow area, which is set equal to bw, where b is the equivalent channel width, and w is the plate heat exchanger width. The equivalent perimeter, denoted as p, is calculated as $p = 2(b + \phi w)$, where ϕ is the surface enlargement factor. This is simplified to $p = 2\phi$w, as b is significantly smaller than w [108]. Thus, the hydraulic diameter is given by

$$D_h = \frac{4A_x}{p} = \frac{4bw}{2\phi w} = \frac{2b}{\phi} \tag{6.9}$$

Single-Phase Flows

For single-phase flows, heat transfer coefficients are obtained using the equations described by Wanniarachchi, et al. [113] and Kim and Park [118]:

$$Nu = \left(Nu_t{}^3 + Nu_l{}^3\right)^{\frac{1}{3}} Pr^{\frac{1}{3}} \left(\mu_b/\mu_w\right)^{0.17} \tag{6.10}$$

$$Nu_l = \frac{3.65\phi^{0.661} Re^{0.339}}{(90-\beta)^{0.455}} \tag{6.11}$$

$$Nu_t = \frac{12.6\phi^{1-m} Re^{m}}{(90-\beta)^{1.142}} \tag{6.12}$$

$$m = 0.646 + 0.0011(90-\beta) \tag{6.13}$$

$$Re = \frac{D_h V \rho}{\mu} = \frac{\dot{m} D_h}{N_{ch} w b \mu} \tag{6.14}$$

Where Re is the Reynolds number, Pr is the Prandtl number, β is the angle of the rib inclination angle of the plates (chevron angle), $\dot{m}$ represents the total mass flow rate, N_{ch} indicates the number of channels for each fluid within the PHX, and μ is the dynamic viscosity of the fluid. These equations are valid on the refrigerant and water sides of the PHX.

Condensation

To calculate the heat transfer coefficient in the condensation mode, the equations proposed by Yan, et al. [120] are used:

$$Nu = \frac{hD_h}{k_l} = 4.118 {Re_{eq}}^{0.4}\ \mathrm{Pr}_l^{\frac{1}{3}} \tag{6.15}$$

$$Re_{eq} = \frac{G_{eq} D_h}{\mu_l} \tag{6.16}$$

$$G_{eq} = G\left[1 - X_m + X_m\left(\frac{\rho_l}{\rho_v}\right)\right] \tag{6.17}$$

The equivalent Reynolds number (Re_{eq}) is computed based on the equivalent mass flux (G_{eq}), while the mean vapor quality (X_m) represents the average vapor quality within the plate heat exchanger. The subscripts 'l' and 'v' signify properties associated with the saturated liquid and saturated vapor state.

Evaporation

In terms of the evaporation mode, García, et al. [136] noted that the model proposed by Cooper [121] closely aligns with experimental findings and this was consequently chosen for the current investigation. This model is represented by

$$\frac{h}{(q/A)^{0.67}} = 55P_r^{[0.12-0.2log_{10}R_p]}(-logP_r)^{-55}M^{-0.5} \tag{6.18}$$

Here, q/A is the heat flux rate, M represents the molecular weight of the substance, and P_r is the reduced pressure, defined as the operating pressure divided by the critical pressure of the fluid. The surfaces roughness parameter is denoted by R_p (with a default value of $R_p = 1$ when not explicitly specified, as is the case in the present study).

Condenser Heat Transfer Model

Figure 6.4 shows how the condenser's counter-current flow is subdivided, with three distinct regions on the refrigeration side. The model can also simulate a parallel flow configuration, but this aspect of the model will not be presented here.

The total condenser heat transferred, $Q_{T_{cond}}$, equals the cumulative heat transfer in the desuperheating zone, Q_{dsh}, in the condensation zone, Q_{cond}, and in the subcooling zone, Q_{sc}.

$$Q_{T_{cond}} = Q_{dsh} + Q_{cond} + Q_{sc} \tag{6.19}$$

The total area for heat transfer is expressed as

$$A_{total} = (N_c - 1)A_p = A_{dsh} + A_{cond} + A_{sc} \tag{6.20}$$

The parameter N_c represents the number of channels in the PHX. End plates, assumed to be adiabatic, are excluded from the total area calculation.

The heat transfer coefficients are significantly different in each section. Figure 6.4 provides an example of the average heat transfer coefficients on the water side (h_w) and on the refrigeration side (h_{ref}), as well as the overall coefficient U_i, for specific conditions: $T_{w_{L_{in}}} = 35$ ℃, $\dot{m}_{w_L} = 0.5 \frac{\text{kg}}{\text{s}}$, $T_2 = 80$ ℃ and $\dot{m}_r = 0.05 \frac{\text{kg}}{\text{s}}$.

The blue dashed line represents the heat transfer coefficient for water, showing values ranging from ~ 9 kW/m^2-K in the superheating region to ~ 7 kW/m^2-K in the subcooling region. In contrast, the refrigerant (orange dashed line) displays coefficients of 0.6 kW/m^2-K in the superheating zone, 0.8 kW/m^2-K in the subcooling zone, and 1.8 kW/m^{2-}K in the condensation zone. Consequently, the heat transfer process is predominantly controlled by the refrigerant side.

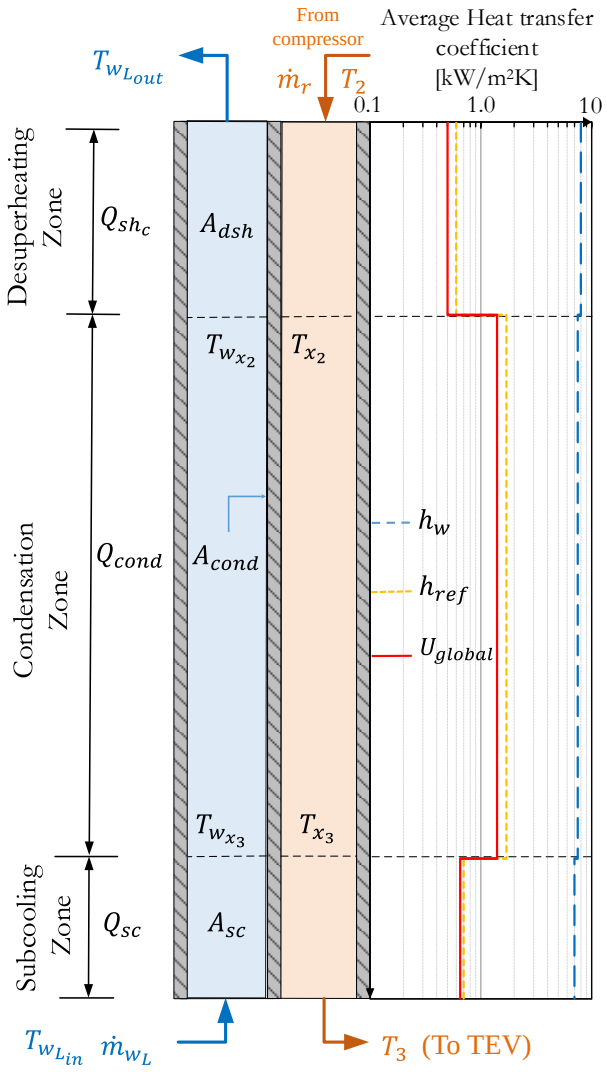

Figure 6.4 Plate heat exchanger: condenser

As a result, the overall heat transfer coefficient (continuous red line) assumes values of U_{sh} = 0.5 kW/m^2-K in the superheating zone, U_{cond} =1.4 kW/m^2-K in the condensation zone, and U_{sc} = 0.7 kW/m^2-K in the subcooling zone.

The plate heat exchanger model and the equations used in each heat exchanger zone are presented below. The thermophysical properties of both fluids are assessed at the average temperature of the inlet and outlet conditions within each zone. All property calculations are performed using EES.

Desuperheating Zone

Equations (6.21–6.29) are the governing equations for this zone.

$$Q_{dsh} = \dot{m}_r C_{p,r}\left(T_2 - T_{x_2}\right) \tag{6.21}$$

$$Q_{dsh} = \varepsilon_{dsh} c_{min}\left(T_2 - T_{w_{x_2}}\right) \tag{6.22}$$

$$Q_{dsh} = \dot{m}_w C_{p,w}\left(T_{w_{L_{out}}} - T_{w_{x2}}\right) \tag{6.23}$$

$$A_{dsh} = \frac{Q_{dsh}}{U_{dsh}\Delta T_{lm_{sh}}} = \frac{Q_{dsh}}{U_{dsh}\left[\left(T_2 - T_{w_{L_{out}}}\right) - \left(T_{x_2} - T_{w_{x_2}}\right)\right]} ln\frac{\left(T_2 - T_{w_{L_{out}}}\right)}{\left(T_{x_2} - T_{w_{x_2}}\right)} \tag{6.24}$$

$$\varepsilon_{dsh} = \frac{1 - e^{[(-NTU_{dsh})(1-C_r)]}}{1 - C_r e^{[(-NTU_{dsh})(1-C_r)]}} \tag{6.25}$$

$$NTU_{dsh} = \frac{U_{dsh} A_{dsh}}{c_{min}} \tag{6.26}$$

$$C_r = {}^{c_{min}}/_{c_{max}} \tag{6.27}$$

$$c_{max} = \max\left(\dot{m}_r C_{p,r}, \dot{m}_w C_{p,w}\right) \tag{6.28}$$

$$c_{min} = \min\left(\dot{m}_r C_{p,r}, \dot{m}_w C_{p,w}\right) \tag{6.29}$$

where $C_{p,w}$ and $C_{p,r}$ are the average heat capacities in the water and refrigerant zones, respectively.

Condensation Zone

Equations (6.30–6.34) model the condensation zone. The heat of condensation is determined by evaluating the enthalpy change during complete condensation, and this value is dependent on the condensation temperature (T_{x_2}), as indicated in Equation (6.30).

$$Q_{cond} = \dot{m}_r \Delta H_{evap(T_{x_2})} \tag{6.30}$$

$$Q_{cond} = \varepsilon_{cond} c_{min} \left(T_{x_2} - T_{w_{x_3}}\right) \tag{6.31}$$

$$A_{cond} = \frac{Q_{cond}}{U_{cond} \Delta T_{lm_{cond}}} = \frac{Q_{cond}}{U_{cond} \left(T_{w_{x_3}} - T_{w_{x_2}}\right)} ln \left[\frac{\left(T_{x_2} - T_{w_{x_2}}\right)}{\left(T_{x_2} - T_{w_{x_3}}\right)}\right] \tag{6.32}$$

$$\varepsilon_{cond} = 1 - e(-NTU_{cond}) \tag{6.33}$$

$$NTU_{cond} = \frac{U_{cond} A_{cond}}{c_{min}} \tag{6.34}$$

Subcooling Zone

In the subcooling zone, the governing equations are as follows:

$$Q_{sc} = \dot{m}_r C_{p,r} \left(T_{x_2} - T_3\right) \tag{6.35}$$

$$Q_{sc} = \dot{m}_w C_{p,w} \left(T_{w_{x_3}} - T_{w_{L_{in}}}\right) \tag{6.36}$$

$$Q_{sc} = \varepsilon_{sc} c_{min} \left(T_{x_3} - T_{w_{L_{in}}}\right) \tag{6.37}$$

$$A_{sc} = A_{total} - A_{cond} - A_{sh} \tag{6.38}$$

$$\varepsilon_{sc} = \frac{1 - e^{[(-NTU_{sc})(1 - C_r)]}}{1 - C_r e^{[(-NTU_{sc})(1 - C_r)]}} \tag{6.39}$$

$$NTU_{sc} = \frac{U_{sc}A_{sc}}{c_{min}} \tag{6.40}$$

Evaporator Heat Transfer Model

The evaporator receives the refrigerant in the form of a vapor–liquid mixture after leaving the expansion valve. The heat transfer area in the plate heat exchanger is primarily utilized for the evaporation of the refrigerant until it reaches a saturated vapor state, and a smaller portion is used for superheating before being directed to the suction of the compressor. Figure 5 depicts the heat exchanges occurring between two adjacent plates of thickness t_p, where the water and the refrigerant flows are in opposite directions.

The total evaporator heat transfer $Q_{T_{evap}}$ is equal to the sum of the heat transferred in the evaporation zone, Q_{evap}, and the superheating zone, Q_{sh} (Equation 6.41).

$$Q_{T_{evap}} = Q_{sh} + Q_{evap} \tag{6.41}$$

The total area for heat transfer is expressed as

$$A_{total_{evap}} = (N_c - 1)A_p = A_{\text{sh}} + A_{evap} \tag{6.42}$$

Figure 6.5 provides an overview of the general variations of each heat transfer coefficient, as well as the overall coefficient U_i for the specific conditions: $T_{w_{s_{in}}} = 10$ °C $\dot{m}_{w_L} = 0.5\,\frac{\text{kg}}{\text{s}}$, $T_4 = 5$ °C, and $\dot{m}_r = 0.05\,\frac{\text{kg}}{\text{s}}$.

The blue dashed line represents the heat transfer coefficient for water, which has values ranging from 7 kW/m^2-K in the superheating region to 6 kW/m^2-K in the evaporating region. In contrast, the refrigerant (orange dashed line) displays coefficients of 0.6 kW/m^2-K in the superheating zone and 1.3 kW/m^2-K in the evaporating zone. Consequently, as was the case for the condenser, the refrigerant side predominantly controls the heat transfer process. As a result, the overall heat transfer coefficient (continuous red line) assumes values of U_{sh} = 0.5 kW/m^2-K in the superheating zone and U_{evap} =1.1 kW/m^2-K in the evaporating zone.

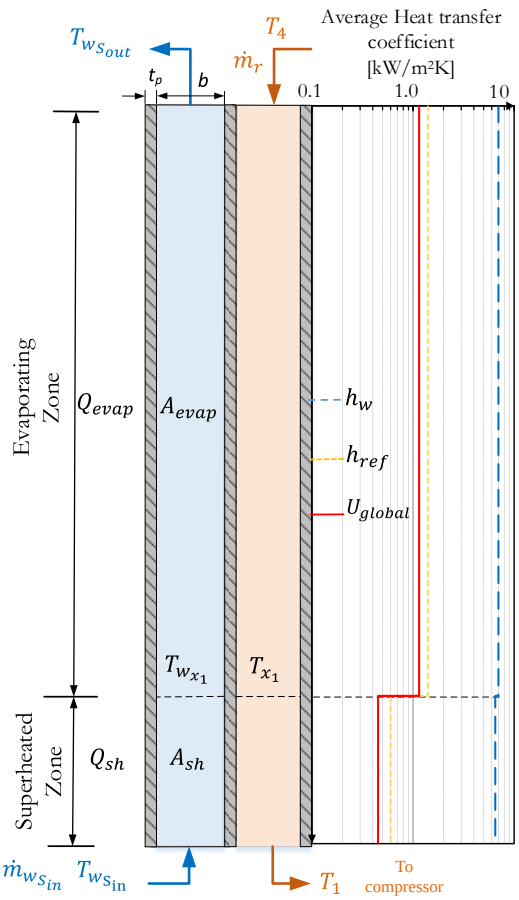

Figure 6.5 Plate heat exchanger: evaporator

Evaporation Zone

Equations (6.43)–(6.47) are the governing equations for the evaporation zone.

$$Q_{evap} = \varepsilon_{evap} c_{min} \left(T_{w_{x1}} - T_{x_1}\right) \tag{6.43}$$

$$\varepsilon_{evap} = 1 - e\left(-NTU_{evap}\right) \tag{6.44}$$

$$NTU_{evap} = \frac{U_{evap} A_{evap}}{c_{min}} \tag{6.45}$$

$$Q_{evap} = \dot{m}_w C_{p,w} \left(T_{w_{x_1}} - T_{ws_{out}}\right) \tag{6.46}$$

$$Q_{evap} = \dot{m}_r (1 - x_4) \Delta H_{evap} = \dot{m}_r (1 - x_4) f\left(T_{x_1}\right) \tag{6.47}$$

Superheating Zone

In this zone, the heat transfer is governed by the following equations:

$$Q_{sh} = \dot{m}_r C_{p,r}\left(T_1 - T_{x_1}\right) = \dot{m}_r C_{p,r} \Delta T_{sh} \tag{6.48}$$

$$Q_{sh} = \dot{m}_w C_{p,w}\left(T_{w_{S_{in}}} - T_{w_{x_1}}\right) \tag{6.49}$$

$$\mathrm{A}_{sh} = \frac{Q_{sh}}{U_{sh} \Delta T_{lm_{sh}}} \tag{6.50}$$

6.4.3 Compressor model

Various approaches to modelling compressors have been proposed. The Winandy model [101] is a semi-empirical gray box model designed to forecast scroll compressor performance. This model has been used as a basis for developing similar models such as those of Meramveliotakis, et al. [184]. Other semi-empirical models have been presented by Tello, et al. [185], Popovic and Shapiro [148] , Klein, et al. [186], Li [187], and Shao, et al. [147].

While most models typically assume a steady state, Ndiaye and Bernier [188] introduced a dynamic model for a hermetic reciprocating compressor operating across on–off cycles in their heat pump model. There is good agreement between this model and experiments conducted under steady-state and transient conditions in both heating and cooling scenarios.

In a recent investigation carried out by Gabel and Bradshaw [149] it was determined that the AHRI model, which features ten coefficients, demonstrates outstanding performance when trained with datasets encompassing both standard and variable superheat scenarios, revealing slight variances of 0.43% and 0.57% for mass flow rate and power, respectively. When compared against the models of Shao, et al. [147], Popovic and Shapiro [148] and Winandy, et al. [101], Aute, et al. [150], also reported similar findings regarding the performance of the AHRI model [128] when trained with data.

Considering these conclusive studies, the AHRI model is used in this work. As shown in Equation (6.51), the AHRI model consists of a third-order polynomial equation with ten coefficients.

$$X = C_1 + C_2T_S + C_3T_D + C_4T_S^2 + C_5T_DT_S + C_6T_D^2 + C_7T_S^3 + C_8T_DT_S^2 + C_9T_ST_D^2 + C_{10}T_D^3 \quad (6.51)$$

Here, X represents the power input or the refrigerant mass flow rate, while C_1 to C_{10} denote the regression coefficients supplied by the manufacturer, T_D stands for the discharge dew-point temperature ($T_{x,2}$ in Figure 6.1), and T_S is the suction dew-point temperature ($T_{x,1}$ in Figure 6.1). Manufacturers typically provide the coefficients for default units specified in °F for temperature, lb/h for mass flow rates, and watts for power.

The coefficients in Equation (6.51) are based on a specific value for the degrees of superheat, typically set at 5 °C. According to the AHRI 540 standard [128] changes in the degrees of superheat have no impact on compressor power; however, an adjustment in the mass flow rate is necessary. For this purpose, Equation (6.52) in Appendix D of the AHRI standard [128], is used to adjust the rated refrigerant mass flow rate, $\dot{m}_{rated}$, for the rated superheat to derive the corrected mass flow rate, $\dot{m}_{corrected}$, under the actual suction conditions.

$$\dot{m}_{corrected} = \left\{1 + F_V\left[\left(\frac{v_{rated}}{v_{corrected}}\right) - 1\right]\right\}\dot{m}_{rated} \quad (6.52)$$

Within this equation, F_V represents the correction factor for volumetric efficiency, which fluctuates according to the volumetric efficiency associated with the compression technology. The standard recommends using a value of one (1) as a general approximation. The additional variables in Equation (6.52) include $v_{corrected}$, the specific volume under the suction condition, and v_{rated}, the specific volume under the rated condition.

Predicting compressor performance following the AHRI 540 model presents two principal sources of uncertainty: the measurement and regression uncertainties encountered during model development. While the literature has quantified measurement uncertainty, the regression uncertainty may lead to average errors of up to 5% and 4% in power and mass flow rate predictions, respectively, as demonstrated in the studies conducted under AHRI-Project-8013 [150], and by Aute and Martin [189]. A technique for quantifying the uncertainty in the compressor map's output was introduced by Cheung, et al. [190], where the most important source of uncertainty is due to data training.

6.4.4 Numerical solution

A set of equations representing the heat pump under study has been described. They include the compressor (governed by the power and mass flow rates in Equation 6.51) and two heat exchangers (described by the heat exchange Equations (6.19–6.50)) as well as the heat transfer model (outlined through Equations (6.5–6.18)), the expansion device (specified by Equation 6.4), and ultimately an equation of state to determine thermodynamic variables and physical properties of the system. A converged solution to this set of equations presents challenges, and two approaches are generally employed [191]. First, a non-simultaneous, component-based successive approach, where each variable or component of the heat pump is individually resolved to convergence before addressing the next unknown variable or component. The second approach, which is used in the present study, solves the set of equations simultaneously. A multi-variable nonlinear equation solver [9], is used to obtain the unknown variables within the convergence criteria which is set at 10^{-6} in the present case. However, the primary challenge when solving this system of equations lies in selecting initial guess values. No general rule can be established for the selection of guess values. Their selection relies on the experience of the modeler.

6.5 Experimental test facility

The heat pump under test is a commercially available 3-Ton (10 kW) machine equipped with a scroll compressor. The set of ten coefficients for this compressor is presented in Table 6.2 and is valid for a superheat of 5 °C.

Table 6.2 Input coefficients for Equation (6.51) for the compressor.

	Power [W]	Mass Flow Rate [lb/h]
C1	−561.362	250.7
C2	−15.626	5.011
C3	46.925	−1.456
C4	−0.2179	0.0409
C5	0.4351	−0.0178
C6	−0.4424	0.0171
C7	0.00022	0.00005
C8	0.00237	-5.09×10^{-6}
C9	−0.00332	0.000147
C10	0.00250	-9.63×10^{-5}

Two (2) SWEP P80 series brazed plate heat exchangers are used as the evaporator and the condenser. The main characteristics of these plate heat exchangers are presented in Figure 6.6 and Table 6.3. They are based on information either provided or calculated based on the manufacturer's data.

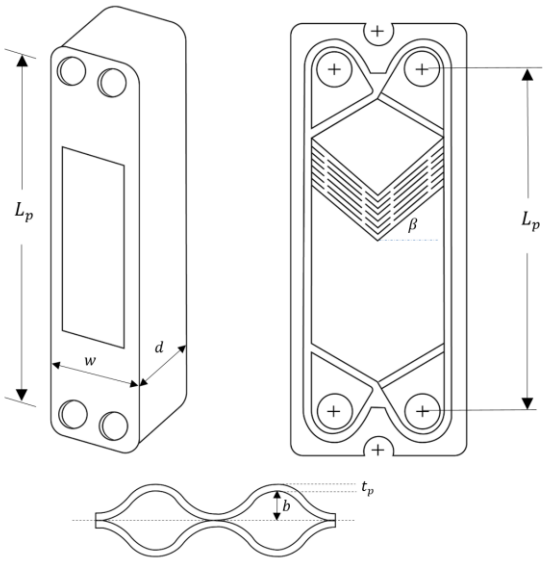

Figure 6.6 Illustration of a Plate Heat Exchanger (PHX) and a cross-sectional view of two adjoining plates

Table 6.3 Plate heat exchanger characteristics.

Parameter	**Value**	**Units**
Width × height	119 × 526	Mm × mm
Depth of the condenser	122	mm
Depth of the **e**vaporator	99	mm
Chevron angle, β	45	
Plate thickness, t_p	0.8	mm
Plate spacing, b	1.7	mm
Surface enlargement factor, ϕ	1.2	-
Hydraulic diameter, D_h (= $2b/\phi$)	2.8	mm
Effective surface area, A_p	0.07	m^2/plaque
Number of plates in the evaporator	40	-
Number of plates in the condenser	50	-
Plate's refrigerant-side thermal conductivity (Cooper), k_{p_r}	380	W/m-K

A schematic representation and a photograph of the experimental test facility are shown in Figure 6.7, and the main elements are presented in Table 6.4. The test bench comprises two precisely

controlled secondary fluid loops and the heat pump under test. The heat pump is instrumented to measure condensation and evaporation pressures, the discharge temperature of the compressor, compressor power, degrees of superheating, and degrees of subcooling.

In heating mode, the condenser is connected to a water-cooled 10 kW recirculating chiller equipped with an electric heater to control and maintain the inlet temperature of the secondary fluid, with a stability of ±0.1 °C. The chiller has a pump capable of delivering a flow rate of up to 0.63 L/s with a stability of ±0.002 L/s. The evaporator is connected to a recirculating temperature-controlled water source available within the building, which provides water at stable temperatures (±0.1 °C) and flow rates (±0.003 L/s).

The total heat exchanged in the evaporator and condenser is determined using Equations (6.53) and (6.54).

$$\dot{Q}_L = \dot{m}_{w,l} C_{p,l} \Delta T_l \tag{6.53}$$

$$\dot{Q}_S = \dot{m}_{w,s} C_{p,s} \Delta T_s \tag{6.54}$$

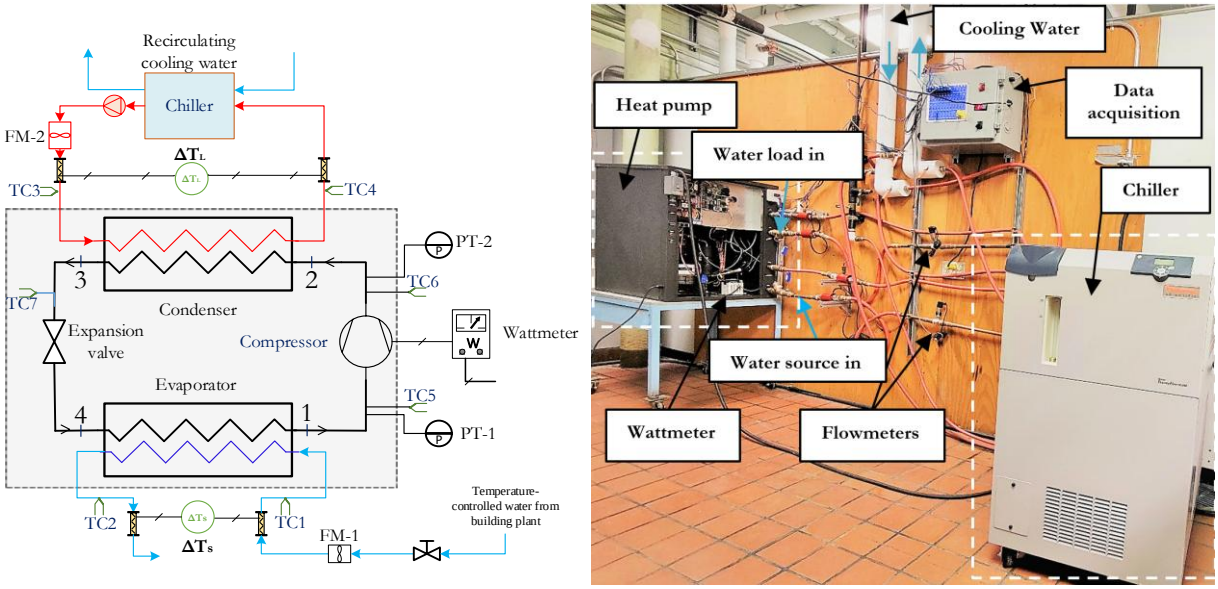

Figure 6.7 Experimental facility for testing a water-to-water heat pump (shown here in heating mode)

where ΔT_l and ΔT_s are the temperature differences of the secondary fluids across the heat exchangers. Given the significance of precisely measuring these temperature differences, two thermopiles have been incorporated into each of the secondary fluids' circuits. Both have a measurement uncertainty of ±0.04 K in terms of the temperature difference, as indicated in Table 6.4. The specific heat of both secondary fluids (water), $C_{p,l}$ and $C_{p,s}$, is evaluated at the mean fluid temperature.

The mass flow rate is measured using a turbine-type flowmeter, the temperature is monitored using thermocouples, and the power is determined using a power meter. Details of the instruments used are outlined in Table 6.4. Sensors are connected to the data acquisition system.

The uncertainty of the measured $COPs$ and capacities reported later are calculated using the propagation of uncertainty technique presented by Taylor and Kuyatt [192], and based on the individual measurement uncertainties reported in Table 6.4.

A total of 32 experiments are reported in the heating mode, with eight different source temperatures ($T_{w_{S_{in}}}$), ranging from 10 °C to 26 °C in increments of 2 °C, and four load temperatures ($T_{w_{L_{in}}}$), ranging from 30 to 45 °C in increments of 5 °C. For the cooling mode, a series of 12 experiments are reported, with three temperatures for the load (10, 12, and 15 °C) and four temperatures for the source (27, 30, 35, and 40 °C). The mass flow rate of the secondary fluids is set at 0.565 L/s for the load and in the range of 0.308–0.462 L/s for the source side.

Table 6.4 Instrumentation used in the test facility

Measurement	Manufacturer	Uncertainty	Range
Flowmeter ($\dot{m}_{w,l}$ and $\dot{m}_{w,s}$)	Omega (Norwalk, CT, USA) 1″ Turbine Flow Meter, 35 GPM (up to 2.2 L/s)	±0.5% of measurement	0.06–2.2 (L/s)
Wattmeter (W)	Ohio Semitronics (Hilliard, OH, USA) #WT3-12-100-D	±0.5% of full scale	0–24 [kW]
Differential temperature (ΔT_l and ΔT_s)	Delta T Company (Pico Rivera, CA, USA) Thermopile, 20 junctions with Type T thermocouples	±0.04 [K]	0–140 [°C]
Pressure transducer (PT1, PT2)	Omega 1000 PSIG PX119 (Norwalk, CT, USA) Pressure transducer	±0.5% of measurement	0 to 7000 kPa
Temperature (TC1 to TC7)	Omega (Norwalk, CT, USA) Type T thermocouples	±0.1 [K]	0–200 [°C]

A typical experiment would proceed as follows: the temperature and flow rates are monitored until they reach a steady state, typically taking about 10 min. This 10 min period is carefully monitored so as to avoid slowly evolving drifts. Then, readings are taken every 0.1 s. for 30 s. The resulting 300 readings are then averaged and represent one data point.

6.6 Results

This results section is divided into three sub-sections. The validation of the complete heat pump model is presented first. This involves the comparison of its COPs and power consumption in both heating and cooling modes. The objective of this validation is to compare the modeling and experimental results for the same set of inlet conditions for both secondary fluids (i.e., $T_{w_{L_{in}}}, \dot{m}_{w_L}, T_{w_{S_{in}}}, \dot{m}_{w_S}$). The second sub-section compares the operational conditions (evaporating and condensing temperatures, degrees of superheat and subcooling, and compressor discharge temperature) predicted by the model and those measured experimentally. Finally, it is shown how the model can be used to predict the non-operational conditions of the heat pump in specific scenarios.

6.6.1 Coefficient of performance (COP)

The coefficient of performance (COP) is defined as the ratio of the useful heating or cooling output to the power input required to achieve that output. Given the terminology used in Figure 6.1, the heating and cooling COP can be expressed as

$$COP_H = \frac{\dot{Q}_H}{W} \tag{6.55}$$

$$COP_C = \frac{\dot{Q}_L}{W} \tag{6.56}$$

As depicted in Figure 6.8, there is excellent agreement between the modeling results and experimental data in both the heating and cooling modes. When accounting for uncertainty, most data points closely align with the 45° line, representing perfect agreement.

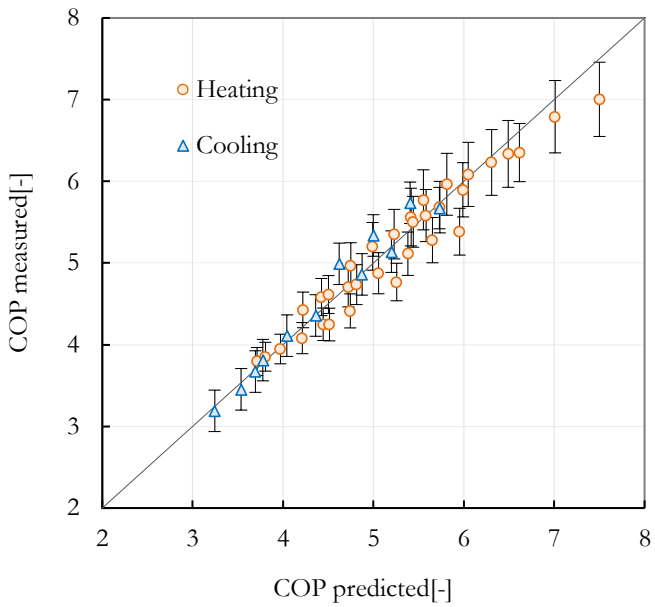

Figure 6.8 Steady-state COPs in heating and cooling mode

Figure 6.9 displays the COP_H across eight values of $T_{w_{S_{in}}}$ and four variations of $T_{w_{L_{in}}}$. As anticipated, the COP_H rises when the temperature difference between the source and load decreases. It increases by a factor of two (from ~3.5 to ~7) when the pair ($T_{w_{S_{in}}}$, $T_{w_{L_{in}}}$) changes from (10, 45 °C) to (20, 30 °C). Additionally, the COP_H increases when the $T_{w_{S_{in}}}$ increases for a given value of $T_{w_{L_{in}}}$.

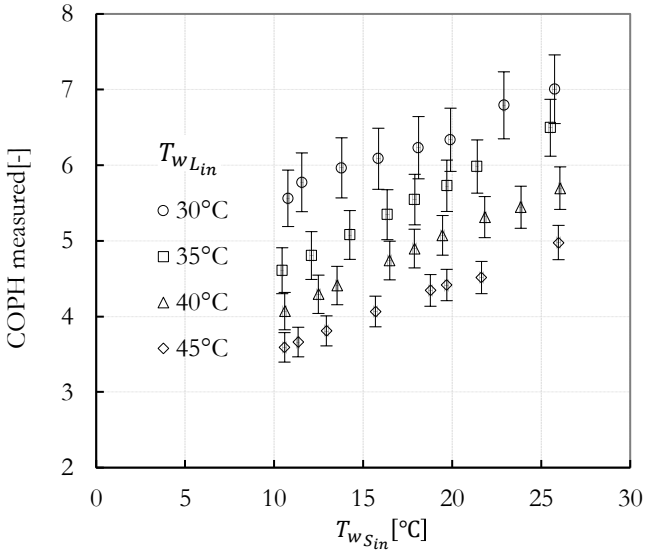

Figure 6.9 Steady-state COPs in the heating mode as a function of the secondary fluid temperatures

Figure 6.10 illustrates the measured power consumption as a function of the inlet temperatures of the secondary fluids, $T_{w_{L_{in}}}$ and $T_{w_{S_{in}}}$. An increase in the difference between these two temperatures leads to an increase in power consumption. However, for a given value of $T_{w_{L_{in}}}$, the source inlet temperature, $T_{w_{S_{in}}}$, has a relatively minor impact on power consumption. This is due to two competing effects. First, recall that the required compressor power is given by $\dot{m}_r(h_2 - h_1)$, where h_2 represents the enthalpy of the refrigerant, which is associated with the discharge temperature T_2, and h_1 is the enthalpy associated with the suction temperature T_1 (Figure 6.1). A rise in suction temperature T_1, induced by an increase in $T_{w_{S_{in}}}$, results in increased density, attributed to the rise in evaporation pressure. There is also a slight increase in the degrees of superheat, which decreases density. However, the increase caused by the rise in the evaporation pressure is much greater. An increase in refrigerant density at the suction of the compressor leads to an increase in the mass flow rate, $\dot{m}_r$. In turn, this increase in mass flow rate contributes to a decrease in the compressor's discharge temperature when operating under a constant condenser pressure, leading to a reduction in enthalpy change $(h_2 - h_1)$. In the end, these effects cancel each other out, leaving the required compressor power almost unaffected by $T_{w_{S_{in}}}$.

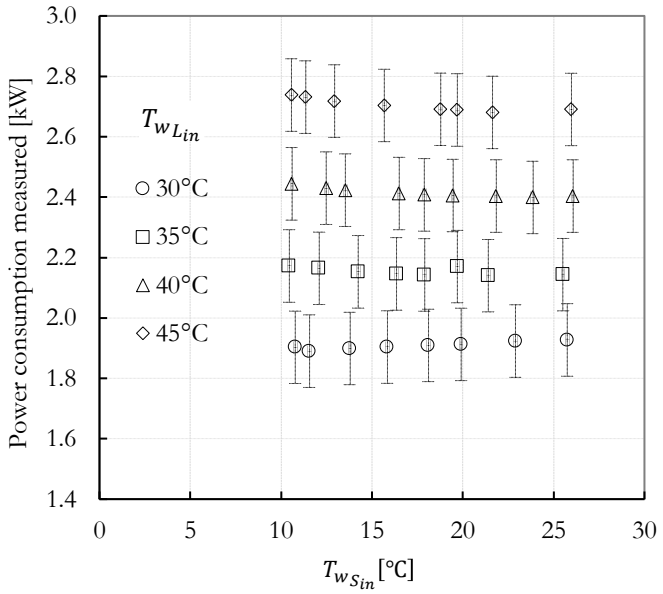

Figure 6.10 Power consumption as a function of the secondary fluid temperatures

6.6.2 Comparison of operational conditions

The model can predict several thermodynamic points. For example, Figures 6.11 and 6.12 show seven points predicted by the model, and their experimental counterparts, in a *P*–*h* diagram for a heating and a cooling case ($T_{ws_{in}} = 10$ °C and $T_{wL_{in}} = 40$ °C in the heating case and $T_{ws_{in}} = 35$ °C and $T_{wL_{in}} = 10$ °C in the cooling case). As can be seen, the agreement between the model and the experiments is good, with a slight difference observed in the evaporating pressure.

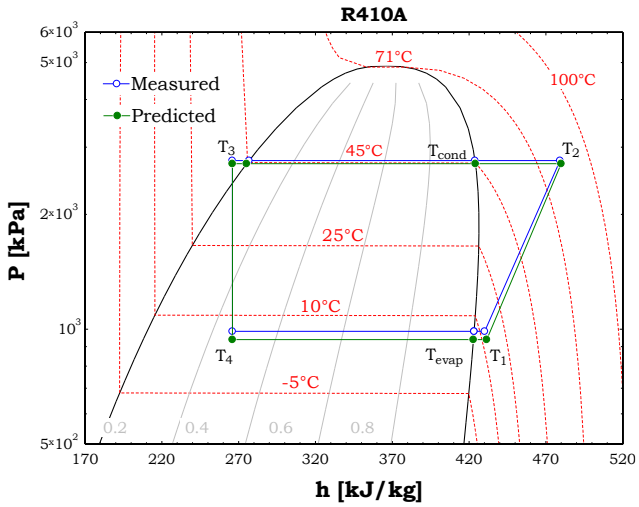

Figure 6.11 Comparison of measured and predicted results during heating

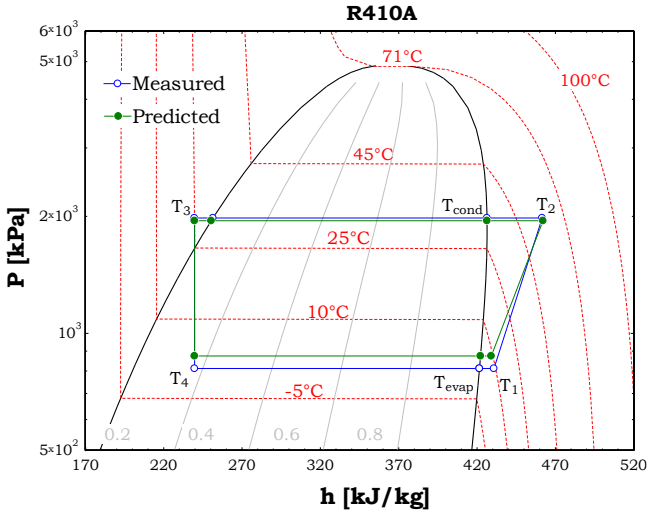

Figure 6.12 Comparison of measured and predicted results during cooling

Figures 6.13 and 6.14 compare the experimentally measured condensing and evaporating pressures and those calculated using the model. In the case of the condensing pressure, the agreement is good, with an RMSE of 27 kPa and corresponding uncertainties of $\pm$ 10 and $\pm$ 15 kPa for condensing

pressures of 2000 and 3000 kPa, respectively. There are noticeable differences between the predictions and the measurements of the evaporating pressure (Figure 6.14). This discrepancy becomes more pronounced with increasing evaporator temperatures: the absolute error is 10 kPa at low pressures (where the experimental uncertainty is $\pm$ 4 kPa at 800 kPa) and reaches 100 kPa at higher pressures (the experimental uncertainty is $\pm$ 6.5 kPa at 1300 kPa).

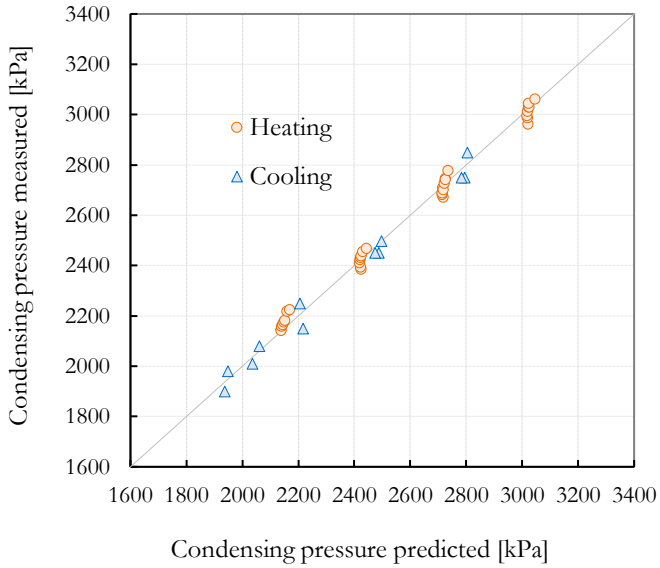

Figure 6.13 Comparison of the measured and modeled results for condensing pressure

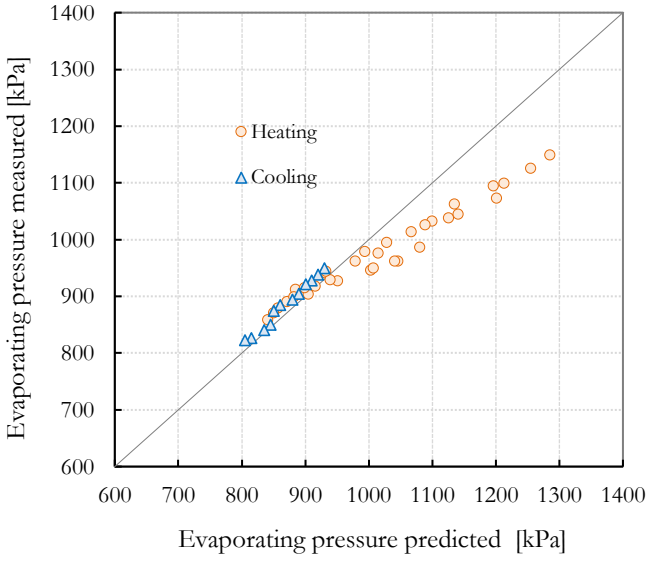

Figure 6.14 Comparison of the predicted and modeled results for evaporating pressure

These differences are probably caused by the inability of the expansion valve model to accurately predict the superheat temperature over the full range of conditions. Any error introduced in the computation of the superheat temperature directly influences the forecasted evaporation pressure.

A comparison between the measured and predicted compressor discharge temperatures is presented in Figure 6.15. The agreement between the model and the experiments is very good in terms of cooling but shows some discrepancies during heating.

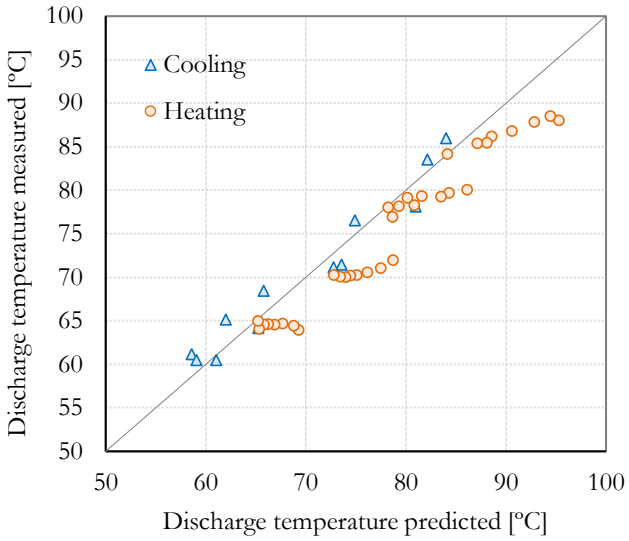

Figure 6.15 Comparison of the predicted and modeled results for discharge temperature

The data points located significantly away from the diagonal line represent cases with higher $T_{ws_{in}}$ values, indicating a high degree of superheating.

A rise in $T_{ws_{in}}$ is associated with an increased error in predicting the evaporation pressure, as indicated in Figure 6.14. This discrepancy adversely impacts the refrigerant mass flow rate forecast, consequently influencing the compressor's discharge temperature.

Figure 6.16 compares the experimentally measured degrees of superheat and those calculated using the model. In heating mode, the data present an RMSE of $\pm$0.54 °C, while it is $\pm$0.14 °C in the cooling mode.

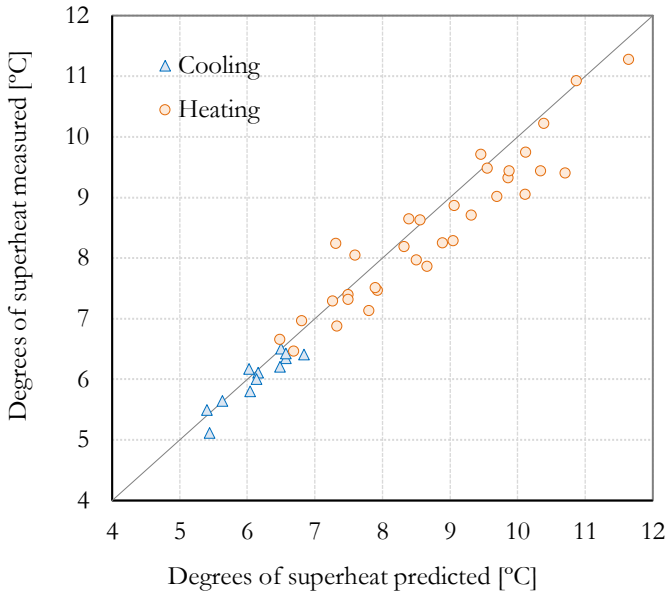

Figure 6.16 Comparison of the measured and modeled results for the degree of superheat

6.6.3 Non-operational conditions

One interesting feature of the present modeling approach is that it is possible to predict non-operational conditions, i.e., operating conditions that are not recommended. Two scenarios that lead to non-operational conditions are examined here. The first one is present in the heating mode, where the refrigerant leaving the condenser has not fully condensed and refrigerant vapor reaches the expansion valve's inlet, an unwanted condition. The second condition occurs in the cooling mode and is related to high subcooling, forcing the expansion valve to operate in the subcooled liquid zone without reaching the vapor–liquid zone.

The first scenario is examined, in Figure 6.17, for three mass flow rates of the secondary fluids. In each case, the same mass flow rate is employed at both the source and the load: 0.29, 0.44, and 0.57 L/s. The load temperature is held constant at 35 °C, while source temperatures equal to 5, 13, and 25 °C are used.

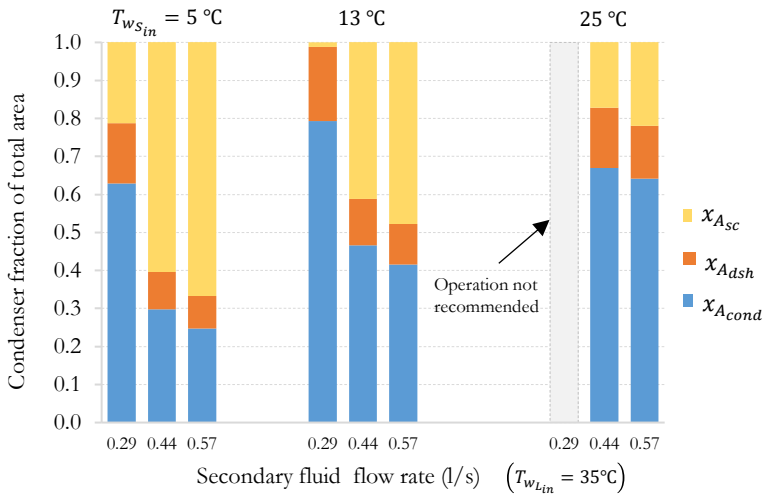

Figure 6.17 Non-operating conditions based on heat exchanger surface area fractions

The figure shows the fraction of the total heat exchanger (condenser) surface area utilized in each zone for desuperheating, $x_{A_{dsh}}$; condensation, $x_{A_{cond}}$; and subcooling $x_{A_{sc}}$. When examining Figure 6.17 with a focus on $T_{ws_{in}}$, it becomes clear that the proportion of the area allocated to condensation ($x_{A_{cond}}$) grows significantly as $T_{ws_{in}}$ rises. This phenomenon can be attributed to the increase in refrigerant density caused by a higher $T_{ws_{in}}$. Consequently, the mass flow rate from the compressor increases proportionally, resulting in an increased heat pump capacity. The value of $x_{A_{cond}}$ also increases drastically when the mass flow rate of the secondary fluids decreases. As illustrated in Figure 6.17, when considering a constant temperature, such as $T_{ws_{in}}$ = 13 °C, $x_{A_{cond}}$ changes from 0.4 at a flow rate of 0.57 L/s to 0.8 at a flow rate of 0.29 L/s. An analysis conducted at the pinch point (The point in a heat exchanger where the temperature discrepancy between the cold and hot fluids is at a minimum) results in a difference of 3 °C at high flow rates (0.57 L/s) but only 0.5 °C at low flow rates (0.27 L/s). This directly reduces the value of the $\Delta T_{lm_{cond}}$ in the zone, and, consequently, a larger heat transfer area is required for condensation.

Similarly, the portion of the surface area dedicated to desuperheating expands in proportion to the rising $T_{ws_{in}}$ temperature. This gradual expansion, however, leads to a diminishing amount of available surface area for subcooling .

It is clear that elevating the $T_{ws_{in}}$ and decreasing the $\dot{m}_w$ can result in an inadequate heat exchange surface area for subcooling. This observation is notable in the case of 0.29 L/s and $T_{ws_{in}}$ = 13 °C,

where the surface area fraction $x_{A_{sc}}$ is nearly negligible. Beyond this temperature, $x_{A_{sc}}$ reduces to zero, indicating that the refrigerant has not fully condensed, potentially causing issues with the expansion valve's operation. The prediction of $x_{A_{sc}} = 0$ is compared to the manufacturer's operating condition recommendations. This comparison with heating is shown in Table 6.5. As seen in these tables, the model can predict the operating conditions not recommended by the manufacturer.

Table 6.5 Heat pump's non-operational conditions, according to the manufacturer, in its heating mode.

Source		**Load (Cooling)**		**Manufacturer Recommendation**	**Prediction of $x_{A_{sc}} = 0$ by the Model**
EWT [°C]	**L/s**	**EWT [°C]**	**L/s**		
15.5	0.284 0.429 0.568	54.4	0.284	Operation not recommended	yes
21.1	0.284 0.429 0.568	54.4	0.284	Operation not recommended	yes
26.7	0.284 0.429 0.568	54.4	0.284	Operation not recommended	yes

A thermal expansion valve (TEV) is a crucial component in a refrigeration system. The main objectives of the TEV are to regulate the refrigerant's flow into the evaporator and maintain proper superheat. The thermal expansion valve typically operates in the liquid–vapor zone rather than the liquid–liquid zone. Operating a TEV in the liquid–liquid zone is generally not desirable. It might result in insufficient evaporation, leading to issues like liquid slugging (liquid entering the compressor), reduced system efficiency, and potential damage to the compressor. This situation is evaluated in the second scenario. Under typical conditions, the refrigerant enters as subcooled liquid and exits the expansion process with a certain vapor quality. Figure 6.18 shows the quality with which the refrigerant leaves the expansion valve before entering the evaporator for three constant temperatures of $T_{w_{S_{in}}}$: 10, 15, and 22 ℃. It can be observed that as the return temperature of the load, $T_{w_{L_{in}}}$, increases, the refrigerant quality tends towards zero, indicating that the TEV will operate in the liquid–liquid zone.

The prediction of a value equal to zero ($X_{evap} = 0$) is compared to the manufacturer's operating condition recommendations. This comparison for cooling is shown in Table 6.6. As seen in these tables, the model can predict the operating conditions not recommended by the manufacturer.

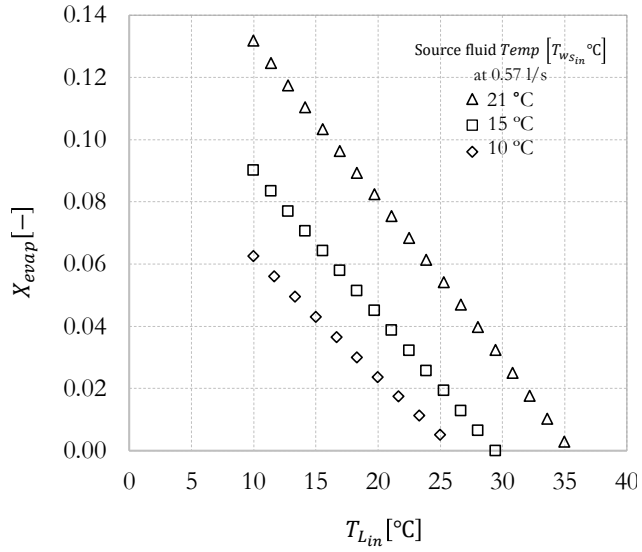

Figure 6.18 Non-operating conditions based on the quality of the refrigerant leaving the TEV

Table 6.6 Heat pump's non-operational conditions, according to the manufacturer, in its cooling mode.

Source		**Load (Cooling)**		**Manufacturer Recommendation**	**Prediction of $X_{evap} = 0$ by the Model**
EWT [°C]	**L/s**	**EWT [°C]**	**L/s**		
10	0.44	32	0.44	Operation not recommended	yes
			0.57		
	0.57	32	0.44		
			0.57		
15	0.29	32	0.44	Operation not recommended	yes
			0.57		
	0.44	32	0.44		
			0.57		
	0.57	32	0.44		
			0.57		
22	0.29	32	0.44	Operation not recommended	yes
			0.57		
	0.44	32	0.44		
			0.57		
	0.57	32	0.44		
			0.57		

6.7 Conclusions

This research introduces and provides experimental validation for a steady-state model of water-to-water heat pumps. The primary objective of the model is to estimate the heat pump's capacity (heating or cooling) and necessary compressor power, given the specified inlet conditions of the secondary fluids on both the load and source sides. The heat pump model includes a detailed

representation of the evaporator and condenser, which are both formed of plate heat exchangers. The fixed-speed scroll compressor is modeled using manufacturer performance maps, and a new semi-empirical model is introduced for the thermostatic expansion valve, accounting for the effects of condensing temperature on superheating prediction.

The assembly of sub-models for individual components results in a global model, leading to a set of nonlinear equations solved using an equation solver and appropriate guess values. The complexity of solving this model arises from the nonlinearity of the equations representing its thermodynamic and physical phenomena, coupled with the permissible operational conditions linked to the design of each component.

The validation of this model is carried out in an experimental test facility, utilizing precisely controlled secondary fluid loops for the secondary fluids' temperature and flow rate. The results demonstrate good agreement between the complete heat pump model predictions and experimental data in both the heating and cooling modes. The comparison includes power consumption, coefficients of performance (COPs), and various operational conditions such as evaporating and condensing temperatures, degrees of superheat, and compressor discharge temperatures.

In the assessed scenarios, the coefficient of performance (COP) ranges from 3.7 to 7.5 in the heating mode and 3.2 to 5.7 in the cooling mode. The COP can double when the temperature difference between the secondary fluids decreases from 35 °C to 10 °C. The model's COP predictions fall within the limits of experimental uncertainty in every case. It is also shown that an increase in the difference between the source and sink inlet temperatures leads to an increase in the required compressor power, and thus lower COPs. However, variations in the source inlet temperature have a relatively minor impact on the required compressor power.

Noted discrepancies between the model and experiments are likely due to the expansion valve model's limitations in precisely predicting the superheat temperature across all conditions. Any inaccuracies in calculating the superheat temperature directly affect the predicted evaporation pressure. This divergence is more noticeable at higher evaporator temperatures: at lower pressures, the absolute error is 10 kPa (with an experimental uncertainty of ±4 kPa at 800 kPa), and it escalates to 100 kPa at higher pressures (where the experimental uncertainty is ±6.5 kPa at 1300 kPa).

The model can predict cases where the surface area for subcooling vanishes to zero, indicating that the refrigerant has not fully condensed, potentially causing issues with the expansion valve's

operation. The predictions of these non-operational conditions match the manufacturer's recommendations.

The model validation was conducted based on specific parameters, including the heat pump's size and operational conditions. Further investigations are recommended for various sizes of heat pumps, along with experimental conditions that allow for the confirmation of non-operational scenarios and improvements to the proposed sub-model for the TEV.

The model has promising applications in various practical contexts. These include assessing the efficiency of new refrigerants, the sizing of plate heat exchangers, gathering performance data to develop performance maps for use in building energy simulation software, and predicting undesirable non-operational states, among others.

CHAPTER 7 GENERAL DISCUSSION

This thesis presented the modeling and validation of a water-to-water heat pump, emphasizing both fixed-speed and variable-speed compressors. This chapter synthesizes the key findings and contributions, highlighting the implications for the design and operation of efficient heat pump systems.

Traditional models for heat pumps often rely on simplifying assumptions that do not accurately reflect real-world conditions and can lead to inaccuracies. Common simplifications include assuming constant temperature differences in heat exchangers between the refrigerant and the secondary fluid, constant isentropic efficiency in compressors and ignoring phase changes variations in heat exchangers. These simplifications can result in significant deviations from actual performance, affecting both energy consumption predictions and system sizing.

The model presented in this thesis addresses limitations found in traditional simplified models. Unlike conventional models that fix either the degrees of superheat or the degrees of subcooling, this approach calculates the refrigerant operating conditions and performance based on secondary fluid inlet conditions (temperature and mass flow). Thus, the degrees of subcooling and superheat are part of the outcome of the model. In addition, the model calculates iteratively the heat exchanger surface area used in various refrigerant phases. Furthermore, it includes an adaptive expansion valve model allowing the mass flow rate of refrigerant to be adapted as a function of the pressure ratio and evaporator pressure. This model offers enhanced performance mapping creation and it could be used for the evaluation of new refrigerants.

Chapter 4 explores the potential improvements in heat pump performance through three distinct studies. The first study investigates the implementation of an intermediate heat exchanger between the condenser and the evaporator. It is shown that the efficiency gains from intermediate heat exchangers depend significantly on the refrigerant and the system's operational parameters. Under ideal conditions with constant mass flow rates, refrigerants like R410A and R134a show substantial capacity increases. However, when temperature effects on compressor suction density and on refrigerant flow rate are considered, the efficiency gains are marginal.

The second investigation focuses on the adoption of an expander or expansion turbine to replace the traditional expansion valve between the condenser and evaporator to generate work. The study finds that using an expander can improve the COP of a heat pump by 6% to 13%, depending on

the refrigerant used. R410A exhibits the highest increase in COP, but the benefits diminish with higher degrees of subcooling.

The third analysis compares the efficiency and performance of variable-speed compressors (VSC) against fixed-speed parallel multi-compressors (MC). The study shows that MC systems, involving compressors of different capacities piped in parallel, can improve the seasonal performance factor (SPF) by about 12%. VSCs offer an additional 8% improvement in SPF over MC systems. VSCs demonstrate superior adaptability and efficiency at varying thermal loads, eliminating the need for auxiliary heating and achieving a more consistent and higher COP across a broader range of temperatures.

Chapter 5 presents a detailed examination of a variable-speed water-to-water heat pump model tailored for ground-source applications. The model requires five inputs: the inlet temperature and mass flow rate of both secondary fluids and the compressor speed. Outputs include capacity and power consumption. The model shows that capacity varies linearly with frequency, while the COP curves exhibit a maximum value that does not necessarily coincide with full capacity and change as a function of frequency and operational conditions.

The implementation of the complete model in annual simulations was not feasible for long simulations due to convergence problems associated with large changes in inlet conditions from one time step to the next. Instead, a performance map approach was implemented in a TRNSYS Type which was modified by incorporating a minimum speed of operation and a more accurate representation of power consumption at part load. This approach produced good results in long-term simulations, with maximum errors of 2.5% for heating capacity and 5.1% for power when compared to the complete model. The model was used in annual simulations of a variable-speed heat pump operating with a ground heat exchanger for a residential building in a heating-dominated climate. It was shown that the classic curve of energy coverage versus effect coverage is similar the one experienced for fixed-speed heat pumps.

Chapter 6 introduces a steady-state model of a water-to-water heat pump with experimental validation. The model aims to predict the capacity and required compressor power based on the inlet conditions of the secondary fluids in the evaporator and condenser. Detailed manufacturer performance maps are used to model the fixed-speed scroll compressor, and a new semi-empirical model for the thermostatic expansion valve is introduced. The validation was conducted in an

experimental test facility with controlled secondary fluid loops, showing good agreement between model predictions and experimental data. The model accurately predicted power consumption, COPs, and various operational conditions such as evaporating and condensing temperatures, degrees of superheat, and compressor discharge temperatures.

The results show that the COP can range from 3.7 to 7.5 in heating mode and from 3.2 to 5.7 in cooling mode. The COP doubles when the temperature difference between the secondary fluids decreases from 35 °C to 10 °C. Discrepancies between the model and experiments are attributed to the limitations of the expansion valve model in predicting superheat temperature. The model's predictions of non-operational conditions align with manufacturer recommendations, highlighting its robustness.

As a complement to Chapter 6, Appendix B presents a methodology to experimentally derive overall heat transfer coefficients for the condenser and evaporator. The determination of these coefficients, based on experimental measurements on the heat pump, simplifies the calculations involved in the heat pump model. Comparative analysis between the complete model and the simplified model shows that the simplified model can predict the heating COP within 10% of the complete model, reducing computation time by 50% and improving solver stability during long-term simulations.

In conclusion, the development of this comprehensive, experimentally validated model represents a significant advancement in the understanding of water-to-water heat pump systems. The model's accuracy, efficiency, and versatility make it a valuable tool for improving the design, operation, and performance of heat pumps.

CHAPTER 8 CONCLUSION AND RECOMMENDATIONS FOR FUTURE WORK

This thesis presents a comprehensive model for water-to-water heat pumps, emphasizing both fixed-speed and variable-speed compressors, which significantly advances the understanding and of these systems. The key contributions and findings of this research are as follows:

- Improved accuracy in predictions: The model addresses limitations found in traditional simplified models by calculating refrigerant operating conditions based on secondary fluid inlet conditions. This approach enhances the accuracy of predictions related to energy consumption and system sizing, incorporating detailed considerations such as evaporator superheat, vapor quality, and refrigerant density at compressor suction.
- Performance enhancements through new technologies: The implementation of intermediate heat exchangers, expanders, and variable-speed compressors (VSC) shows possible improvements in heat pump efficiency. Intermediate heat exchangers increase capacity depending on refrigerant and operational parameters, expanders boost the COP by utilizing pressure differences to produce work, and VSCs improve the seasonal performance factor by adapting to varying thermal loads.
- Comprehensive model implementation: The model includes an adaptive expansion valve that adjusts the mass flow rate of refrigerant and heat exchanger models that predict separate heat exchange area for desuperheating, condensation, subcooling, evaporation and superheating.
- Experimental data: There are very few experimental results on water-to-water heat pumps in the literature. This work attempted to alleviate this deficiency. The experimental validation demonstrated good agreement between model predictions and experimental data, accurately predicting power consumption, COPs, and various operational conditions.
- Prediction of non-operational states. The model's ability to predict non-operational states and undesirable conditions ensures reliable operation and helps prevent potential issues.
- Modifications to a TRNSYS Type: To address convergence problems in long-term simulations of variable speed heat pumps, a performance map approach based on the complete model was developed. This was achieved by modifying an existing TRNSYS type

to include a better representation of the minimum allowable speed and of part-load operation. This approach produced good results, with maximum errors of 2.5% for heating capacity and 5.1% for power, significantly improving computational speed and stability.

These contributions enable more accurate, efficient, and versatile thermal modeling of water-to-water heat pump systems, filling a critical gap in the scientific literature and supporting the development of more sustainable and energy-efficient HVAC solutions.

8.1 Thesis limitations and future research

One of the primary challenges of the model is its dependence on initial values for solving the system of nonlinear equations representing each component of the heat pump. During long-term simulations involving cooling, heating, and on/off cycles, the inputs related to secondary fluid variables, particularly temperature, can vary significantly from one time step to the next. This variability can cause the solver to encounter difficulties in evaluating the system of equations. While updating “manually” the guess values can generally resolve this issue, this approach is not feasible during annual simulations particularly when a ground heat exchanger is involved as this can result in the loss of ground thermal history.

From a component modeling perspective, several areas need further analysis:

Compressor model limitations: The reliability of the data provided by the manufacturer, which must adhere to AHRI 540 standards, limits the compressor's operation within its specified map. Hence the TRNSYS type developed for this study is for a particular compressor but it was assumed that the model could be scaled. In other words, the TRNSYS type could be scaled to simulate the performance of a 15 kW heat pump based on the compressor of a 10 kW heat pump. As reported in Chapter 5, preliminary calculations indicated that the performance of the selected compressor could be scaled to represent the power usage and capacity of compressors of the same family. However, a more thorough study to clearly demonstrate that scaling is possible is recommended.

Heat exchanger modeling: Although the model divides the heat exchanger into subzones (desuperheating, condensation, and subcooling in the condenser), it uses average heat transfer coefficients between the initial and final conditions of each zone. Other thermophysical properties are also averaged. The literature indicates that using generalized correlations for coefficient

calculations is challenging and typically involves a 10-20% error margin. This significantly affects heat transfer calculations in each zone. Verifying the impact of this issue can be achieved by calculating specific heat transfer coefficients for the plate heat exchanger used and performing a more detailed discretization of the exchanger to calculate thermophysical properties in each section accurately.

Expansion valve: Despite being adjusted based on experimental data, the expansion valve model's coefficients heavily depend on the integrated performance of the heat pump (compressor and heat exchangers). Consequently, new coefficient adjustments are necessary for scaling. Conducting this study with heat pumps of different sizes could provide a correlation that allows accurate scaling.

Addressing these limitations will advance the state of heat pump modeling, leading to more reliable and efficient HVAC systems.

REFERENCES

[1] EN-14511-1:2018, "Air conditioners, liquid chilling packages and heat pumps for space heating and cooling and process chillers, with electrically driven compressors.- Part 1: Terms and definitions," *Comite Europeen de Normalisation,* 2018.

[2] EN-14825:2016, "Air conditioners, liquid chilling packages and heat pumps, with electrically driven compressors, for space heating and cooling. Testing and rating at part load conditions and calculation of seasonal performance," *Comite Europeen de Normalisation,* 2016.

[3] AHRI-210/240:2008, "Standard for performance rating of unitary air-conditioning & air-source heat pump equipment," *Air-Conditioning, Heating, and Refrigeration Institute,* 2008.

[4] AHRI-340/360:2022, "Standard for performance rating of commercial and industrial unitary air-conditioning and heat pump equipment," *Air-Conditioning, Heating and Refrigeration Institute,* 2022.

[5] ISO-13256-1:2020, "Water-source heat pumps. Testing and rating for performance. Part 1. Water-to-air and brine-to-air heat pumps."

[6] ISO-13256-2:2020, "Water-source heat pumps. Testing and rating for performance. Part 2. Water-to-water and brine-to-water heat pumps."

[7] S. A. Klein, W. A. Beckman, J. W. Mitchell, J. A. Duffie, N. A. Duffie, T. L. Freeman*, et al.*, "TRNSYS 18: A Transient System Simulation Program," *Solar Energy Laboratory, University of Wisconsin, Madison, USA.,* 2017.

[8] EnergyPlus™, "Energy Simulation Software. U.S. Department of Energy. https://www.osti.gov/biblio/1395882," 2017.

[9] EES, "Engineering Equation Solver," *F-Chart Software. https://fchartsoftware.com/ees/,* vol. Version 11.755, 2024.

[10] Modelica, "Modelica Association– A Unified Object-Oriented Language for Systems Modeling. https://modelica.org/," 2021.

[11] H. Jouhara, A. Żabnieńska-Góra, B. Delpech, V. Olabi, T. El Samad, and A. Sayma, "High-temperature heat pumps: Fundamentals, modelling approaches and applications," *Energy,* vol. 303, p. 131882, 2024.

[12] B. Shen, Z. Li, and K. R. Gluesenkamp, "Experimental study of R452B and R454B as drop-in replacement for R410A in split heat pumps having tube-fin and microchannel heat exchangers," *Applied Thermal Engineering,* vol. 204, p. 117930, 2022.

[13] K. Thu, K. Takezato, N. Takata, T. Miyazaki, and Y. Higashi, "Drop-in experiments and exergy assessment of HFC-32/HFO-1234yf/R744 mixture with GWP below 150 for domestic heat pumps," *International Journal of Refrigeration,* vol. 121, pp. 289-301, 2021.

[14] J. Sieres, I. Ortega, F. Cerdeira, and E. Álvarez, "Drop-in performance of the low-GWP alternative refrigerants R452B and R454B in an R410A liquid-to-water heat pump," *Applied Thermal Engineering,* vol. 182, p. 116049, 2021.

[15] I. H. Bell, P. A. Domanski, M. O. McLinden, and G. T. Linteris, "The hunt for nonflammable refrigerant blends to replace R-134a," *International Journal of Refrigeration,* vol. 104, pp. 484-495, 2019.

[16] P. Eslami-Nejad, A. Nguyen, M. Cimmino, A. Bastani, and M. Badache, "Performance comparison of a vertical direct expansion geothermal evaporator: Part I, single U-pipe using different refrigerants," *International Journal of Refrigeration,* vol. 116, pp. 119-128, 2020.

[17] B. T. Austin and K. Sumathy, "Parametric study on the performance of a direct-expansion geothermal heat pump using carbon dioxide," *Applied Thermal Engineering,* vol. 31, pp. 3774-3782, 2011.

[18] M. Badache, P. Eslami-Nejad, A. Bastani, Z. Aidoun, and A. Nguyen, "Theoretical and experimental analysis of a vertical direct expansion geothermal evaporator using CO2 as refrigerant," *Science and Technology for the Built Environment,* vol. 25, pp. 1081-1094, 2019.

[19] M. Badache, Z. Aidoun, and F. Manneh, "A CO2 geothermal thermosiphon to preheat supply air for ventilation heat recovery systems in cold climates," *Geothermics,* vol. 119, p. 102922, 2024.

[20] M. Badache, Z. Aidoun, P. Eslami-Nejad, and D. Blessent, "Ground-Coupled Natural Circulating Devices (Thermosiphons): A Review of Modeling, Experimental and Development Studies," *Inventions,* vol. 4, p. 14, 2019.

[21] A. Wagner, "Review of Thermosyphon Applications," *The US Army Engineer Research and Development Center: Hanover, NH, USA ERDC/CRREL-TR-14-1.,* 2014.

[22] C. Arpagaus, F. Bless, M. Uhlmann, J. Schiffmann, and S. S. Bertsch, "High temperature heat pumps: Market overview, state of the art, research status, refrigerants, and application potentials," *Energy,* vol. 152, pp. 985-1010, 2018.

[23] J. Kim, S. Park, Y. Baik, K. Chang, H. Ra, M. Kim, *et al.*, "Experimental study of operating characteristics of compression/absorption high-temperature hybrid heat pump using waste heat," *Renewable Energy,* vol. 54, pp. 13-19, 2013.

[24] M. Kim, Y. Baik, S. Park, K. Chang, and H. Ra, "Design of a high temperature production heat pump system using geothermal water at moderate temperature," *Current Applied Physics,* vol. 10, pp. S117-S122, 2010.

[25] T. Ommen, J. Jensen, W. Markussen, L. Reinholdt, and B. Elmegaard, "Technical and economic working domains of industrial heat pumps: Part 1 – Single stage vapour compression heat pumps," *International Journal of Refrigeration,* vol. 55, pp. 168-182, 2015.

[26] O. Bamigbetan, T. Eikevik, P. Nekså, and M. Bantle, "Review of vapour compression heat pumps for high temperature heating using natural working fluids," *International Journal of Refrigeration,* vol. 80, pp. 197-211, 2017.

[27] M. Konrad and B. MacDonald, "Cold climate air source heat pumps: Industry progress and thermodynamic analysis of market-available residential units," *Renewable and Sustainable Energy Reviews,* vol. 188, p. 113739, 2023.

[28] A. Redón, E. Navarro-Peris, M. Pitarch, J. Gonzálvez-Macia, and J. M. Corberán, "Analysis and optimization of subcritical two-stage vapor injection heat pump systems," *Applied Energy,* vol. 124, pp. 231-240, 2014.

[29] K. Qiu and M. Thomas, "Modeling and optimization of two-stage compression heat pump system for cold climate applications," *Journal of Building Engineering,* vol. 82, p. 108407, 2024.

[30] R. Radermacher and Y. Hwang, *Vapor Compression Heat Pumps with Refrigerant Mixtures*: CRC Press: Boca Raton, FL, USA, 2005.

[31] G. Viviescas, S. Houaida, M. Bernier, and M. Kummert, "Energy performance advantages of using multiple compressors in a heat pump operating in heating mode," *eSim 2021 - IBPSA-Canada conference,* 2021.

[32] J. A. Sumner, "Domestic Heat Pumps," *Prism Press London,* 1976.

[33] B. C. Langley, "Heat Pump Technology," *Prentice Hall,* 2002.

[34] J. M. Corberán, D. Donadello, I. Martínez-Galván, and C. Montagud, "Partialization losses of ON/OFF operation of water-to-water refrigeration/heat-pump units," *International Journal of Refrigeration,* vol. 36, pp. 2251-2261, 2013.

[35] H. Henderson, D. Parker, and Y. Huang, "Improving DOE2's RESYS routine: User defined functions to provide more accurate part load energy use and humidity predictions," *Proceedings ACEEE Summer Study on Energy Efficiency in Buildings,* 2000.

[36] W. H. Parken, R. W. Beausoliel, and G. E. Kelly, "Factors Affecting the Performance of a Residential Airto-Air Heat Pump," *ASHRAE Transactions. 83(1), 839-849,* 1977.

[37] L. Cecchinato, M. Chiarello, and M. Corradi, "A simplified method to evaluate the seasonal energy performance of water chillers," *International Journal of Thermal Sciences,* vol. 49, pp. 1776-1786, 2010.

[38] M. Dongellini, C. Naldi, and G. L. Morini, "Seasonal performance evaluation of electric air-to-water heat pump systems," *Applied Thermal Engineering,* vol. 90, pp. 1072-1081, 2015.

[39] L. Schibuola, "Heat pump seasonal performance evaluation: a proposal for a European standard," *Applied Thermal Engineering,* vol. 20, pp. 387-398., 2000.

[40] Bettanini E, Gastaldello A, and S. L., "Simplified models to simulate part load performances of air conditioning equipments," *8th international IBPSA conference, Eindhoven, Netherland,* 2003.

[41] UNI-10963, "Air conditioners, water chilling packages and heat pumps. Calculation of the seasonal efficiency.," *UNI standard,* 2001.

[42] E. Fuentes, D. A. Waddicor, and J. Salom, "Improvements in the characterization of the efficiency degradation of water-to-water heat pumps under cyclic conditions," *Applied Energy,* vol. 179, pp. 778-789, 2016.

[43] C. Park, H. Lee, Y. Hwang, and R. Radermacher, "Recent advances in vapor compression cycle technologies," *International Journal of Refrigeration,* vol. 60, pp. 118-134, 2015.

[44] E. Hervas-Blasco, M. Pitarch, E. Navarro-Peris, and J. M. Corberan, "Study of different subcooling control strategies in order to enhance the performance of a heat pump," *International Journal of Refrigeration,* vol. 88, pp. 324-36, 2018.

[45] J. Jensen and S. Skogestad, "Optimal operation of simple refrigeration cycles: Part II: Selection of controlled variables," *Computers & Chemical Engineering,* vol. 31, pp. 1590-1601, 2007.

[46] M. Pitarch, E. Hervas-Blasco, E. Navarro-Peris, J. Gonzalvez-Macia, and J. M. Corberan, "Evaluation of optimal subcooling in subcritical heat pump systems," *International Journal of Refrigeration,* vol. 78, pp. 18-31, 2017.

[47] A. S. Dalkilic and S. Wongwises, "A performance comparison of vapour-compression refrigeration system using various alternative refrigerants," *International Communications in Heat and Mass Transfer,* vol. 37, pp. 1340-1349, 2010.

[48] Y. Min-Hsiung and Y. Rong-Hua, "Performance and exergy destruction analyses of optimal subcooling for vapor-compression refrigeration systems," *International Journal of Heat and Mass Transfer,* vol. 87, pp. 1-10, 2015.

[49] P. A. Domanski, D. A. Didion, and J. P. Doyle, "Evaluation of suction-line/liquid-line heat exchange in the refrigeration cycle," *International Journal of Refrigeration,* vol. 17, pp. 487-493, 1994.

[50] S. A. Klein, D. T. Reindl, and K. Brownell, "Refrigeration system performance using liquid-suction heat exchangers," *International Journal of Refrigeration,* vol. 23, pp. 588-596, 2000.

[51] G. Pottker and P. Hrnjak, "Experimental investigation of the effect of condenser subcooling in R134a and R1234yf air-conditioning systems with and without internal heat exchanger," *International Journal of Refrigeration,* vol. 50, pp. 104-113, 2015.

[52] Y. Wang, Z. Ye, X. Yin, Y. Song, and F. Cao, "Energy, exergy and exergoeconomic evaluation of the air source transcritical CO2 heat pump with internal heat exchanger for space heating," *International Journal of Refrigeration,* vol. 130, pp. 14-26, 2021.

[53] R. Otón-Martínez, F. Illán-Gómez, J. García-Cascales, F. J. S. Velasco, and M. Reda, "Impact of an internal heat exchanger on a transcritical CO2 heat pump under optimal pressure conditions: Optimal-pressure performance of CO2 heat pump with IHX," *Applied Thermal Engineering,* vol. 215, p. 118991, 2022.

[54] D. Sánchez, R. Larrondo, F. Vidan-Falomir, and R. Cabello, "Experimental evaluation of the CO2-based mixtures CO2/R32, CO2/R1234yf and CO2/R1270 in a transcritical refrigerating plant considering the effect of the internal heat exchanger (IHX)," *Applied Thermal Engineering,* vol. 236, p. 121473, 2024.

[55] J. W. Thornton, S. A. Klein, and J. W. Mitchell, "Dedicated mechanical subcooling design strategies for supermarket applications," *International Journal of Refrigeration,* vol. 17, pp. 508-515, 1994.

[56] N. Solanki, A. Arora, and R. Singh, "A comprehensive parametric and structural bond analysis of an actual vapor compression refrigeration system with dedicated mechanical

subcooled system," *Journal of Mechanical Science and Technology,* vol. 38, pp. 439-452, 2024.

[57] J. Khan and S. M. Zubair, "Design and rating of an integrated mechanical-subcooling vapor-compression refrigeration system," *Energy Conversion and Management,* vol. 41, pp. 1201-1222, 2000.

[58] Á. Casi, P. Aranguren, D. Sanchez, M. Araiz, R. Cabello, and D. Astrain, "Experimental validation and development of an advanced computational model of a transcritical carbon dioxide vapour compression cycle with a thermoelectric subcooling system," *Applied Thermal Engineering,* vol. 206, p. 118045, 2022.

[59] D. Sánchez, P. Aranguren, A. Casi, R. Llopis, R. Cabello, and D. Astrain, "Experimental enhancement of a CO2 transcritical refrigerating plant including thermoelectric subcooling," *International Journal of Refrigeration,* vol. 120, pp. 178-187, 2020.

[60] D. Astrain, A. Merino, L. Catalán, P. Aranguren, M. Araiz, D. Sánchez, *et al.*, "Improvements in the cooling capacity and the COP of a transcritical CO2 refrigeration plant operating with a thermoelectric subcooling system," *Applied Thermal Engineering,* vol. 155, pp. 110-122, 2019.

[61] P. Aranguren, D. Sánchez, A. Casi, R. Cabello, and D. Astrain, "Experimental assessment of a thermoelectric subcooler included in a transcritical CO2 refrigeration plant," *Applied Thermal Engineering,* vol. 190, p. 116826, 2021.

[62] A. D. Chiasson, "Geothermal Energy," in *Geothermal Heat Pump and Heat Engine Systems: Theory and Practice*, ed: ASME-Wiley, 2016.

[63] R. Barta, D. Ziviani, and E. Groll, "Experimental analyses of different control strategies of an R-410A split-system heat pump by employing a turbomachinery expansion recovery device," *International Journal of Refrigeration,* vol. 112, pp. 189-200, 2020.

[64] A. A. Murthy, S. Norris, and A. Subiantoro, "Performance of a four-intersecting-vane expander in a R134a refrigeration cycle," *Applied Thermal Engineering,* vol. 209, p. 118244, 2022.

[65] H. J. Huff, D. Lindsay, and R. Radermacher, "Positive Displacement Compressor And Expander Simulation," *International Compressor Engineering Conference. Paper 1527.*, 2002.

[66] J. Nickl, G. Will, H. Quack, and W. E. Kraus, "Integration of a three-stage expander into a CO2 refrigeration system," *International Journal of Refrigeration,* vol. 28, pp. 1219-1224, 2005.

[67] O. Dumont, A. Parthoens, R. Dickes, and V. Lemort, "Experimental investigation and optimal performance assessment of four volumetric expanders (scroll, screw, piston and roots) tested in a small-scale organic Rankine cycle system," *Energy,* vol. 165, pp. 1119-1127, 2018.

[68] K. Ameur and Z. Aidoun, "Two-phase ejector enhanced carbon dioxide transcritical heat pump for cold climate," *Energy Conversion and Management,* vol. 243, p. 114421, 2021.

[69] G. Pottker and P. Hrnjak, "Ejector in R410A vapor compression systems with experimental quantification of two major mechanisms of performance improvement: Work recovery and liquid feeding," *International Journal of Refrigeration,* vol. 50, pp. 184-192, 2015.

[70] S. Barbouchi, "High temperature air to water heat pump for the refurbishing of heating systems in existing buildings. Pompe à chaleur haute température pour la réhabilitation des systèmes de chauffage dans le résidentiel," thèse de doctorat, École nationale supérieure des mines de Paris, 2007.

[71] S. H. Lee, Y. Jeon, B. Kim, S. Yun, and Y. Kim, "Simulation-based comparative seasonal performance evaluation of single-stage heat pump and modulated two-stage injection heat pump using rotary compressors with various cylinder volume ratios," *Applied Thermal Engineering,* vol. 159, p. 113892, 2019.

[72] K. J. Chua, S. K. Chou, and W. M. Yang, "Advances in heat pump systems: A review," *Applied Energy,* vol. 87, pp. 3611-3624, 2010.

[73] H. W. Jung, H. Kang, W. J. Yoon, and Y. Kim, "Performance comparison between a single-stage and a cascade multi-functional heat pump for both air heating and hot water supply," *International Journal of Refrigeration,* vol. 36, pp. 1431-1441, 2013.

[74] N. Agrawal and S. Bhattacharyya, "Studies on a two-stage transcritical carbon dioxide heat pump cycle with flash intercooling," *Applied Thermal Engineering,* vol. 27, pp. 299-305, 2007.

[75] C. Arpagaus, F. Bless, J. Schiffmann, and S. Bertsch, "Multi-temperature heat pumps: A literature review," *International Journal of Refrigeration,* vol. 69, pp. 437-465, 2016.

[76] S. Bertsch and E. Groll, "Two-stage air-source heat pump for residential heating and cooling applications in northern U.S. climates," *International Journal of Refrigeration,* vol. 31, pp. 1282-1292, 2008.

[77] L. Chen, J. Li, F. Sun, and F. Wu, "Performance optimization for a two-stage thermoelectric heat-pump with internal and external irreversibilities," *Applied Energy,* vol. 85, pp. 641-649, 2008.

[78] S. Jiang, S. Wang, X. Jin, and T. Zhang, "A general model for two-stage vapor compression heat pump systems," *International Journal of Refrigeration,* vol. 51, pp. 88-102, 2015.

[79] G. Wang, Z. Chen, C. Li, and B. Jiang, "Preliminary theoretical analyses of thermal performance and available energy consumption of two-stage cascade cycle heat pump water heater," *International Journal of Refrigeration,* vol. 82, pp. 381-388, 2017.

[80] S. T. Inampudi and S. Elbel, "Experimental comparison and seasonal performance evaluation of different scroll compressor capacity modulation methods in an R410A water to water system," *Applied Thermal Engineering,* vol. 247, p. 123033, 2024.

[81] B. Shen, O. Abdelaziz, V. Baxter, and E. Vineyard, "Cold Climate Heat Pump Using Tandem Vapor-Injection Compressors. ," *Cold Climate HVAC. Kiruna, Sweden,* pp. 429-439, 12-15 March 2018.

[82] B. Shen, O. Abdelaziz, K. Rice, and V. Baxter, "Field Investigation of an Air-Source Cold Climate Heat Pump. ," *12th IEA Heat Pump Conference. Rotterdam, Netherlands,* 2017.

[83] B. Hu, S. Xu, R. Z. Wang, H. Liu, L. Han, Z. Zhang, *et al.*, "Investigation on advanced heat pump systems with improved energy efficiency," *Energy Conversion and Management,* vol. 192, pp. 161-170, 2019.

[84] C. Arpagaus, F. Bless, S. Bertsch, A. Javed, and J. Schiffmann, "Heat Pump driven by a Small-Scale Oil-Free Turbocompressor – System Design and Simulation," *12th IEA Heat Pump Conference. Rotterdam, Netherlands,* May 14-18 2017.

[85] J. Schiffmann, "Small-Scale and Oil-Free Turbocompressor for Refrigeration Application," *International Compressor Engineering Conference. Purdue. Paper 2354,* July 14-17 2014.

[86] G. Viviescas and M. Bernier, "A Water-to-Water Heat Pump Model with Experimental Validation," *Energies,* vol. 17, p. 1858, 2024.

[87] A. Heinz, W. Lerch, and R. Heimrath, "Heat pump condenser and desuperheater integrated into a storage tank: Model development and comparison with measurements," *Applied Thermal Engineering,* vol. 102, pp. 465-475, 2016.

[88] S. Bordignon, G. Emmi, A. Zarrella, and M. De Carli, "Energy analysis of different configurations for a reversible ground source heat pump using a new flexible TRNSYS Type," *Applied Thermal Engineering,* vol. 197, p. 117413, 2021.

[89] A. Mbaye and M. Cimmino, "Variable refrigerant flow heat pump model with estimated parameters and emulated controller based on manufacturer data," *Science and Technology for the Built Environment,* vol. 30, pp. 341-358, 2024.

[90] O. Sarfraz, C. K. Bach, and C. R. Bradshaw, "A Literature Review of Numerical Modeling Techniques for Vapor Compression Systems with Focus on Heat Exchanger Modeling," *International Refrigeration and Air Conditioning Conference. West Lafayette, USA. July Paper 1966,* 2018.

[91] G. A. Longo, C. Zilio, G. Righetti, and J. S. Brown, "Condensation of the low GWP refrigerant HFO1234ze(E) inside a brazed plate heat exchanger," *International Journal of Refrigeration,* vol. 38, pp. 250-259, 2014.

[92] T. B. Herbas, E. C. Berlinck, C. A. T. Uriu, R. P. Marques, and J. A. R. Parise, "Steady-state simulation of vapour-compression heat pumps," *International Journal of Energy Research,* vol. 17, pp. 801-816, 1993.

[93] M. L. Martins Costa and J. A. R. Parise, "A three-zone simulation model for a air-cooled condensers," *Heat Recovery Systems and CHP,* vol. 13, pp. 97-113, 1993.

[94] Y. Chen and Q. Yang, "A new moving-boundary algorithm to predict heat transfer rate of counter-flow water-cooled transcritical CO2 gas cooler," *International Journal of Refrigeration,* vol. 146, pp. 357-365, 2023.

[95] Y. T. Ge and R. Cropper, "Performance evaluations of air-cooled condensers using pure and mixture refrigerants by four-section lumped modelling methods," *Applied Thermal Engineering,* vol. 25, pp. 1549-1564, 2005.

[96] J. Judge and R. Radermacher, "A heat exchanger model for mixtures and pure refrigerant cycle simulations," *International Journal of Refrigeration,* vol. 20, pp. 244-255, 1997.

[97] S. Gholamrezaie, M. Cimmino, and P. Eslami-Nejad, "Heating and cooling of an office building using distributed heat pumps connected to a two-phase CO2 thermal management

system: Detailed simulation.,". eSim Building Performance Simulation Conference. Edmonton, Canada, June 5-7 2024.

[98] D. Sánchez, R. Cabello, R. Llopis, and E. Torrella, "Development and validation of a finite element model for water – CO2 coaxial gas-coolers," *Applied Energy,* vol. 93, pp. 637-647, 2012.

[99] B. J. Dechesne and V. Lemort, "Modeling and experimental results of a residential heat pump with vapor injection and variable speed scroll compressor," *Proceedings of the REHVA Annual Meeting Conference,* 23 April 2018. Brussels, Belgium. 2018.

[100] P. Byrne, R. Ghoubali, and J. Miriel, "Scroll compressor modelling for heat pumps using hydrocarbons as refrigerants," *International Journal of Refrigeration,* vol. 41, pp. 1-13, 2014.

[101] E. Winandy, C. Saavedra, and J. Lebrun, "Experimental analysis and simplified modelling of a hermetic scroll refrigeration compressor," *Applied Thermal Engineering,* vol. 22, pp. 107-120, 2002.

[102] H. Cheung and J. E. Braun, "Simulation of fault impacts for vapor compression systems by inverse modeling. Part I: Component modeling and validation," *HVAC&R Research,* vol. 19, pp. 892-906, 2013.

[103] D. Ndiaye and M. Bernier, "Modelling the bleed port of a thermostatic expansion valve," *International Journal of Refrigeration,* vol. 32, pp. 826-836, 2009.

[104] M. R. Conde and P. Suter, "A mathematical simulation model for thermostatic expansion valves," *Heat Recovery Systems and CHP,* vol. 12, pp. 271-282, 1992.

[105] I. Eames, A. Milazzo, and G. Maidment, "Modelling thermostatic expansion valves," *International Journal of Refrigeration,* vol. 38, pp. 189-197, 2014.

[106] A. Behfar and D. Yuill, "Evaluation of gray box thermostatic expansion valve mass flow models," *International Journal of Refrigeration,* vol. 96, pp. 161-168, 2018.

[107] B. Palm and J. Claesson, "Plate Heat Exchangers: Calculation Methods for Single and Two-Phase Flow," *Heat Transfer Engineering,* vol. 27, pp. 88-98, 2006.

[108] Z. H. Ayub, "Plate Heat Exchanger Literature Survey and New Heat Transfer and Pressure Drop Correlations for Refrigerant Evaporators," *Heat Transfer Engineering,* vol. 24, pp. 3-16, 2003.

[109] R. A. Troupe, J. C. Morgan, and J. Prifiti, "The Plate Heater Versatile Chemical Engineering Tool," *Chemical Engineering Progress,* vol. 56, pp. 124-128, 1960.

[110] A. Muley and R. M. Manglik, "Experimental Study of Turbulent Flow Heat Transfer and Pressure Drop in a Plate Heat Exchanger With Chevron Plates," *Journal of Heat Transfer,* vol. 121, pp. 110-117, 1999.

[111] H. Kumar, "The Plate Heat Exchanger: Construction and Design," *Institute of Chemical Engineering Symposium Series,* vol. 86, pp. 1275-1288, 1984.

[112] B. Thonon, "Design Method for Plate Evaporators and Condensers," *1st International Conference on Process Intensification for the Chemical Industry.* , vol. 18, pp. 37-47, 1995.

[113] A. Wanniarachchi, U. Ratnam, E. Tilton, and K. Dutta-Roy, "Approximate correlations for chevron-type plate heat exchangers," *30th National Heat Transfer Conference,* vol. 12, pp. 145-151, 1995.

[114] J. Marriott, "Where and How to Use Plate Heat Exchangers," *Chemical Engineering Progress,* vol. 78, pp. 127-134, 1971.

[115] K. Okada, M. Ono, T. Tomimura, T. Okuma, H. Konno, and S. Ohtani, "Design and heat transfer characteristics of new plate heat exchanger," *Heat Transfer - Japanese Research,* vol. 1, pp. 90-95, 1972.

[116] W. Roetzel, S. K. Das, and X. Luo, "Measurement of the heat transfer coefficient in plate heat exchangers using a temperature oscillation technique," *International Journal of Heat and Mass Transfer,* vol. 37, pp. 325-331, 1994.

[117] A. C. Talik, L. S. Fletcher, A. N. K., and L. Swanson, "Heat Transfer and Pressure Drop Characteristics of a Plate Heat Exchanger," *Proceedings of the ASME/JSME Thermal Engineering Conference ASME New York,* vol. 4, pp. 321-329, 1995.

[118] M. B. Kim and C. Y. Park, "An experimental study on single phase convection heat transfer and pressure drop in two brazed plate heat exchangers with different chevron shapes and hydraulic diameters," *Journal of Mechanical Science and Technology,* vol. 31, pp. 2559-2571, 2017.

[119] G. Cattelan, A. Diani, and M. Azzolin, "Condensation heat transfer of R1234ze(E) and R134a inside a brazed plate heat exchanger: Experimental data and model assessment," *International Journal of Refrigeration,* vol. 143, pp. 57-67, 2022.

[120] Y. Yan, H. Lio, and T. Lin, "Condensation heat transfer and pressure drop of refrigerant R-134a in a plate heat exchanger," *International Journal of Heat and Mass Transfer,* vol. 42, pp. 993-1006, 1999.

[121] M. G. Cooper, "Heat Flow Rates in Saturated Nucleate Pool Boiling-A Wide-Ranging Examination Using Reduced Properties," in *Advances in Heat Transfer*, ed: Elsevier, 1984, pp. 157-239.

[122] A. Jokar, M. H. Hosni, and S. J. Eckels, "Dimensional analysis on the evaporation and condensation of refrigerant R-134a in minichannel plate heat exchangers," *Applied Thermal Engineering,* vol. 26, pp. 2287-2300, 2006.

[123] J. Park and Y. Kim, "Evaporation heat transfer and pressure drop characteristics of r-134a in the oblong shell and plate heat exchanger," *KSME International Journal,* vol. 18, pp. 2284-2293, 2004.

[124] Z. H. Ayub, T. S. Khan, S. Salam, K. Nawaz, A. H. Ayub, and M. S. Khan, "Literature survey and a universal evaporation correlation for plate type heat exchangers," *International Journal of Refrigeration,* vol. 99, pp. 408-418, 2019.

[125] O. Kwon, J. Jung, and Y. Kang, "Development of experimental Nusselt number and friction factor correlations for condensation of R-1233zd(E) in plate heat exchangers," *International Journal of Heat and Mass Transfer,* vol. 158, p. 120008, 2020.

[126] S. Mancin, D. Del Col, and L. Rossetto, "Condensation of superheated vapour of R410A and R407C inside plate heat exchangers: Experimental results and simulation procedure," *International Journal of Refrigeration,* vol. 35, pp. 2003-2013, 2012.

[127] S. Mancin, D. Del Col, and L. Rossetto, "Partial condensation of R407C and R410A refrigerants inside a plate heat exchanger," *Experimental Thermal and Fluid Science,* vol. 36, pp. 149-157, 2012.

[128] AHRI, "National standard CAN / ANSI / AHRI 540-2020 Performance Rating of Positive Displacement Refrigerant Compressors," 2020.

[129] J. Ahamed, R. Saidur, and H. Masjuki, "A review on exergy analysis of vapor compression refrigeration system," *Renewable and Sustainable Energy Reviews,* vol. 15, pp. 1593-1600, 2011.

[130] M. Pitarch, E. Hervas-Blasco, E. Navarro-Peris, and J. M. Corberán, "Exergy analysis on a heat pump working between a heat sink and a heat source of finite heat capacity rate," *International Journal of Refrigeration,* vol. 99, pp. 337-350, 2019.

[131] S. Elbel and N. Lawrence, "Review of recent developments in advanced ejector technology," *International Journal of Refrigeration,* vol. 62, pp. 1-18, 2016.

[132] G. Besagni, R. Mereu, and F. Inzoli, "Ejector refrigeration: A comprehensive review," *Renewable and Sustainable Energy Reviews,* vol. 53, pp. 373-407, 2016.

[133] R. Barta, S. Florian, and G. Eckhard, "Experimental Analysis and Design Improvements on Combined Viper Expansion Work Recovery Turbine and Flow Phase Separation Device Applied in R410A Heat Pump," *17th International Refrigeration and Air Conditioning Conference, Purdue, United States of America, July 9-12, 2018.*, 2018.

[134] GeoConfort, "Guide WV: Variable-speed water-to-water wnstallation & operations manual," 2023.

[135] H. Saidi, "Modélisation de pompes à chaleur à multiples compresseurs," *Mémoire de maîtrise, Polytechnique Montréal.*, 2019.

[136] J. R. García, F. Vera, S. Corberán, and J. Gonzálvez M, "Assessment of boiling and condensation heat transfer correlations in the modelling of plate heat exchangers," *International Journal of Refrigeration,* vol. 30, pp. 1029-1041, 2007.

[137] G. A. Longo, A. Gasparella, and R. Sartori, "Experimental heat transfer coefficients during refrigerant vaporisation and condensation inside herringbone-type plate heat exchangers with enhanced surfaces," *International Journal of Heat and Mass Transfer,* vol. 47, pp. 4125-4136, 2004.

[138] C. P. Underwood, "Chapter 14 - Heat pump modelling," in *Advances in Ground-Source Heat Pump Systems*, S. J. Rees, Ed., ed: Woodhead Publishing, United Kingdom., 2016, pp. 387-421.

[139] R. Ossorio and E. Navarro-Peris, "Study of oil circulation rate in variable speed scroll compressor working with propane," *International Journal of Refrigeration,* vol. 123, pp. 63-71, 2021.

[140] N. Stefanuk, J. Aplevich, and M. Renksizbulut, "Modeling and simulation of a superheat sontrolled water-to-water heat pump," *ASHRAE Transactions,* vol. 98, pp. 172-184, 1992.

[141] H. Jin and J. Spitler, "A Parameter Estimation Based Model of Water-to-Water Heat Pumps for Use in Energy Calculation Programs," *ASHRAE Transactions,* vol. 108, 2002.

[142] K. Rice, V. Baxter, S. Hern, T. McDonwell, J. Munk, and B. Shen, "Development of a residential ground-Source Integrated heat pump," *ASHRAE Transactions. Dallas, TX, USA,*, Jan 26-30 2013.

[143] S. Bouheret and M. Bernier, "Modelling of a water-to-air variable capacity ground-source heat pump," *Journal of Building Performance Simulation,* vol. 11, pp. 283-293, 2018.

[144] D. Ndiaye, "Étude numérique et expérimentale de la performance en régime transitoire de pompes à chaleur eau-air en cyclage," thèse de doctorat, Department of Mechanical Engineering, École Polytechnique de Montréal, 2007.

[145] C. K. Rice, "The ORNL Modulating Heat Pump Design Tool User's Guide, United States," 2001.

[146] G. Viviescas and M. Bernier, "Ground heat exchanger performance with variable speed ground-source heat pumps," *International Ground Source Heat Pump Association (IGSHPA) Research Track (2022). Annual Conference, Las Vegas, Nevada. December 6 to 8,* 2022.

[147] S. Shao, W. Shi, X. Li, and H. Chen, "Performance representation of variable-speed compressor for inverter air conditioners based on experimental data," *International Journal of Refrigeration,* vol. 27, pp. 805-815, 2004.

[148] P. Popovic and H. N. Shapiro, "A semi-empirical method for modeling a reciprocating compressor in refrigeration systems," *ASHRAE Transactions. Paper 1497. San Diego, CA. United States,* vol. 101(2), p. 1497, 1995.

[149] K. S. Gabel and C. R. Bradshaw, "Evaluation and quantification of compressor model predictive capabilities under modulation and extrapolation scenarios," *International Journal of Refrigeration,* vol. 149, pp. 1-10, 2022.

[150] V. Aute, C. Martin, and R. Radermacher, "AHRI project 8013 : A study of methods to represent compressor performance data over an operating envelope based on a finite set of test data," *Air-Conditioning, Heating, and Refrigeration Institute (AHRI),* 2015.

[151] I. H. Bell, J. Wronski, S. Quoilin, and V. Lemort, "Pure and Pseudo-pure Fluid Thermophysical Property Evaluation and the Open-Source Thermophysical Property Library CoolProp," *Industrial & Engineering Chemistry Research,* vol. 53, pp. 2498-2508, 2014.

[152] Y. Okawa, "A manual for the Modi ed Powell's Hybrid Method," 2020.

[153] S. P. Hackel, "Development of Design Guidelines for Hybrid Ground-Coupled Heat Pump Systems," *ASHRAE TRP-1384,* 2008.

[154] D. Knapp, M. Michalak, and M. Sing, "Modelling Waste Heat Recovery for Renewable Thermal Energy," *Proceedings of eSim 2022: 12th Conference of IBPSA-Canada,* vol. 12, 2022/June 2022.

[155] J. J. Hirsch, "DOE-2.2 Building Energy Use and Cost Analysis Program," *Volume 2: Dictionary. James J. Hirsch & Associates. Camarillio (US).* 2014.

[156] B. Rosén, A. Gabrielsson, J. Fallsvik, G. Hellström, and G. Nilson, "Systems for ground source heating and cooling – a status report," *Swedish Geotechnical Institute,* 2001.

[157] S. J. Rees, "An introduction to ground-source heat pump technology," in *Advances in Ground-Source Heat Pump Systems*, S. J. Rees, Ed., ed: Woodhead Publishing, 2016, pp. 1-25.

[158] A. R. Parise, "Simulation of vapour-compression heat pumps," *Simulation,* vol. 46, pp. 71-76, 1986.

[159] M. O. McLinden, "Theoretical Vapor Compression Cycle Model, Cycle 7," *National Bureau of Standards, Gaithersburg, MD,* 1987.

[160] P. A. Domanski and M. O. McLinden, "A Simplified Cycle Simulation Model for the Performance Rating of Refrigerants and Refrigerant Mixtures," *International Journal of Refrigeration,* vol. 15, pp. 81-88, 1992.

[161] J. Pannock and D. A. Didion, "The Performance of Chlorine-Free Binary Zeotropic Refrigerant Mixtures in a Heat Pump," *NISTIR 4748, National Institute of Standards and Technology, Gaithersburg, MD.,* 1991.

[162] P. A. Domanski and D. A. Didion, "Thermodynamic Evaluation of R-22 Alternative Refrigerants and Refrigerant Mixtures," *ASHRAE Transactions,* vol. 99, pp. 636-648, 1993.

[163] C. K. Rice, L. S. Wright, and P. K. Bansal, "Thermodynamic Evaluation Model for R22 Alternatives in Heat Pumps-Initial Results and Comparisons," *2nd International Conference on Heat Pumps in Cold Climates, New Brunswick, Canada.*, pp. 81–96., 1993.

[164] C. K. Rice, "DOE/ORNL Heat Pump Design Model, Overview and Application to R22 Alternatives," *3rd International Conference on Heat Pumps in Cold Climates, Nova Scotia, Canada.,* 1997.

[165] M. Scarpa, G. Emmi, and M. De Carli, "Validation of a numerical model aimed at the estimation of performance of vapor compression based heat pumps," *Energy and Buildings,* vol. 47, pp. 411-420, 2012.

[166] D. Ndiaye and M. Bernier, "Transient model of a geothermal heat pump in cycling conditions – Part A: The model," *International Journal of Refrigeration,* vol. 35, pp. 2110-2123, 2012.

[167] D. Ndiaye and M. Bernier, "One- and two-time-constant models to predict the capacity of geothermal heat pumps in cycling conditions," *ASHRAE Transactions,* vol. 120, pp. 320-333, 2014.

[168] J. M. Corberán, J. Gonzálvez, P. Montes, and R. Blasco, "'ART' A Computer Code To Assist The Design Of Refrigeration and A/C Equipment," Purdue University, 2002.

[169] B. J. Dechesne, F. M. Tello-Oquendo, S. Gendebien, and V. Lemort, "Residential air-source heat pump with refrigerant injection and variable speed compressor: Experimental investigation and compressor modeling," *International Journal of Refrigeration,* vol. 108, pp. 79-90, 2019.

[170] F. Correa and C. Cuevas, "Air-water heat pump modelling for residential heating and domestic hot water in Chile," *Applied Thermal Engineering,* vol. 143, pp. 594-606, 2018.

[171] R. Gupta and R. Irving, "Development and application of a domestic heat pump model for estimating CO2 emissions reductions from domestic space heating, hot water and potential cooling demand in the future," *Energy and Buildings,* vol. 60, pp. 60-74, 2013.

[172] J. Ruschenburg, T. Ćutić, and S. Herkel, "Validation of a black-box heat pump simulation model by means of field test results from five installations," *Energy and Buildings,* vol. 84, pp. 506-515, 2014.

[173] S. Nyika, S. O. Holloway, W. T. Horton, and J. E. Braun, "Generalized Performance Maps for Variable-Speed,Ducted, Residential Heat Pumps," *ASHRAE Transactions,* vol. 120 (2), pp. 80–89, 2014.

[174] S. A. Tabatabaei, J. Treur, and E. Waumans, "Comparative Evaluation of Different Computational Models for Performance of Air Source Heat Pumps Based on Real World Data," *Energy Procedia,* vol. 95, pp. 459-466, 2016.

[175] R. Ghoubali, P. Byrne, J. Miriel, and F. Bazantay, "Simulation study of a heat pump for simultaneous heating and cooling coupled to buildings," *Energy and Buildings,* vol. 72, pp. 141-149, 2014.

[176] G. St-Onge, "Variable capacity mini-split air source heat pump model for TRNSYS," *Proceedings of eSim 2018: 10th Conference of IBPSA-Canada, 2018,* May 9-10 2018.

[177] S. Bordignon, J. D. Spitler, and A. Zarella, "A. Simplified water-source heat pump models for predicting heat extraction and rejection," *Renew. Energy* vol. 220, 119701, 2024.

[178] J. Woods and E. Bonnema, "Regression-based approach to modeling emerging HVAC technologies in EnergyPlus: A case study using a Vuilleumier-cycle heat pump," *Energy and Buildings,* vol. 186, pp. 195-207, 2019.

[179] C. P. Underwood, M. Royapoor, and B. Sturm, "Parametric modelling of domestic air-source heat pumps," *Energy and Buildings,* vol. 139, pp. 578-589, 2017.

[180] E. Kinab, D. Marchio, P. Rivière, and A. Zoughaib, "Reversible heat pump model for seasonal performance optimization," *Energy and Buildings,* vol. 42, pp. 2269-2280, 2010.

[181] M. Cimmino and M. Wetter, "Modelling of Heat Pumps with Calibrated Parameters Based on Manufacturer Data," in *International Modelica Conference*, 2017.

[182] G. Viviescas and M. Bernier, "A variable speed water-to-water heat pump model used for ground-source applications," *Science and Technology for the Built Environment,* vol. 30(3), pp. 266-279, 2023.

[183] D. Carbonell, J. Cadafalch, P. Pärisch, and R. Consul, *Numerical analysis of heat pump models. Comparative study between equation-fit and refrigerant cycle based models*. Universitat Politecnica de Catalunya, 2012.

[184] G. Meramveliotakis, G. Kosmadakis, and S. Karellas, "Methods based on a semi-empirical model for simulating scroll compressors with HFC and HFO refrigerants," *Open Research Europe,* vol. 1, 2022.

[185] F. M. Tello, E. Navarro, F. Barceló, and J. Gonzálvez, "Semi-empirical model of scroll compressors and its extension to describe vapor-injection compressors. Model description and experimental validation," *International Journal of Refrigeration,* vol. 106, pp. 308-326, 2019.

[186] S. Klein, D. T. Reindl, and D. Jähnig, "Develop Data Base for Determining Optimum Compressor Rating Points for Residential Refrigerator and Freezer Compressors," *ASHRAE RP-870,* 1999.

[187] W. Li, "Simplified steady-state modeling for hermetic compressors with focus on extrapolation," *International Journal of Refrigeration,* vol. 35, pp. 1722-1733, 2012.

[188] D. Ndiaye and M. Bernier, "Dynamic model of a hermetic reciprocating compressor in on–off cycling operation," *Applied Thermal Engineering,* vol. 30, pp. 792-799, 2010.

[189] V. C. Aute and C. Martin, "A Comprehensive Evaluation of Regression Uncertainty and the Effect of Sample Size on the AHRI-540 Method of Compressor Performance Representation," 2016.

[190] H. Cheung, O. Sarfraz, and C. K. Bach, "A method to calculate uncertainty of empirical compressor maps with the consideration of extrapolation effect and choice of training data," *Science and Technology for the Built Environment,* vol. 24, pp. 743-758, 2018.

[191] J. Winkler, V. Aute, and R. Radermacher, "Comprehensive investigation of numerical methods in simulating a steady-state vapor compression system," *International Journal of Refrigeration,* vol. 31, pp. 930-942, 2008.

[192] B. N. Taylor and C. E. Kuyatt, " Guidelines for Evaluating and Expressing the Uncertainty of NIST Measurement Results," *National Institute of Standards and Technology Technical Note 1297,* 1994.

APPENDIX A CALIBRATION PROCEDURE AND RESULTS

This appendix provides an overview of the procedures and experimental setups used to calibrate the thermocouples, thermopiles, and flowmeters utilized in this study.

A.1 Thermocouples

The heat pump test bench used in this study employs seven Type T (copper-constantan) thermocouples, allocated as follows. Four thermocouples are dedicated to measuring the inlet and outlet temperatures of the secondary fluid (water) on both the source and load sides. Additionally, one thermocouple measures the compressor discharge temperature, while another measures the compressor suction temperature, which also coincides with the evaporator outlet temperature, providing a measure of the degrees of superheat. Lastly, one thermocouple is used to monitor the outlet temperature of the refrigerant side of the condenser. The four thermocouples used on the source and load sides are only used for display purposes as the heat transfer in both the evaporator and condenser is based on more precise temperature differences obtained with thermopiles.

Figure A.1 shows the traditional representation of a thermocouple measurement with the cold junction immersed in an ice bath. Thermocouples connected to modern data acquisition systems (such as the one used in the present study) do not use ice baths to determine the temperature because these systems usually feature built-in electronic cold junction compensation (CJC). As shown in Figure A.1, voltage measurements (in mV) are made and converted to temperatures using standard thermocouple tables that provide a typical uncertainty of the order of $\pm$ 1.0℃. The objective of the calibration is to reduce this uncertainty by providing calibration curves that relate the measured voltage to the “true” temperature.

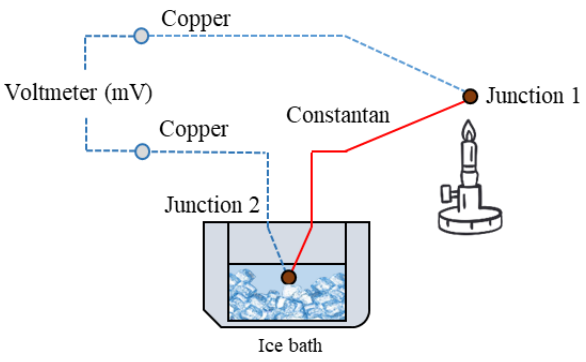

Figure A.1 Typical representation of a thermocouple temperature measurement

Figure A.2 illustrates the calibration setup for the thermocouples. The thermocouples are immersed in a high-precision water bath (Julabo FP40) which provides a stable temperature. To minimize temperature fluctuations within the bath, a perforated copper block is immersed in the bath, and the thermocouples are inserted into this block. The thermocouples are linked to a data acquisition card (National Instrument – Compact Rio NI9205) which has an internal CJC. The output is sent to data acquisition software (LabVIEW) for analysis.

The calibration was performed by comparing the thermocouples with a platinum RTD reference thermometer (GUILDLINE brand, model 9540). The temperature reading of the thermostatic bath was also used as a secondary reference temperature. Typically, both the RTD and temperature bath temperatures agree within $\pm$ 0.01 ℃.

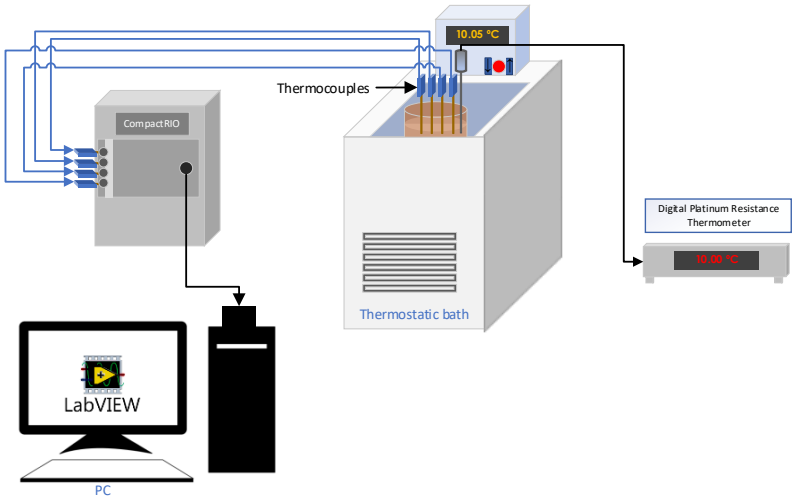

Figure A.2 Thermocouple calibration setup

Tests were conducted in steps of 5°C, ranging from 5°C to 65°C, with water used in the bath. Once the temperature was selected, it was allowed to stabilize for 30 minutes, and temperature measurements were taken for 30 seconds. Thermocouple readings were recorded every 0.5 seconds resulting in a total of 60 readings for each test. The average temperature of these 60 measurements was then related to the reference temperature of the RTD using a first-order equation:

$$T_{RTD} = a_i \times T_{TC_i} + b_i \qquad \text{A.1}$$

Where T_{TC_i} is the temperature of each thermocouple i (in ℃), obtained directly from the data acquisition system. Thus, the output temperatures given by the data acquisition system are

corrected to obtain the "true" temperature. Table A.1 gives the value of a and b for all seven thermocouples and Figure A.3 presents Equation A.1 graphically.

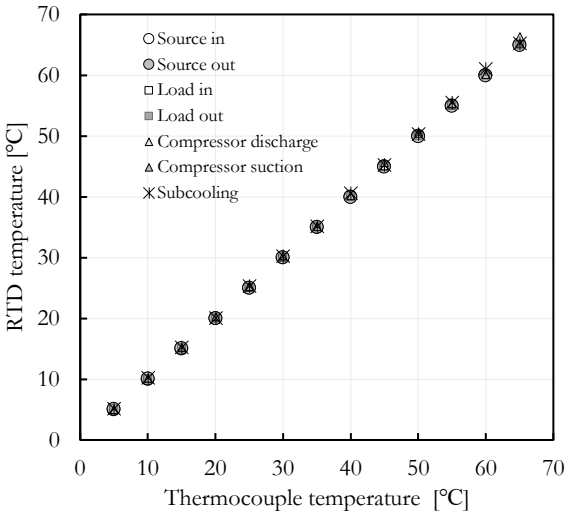

Figure A.3 Calibration of thermocouples against the reference (RTD) temperature

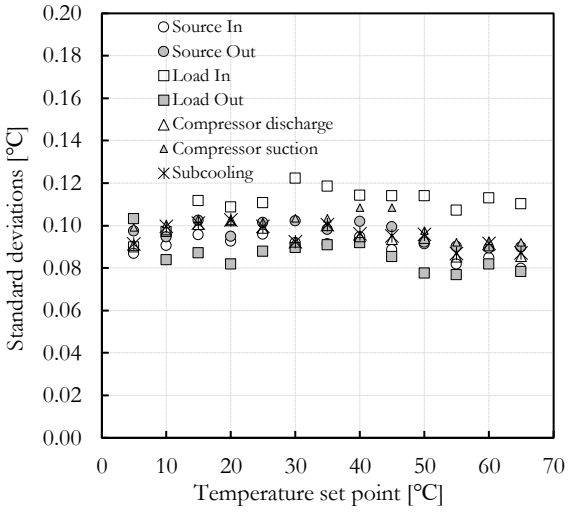

Figure A.4 Standard deviation of thermocouple temperature measurements

The uncertainties associated with the thermocouple measurements are of three types: i) those related to the calibration curve (u_c); ii) uncertainties associated with the fluctuations of temperatures recorded by the thermocouples (u_{st}); and iii) the uncertainty related to the reference thermometer (u_{RTD}); The overall uncertainty, u_{global} is evaluated using the uncertainty propagation technique [192] as shown in Equation A.2

$$u_{global} = \sqrt{u_c^2 + u_{st}^2 + u_{RTD}^2} \qquad \text{A.2}$$

Calibration curve uncertainty (u_c).

The maximum difference between the reference temperature and the thermocouples over the measuring range is shown in Table A.1. These differences are the calibration curve uncertainties, u_c. As shown in Table A.1, the values of u_c are less than $\pm$0.005 °C and this value constitutes the value of u_c for thermocouple measurements.

Table A.1 Thermocouple calibration results

Thermocouple	a	b	Calibration curve uncertainty (u_c) [°C]	R^2
Source in	1.000812	-0.1155	±0.00021	1
Source out	0.996888	0.016769	±0.00037	0.999998
Load in	0.998457	0.004615	±0.00040	0.999998
Load out	0.996981	0.098808	±0.00022	0.999999
Suction	1.009352	-0.05731	±0.00449	0.999782
Discharge	1.003275	0.073077	±0.00227	0.999944
Subcooling	1.001524	0.053024	±0.00125	0.999848

Uncertainties related to temperature fluctuations (u_{st})

Following the work of Ndiaye [144], the uncertainties related to temperature fluctuations (u_{st}) are calculated based on twice the standard deviation (2σ) of the 60 measurements made during calibration for each reference temperature. Figure A.4 shows the uncertainty related to these fluctuations and Table A.2 shows the corresponding values of 2σ for each thermocouple. Based on these results a value of ±0.2 °C was selected for u_{st}.

Table A.2 Thermocouple uncertainty associated with fluctuations

Thermocouple uncertainty u_{st} (2σ) [°C]						
Source in	Source out	Load in	Load out	Suction	Discharge	Subcooling
±0.179	±0.193	±0.220	±0.171	±0.189	±0.201	±0.175

Uncertainty of the reference thermometer (u_{RTD})

According to the manufacturer's specifications, the 9540 Digital platinum resistance thermometer (RTD) has an uncertainty of ± 0.03 °C within the temperature range of -40 to +180 °C. These values were confirmed during calibration by making a comparison with temperature readings from the thermostatic baths which have an uncertainty of ± 0.01 °C according to the bath manufacturer. Therefore, it was decided to assign a ± 0.03°C uncertainty to the reference temperature, u_{RTD}.

Global uncertainty (u_{global})

Table A.3 shows the global uncertainty for the seven thermocouples. The analysis shows that the global uncertainties for the thermocouples range from ± 0.178 °C to ± 0.226 °C with an average of ± 0.191 °C. The stability uncertainty, u_{st}, is the dominant factor contributing to the global uncertainty in all cases, significantly outweighing the contributions from the curve uncertainty (u_c)

and RTD uncertainty (u_{RTD}). Based on the results of Table A.3 a global uncertainty of $\pm$ 0.2 °C was assigned to thermocouples.

Table A.3 Global thermocouple uncertainties

	Global uncertainties on thermocouples [°C]						
	Source in	Source out	Load in	Load out	Suction	Discharge	Subcooling
u_c	±0.00021	±0.00037	±0.0004	±0.00022	±0.00449	±0.00227	±0.00248
u_{st}	±0.179	±0.193	±0.220	±0.171	±0.189	±0.201	±0.185
u_{RTD}	±0.03	±0.03	±0.03	±0.03	±0.03	±0.03	±0.0
u_{global}	±0.19	±0.200	±0.23	±0.18	±0.20	±0.21	±0.19

A.2. Thermopile

For applications requiring greater precision, thermocouples can be connected in series to form a thermopile. This configuration increases the potential difference measured by the potentiometer by a factor of n, where n is the number of junction pairs. Two thermopiles are installed in the system on the source and load sides. Figure A.5 displays a photograph of a thermopile (left) and the position of both thermopiles within the heat pump test bench at the inlet/outlet of the evaporator and condenser.

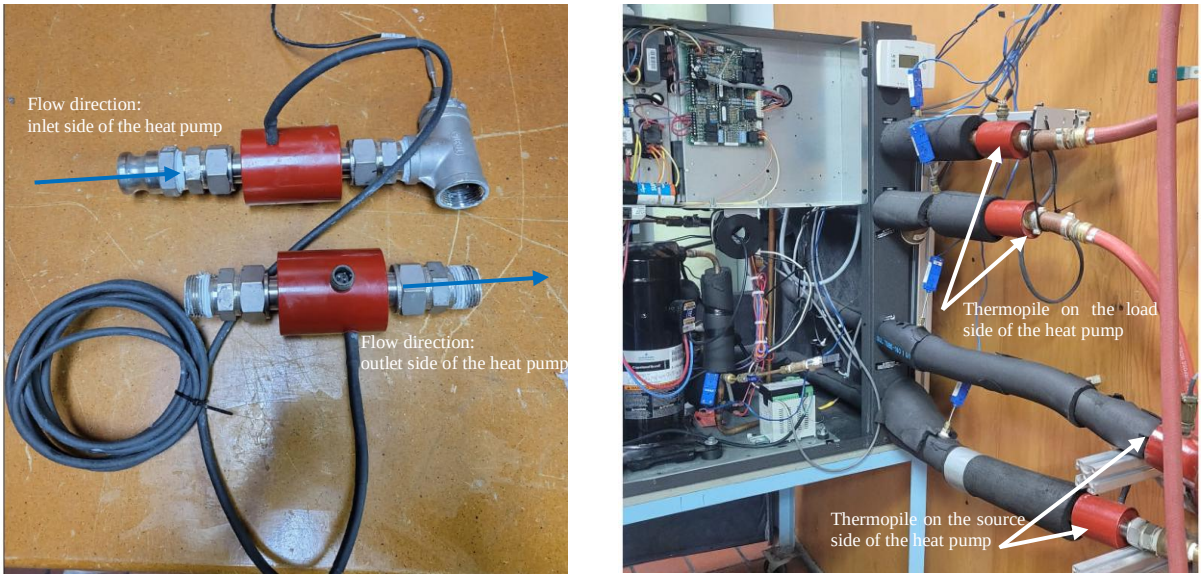

Figure A.5 Thermopile (left) and location in the heat pump test bench (right)

Since the temperature differences are relatively small (in the range of 3 to 7 K), it is imperative to obtain precise temperature differences to obtain an accurate determination of the heat exchanged in the evaporator and condenser. The thermopiles are manufactured by Delta-T who claims that they have an accuracy of $\pm$ 0.04 K.

Figure A.6 presents a schematic of a thermopile which consists of two pipe sections (in red) linked together with a cable (black in Figure A.5). Each section of the thermopile has 10 junction pairs of Type T thermocouples embedded radially inside a 19 mm pipe from the outer diameter to the center. Each thermocouple junction is made up of a copper (solid red lines) and constantan wire (dotted blue lines). The 10 junctions are enclosed in a cable wrap and connected to the second section of the thermopile, which has the same configuration. These thermocouples are connected in series to provide a cumulative voltage output that corresponds to the temperature difference between the two fluid sections. There is no need for an ice bath reference point with a thermopile.

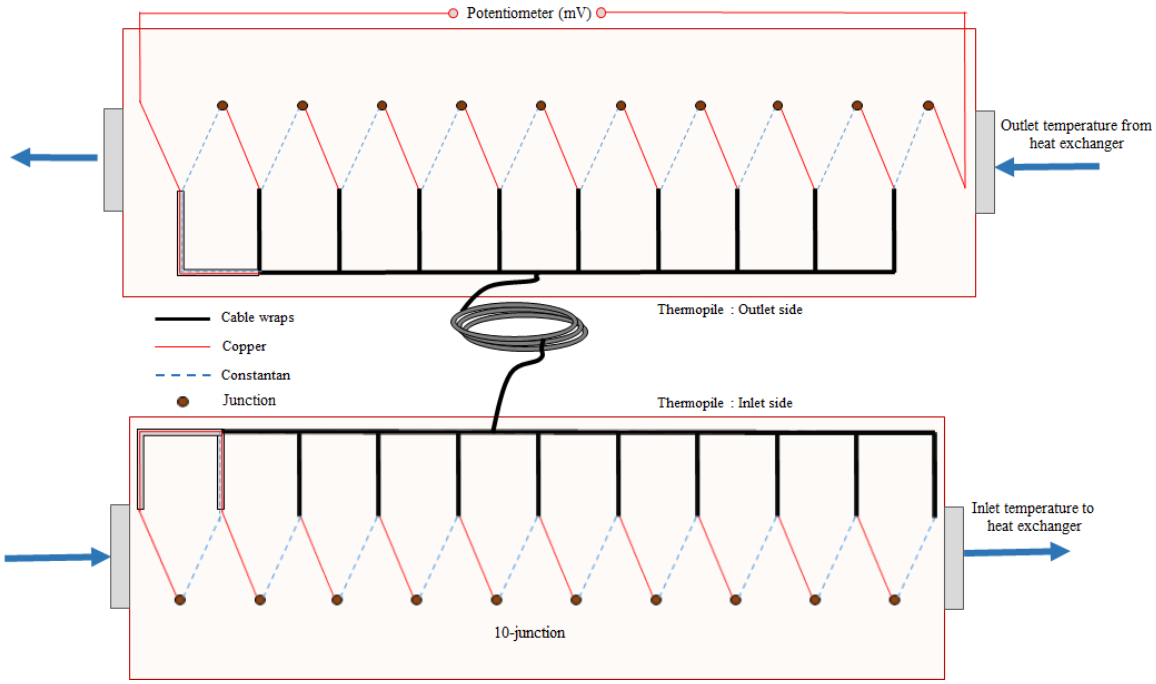

Figure A.6 Thermopile with 10 pairs of type T thermocouples

The temperature difference measured by a thermopile, ΔT, is given by:

$$\Delta T = \frac{\Delta V}{n\alpha} \qquad \text{A.3}$$

where ΔV is the measured voltage from the thermopile, α is the Seebeck coefficient, and n is the number of junction pairs (10 in the present case). The Seebeck coefficient for Type T thermocouples is approximately equal to 0.04 mV/°C. This value is slightly dependent on the temperature.

The objective of the calibration is to determine the value of $n\alpha$ in Equation A.3 and check the accuracy provided by the manufacturer.

Figure A.7 depicts the setup for calibrating the thermopile. Each section (red cylinder in Figure A.7) of the thermopile is placed in a separate thermostatic bath. Each bath is maintained at a constant (but different) temperature, thus creating a constant temperature differential. Each bath is equipped with a recirculation pump to ensure the temperature is evenly distributed within the water-filled reservoir. Each section of the thermopile is fully submerged in the bath and strategically positioned to allow the pumped coolant fluid to flow through them as it would in a normal operation. In the example given in Figure A.7, the bath temperatures are set to 15.05 °C and 10.05 °C, respectively, giving a 5 K temperature difference. The surface of the bath was covered with insulating material (not shown in the figure) to prevent unwanted heat gains/losses. The data from the thermopile is collected and analyzed using the data acquisition system, allowing for real-time monitoring and recording of the temperature difference.

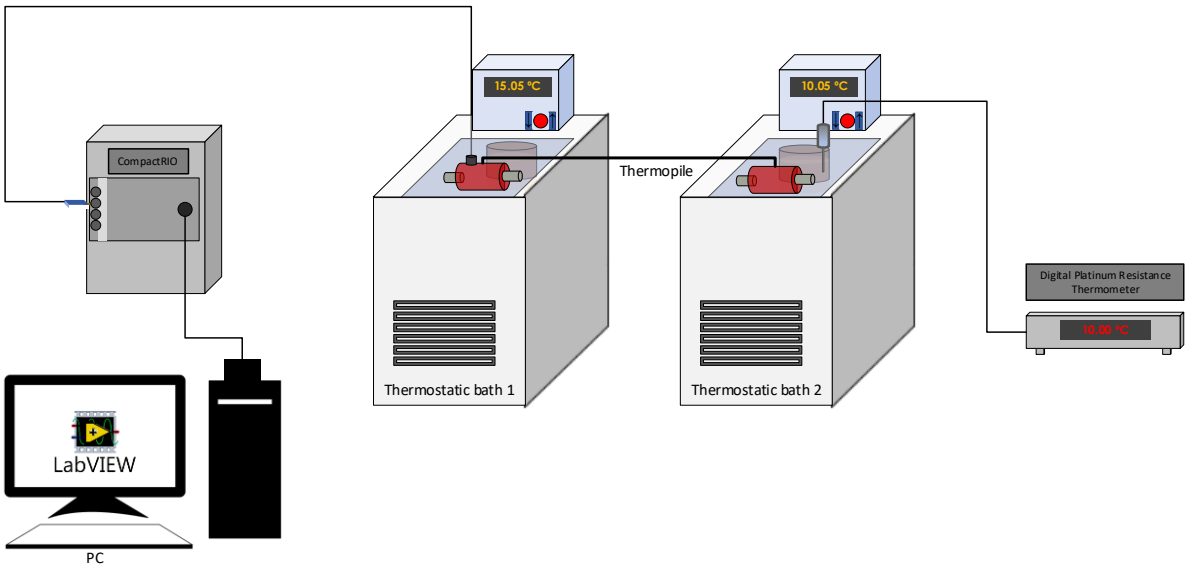

Figure A.7 Thermopile calibration setup

Calibration was performed over the temperature difference range from ~1 to ~10 K. Each experimental point requires the system to stabilize for at least 30 minutes after setting the desired temperature, followed by the collection of 60 data points over 30 seconds using the data acquisition system. Results are shown in Figure A.8 for the load and source thermopiles. The reference temperature difference is plotted against the millivolt output of the thermopiles. This reference temperature difference is measured by successively placing the RTD in each of the thermostatic baths. For example, to achieve a temperature difference of 5 °C, one bath is set to 10 °C and the other to 15 °C. This process was repeated in 1 °C increments until a differential of 10 °C was obtained.

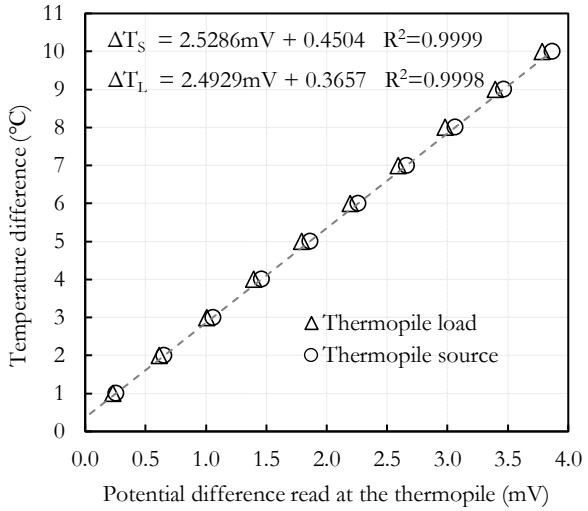

Figure A.8 Calibration of thermopiles: "reference" temperature difference as a function of potential difference

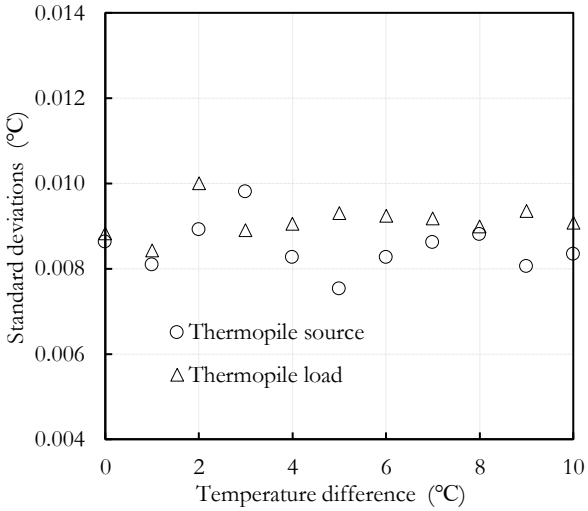

Figure A.9 Standard deviations of temperature difference measurements from the thermopiles

A linear fit is performed to the data which is sufficient considering the relatively high value of R^2. The straight line does not go through the origin indicating a slight dependency on temperature. Figure A.9 shows the standard deviation of temperature difference measurements for the 60 data points in every experiment. It is shown that the standard deviation is less than $\pm$ 0.01°C.

It is interesting to look at the average of the Seebeck coefficient ($n\alpha$) obtained with the calibration. This value is simply the inverse of the slope of the linear curves presented in Table A.4 As shown in Table A.4, the measured Seebeck coefficients are very close to the value of 0.04 mV/°**C** (or 0.4 mV/°**C** for ten junctions) indicated earlier.

Table A.4 Seebeck coefficient $(n\alpha)$ for the calibrated thermopile

Thermopile	Seebeck coefficient (mV/°C)
Thermopile - Source	0.3957
Thermopile - Load	0.3988

Much like for the uncertainty of thermocouples, the uncertainty of the thermopiles is assumed the sum of three values (Equation A.2).

Those related to the calibration curve (u_c); uncertainties associated with the fluctuations of temperatures recorded by the thermocouples (u_{st}); and the uncertainty related to the reference thermometer (u_{RTD}).

Table A.5 summarizes the combined uncertainties associated with the thermopiles.

Table A.5 Combined uncertainties in the thermopiles.

Thermopile uncertainties [°C]		
Uncertainty	Source	Load
u_c	±0.0023	±0.0057
u_{st}	±0.018	±0.02
u_{RTD}	±0.03	±0.03
u_{global}	±0.04	±0.04

Reference temperature uncertainty (u_{RTD}) is the most significant contributor to the global uncertainty for both thermopiles, accounting for an average of approximately 75% of the total uncertainty. A value of ±0.04 ℃ was selected as the uncertainty for both thermopiles This value corresponds to the value given by the manufacturer. For the measurements made in this study, which on average present a temperature difference of about 5 K, this represents around a 1% uncertainty in the measurement of the temperature differential.

Aside from having a lower uncertainty, a temperature difference obtained with a thermopile exhibits less fluctuations. Figure A.10 shows the results of an experiment where the secondary fluid mass flow rate to the heat pump is set at 0.567 kg/s and the inlet temperature is 30 °C. The heat pump operates in heating. The temperature difference across the condenser (red and blue square markers) was measured using the thermopile (circles) and thermocouples (crosses) over an experimental period of 100 seconds during which 200 data points were collected. Both devices captured similar trends; however, the thermopile measurement exhibited significant less scatter,

indicating lower variability. The previous results demonstrate a significant improvement in the calculation of heat transfer within the secondary loops when thermopiles are utilized in each of the heat exchangers.

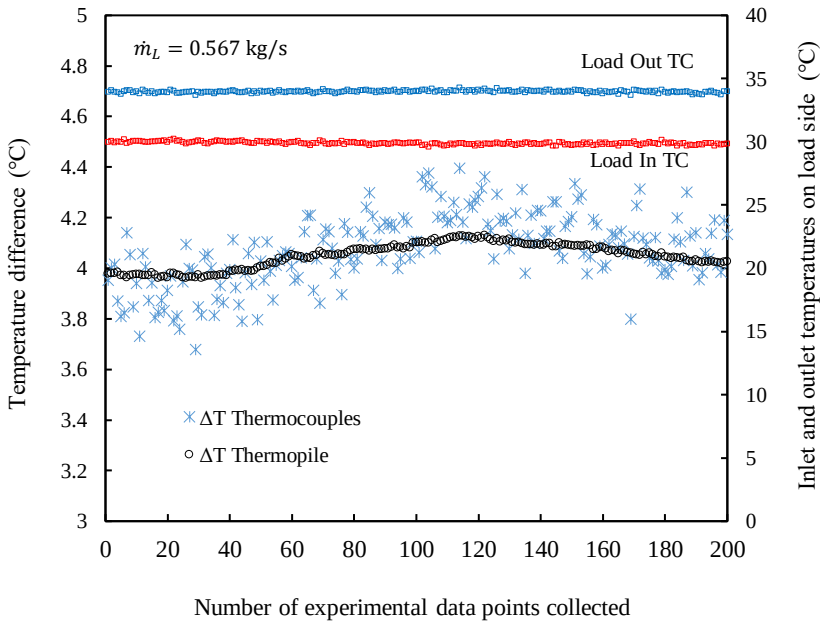

Figure A.10 Comparison of temperature difference measurements between the inlet and outlet on the load side of a heat pump using a thermopile and thermocouples

A.3. Flowmeters

Two turbine-type flowmeters (FTB-815 – OMEGA) with a 4 to 20 mA output are utilized, each featuring a capacity range of 0.06–2.2 L/s for a 1-inch (25 mm) diameter connection. According to the manufacturer, these flowmeters have an accuracy of ±0.5% of the reading. The primary objective of this calibration is to relate the mA output of the devices to the actual mass flow rate and to verify the precision claimed by the manufacturer. Figure A.11 presents a picture of the device (on the left) and its placement on the test bench on the right.

The calibration of both turbine-type flowmeters was performed using a volumetric method. This approach involved measuring the volume of fluid passing through the flowmeter over a specified period using a precise scale and a stopwatch.

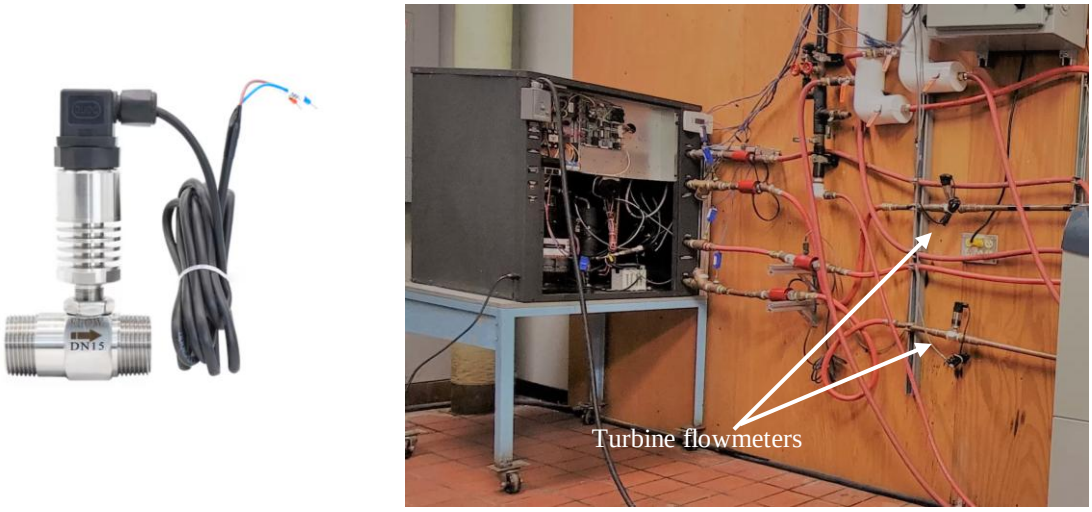

Figure A.11 Turbine flowmeter (left). Position of both flowmeters in the test bench (right).

Figure A.12 illustrates the experimental setup used for calibrating the turbine flowmeters. The system consists of the water supply, the turbine flowmeter, and a drainage system. Water is passing through the turbine flowmeter, which measures the flow rate and sends a current signal in milliamperes (mA) to the data acquisition system.

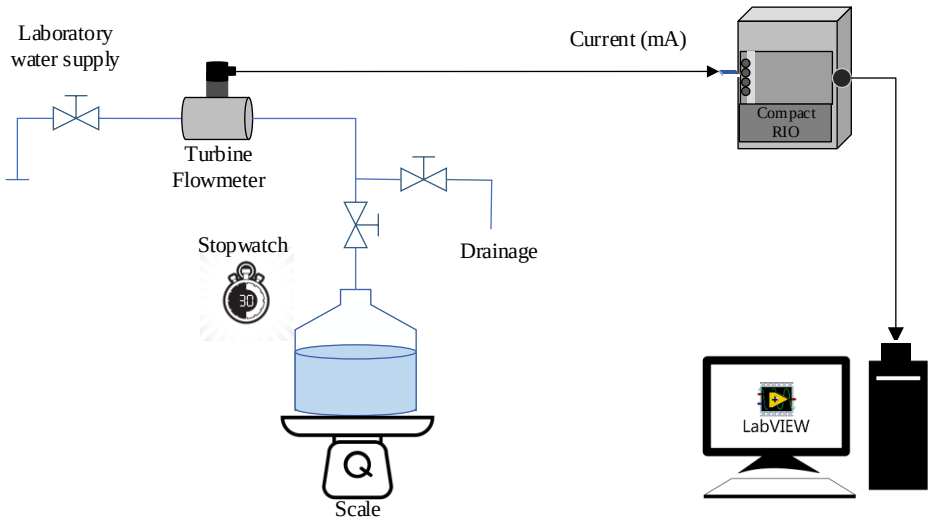

Figure A.12 Turbine flowmeter calibration setup

Downstream of the turbine flowmeter, the water flows into a container placed on a scale, which measures the mass of the water collected (Δm), over a time period (Δt). This setup allows for the determination of the actual flow rate by correlating the mass of water collected with the time elapsed and the current (mA) data. The mass flow rate is calculated according to:

$$\dot{m} = \frac{\Delta m}{\Delta t} \qquad \text{A.5}$$

Tables A6 and A7 present the experimental data collected for calibrating the flowmeters located on the source side and the load side (see Figure A.12). In total, five (5) flow rates were tested, and each flow rate was repeated five (5) times to assess repeatability and calculate the uncertainty due to measurement stability.

Table A.6 Calibration results of the load side of flowmeter

Load Flowmeter					
Elapsed Time, Δt, (s)	**90.0**	**60.0**	**30.0**	**40.0**	**30.0**
Average measured mass, Δm, (kg)	11.550	12.704	8.038	11.583	13.038
Average calculated flow rate (kg/s)	0.128	0.211	0.267	0.289	0.435
Standard deviation on calculated flow rate (kg/s) (u_Q) (2σ)	0.00071	0.00144	0.00150	0.00074	0.00121
Average current measurement from turbine flow meter (mA)	4.94	5.56	5.98	6.14	7.19
Standard deviation on average current (mA)	0.025	0.015	0.019	0.021	0.011

Table A.7 Calibration results of the source side flowmeter

Source Flowmeter					
Elapsed Time, Δt, (s)	**90.0**	**60.0**	**30.0**	**40.0**	**30.0**
Average measured mass, Δm, (kg)	13.444	10.160	14.218	8.230	11.459
Average calculated flow rate (kg/s)	0.112	0.169	0.237	0.274	0.382
Standard deviation on calculated flow rate (kg/s) (u_Q) (2σ)	0.00061	0.00109	0.00134	0.00139	0.00157
Average current measurement from turbine flow meter (mA)	4.81	5.23	5.71	5.99	6.74
Standard deviation on average current (mA)	0.008	0.011	0.015	0.012	0.021

Figure A.13 displays the relationship between the output current (in mA) and the mass flow rate (in kg/s) for the two turbine flowmeters. The graph shows a linear relationship between the mass flow rate and the output current for both flowmeters. The dotted lines represent the best-fit linear regression for each set of data points, showing a strong correlation between the calculated mass flow rate and the measured current. The curves presented in this figure are coded in the data acquisition system to relate the current reading to the actual flow rate.

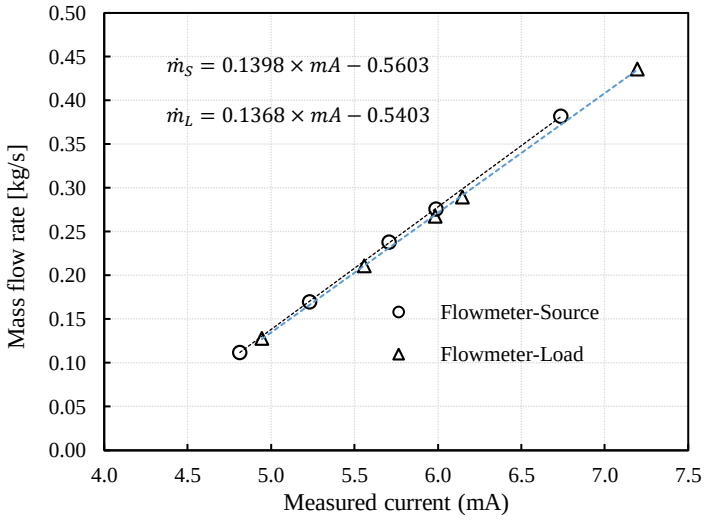

Figure A.13 Calibration curve for turbine flowmeters

Global Uncertainty (u_{global})

To quantify the uncertainty associated with the flow rate measurements, several sources of error were considered, including the accuracy of the scale and stopwatch, the repeatability of the measurements and the uncertainty of the curve fit. The following steps detail the calculation of the global uncertainty.

The global uncertainty (u_{global}) is given by:

$$u_{global} = \sqrt{u_v^2 + u_Q^2 + u_{fit}^2} \tag{A.4}$$

This uncertainty incorporates the uncertainties from volume/time measurements (u_v), the standard deviation of the flow rate measurements calculated from multiple flow rate measurements (u_Q) and the curve fit uncertainty (u_{fit}).

The uncertainty u_v is calculated as the combined uncertainty of the scale, $u_{\Delta m}$, and the stopwatch uncertainty. The uncertainty u_v is calculated using the propagation of uncertainties for independent measurements:

$$u_v = \sqrt{\left(\frac{\partial \dot{m}}{\partial \Delta m} \times u_{\Delta m}\right)^2 + \left(\frac{\partial \dot{m}}{\partial \Delta t} \times u_{\Delta t}\right)^2} \tag{A.6}$$

Where the partial derivatives are:

$$\frac{\partial \dot{m}}{\partial \Delta m} = \frac{1}{\Delta t} \quad \text{A.7}$$

$$\frac{\partial \dot{m}}{\partial \Delta t} = -\frac{\Delta m}{\Delta t^2} \quad \text{A.8}$$

The maximum uncertainty for u_v is obtained for $\Delta m = 8$ kg, $\Delta t = 30\ s$.

Given the uncertainties: $u_{\Delta m} = \pm 0.01$ kg and $u_{\Delta t} = \pm 0.01\ s$ the value of u_v is 3.44×10^{-4} kg/s. The uncertainty in the mass measurement contributes approximately 94.1% to u_v, while the uncertainty in the stopwatch contributes approximately 5.9%.

Table A.8 provides a detailed breakdown of different sources of uncertainty in the flow rate measurements at both the source and the load sides. The global uncertainty (u_{global}) gives an overall measure of the accuracy of the flowmeter readings, considering the various sources of error. The main source of uncertainty is related to the standard deviation of the flow rate measurements for each experiment u_Q.

Table A.8 Global uncertainties in flowmeters.

Flowmeter uncertainties [kg/s]		
Uncertainty	Source	Load
$\boldsymbol{u_v}$	±0.000344	±0.000344
$\boldsymbol{u_Q}$	±0.00150	±0.000157
$\boldsymbol{u_{fit}}$	±0.000110	±0.000125
$\boldsymbol{u_{global}}$	±0.00153	±0.000398

In this study, the flow rate measured ranged from 0.3 kg/s to 0.6 kg/s. For the source flowmeter, the global uncertainty was determined to be ±0.00153 kg/s, which translates to a relative uncertainty of ±0.5% at the 0.3 kg/s to ±0.255% at the maximum flow rate of 0.6 kg/s. For the load flowmeter, the global uncertainty was found to be ±0.000384 kg/s, resulting in relative uncertainties of ±0.0128% at 0.3 kg/s to ±0.043% at 0.6 kg/s. These uncertainty results are in-line with the manufacturer specifications and an uncertainty of ±0.5% was used.

A.4 Pressure and power measurements

Additional instruments were employed to measure gauge pressure at the suction and discharge of the compressors, and a wattmeter for monitoring compressor power consumption. The PX119-1KGI pressure gauge (OMEGA), capable of measuring pressures in the range of 0-69 bar, was used. According to the manufacturer's specifications, the gauge provided accurate pressure readings with an accuracy of $\pm$0.5% of measurement. No independent calibration could be performed due to the lack of a reference pressure apparatus; the accuracy provided by the manufacturer was thus used. Similarly, for power measurement, the Ohio Semitronics wattmeter WT3-12-100-D (0-24 kW) was used, with an accuracy specified by the manufacturer as $\pm$0.5% of full scale. Here again, an independent calibration could not be performed, and the manufacturer specification was used

APPENDIX B EXPERIMENTALY-DERIVED OVERALL HEAT TRANSFER COEFFICIENTS FOR THE CONDENSER AND EVAPORATOR

This appendix offers a complement to the article presented in Chapter 6. Experimental results are used to derive overall heat transfer coefficients (UA values) in the condenser and in the evaporator. This constitutes a preliminary evaluation that would require further testing.

To solve the complete heat pump model involves not only a more complex system of nonlinear equations, but also the calculation of thermo-physical properties and correlations to predict the heat transfer coefficients. Additionally, the calculation of the heat transfer area involved in each zone, which is computed using the logarithmic mean temperature difference (LMTD) method, is highly sensitive to the guess values used to solve the problem.

Solving this problem under specific conditions, such as constant temperature and mass flow rates of secondary fluids, is straightforward in most instances. The key lies in correctly selecting the guess values, which hinge on the modeler's expertise and an understanding of the physical phenomena involved.

However, when integrating the heat pump with a building simulation program and conducting long-term modeling throughout entire heating seasons, the model faces constant changes in the input variables. This situation leads to two issues. First, an increase in computation time Secondly, a stability problem in solving the system of nonlinear equations, as the guess values used might vary significantly from one time-step to another, potentially resulting in the failure of both the solution and the modeling process.

One possible way to facilitate calculations is to incorporate experimentally derived overall heat transfer coefficients. The determination of overall heat transfer coefficients, $U_i A_i$, in each zone of the heat exchangers is evaluated in this appendix based on measurements of temperature and pressure in the heat pump. They will be referred to as $(U_i A_i)_m$. These values are compared with the predictions of the complete model, $(U_i A_i)_p$.

The 32 experimental results in heating mode reported earlier in chapter 6 are used for the calculation of $(U_i A_i)_m$. Eight different source temperatures ($T_{w_{S_{in}}}$), ranging from 10 ºC to 26 ºC,

and four load temperatures ($T_{w_{L_{in}}}$), ranging from 30 ºC to 45 ºC are used. The mass flow rate of the secondary fluids is set at 0.565 L/s for the load and in the range of 0.308–0.462 L/s for the source side.

B.1 Overall heat transfer coefficients in the condenser

B.1.1 Desuperheating zone

The various parameters involved in the determination of the overall heat transfer coefficient in the desuperheating zone, $(U_{dsh}A_{dsh})_m$, are presented in Figure B.1. In the complete model, U_{dsh} and A_{dsh} are determined iteratively (see equations 6-21 to 6-29 in chapter 6). In particular, the determination of U_{dsh} involves the use of correlations for the calculation of the heat transfer coefficients on the refrigerant and water sides of the plate heat exchanger.

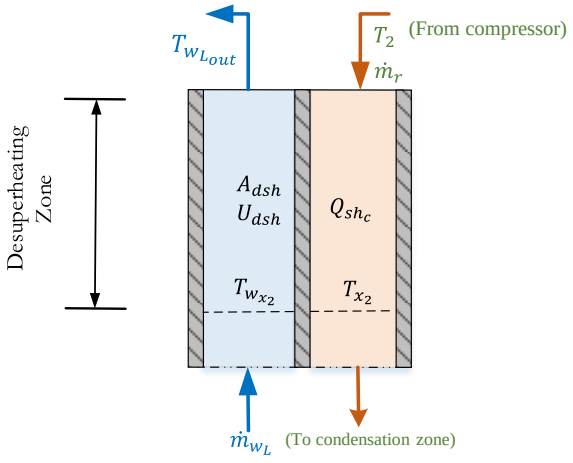

Figure B.1 Schematic representation of the desuperheating zone of the condenser

It is proposed here to evaluate the product $U_{dsh}A_{dsh}$ directly from experimental measurements. The basic equation to obtain this value is:

$$(U_{dsh}A_{dsh})_m = \frac{Q_{dsh}}{\Delta T_{lm_{sh}}} = \frac{Q_{dsh}}{U_{dsh}\left[\left(T_2 - T_{w_{L_{out}}}\right) - \left(T_{x_2} - T_{w_{x_2}}\right)\right]} ln \frac{\left(T_2 - T_{w_{L_{out}}}\right)}{\left(T_{x_2} - T_{w_{x_2}}\right)} \qquad \text{(B.1)}$$

In this equation, T_2 , the compressor discharge temperature, is measured as well as the outlet water temperature from the condenser, $T_{w_{L_{out}}}$. The value of T_{x_2}, the saturation temperature in the

condenser, is derived from the condenser pressure measurement. These temperatures are also used to determine the heat transfer rate in the desuperheating zone, Q_{dsh} :

$$Q_{dsh} = \dot{m}_r C_{p,r}(T_2 - T_{x_2}) \tag{B.2}$$

In Equation B.2, the refrigerant mass flow rate, $\dot{m}_r$, is determined using the AHRI-540 model based on T_{x_2} (see equation 6-51 in chapter 6) and the suction dew-point temperature T_{x_1} which is determined based on the evaporating pressure measurement.

Then, the water temperature at the entrance of the desuperheating zone, $T_{w_{x2}}$, is calculated using the heat balance on the water side:

$$Q_{dsh} = \dot{m}_w C_{p,w}\left(T_{w_{L_{out}}} - T_{w_{x2}}\right) \tag{B.3}$$

The variation of $(U_{dsh}A_{dsh})_m$ as a function of the secondary fluids inlet temperatures ($T_{w_{S_{in}}}$, $T_{w_{L_{in}}}$) is depicted in Figure B.2.

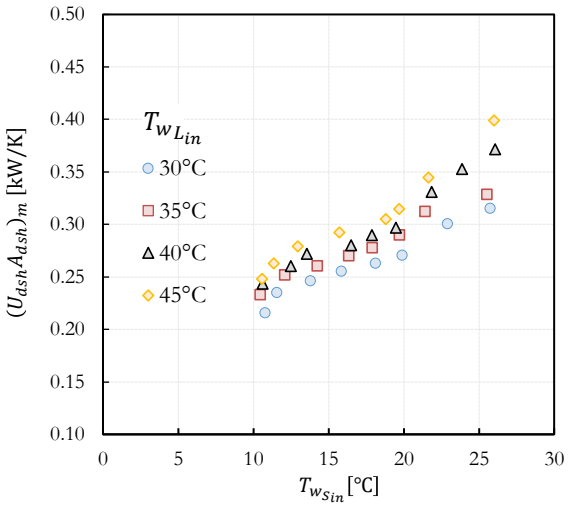

Figure B.2 Overall heat transfer coefficient in the desuperheating zone as a function of $T_{w_{S_{in}}}$ and $T_{w_{L_{in}}}$

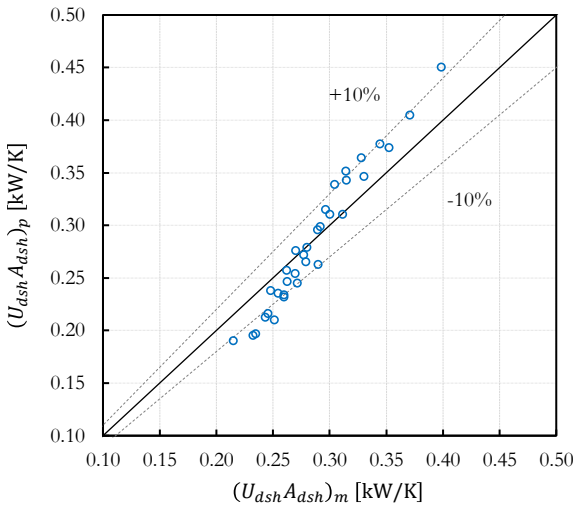

Figure B.3 Comparison of measured and predicted values of $U_{dsh}A_{dsh}$

For these operating conditions, values ranging from 0.2 kW/K to 0.4 kW/K are typically observed. An almost linear increase is noted with increasing values of $T_{w_{S_{in}}}$, primarily attributable to the rise

in refrigerant mass flow rate and an increase in the discharge temperature. Figure B.3 presents a comparison between the value of $U_{dsh}A_{dsh}$ obtained with the approach presented in this chapter and the same value predicted by the complete model.

As shown in this figure, these two values are typically within 10% of each other.

B.1.2 Condensation zone

A comparable analysis is conducted for $U_{cond}A_{cond}$ in the condensation zone of the condenser. The various parameters are indicated in Figure B.4

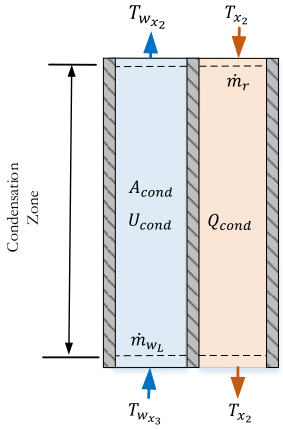

Figure B.4 Schematic representation of the condensation zone of the condenser

The value of $(U_{cond}A_{cond})_m$ is determined based on the following equation:

$$(U_{cond}A_{cond})_m = \frac{Q_{cond}}{\Delta T_{lm_{cond}}} = \frac{Q_{cond}}{\left(T_{w_{x_3}} - T_{w_{x_2}}\right)} ln\left[\frac{\left(T_{x_2} - T_{w_{x_2}}\right)}{\left(T_{x_2} - T_{w_{x_3}}\right)}\right] \quad \text{(B.4)}$$

In this case, Q_{cond} is computed using the enthalpy of vaporization $\Delta H_{evap(T_{x_2})}$ at the saturation temperatures T_{x_2}, determined as indicated earlier from the condenser pressure measurement:

$$Q_{cond} = \dot{m}_r \Delta H_{evap(T_{x_2})} \quad \text{(B.5)}$$

The water temperature at the entrance of the condensation zone, $T_{w_{x3}}$, is calculated using Equation B.6.

$$Q_{cond} = \dot{m}_r C_{p,w} \left(T_{w_{x_2}} - T_{w_{x3}} \right) \tag{B.6}$$

The presentation of the calculated coefficients derived from the experimental results is depicted in Figure B.5, and the comparison with the model results is shown in Figure B.6.

As shown in Figure B.5, values ranging from 2.5 kW/K to 4.4 kW/K are typically observed for $U_{cond}A_{cond}$. An almost linear increase is noted with an increase in $T_{w_{S_{in}}}$ for a given value of $T_{w_{L_{in}}}$, This is primarily due to the increase in refrigerant mass flow rate and a decrease in condensing temperature, which leads to an increase in the enthalpy of vaporization.

In general, the condensation zone covers the greatest surface area of the heat exchanger, typically between 50 to 70% of the total area based on modeling results.

There are two factors that explain significant differences in some experimental values compared with those from the model. Firstly, as observed in Chapter 6, as $T_{w_{S_{in}}}$ increases, the error in predicting superheat also increases, which impacts the prediction of the refrigerant mass flow rate, since it is dependent on the density at the compressor suction. Secondly, the heat of vaporization $\Delta H_{evap(T_{x_2})}$ is greatly affected by the accuracy in measuring the saturation pressure of the condenser. However, Figure B.6 shows that the agreement between the measured $(U_{cond}A_{cond})_m$ and the predicted $(U_{cond}A_{cond})_p$ is relatively good.

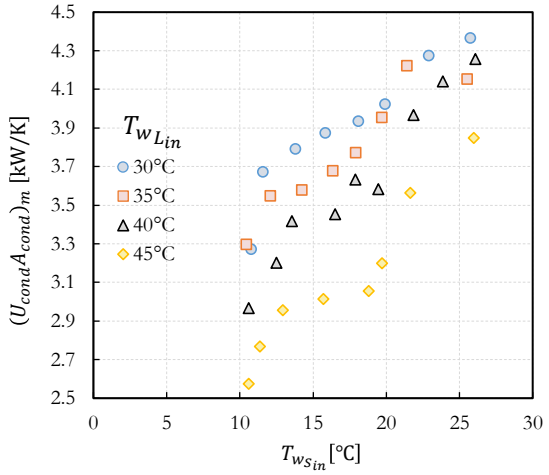

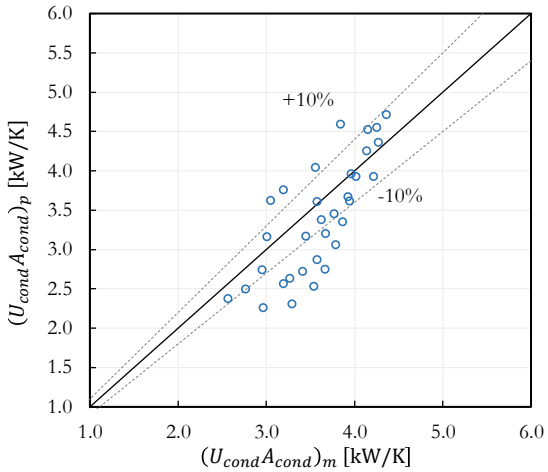

Figure B.5 Overall heat transfer coefficient in the condensation zone as a function of $T_{w_{S_{in}}}$ and $T_{w_{L_{in}}}$

Figure B.6 Comparison of measured and predicted values of $U_{cond}A_{cond}$.

B.1.3 Subcooling zone

The subcooling zone is presented schematically in Figure B.7. The calculation of $(U_{sc}A_{sc})_m$ follows the same procedure as the two previous sub-sections.

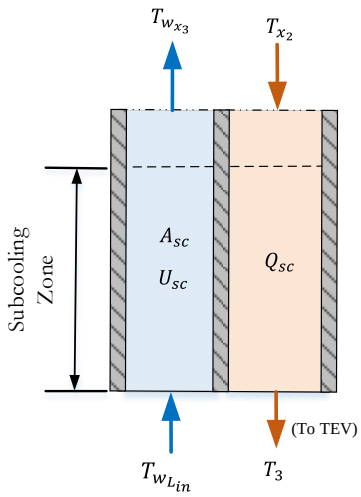

Figure B.7 Schematic representation of the subcooling zone of the condenser

The governing equation is given by:

$$(U_{sc}A_{sc})_m = \frac{Q_{sc}}{\Delta T_{lm_{sc}}} = \frac{Q_{sc}}{U_{sc}\left[\left(T_3 - T_{w_{L_{in}}}\right) - \left(T_{x_2} - T_{w_{x_3}}\right)\right]} ln \frac{\left(T_3 - T_{w_{L_{in}}}\right)}{\left(T_{x_2} - T_{w_{x_3}}\right)} \tag{B.7}$$

In this equation, all temperatures are measured or inferred from other measurements. The value of heat exchange rate in the subcooling zone is evaluated from the following equation:

$$Q_{sc} = \dot{m}_r C_{p,w}\left(T_{w_{x_3}} - T_{w_{L_{in}}}\right) \tag{B.8}$$

As previously discussed, an increase in the temperature of the secondary fluid in the evaporator ($T_{w_{S_{in}}}$) results in a corresponding increase in the mass flow rate of refrigerant due to the increase in density caused by a higher vaporization temperature. A higher refrigerant flow rate requires a larger surface area in the desuperheating zone and also in the condensation zone. Therefore, the

remaining area used for subcooling will be reduced which lowers the value of $U_{sc}A_{sc}$ as shown in Figure B.8.

As presented in Chapter 6, there are even operational conditions in which the refrigerant can exit the condenser as two-phase flow outside the subcooled region.

This phenomenon can be seen in Figure A.8. where some $U_{sc}A_{sc}$ values tend towards zero. This can be interpreted as operational conditions under which the refrigerant will leave the condenser in the mixing zone. i.e. A_{sc}tends towards zero.

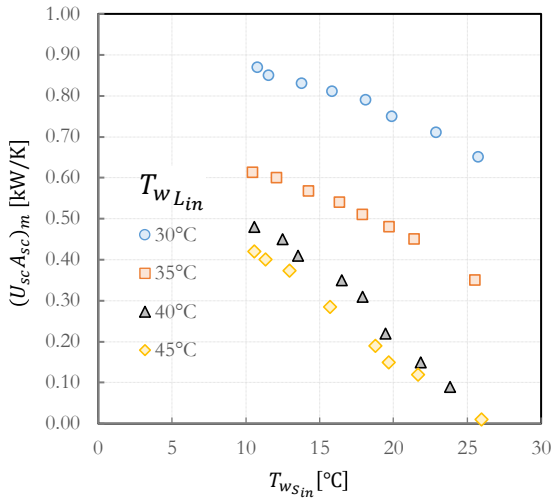

Figure B.8 Overall heat transfer coefficient in the subcooling zone as a function of $T_{w_{S_{in}}}$ and $T_{w_{L_{in}}}$

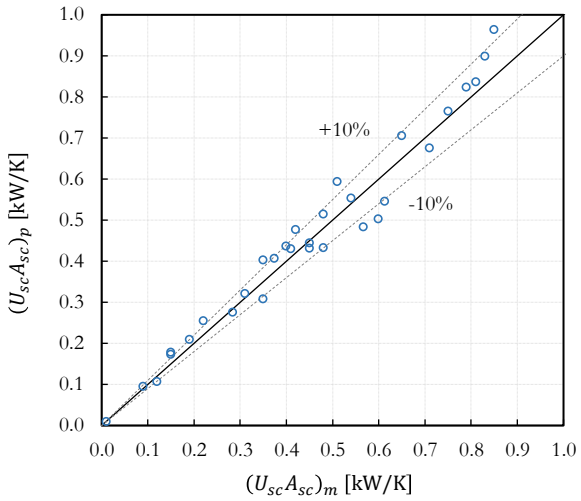

Figure B.9 Comparison of measured and predicted values of $U_{sc}A_{sc}$

Figure B.9 shows that the agreement between $(U_{sc}A_{sc})_m$ and $(U_{sc}A_{sc})_p$ is very good with most points within the ± 10% agreement line.

B.2 Overall heat transfer coefficients in the evaporator

B.2.1 Evaporation zone

The value of $(U_{evap}A_{evap})_m$ follows a similar approach to the ones established in the previous sections. The relevant nomenclature is presented in Figure B.10.

The value of $\left(U_{evap}A_{evap}\right)_m$ is determined based on the following equation:

$$\left(U_{evap}A_{evap}\right)_m = \frac{Q_{evap}}{\Delta T_{lm_{evap}}} = \frac{Q_{evap}}{\left(T_{w_{x_1}} - T_{w_4}\right)} ln\left[\frac{\left(T_{x_1} - T_{w_{x_1}}\right)}{\left(T_{x_1} - T_{w_4}\right)}\right] \quad \text{(B.9)}$$

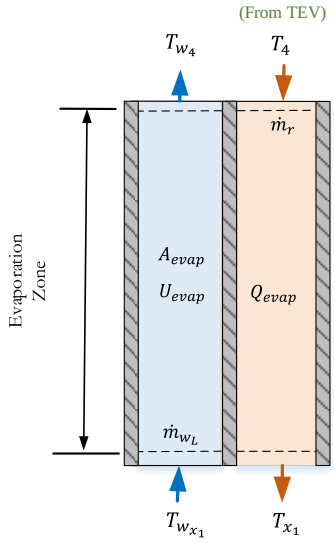

Figure B.10 Schematic representation of the evaporation zone in the evaporator

Here, Q_{evap} is determined by evaluating the enthalpy of vaporization $\Delta H_{evap(T_{x_1})}$ based on Equation A.10 at the saturation temperatures T_{x_1}, which is obtained from corresponding saturation pressure measurements.

$$Q_{evap} = \dot{m}_r(1 - x_4)\Delta H_{evap(T_{x_1})} \quad \text{(B.10)}$$

The vapor quality x_4 is calculated by assuming isenthalpic expansion based on enthalpy h_3 determined using measurements of T_3 and P_{cond} along with the pressure in the evaporator.

The calculated coefficients derived from the experimental results are presented in Figure B.11, and the comparison with the modeling results is shown in Figure B.12. As shown in Figure B.11, values ranging from 1.6 kW/K to 4.1 kW/K are typically observed.

An almost linear increase is noted with an increase in $T_{w_{S_{in}}}$ for a given value of $T_{w_{L_{in}}}$, primarily due to the increase in refrigerant mass flow rate and a decrease in condensing temperature, which leads to an increase in the enthalpy of vaporization. Figure B.12 shows that there is a relatively good agreement between $(U_{evap}A_{evap})_m$ and $(U_{evap}A_{evap})_p$.

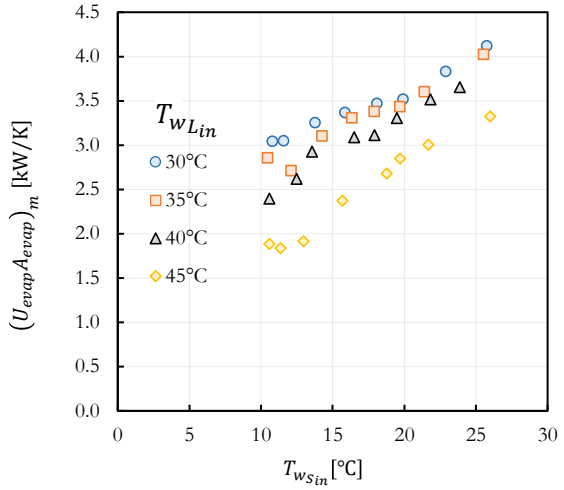

Figure B.11 Overall heat transfer coefficients in the evaporation zone a as a function of $T_{w_{S_{in}}}$ and $T_{w_{L_{in}}}$

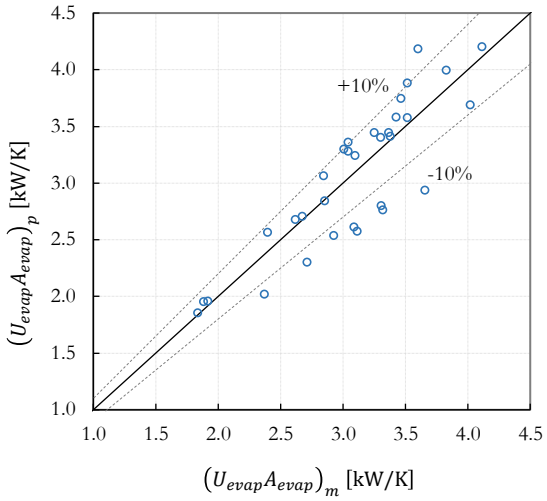

Figure B.12 Comparison between measured and predicted values of $U_{evap}A_{evap}$

B.2.2 Superheated zone

The calculation of $(U_{sh}A_{sh})_m$ (see Figure B.13) is determined based on the following equation:

$$(U_{sh}A_{sh})_m = \frac{Q_{sh}}{\Delta T_{lm_{sh}}} = \frac{Q_{sh}}{U_{sh}\left[\left(T_1 - T_{w_{S_{in}}}\right) - \left(T_{x_1} - T_{w_{x_1}}\right)\right]} ln \frac{\left(T_1 - T_{w_{S_{in}}}\right)}{\left(T_{x_1} - T_{w_{x_1}}\right)} \quad \text{(B.11)}$$

Q_{sh} is calculated from Equation B.12 where T_1 is the temperature of the secondary fluid at the outlet of the evaporator and T_{x_1} is the evaporation temperature calculated as indicated earlier using the evaporator pressure measurement.

$$Q_{sh} = \dot{m}_r C_{p,r}\left(T_1 - T_{x_1}\right) \quad \text{(B.12)}$$

The presentation of the calculated coefficients derived from the experimental results is depicted in Figure B.14, and the comparison with the model results is shown in Figure B.15.

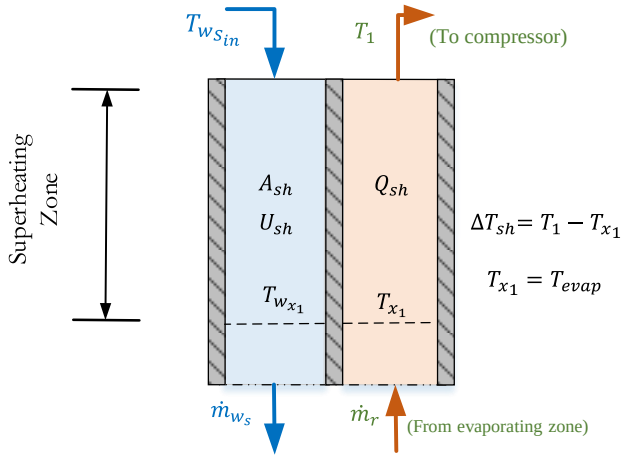

Figure B.13 Schematic representation of the superheating zone in the evaporator

In this case, the increase in $(U_{sh}A_{sh})_m$ alongside the rise in $T_{w_{s_{in}}}$ is more noticeable due to two factors: firstly, the increase in refrigerant mass flow rate, and secondly, the increase in superheat, which, as demonstrated in Chapter 6, escalates with a higher $T_{w_{s_{in}}}$. Values ranging from 0.2 kW/K to 0.9 kW/K are typically observed. Figure B.15 shows that the agreement between $(U_{sh}A_{sh})_m$ and $(U_{sh}A_{sh})_p$ is very good with most points within the ± 10% agreement line.

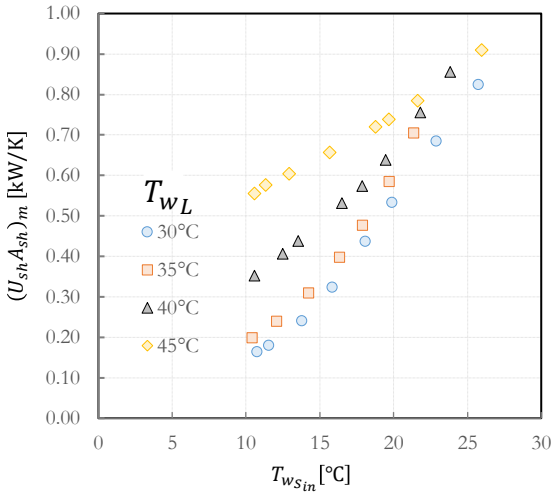

Figure B.14 Overall heat transfer coefficients in the superheating region as a function of $T_{w_{s_{in}}}$ and $T_{w_{L_{in}}}$

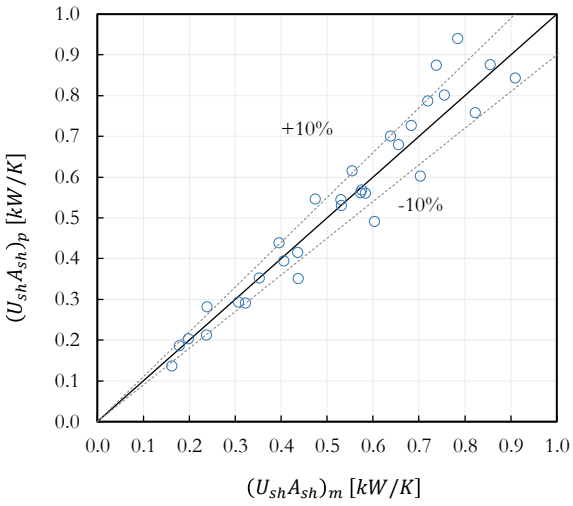

Figure B.15 Comparison of measured and predicted values of $U_{sh}A_{sh}$

B.3 Simplified heat pump model using $(U_iA_i)_m$

In this section a simplified heat pump model is presented. It is essentially based on the complete heat pump model with the heat exchanges in the evaporator and condenser based on the use of experimentally derived values of U_iA_i as determined in the previous sections.

B.3.1 Correlations for UiAi

Based on the analysis of the previous sections, it is proposed to approximate the behavior of U_iA_i as a linear function of the inlet temperature of the secondary fluids:

$$U_iA_i = a + bT_{w_{L_{in}}} + cT_{w_{S_{in}}} \tag{B.13}$$

Through a parameter adjustment of the values calculated from experimental data, the values a, b, and c are presented in Table B.1. As shown in the bottom two lines of this table, the linear relationship proposed with Equation B.13 leads to adequate values of the RMSE and R^2

The model is valid within source temperatures of 10 ºC to 26 ºC and load temperatures of 30 ºC to 45 ºC. Mass flow rates are 0.565 L/s for the load and 0.308–0.462 L/s for the source.

Table B.1 Adjusted coefficients for Equation B.13 for each zone

	$U_{dsh}A_{dsh}$	$U_{cond}A_{cond}$	$U_{sc}A_{sc}$	$U_{evap}A_{evap}$	$U_{sh}A_{sh}$
a	-0.38144	-4.466	2.248	3.5490	-0.821
b	0.01116	0.1126	-0.02169	0.09063	0,0361
c	0.01317	0.1549	-0.03767	-0.05282	0.0196
RMSE [kW/K]	0.0265	0.465	0.0679	0.191	0.0566
R^2 [%]	92.5	84.1	92.6	90.1	93.3

B.3.2 Governing equations for the simplified heat pump model

This approach allows for a simplification of the heat pump model, requiring only two balance equations for each zone as shown in Figure B.16, for six equations with six unknowns for the condenser and a system of four equations with four unknowns for the evaporator. Using simplified U_iA_i correlations reduces the number of equations since it eliminates the calculation of heat transfer coefficients based on correlations for each fluid in each zone. Additionally, it eliminates the calculation of the surface area used in each zone. Given that the U_iA_i term is calculated as a function of the model inputs at time i, i.e., $U_iA_i = f(T_{w_{L_{in_i}}}, T_{w_{S_{in_i}}})$, the resolution of the heat exchanger

model is simplified since the NTU_i in each section is now known, and therefore the local effectiveness in each zone, ε_i, is also known.

The governing equations are presented in Figure B.16.

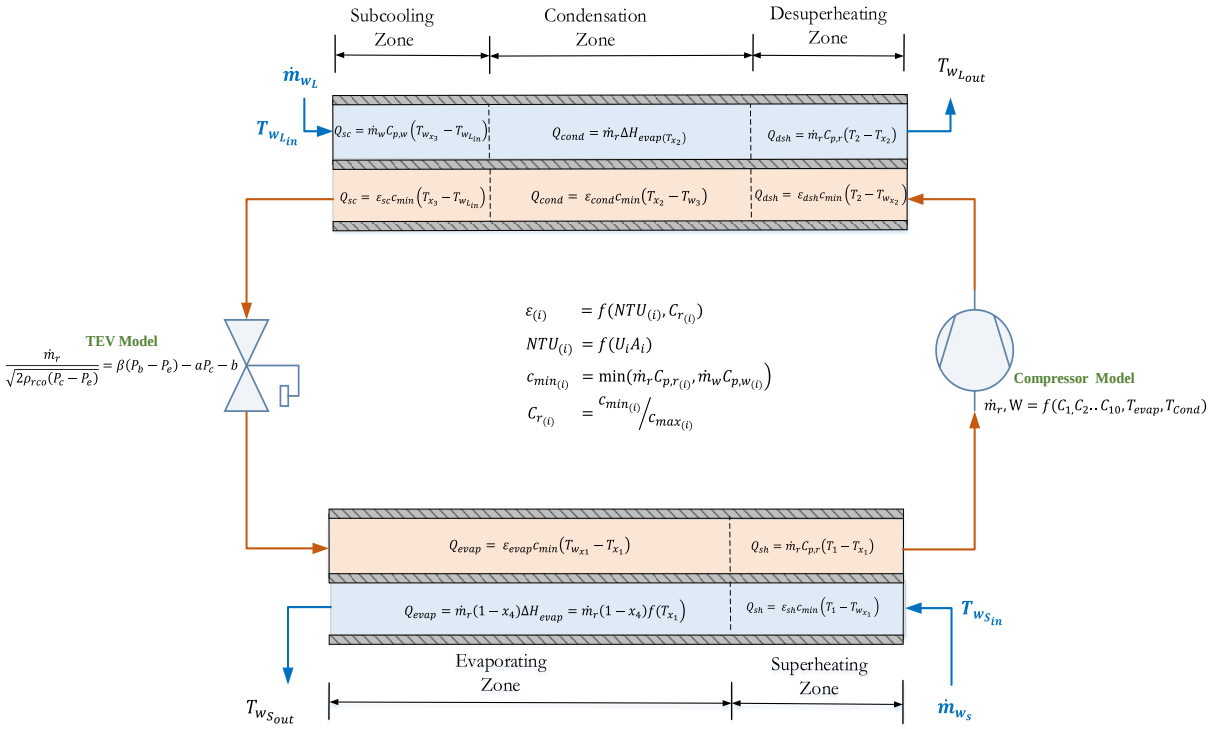

Figure B.16 Governing equations in the simplified model

The compressor model remains based on the standard AHRI 540, and the expansion valve model is the one presented in Chapter 6.

B.4 Comparative analysis between the complete model and the simplified model

The simplified model was used to predict the COP for 32 experiments in heating mode. The results all fall within a 10% deviation from the complete model, as shown in Figure B.17.

Additionally, using the model to perform long-term calculations during simulations over an entire heating season shows a 50% reduction in computation time. Furthermore, reduction in convergence issues were significant.

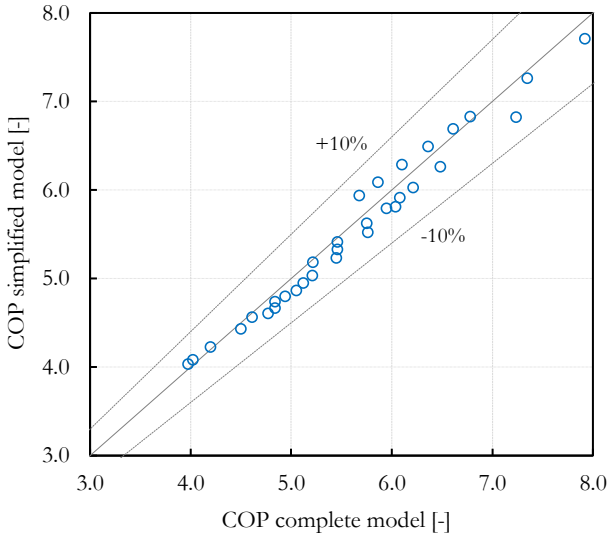

Figure B.17 Comparison of COP values for the complete model and the simplified model

B.5 Conclusion

The development of comprehensive heat pump models presents a significant challenge, primarily due to the complexity involved in accurately modeling heat exchanges in the evaporator and condenser. This section highlights the pivotal role of experimentally-derived overall heat transfer coefficients ($U_i A_i$) in simplifying these calculations, thereby enhancing the computational efficiency and stability of the models. The behavior of the heat transfer coefficients is approximated as linear functions of the inlet temperatures of the secondary fluids, with the coefficients being adjusted based on direct measurements from experiments.

This approach substantially reduces the complexity of the heat pump model, converting what would be a highly nonlinear system into a manageable series of equations.

The verification against the results of 32 experiments in heating mode shows that the simplified model can predict the heating COP within 10% of the complete model, confirming its reliability for practical applications. Incorporating these simplifications allows for a 50% reduction in computation time and enhances solver stability during long-term simulations, which is crucial for seasonal performance evaluations of such heat pumps in building simulation programs. In the future, the simplified model needs to be tested outside the range of the 32 experiments on which it is based to demonstrate its accuracy.